

Magazine of Civil Engineering

114(6), 2022

ISSN
2712-8172



Magazine of Civil Engineering

ISSN 2712-8172

Online peer-reviewed open-access scientific journal in the field of Civil and Construction Engineering

Founder and Publisher: Peter the Great St. Petersburg Polytechnic University

This journal is registered by the Federal Service for Supervision of Communications, Information Technology, and Mass Media (ROSKOMNADZOR) in 2020. Certificate EI No. FS77-77906 issued February 19, 2020.

Periodicity: 8 issues per year

Publication in the journal is open and free for all authors and readers.

Indexing: Scopus, Web of Science (ESCI, RSCI), DOAJ, Compendex, EBSCO, Google Academia, Index Copernicus, ProQuest, Ulrich's Serials Analysis System, CNKI

Corresponding address: 29 Polytechnicheskaya st., Saint Petersburg, 195251, Russia

Chief science editor: associate member of RAS, Sc.D. in Engineering, Vitaly V. Sergeev

Deputy chief science editor: Sc.D. in Engineering, Galina L. Kozinetc

Executive editor: Ekaterina A. Linnik

Translator, editor: Darya Yu. Alekseeva

DT publishing specialist: Anastasiya A. Kononova

Contacts:

E-mail: mce@spbstu.ru

Web: <http://www.engstroy.spbstu.ru>

Date of issue: 03.10.2022

© Peter the Great St. Petersburg Polytechnic University. All rights reserved.

© Coverpicture – Ilya Smagin

Editorial board:

T. Awwad, PhD, professor, Damascus University, Syrian Arab Republic

M.I. Balzannikov, D.Sc., professor, Samara State University of Economics, Russia

A.I. Belostotsky, D.Sc., professor, StaDyO Research & Engineering Centre, Russia

A.I. Borovkov, PhD, professor, Peter the Great St. Petersburg Polytechnic University, Russia

A. Borodinecs, Dr.Sc.Ing., professor, Riga Technical University, Latvia

M. Veljkovic, PhD, professor, Delft University of Technology, The Netherlands

R.D. Garg, PhD, professor, Indian Institute of Technology Roorkee (IIT Roorkee), India

M. Garifullin, PhD, postdoctoral researcher, Tampere University, Finland

T. Gries, Dr.-Ing., professor, RWTH Aachen University, Germany

T.A. Datsyuk, D.Sc., professor, Saint-Petersburg State University of Architecture and Civil Engineering, Russia

V.V. Elistratov, D.Sc., professor, Peter the Great St. Petersburg Polytechnic University, Russia

T. Kärki, Dr.-Ing., professor, Lappeenranta University of Technology, Russia

G.L. Kozinetc, D.Sc., professor, Peter the Great St. Petersburg Polytechnic University, Russia

D.V. Kozlov, D.Sc., professor, National Research Moscow State Civil Engineering University, Russia

S.V. Korniyenko, D.Sc., professor, Volgograd State Technical University, Russia

Yu.G. Lazarev, D.Sc., professor, Peter the Great St. Petersburg Polytechnic University, Russia

M.M. Muhammadiev, D.Sc., professor, Tashkent State Technical University, Republic of Uzbekistan

H. Pasternak, Dr.-Ing.habil., professor, Brandenburgische Technische Universität, Germany

F. Rögner, Dr.-Ing., professor, Technology Arts Science TH Köln, Germany

V.V. Sergeev, D.Sc., professor, Peter the Great St. Petersburg Polytechnic University, Russia

T.Z. Sultanov, D.Sc., professor, Tashkent Institute of Irrigation and Agricultural Mechanization Engineers, Republic of Uzbekistan

M.G. Tyagunov, D.Sc., professor, National Research University "Moscow Power Engineering Institute", Russia

M.P. Fedorov, D.Sc., professor, Peter the Great St. Petersburg Polytechnic University, Russia

D. Heck, Dr.-Ing., professor, Graz University of Technology, Austria

A.G. Shashkin, D.Sc., "PI Georekonstruktsiya", LLC, Russia

V.B. Shtilman, D.Sc., JSC "B.E. Vedeneev VNIIG", Russia

Contents

Gai, X., He, D., Wang, H. Shear strengthening of RC beam using RFRP composites	11401
Ngo, V.T., Bui, T.T., Lam, T.Q.K., Do, T.M.D., Nguyen, T.T.N. Fracture characteristics of high-performance concrete using nano-silica	11402
Zakharov, A.V., Ponomaryov, A.B., Ofrikhter, I.V. Model of soil thermal conductivity in the form of a truncated sphere	11403
Shevchenko, G.G., Brin, M.Ya., Gura, D.A., Khusht, N.I., Tamov, M.M. The method of determining the trend equation for predicting vertical displacements by the search method of nonlinear programming	11404
Rodriguez Vazquez, S., Mokrova, N. AHP-TOPSIS hybrid decision support system for dam site selection	11405
Usarov, M.K., Mamatisaev, G.I., Ayubov, G.T. Forced vibrations of a box element of a multi-story building under dynamic impact	11406
Bostel, R., dos Santos, A.C.P., Lopes, J.B.O., Willrich, F.L., Basso, R.L.O., Honnicke, M.G. Bond testing of salty-sand concrete reinforced with different rebars	11407
Ibragimov, R.A., Korolev, E.V. Influence of electromagnetic field on characteristics of crushed materials	11408
Valiullin, D.A., Chizhov, S.V. Bolted connections stiffness of steel trusses for bridge superstructures	11409
Stekalovskaya, D.A., Baturova, L.P., Semencha, A.V., Aleksandrova, E.K. Functional indium oxide-based thin-film coatings with variable light transmission	11410
Sainov, M.P. Assessment of crack resistance of ultra-high earth core rockfill dam by pore pressure	11411
Korniyenko, S.V. The influence of the sky radiative temperature on the building energy performance	11412
Rassokhin, A.S., Ponomarev, A.N., Karlina, A.I. High-performance fine-grained nanostructured concrete based on low strength aggregates	11413
Fedorovskaya, A.A., Sheina, S.G. Comprehensive assessment for optimal wind energy use in cottage construction	11414



Research article

UDC 69.07

DOI: 10.34910/MCE.114.1



Shear strengthening of RC beam using RFRP composites

X. Gai , D. He , H. Wang 

Northeast Forestry University, Harbin, Heilongjiang, China

✉ wanghongguang@zoho.com

Keywords: natural fibers, surface treatment, strength of materials, shear stress

Abstract. Partial or complete replacement of non-renewable composite materials with natural fiber reinforced polymer composites, such as basalt fiber, carbon fiber and glass fiber reinforced polymer composite can reduce the consumption of non-renewable resources and damage to the ecological environment in civil engineering construction. It is of great significance for solving global warming, developing green manufacturing and low-carbon cities, and promoting sustainable development in civil engineering. Therefore, this paper focused on mechanical properties of ramie fiber reinforced polymer (RFRP) composites. Furthermore, the shear capacity of RC beams strengthened with ramie fiber sheet was studied, and the bearing characteristics and failure modes of RC beams strengthened with fiber reinforced polymer composites was analyzed. The results show that after the surface treatment with dilute hydrochloric acid, silane coupling agent (KH-550 and KH-560) and aluminum zirconium coupling agent, the mechanical properties of RFRP composites enhanced significantly. Moreover, the surface wettability and interfacial properties of ramie fiber to the epoxy resins were improved by about 40 %. The shear strength results show that after the reinforcement of ramie fiber sheets, the bearing capacity and mid-span deflection of RC beams were greatly improved, and the silane coupling agent (KH-560) modifying ramie fiber sheets had better reinforcement than other fiber sheets. It could be concluded that the replacement of ordinary fiber sheets by ramie fiber sheets can not only reduce the consumption of non-renewable resources, but also improve the shear resistance of RC beams strengthened with the fiber sheets.

Acknowledge: The work was financially supported by the Heilongjiang Natural Science Foundation (Project No. LH2019E112).

Citation: Gai, X., He, D., Wang, H. Shear strengthening of RC beam using RFRP composites. Magazine of Civil Engineering. 2022. 114(6). Article No. 11401. DOI: 10.34910/MCE.114.1

1. Introduction

Material is the material basis for human survival and a pillar industry for the development of the country's national economy. With the continuous development of new technologies and new processes in the field of engineering, higher requirements are imposed on new materials, which not only require excellent mechanical properties and good durability, but also have environmental protection, renewable, and degradable functions [1, 2]. Fiber reinforced composite (FRP) material is a kind of structural material with high strength, low density and excellent design performance [3], which is composed of reinforcing fiber and resin matrix. It has a wide range of applications in machinery, aviation, chemical industry, etc. The fiber in FRP composite material is widely used carbon fiber, glass fiber and basalt fiber, including new high-performance fibers, such as alumina fiber and silicon carbide fiber. With the continuous development of new technologies and new equipment, high-performance fibers make composites materials functionalization and high-performance development.

At present, in the fields of aerospace, transportation, infrastructure construction, energy and environmental protection, high-performance fibers and their FRP composite materials have played an increasingly important role and have become irreplaceable. Basalt fiber has excellent properties such as high strength, high modulus and corrosion resistance [4]. It is an ideal and reinforcing material with no pollution. Ramie fiber has high specific strength, short growth period, environmental friendliness, wide source and low price [5]. Advantages, as reinforcing fiber materials used in civil engineering structures, can be reduced the consumption of non-renewable resources and the destruction of the ecological environment in civil engineering construction are of great significance for solving global warming, developing low-carbon buildings and cities, and promoting the sustainable development of civil engineering.

China is the largest country use concrete in the world. Under the dual action of long-term natural environment and service load, the bearing capacity of the structure gradually decreases. The reliability of the structure will gradually decline, threatening the safety of the use of the structure. In recent years, the application of FRP composite materials in the field of civil engineering reinforcement has been a research hotspot at home and abroad [6–8]. With the continuous development of composite technology, high-strength and high-performance carbon fiber sheets, glass fiber sheets and basalt fiber sheets have been applied in practical engineering. The strength of carbon fiber sheets is the highest among various FRPs, but the carbon fiber elongation (about 1 % to 1.5 %) is smaller than that of glass fiber (about 2 % to 5 %) [9]. The confined concrete finally shows sudden brittle failure, and the price of carbon fiber sheets is several times higher than that of glass fiber sheets [10]. So the reinforcement cost is relatively high.

Over the last few years, research works found that natural fiber reinforced polymer composite provide a good alternatives to synthetic fiber composites and it has been accepted as a repairing and strengthening materials for structures in the construction industry [11, 12]. Ramie fiber is derived from the phloem portion of ramie and is a naturally renewable plant fiber. Compared to synthetic fibers, the mechanical properties of ramie fiber monofilaments are relatively low, only one-third to one-quarter of that of glass fibers. At the same time, because the surface of the ramie fiber contains a large amount of hydrophilic hydroxyl groups, the water absorption is large, and the wet heat durability of the composite material is poor, which greatly limits the application potential of the ramie fiber as a reinforcing material in the field of civil engineering. At present, the modification methods of ramie fiber surface are mainly treatment [13, 14], ultrasonic treatment [15, 16], chemical coating modification [17–19] and coupling agent modification [20, 21]. These methods only have mechanical properties or interfacial adhesion to ramie fiber monofilament from a single angle [22–24]. The performance of the modification study, without considering the synergistic enhancement of mechanical and interfacial adhesion properties, the modification effect and application prospects are not ideal.

In this paper, the shear capacity, the bearing characteristics and failure modes of RC beams and the RC beams strengthened with ramie fiber sheets, unidirectional basalt fiber sheets by contrast test were studied.

2. Materials and methods

2.1. Materials

(1) Concrete

RC test beam with commercial concrete (concrete grade is C30), water-cement ratio is 0.42, the ratio is cement : water : sand : gravel = 360 : 151 : 632 : 1282. The cement adopts the Swan brand P.O grade 42.5 ordinary Portland cement produced by Harbin Cement Factory of Jilin Yatai Group of China. The maximum particle size of coarse aggregate is about 25 mm. The measured concrete slump is 43 mm. After the pouring is completed, the RC test beam is continuously subjected to room temperature watering for 7 days, and then remove the mold and rinse it to 28 days. The concrete cube compressive strength test was prepared in the same batch after pouring RC test beams, and place it in a standard maintenance room for maintenance 28 days. According to the requirements of the national standard for the test of mechanical properties of ordinary concrete (GB/T 50081-2011), the compressive strength of the concrete cube was measured to be 35 MPa to 40 MPa.

(2) Reinforcement

The longitudinal reinforcement, structural reinforcement and standing reinforcement are respectively 25 mm, 14 mm and 12 mm, using HRB400 grade ordinary hot rolled ribbed steel bar. The diameter of the stirrup is 8 mm, using HPB300 grade hot rolled round bar.

According to the requirements of the national standard test method for tensile testing of metallic materials (GB/T 228-2010), the mechanical properties of the steel bars measured are shown in Table 1.

Table 1. Mechanical properties of reinforcements in the RC beams

Rebar type	Reinforcement grade	Diameter (mm)	Yield Strength (MPa)	Tensile strength (MPa)	Elongation (%)
Vertical reinforcement	HRB400	25	410	570	20.0
Structural reinforcement	HRB400	14	410	565	21.5
Erecting steel bars	HRB400	12	390	560	20.0
Stirrup	HPB300	8	310	450	25.0

(3) Ramie fiber sheets and basalt fiber sheets

In order to study on the effect of ramie fiber sheet on the shear resistance of RC beams in different directions and compositions, the preparation of ramie fiber composite material by using two-way ramie fiber sheets produced by China Harbin Linum Textile Co., Ltd. The density of the fiber cloth is 1.5g/cm^3 , nominal thickness is 0.16 mm, the spinning process is ring spinning.

In order to compare the effects of different types of ramie fiber sheets on the shear reinforcement of RC beams, this paper also uses basalt fiber sheets to reinforce the RC beams. Basalt fiber sheets is produced by Sichuan Aerospace Tuoxin Basalt Industrial Co., Ltd.

(4) Epoxy resin and curing agent

Attach ramie fiber sheets to the outer surface of RC beams, making it work with RC. The epoxy resin impregnating rubber JZ-A and the curing agent JZ-B are mixed according to a mass ratio of 100:34.5, and cured at room temperature. Measured in the laboratory, the tensile strength and modulus of the epoxy resin impregnated rubber are 59.1 MPa and 3.08 GPa, the glass transition temperature is about $62.5\text{ }^\circ\text{C}$.

2.2. Main instruments and equipment

In the test of shear capacity of RC beams strengthened with ramie fiber sheets, the main test instruments and equipment used are shown in Table 2.

Table 2. Main experimental instruments and equipment

Test instrument and equipment	Specifications and models	Manufacturer
High-speed static strain test analysis system	16 aisle, DH3820	Jiangsu Donghua Testing Technology Co., Ltd.
Pressure Sensor	250t, GD-250T	Fuzhou Jingkong Automation Equipment Co., Ltd.
Linear variable differential transformer	25 mm, MHR-25	Shanghai Ruihong Testing Technology Co., Ltd.
Resistance strain gauge	120 Ω , BE120-10AA 120 Ω , BQ120-60AA	AVIC Electric Instrument Co., Ltd.

2.3. Experimental program

2.3.1. Structural design of RC beams

Comparative test on shear reinforcement of RC beams with ordinary ramie fiber sheets and basalt fiber sheets. The RC beam has a length of 1800 mm and a section size of 200 mm \times 400 mm, and the main structural dimensions are shown in Fig. 1.

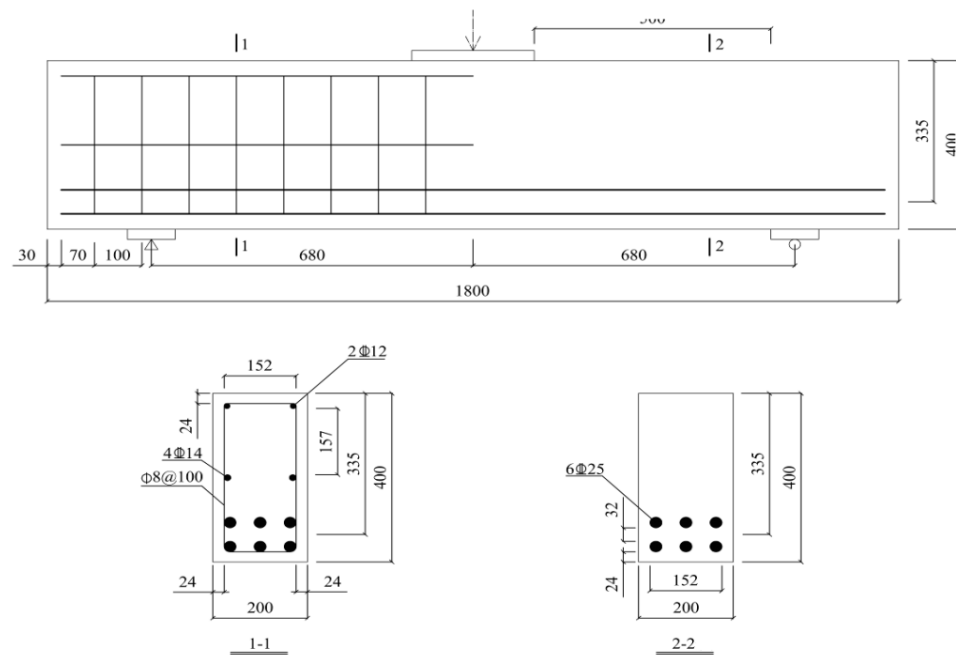


Figure 1. Structural design of the RC beam.

According to the requirements of the national standard of Concrete Structure Design Code (GB 50010-2010), in order to cause shear failure of RC beams, a sufficient number of longitudinal steel bars should be placed in the span of the beams to ensure that the bending failure does not occur before the shear failure. As shown in Fig. 1, the RC beams are equipped with a certain number of stirrups in the left half span, and half-span structural steel bars are arranged in the middle of the cross section to improve the shear capacity of the left half span. At the same time, ensuring the shear failure occurs only in the right half span to facilitate test measurements.

2.3.2. Experimental program of FRP strengthened RC beams in shear capacity

This paper designs 6 RC beams, RC-control is not reinforced, RC-FRP 1 to RC-FRP4 are reinforced with ordinary ramie fiber sheets, and the number of layers is 3 and 6 respectively, the main direction of the ramie fiber sheets is the warp and weft directions. The main direction of the ramie fiber sheets is the warp direction. RC-FRP 5 is reinforced with unidirectional basalt fiber sheets and the number of layers is 1 layer. The experimental program of FRP strengthened RC beams in shear capacity is shown in Table 3.

Table 3. Experimental program of FRP strengthened RC beams in shear capacity

RC beam	Fiber sheets type	Main direction of force	Paste layer
RC-FRP1	Ordinary fiber sheets	vertical	3
RC-FRP2	Ordinary fiber sheets	vertical	3
RC-FRP3	Ordinary fiber sheets	Latitude	6
RC-FRP4	Ordinary fiber sheets	Latitude	6
RC-FRP5	Unidirectional basalt fiber sheets	—	1

The width of fiber sheets is 300 mm and the length of fiber sheets is 1000 mm. Paste mode is U-shaped reinforcement. The paste position is shown in Fig. 2. After the RC beam is finished, transporting it to the experimental site for loading test. In order to facilitate the centering and crack width measurement and recording of the concrete beam loading device and describing the test phenomenon, the side of the RC-control is painted, and the extension direction is divided into 100 mm × 100 mm standard grid. During the test, the three-point bending load is applied and loaded by force. The support mode is the left fixed hinge support and the right movable hinge support. The LVDT sensor is arranged in the span of the RC beam, on the side of the bonded fiber sheets and at the fulcrum, collecting the longitudinal displacement of the beam at different positions. A resistance strain gauge is attached to the surface of the RC-control concrete surface and the fiber sheets surface of the remaining beams to collect the strain generated by the concrete and the fiber sheets. All displacement and strain signals in the test are converted into potential signals by the strain collector.

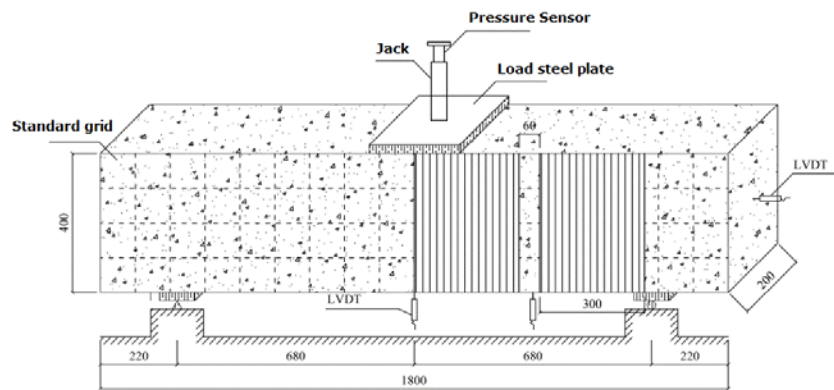


Figure 2. Experimental program of FRP strengthened RC beams in shear capacity.

3. Results and Discussion

3.1. Experimental results and analysis of ordinary RC beams in shear capacity

3.1.1. Major damage phenomena and processes

After 28 days of standard maintenance of all reinforced concrete, transfer it to the test site and attach the fiber cloth according to the experimental program of FRP strengthened RC beams in shear capacity. Firstly, the shear capacity test of RC-control was performed. Before the test, in order to facilitate the centering and crack width measurement and recording of the concrete beam loading device and describing the test phenomenon, the side of the RC-control is painted, and the extension direction is divided into 100 mm × 100 mm standard grid. The mesh and strain gauge placement of the RC-control is shown in Fig. 3.



Figure 3. Mesh and strain gauges on the surface of the RC-control beam.

At the beginning of the test, RC-control produces vertical micro cracks near the beam's span, and there are also many tiny cracks perpendicular to the lower edge of the concrete beam in the unformed stirrups on the right side. As the load continues to increase, the number of right half-span cracks of the beam gradually increases and extends upward. It can be clearly seen that one of the many oblique cracks has the largest width and gradually forms a critical oblique crack. After the occurrence of critical oblique cracks, the number of vertical cracks at the bottom of the mid-span section tends to be stable, and the crack width increases slowly. When the oblique crack expands to a certain extent, the oblique crack begins to branch near the bottom side of the beam, that is, a gentle steel bond crack occurs. As the load increases, the critical oblique crack continues to develop upward and extends below the mid-span loading point. No new oblique cracks will occur until the concrete in the span is crushed and destroyed. RC-control is a typical shear failure mode, and its failure mode and crack distribution are shown in Fig. 4.

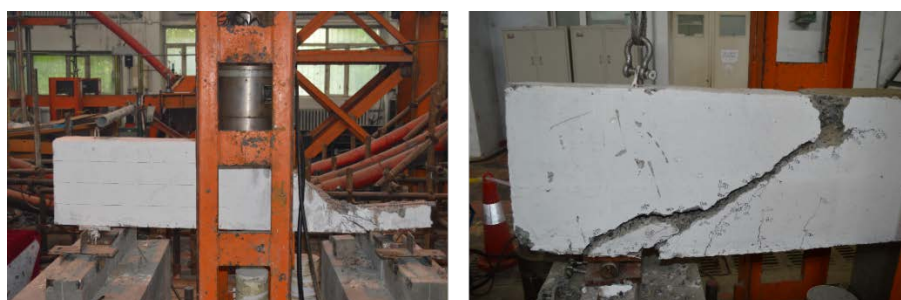


Figure 4. Failure modes and crack distribution of RC-control beam.

3.1.2. Characteristic load and load-span displacement curve

Central deflection and load curves of RC-control is shown in Fig. 5. Central deflection and load curves of RC-control is divided into three main stress processes: elastic phase, cracked working phase and critical failure phase. At the beginning of loading, as the load is gradually increased, the mid-span deflection value of RC-control increases linearly.

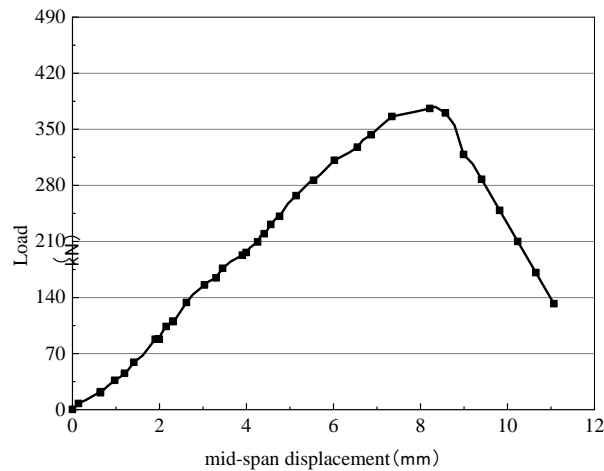


Figure 5. Central deflection and load curves of RC-control beam.

When the load reaches about 176 kN (46.6 %), a crack with the largest width can be found in the right half span of the beam, and a critical oblique crack is gradually formed. When the load reaches 352 kN (93.1 %), the critical oblique crack extends below the mid-span loading point, after which no new oblique cracks appear until the concrete in the span is crushed and destroyed. Finally, the ultimate bearing capacity of the RC-control is 378 kN, and the mid-span ultimate deflection is 8.3 mm.

3.2. Experimental results and analysis of FRP strengthened RC beams in shear capacity

3.2.1. Major damage phenomena and processes

(1) RC beam reinforced with ramie fiber sheets

When the RC beam reinforced with ramie fiber sheets, at the beginning of the loading, no obvious oblique cracks were observed on the RC surface. As the RC beam is subjected to increasing loads, the ramie fiber sheets occasionally makes a slight sound, but no visible damage is seen from the appearance. After that, the load continued to increase, and the RC beam continued to emit a slight crack, and the ramie fiber sheets near the support showed clear cracks in the middle and lower parts, and continued to expand. As the load continued to increase, the ramie fiber sheets suddenly burst into a crisper sound. According to the different reinforcement methods, the load level at this time is 470 kN ~ 495 kN, and the mid-span deflection value is 9.7 mm ~ 10.1 mm. Finally, along with the crisp and loud cracking sound, the ramie fiber sheets near the loading point of the mid-span also exits the work, showing obvious delamination and bulging outward. The concrete in the middle of the span is rapidly crushed, and the RC beam is broken by compression shearing. At the same time, a thin layer of concrete is attached to the inside of the ramie fiber sheets. The failure mode of RC beams strengthened with ramie fiber sheets is shown in Fig. 6.

(2) RC beam reinforced with unidirectional basalt fiber sheets

In order to compare the effect of reinforcing RC with ramie fiber sheets, basalt fiber sheets reinforcement is used as a comparison. At the beginning of the test, no obvious cracks were observed on the surface of the RC beam tension zone. As the load continues to increase, the RC beam is placed on one side of the stirrup first with obvious oblique cracks, and gradually expands and deepens. When the load is increased to about 484 kN, the concrete beam suddenly has a large cracking sound, and the concrete at the bottom of the left beam is peeled off. The reinforcement of the tension zone has reached the yield strength, and the concrete in the compression zone is crushed. The increase of the bearing capacity of the beam is obviously slowed down. When the load reached 543 kN, the reinforced concrete beam suddenly broke. Different from the failure mode of RC beams strengthened with ramie fiber sheets, the basalt fiber sheets did not appear to be broken or peeled off. Finally, the shear capacity of concrete beams is close to the test results of ramie fiber sheets reinforced. The failure mode of RC beams strengthened with basalt fiber sheets is shown in Fig. 6.



Figure 6. Failure mode of the RC beam strengthened with basalt fiber sheets.

3.2.2. Characteristic load and load-span displacement curve

The characteristic loads of RC beams are shown in Table 4.

Table 4. Characteristics load of the RC beams

Numbering	P_1 (kN)	δ_1 (mm)	P_2 (kN)	δ_2 (mm)	P_u (kN)	δ_u (mm)	P_1/P_u (%)	P_2/P_u (%)	ΔP_u (%)
RC-control	–	–	–	–	378	8.3	–	–	–
RC-FRP1	470	9.7	519	10.5	550	11.6	85.6	94.5	45.4
RC-FRP2	488	10.1	528	11.2	565	12.2	86.2	93.3	49.6
RC-FRP3	495	10.1	551	11.1	579	12.3	85.4	95.1	53.2
RC-FRP4	473	10.0	535	11.2	559	11.8	84.7	95.8	47.8
RC-FRP5	–	–	–	–	543	11.7	–	–	43.5

Since the concrete crack in the tension zone cannot be observed after the ramie fiber sheets is reinforced, the cracking load of the concrete is not listed in the table. In Table 4, P_u is the maximum load that the RC beam is subjected to when it is destroyed, that is, the ultimate load value of the beam. P_1 and P_2 are the load values of the first and second ramie fiber sheets of the RC beam when they exit the work, respectively. δ and δ_u are the measured deflection and ultimate deflection of the RC beam. δP_u is the RC after reinforced with ramie fiber sheets, the shear capacity increase percentage of RC.

Characteristics load of the RC beams was shown in Table 4. It can be seen that the ultimate bearing capacity of the beam without reinforcement is 378 kN, and the value of the mid-span deflection is 8.3 mm. When the RC beam is reinforced with ramie fiber sheets, the bearing capacity level is significantly improved. After reinforcement by ordinary ramie fiber sheets, the bearing capacity of the beam reaches 550 kN ~ 579 kN, which is 45.4 % ~ 53.2 % higher than that of the unreinforced beam. Among them, the shear capacity of the beams strengthened with three layers of radial ordinary ramie fiber sheets are 550 kN and 560 kN, respectively, and the mid-span ultimate deflection values are 11.6 mm and 12.2 mm respectively.

While the 6-layer latitudinal ordinary ramie fiber sheets is used to reinforce the beam, the shear capacity of the beams are 579 kN and 559 kN, respectively, and the mid-span ultimate deflection values are 12.3 mm and 11.8 mm, respectively. The test results of the above four RC beams are relatively close. When reinforced with 1 layer of unidirectional basalt fiber sheets, the shear capacity of RC beam is 543 kN, and the mid-span ultimate deflection value is 14.6 mm. The shear reinforcement effect of RC beam is similar to that of ordinary ramie fiber sheets, moreover, the shear capacity of RC beams strengthened with ramie fibers sheets is higher than that of RC beams reinforced with basalt fibers sheets.

The load-span displacement curve of RC beams strengthened with ramie fiber sheets and basalt fiber sheets are shown in Fig. 7. It can be seen that the ramie fiber sheets can significantly improve the shear capacity of the RC beam, and the development trend of the load-span displacement curve under different reinforcement schemes is relatively close. When the load is small, the mid-span displacement value of the RC beam increases slowly. When the ramie fiber sheets is subjected to an increasingly large external force, the growth of the mid-span displacement of the concrete gradually slows down, indicating that the stress redistribution process is taking place inside the concrete.

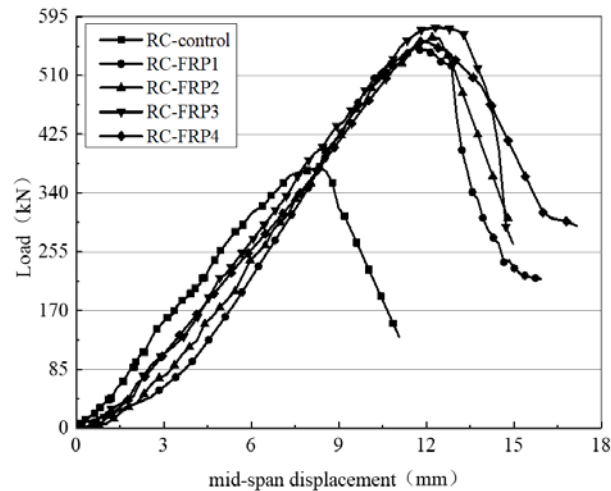


Figure 7. Central deflection and load curves of the RC beam strengthened with fiber sheets.

The test results show that, on the one hand, ramie fiber sheets can effectively enhance the shear resistance of RC beams and improve the shear capacity of concrete beams. The effectiveness of structural reinforcement has been verified. On the other hand, the ductility of the concrete beam is improved, and the resistance of the concrete beam to deformation is enhanced. Therefore, RC beams reinforced with ramie fiber sheets not only meet the bearing capacity requirements, but also meet the structural ductility requirements.

3.2.3. Strain distribution of ramie fiber sheets

As a comparative test beam, 10 sets of resistance strain gauges were placed on the right side of the unplaced stirrups, and the pasting positions and numbers are shown in Fig. 8. All the resistance strain gauges are attached to both sides of the main oblique crack, which can accurately detect the strain change generated when the concrete beam cracks.

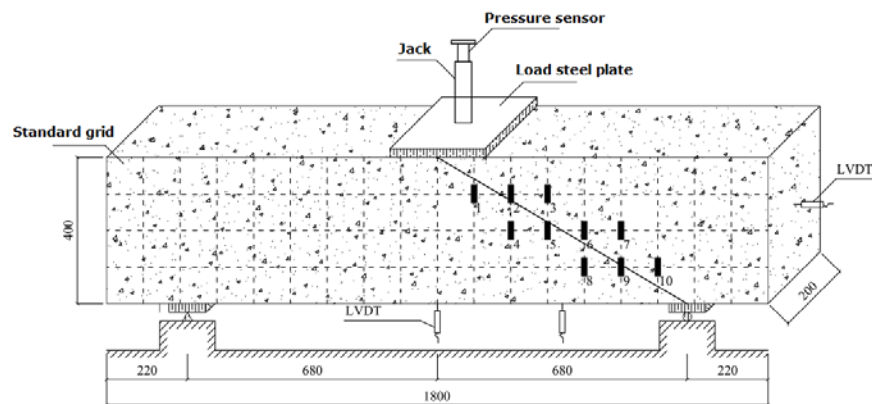


Figure 8. Strain gauges on the RC-control beam.

Taking the mid-plane of the concrete beam as the reference plane, dividing 10 resistance strain gauges into three groups, the first group (numbered 1, 2, and 3), the second group (numbered 4, 5, 6, and 7) and the third group (numbered 8, 9, and 10). Each set of resistance strain gauges collected load levels of 50 kN (13.2%), 150 kN (39.7%), 220 kN (58.2%), 300 kN (79.4%) and 350 kN (92.6%) as representative measurement points. The strain distribution of each resistance strain gauge is shown in Fig. 8 (the abscissa number in the figure is the corresponding resistance strain gauge number).

It can be seen from Fig. 9 that as the load level is gradually increased, part of the resistance strain gauges are out of operation due to excessive deformation, so some data points in the figure are missing. The oblique crack of ordinary reinforced concrete beam is gradually developed from the support to the oblique upward. With the gradual increase of the load, the direction of the main oblique crack may appear in Fig. 6, and a major oblique crack is formed in several oblique cracks called critical oblique crack.

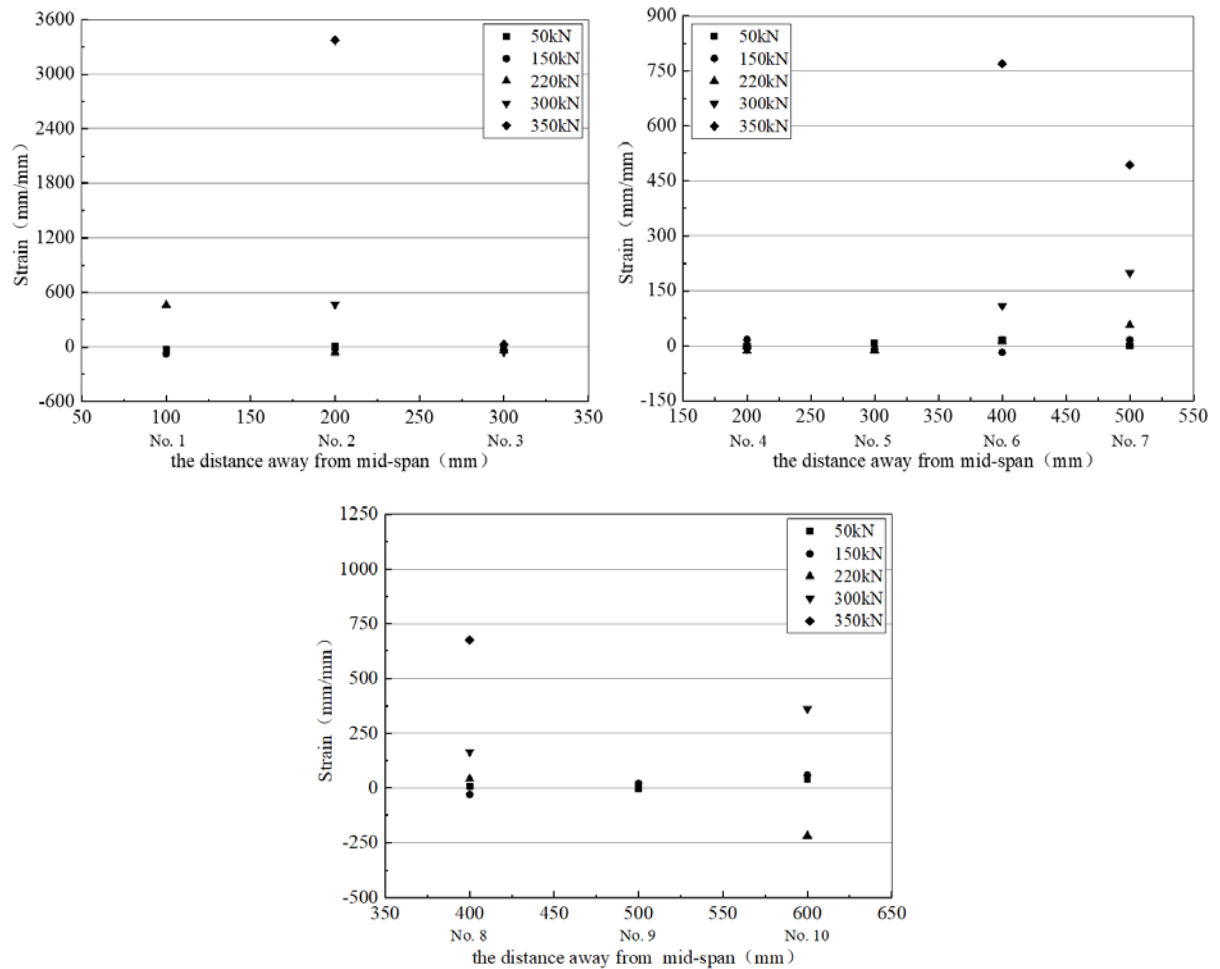


Figure 9. Strain distribution of concrete for RC-control beam.

According to the curve in Fig. 9, it can be found that the development of the oblique crack of the ordinary RC beam has passed through the 8th, 6th and 2nd resistance strain gauges. After the critical oblique crack occurs, the beam can continue to bear the load until the stirrup intersecting the oblique crack reaches the yield strength, and the concrete in the shear zone is crushed. At the same time, the concrete at the uppermost shearing zone of the oblique crack reaches the ultimate strength under the combined action of shear stress and compressive stress, and the steel and coagulation are fully utilized, similar to the normal section of the reinforced failure. However, compared with the normal section failure of the beam, the damage is sudden and belongs to brittle failure. Since the shear span ratio of the reinforced concrete beams prepared in this paper is between 1 and 3, the damage of the reinforced concrete beams is a typical shear failure.

Unlike the ordinary RC beams, after reinforcement with ramie fiber sheets, most of the surface of the concrete beam is covered and does not have the conditions for determining the strain of the concrete. Therefore, in this paper, the same type of 10 resistance strain gauges are attached to the surface of the ramie fiber sheets of each RC beam to measure the strain distribution of the ramie fiber sheets. The position and number of the resistance strain gauges of the RC beams are shown in Fig. 8.

All the resistance strain gauges are attached to both sides of the main oblique crack, which can accurately detect the cracking of the RC and cause the strain change of the ramie fiber sheets. The same as the strain distribution on the concrete surface, when calculating the strain distribution of the ramie fiber sheets, the 10 resistance strain gauges are divided into three groups. The first group (numbered 1, 2, and 3), the second group (numbered 4, 5, 6, and 7) and the third group (numbered 8, 9, and 10). At the same time, the resistance values generated by the respective strain gauges as the load is gradually increased are collected.

Each set of resistance strain gauges collected load levels of 15 %, 40 %, 60 %, 80 %, and 95 % as representative measurement points. The strain distribution of each of the resistance strain gauges of RC-FRP2, RC-FRP4, and RC-FRP5 is as shown in Fig. 10 to 12 (the abscissa number in the figure is the corresponding resistance strain gauge number).

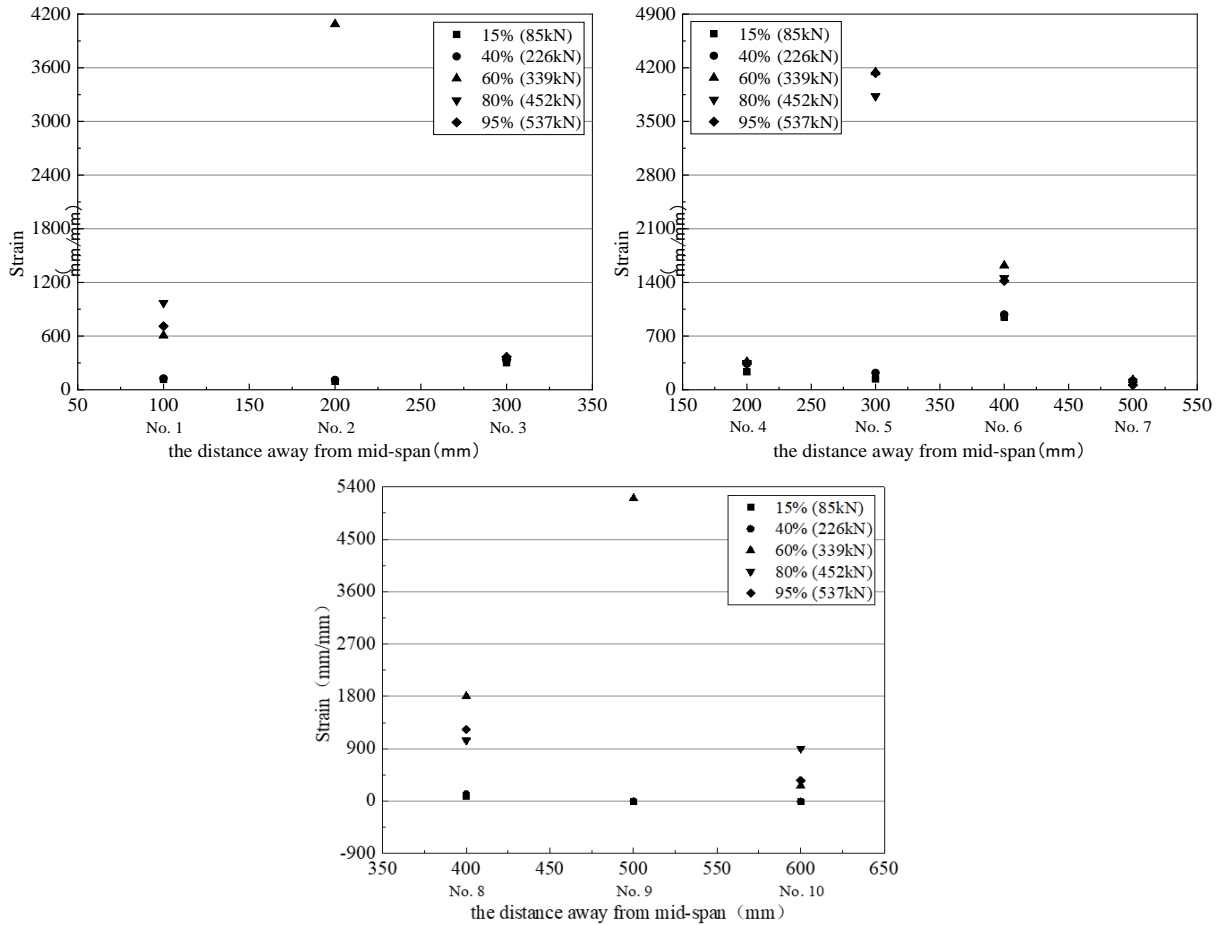


Figure 10. Strain distribution of flax fiber sheets for the RC-FRP2 beam.

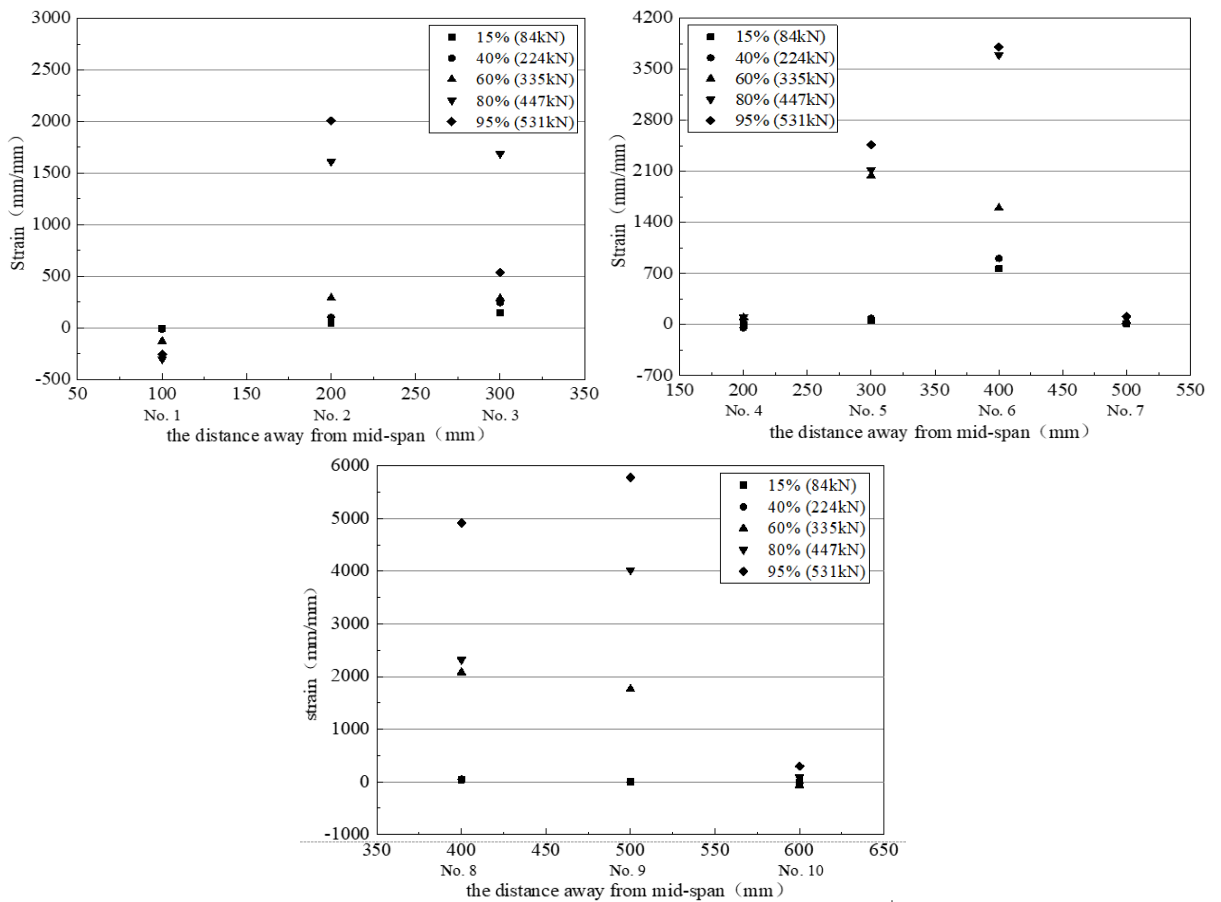


Figure 11. Strain distribution of flax fiber sheets for the RC-FRP4 beam.

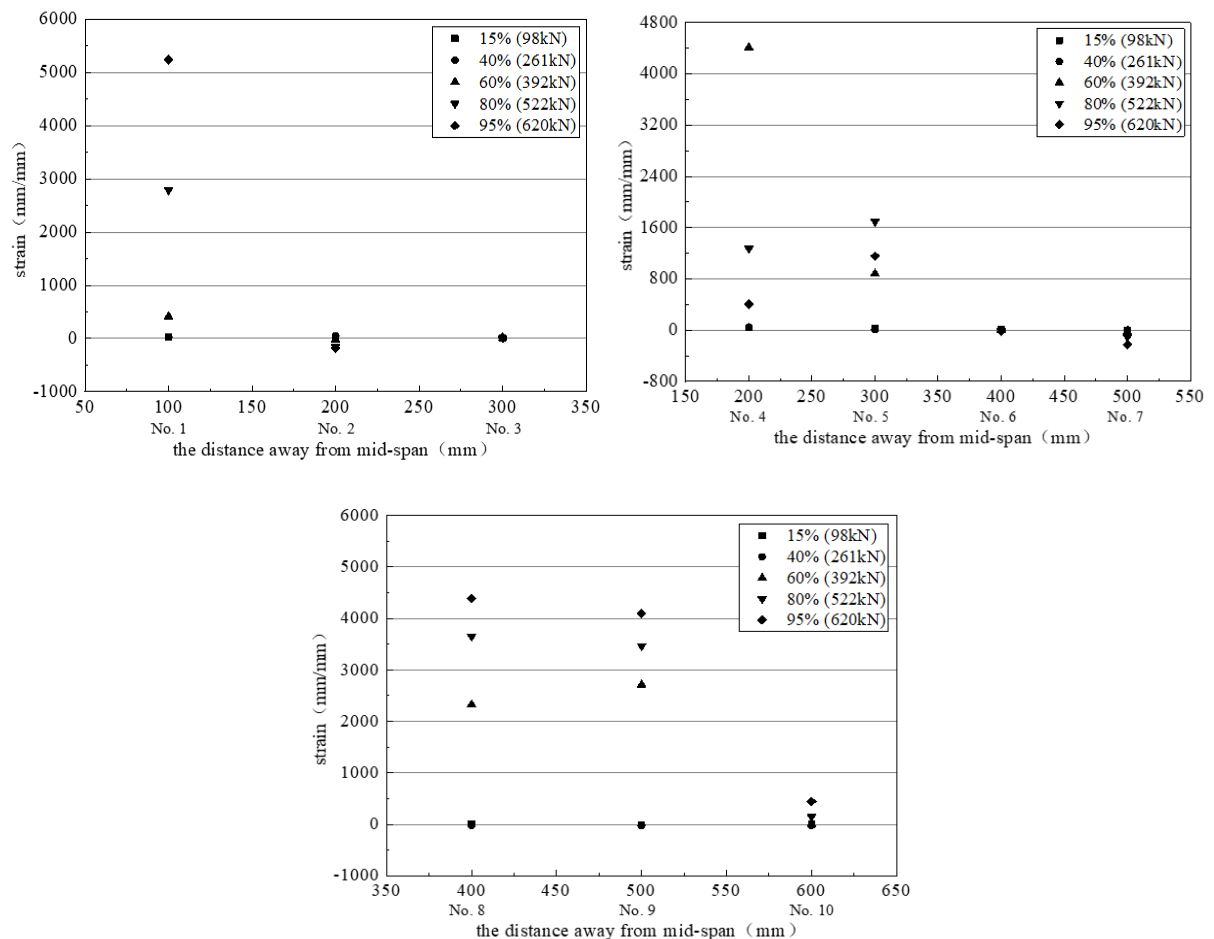


Figure 12. Strain distribution of flax fiber sheets for the RC-FRP5 beam.

It can be seen that the strain distribution of the ramie fiber sheets has a certain regularity. When the load level is low, that is, before the cracking of the RC beam occurs, the strain of the fiber cloth is small, this indicates that the ramie fiber sheets has not yet assumed sufficient external force. As the load level gradually increases, the RC beam gradually approaches the cracking load, and the strain value of the ramie fiber sheets suddenly increases, indicating that the ramie fiber sheets attached to the side of the concrete beam begins to function (the 60 % horizontal curve in Fig. 10 to 12).

At this stage, the ramie fiber sheets shown the same effect as the other side stirrup, and as the load level is gradually increased, the load on the ramie fiber sheets is gradually increased, and the generated strain value is gradually increased.

As shown in Fig. 8, the main oblique crack of the RC beam passes through the strain gauges No. 9, No. 6, No. 5 and No. 2 in sequence. Therefore, as the load level is gradually increased, the above-mentioned resistance strain gauge gradually withdraws from the working state. The cracking of the concrete oblique section causes the concrete to basically withdraw from the work, so the contribution to the shear performance is low. At this time, the shear capacity is mainly provided by the ramie fiber sheets, and the ramie fiber sheets has the largest strain in the middle of the beam.

As can be seen from Fig. 10 to 12, the ramie fiber sheets near the crack has a larger strain value and the strain value away from the crack is smaller. The main reason is that the peeling of the ramie fiber sheets is gradually extended from the crack to the upper and lower free ends. At the same time, the failure mode of RC beams strengthened with ramie fiber sheets indicates that the fracture failure of the ramie fiber sheets occurs before the peeling damage of the ramie fiber sheets and concrete interface, which is due to the low tensile strength of the ramie fiber sheets. According to the existing research results, the effect of the fiber cloth attached to the longitudinal direction of the concrete beam on the shear capacity of the beam is not obvious, however, the ramie fiber sheets attached to the side of the concrete beam at other angles can improve the shear capacity of the concrete beam [25]. Therefore, the arrangement of the main force direction of the ramie fiber sheets should form a certain angle with the oblique crack of the reinforced concrete, which is beneficial to the performance of the ramie fiber sheets, and has strong engineering feasibility and economic rationality.

4. Conclusion

This paper using the ramie fiber sheets to strengthen the shear capacity of the RC beams and investigating the bearing characteristics and failure behavior of the strengthened RC beams were. After that, the shear capacity formula for the RC beams strengthened by the ramie fiber sheets was put forward. The main conclusions of the research are as follows:

(1) Compared with unreinforced RC beams, the shear capacity and mid-span deflection of RC strengthened with ramie fiber sheets fabrics have been greatly improved. After reinforcement of ordinary ramie fiber sheets, the shear capacity of RC beams is 550 kN ~ 579 kN, which is 45.4 % ~ 53.2 % higher than that of unreinforced RC beams. At the same time, the beam's mid-range deflection reached 11.6 mm ~ 12.3 mm, which were 39.8 % ~ 48.2 % higher than that of unreinforced RC beams.

(2) Through the results of the shear capacity, it can be concluded that the shear capacity and mid-span deflection of RC beams strengthened with ramie fiber sheets are higher than those of basalt fiber sheets. Moreover, the main producing area of ramie fiber is Heilongjiang Province, accounting for 80 % of the country's ramie fiber planting area, and the price is cheap. The use of ramie fiber sheets instead of non-renewable composite materials can reduce the consumption of non-renewable resources and damage to the ecological environment in civil engineering construction, solve global warming, develop green manufacturing and low-carbon cities, and promote the sustainability of civil engineering has a great significance.

(3) Taking the ultimate strain of ramie fiber sheets as a control index, the shear capacity of RC beams after reinforcement has a good linear relationship with the cuff ratio of ramie fiber sheets. The calculation formula of shear capacity of RC beams strengthened with ramie fiber sheets reinforced by ordinary ramie fiber sheets was preliminarily proposed by curve fitting.

References

1. Teng, J.G., Yu, T., Fernando, D. Strengthening of Steel Structures with Fiber-Reinforced Polymer Composites. *Journal of Constructional Steel Research*. 2012. No. 78. Pp. 131–43. <http://dx.doi.org/10.1016/j.jcsr.2012.06.011>
2. Ramesh, M. Flax (*Linum Usitatissimum* L.) Fibre Reinforced Polymer Composite Materials: A Review on Preparation, Properties and Prospects. *Progress in Materials Science*. 2019. No. 102. Pp. 109–66. <http://dx.doi.org/10.1016/j.pmatsci.2018.12.004>
3. El-Enein, H.A., Azimi, H., Sennah, K., Ghrib, F. Flexural Strengthening of Reinforced Concrete Slab-Column Connection Using CFRP Sheets. *Construction and Building Materials*. 2014. No. 57. Pp. 126–137. <http://dx.doi.org/10.1016/j.conbuildmat.2014.01.077>
4. Sateshkumar, S.K., Awoyera, P.O., Kandasamy, T., Nagaraj, S., Murugesan, P., Ponnusamy, B. Impact Resistance of High Strength Chopped Basalt Fibre-Reinforced Concrete. *Revista De La Construcción*. 2018. No. 17, no. 2. Pp. 240–248. <http://dx.doi.org/10.7764/rdlc.17.2.240>
5. Wang, X.M. Petru, M. Effect of Hygrothermal Aging and Surface Treatment on the Dynamic Mechanical Behavior of Flax Fiber Reinforced Composites. *Materials*. 2019. No. 12, no. 15. Pp. 10. <http://dx.doi.org/10.3390/ma12152376>
6. Mahmoudi, S., Kervoelen, A., Robin, G., Duigou, L., Daya, E.M., Cadou, J.M. Experimental and Numerical Investigation of the Damping of Flax-Epoxy Composite Plates. *Composite Structures*. 2019. No. 208. Pp. 426–33. <http://dx.doi.org/10.1016/j.compstruct.2018.10.030>
7. Li, Yeou-Fong, Ming-Jer Tsai, Ting-Fang Wei, Wei-Chou Wang. A Study on Wood Beams Strengthened by FRP Composite Materials. *Construction and Building Materials*. 2014. No. 62. Pp. 118–25. <http://dx.doi.org/10.1016/j.conbuildmat.2014.03.036>
8. Chroscielowski, J., Ferenc, T., Mikulski, T., Miskiewicz, M., Pyrzowski, L. Numerical Modeling and Experimental Validation of Full-Scale Segment to Support Design of Novel GFRP Footbridge. *Composite Structures*. 2019. No. 213. Pp. 299–307. <http://dx.doi.org/10.1016/j.compstruct.2019.01.089>
9. Bulut, M., Erklig, A., Alsaadi, M., Kchany, S. Effects of Stacking Sequence on Mechanical Properties of Hybrid Composites Reinforced with Carbon, Kevlar and S-Glass Fibers. *Materials Testing*. 2017. No. 59, no. 5. Pp. 472–79. <http://dx.doi.org/10.3139/120.111022>
10. Pothnis, J.R., Kalyanasundaram, D., Gururaja, S. Enhancement of Open Hole Tensile Strength Via Alignment of Carbon Nanotubes Infused in Glass Fiber – Epoxy – CNT Multi-Scale Composites. *Composites Part a-Applied Science and Manufacturing*. 2021. No. 140. Pp. 106–155. <http://dx.doi.org/10.1016/j.compositesa.2020.106155>
11. Alam, M.A., Sami, A., Mustapha, K.N. Embedded Connectors to Eliminate Debonding of Steel Plate for Optimal Shear Strengthening of RC Beam. *Arabian Journal For Science And Engineering*, 2017. No. 42, no. 9. Pp. 4053–68. <http://dx.doi.org/10.1007/s13369-017-2572-5>
12. Alam, M.A. Al Riyami, K. Shear Strengthening of Reinforced Concrete Beam Using Natural Fibre Reinforced Polymer Laminates. *Construction and Building Materials*. 2018. No. 162. Pp. 683–96. <http://dx.doi.org/10.1016/j.conbuildmat.2017.12.011>
13. Van de Weyenberg, I., Truong, T.C., Vangrimde, B., Verpoest, I. Improving the Properties of Ud Flax Fibre Reinforced Composites by Applying an Alkaline Fibre Treatment. *Composites Part a-Applied Science and Manufacturing*. 2006. No. 37, no. 9. Pp. 1368–76. <http://dx.doi.org/10.1016/j.compositesa.2005.08.016>
14. Goncalves, A.P.B., de Miranda, C.S., Guimaraes, D.H., de Oliveira, J.C., Cruz, A.M.F., Flbm da Silva, Luporini, S., Jose, N.M. Physicochemical, Mechanical and Morphologic Characterization of Purple Banana Fibers. *Materials Research-Ibero-American Journal of Materials*. 2015. No. 18. Pp. 205–209. <http://dx.doi.org/10.1590/1516-1439.366414>
15. El-Sabbagh, A., Steuernagel, L., Ziegmann, G. Characterisation of Flax Polypropylene Composites Using Ultrasonic Longitudinal Sound Wave Technique. *Composites Part B-Engineering*. 2013. No. 45, no. 1. Pp. 1164–72. <http://dx.doi.org/10.1016/j.compositesb.2012.06.010>

16. Renouard, S., Hano, C., Doussot, J., Blondeau, J.P., Laine, E. Characterization of Ultrasonic Impact on Coir, Flax and Hemp Fibers. *Materials Letters*. 2014. No. 129. Pp. 137–41. <http://dx.doi.org/10.1016/j.matlet.2014.05.018>
17. Prasad, V., Sekar, K., Varghese, S., Joseph, M.A. Evaluation of Interlaminar Fracture Toughness and Dynamic Mechanical Properties of Nano TiO₂ Coated Flax Fibre Epoxy Composites. *Polymer Testing*. 2020. No. 91. Pp. 106784. <http://dx.doi.org/10.1016/j.polymertesting.2020.106784>
18. Ghaffar, S.H., Al-Kheetan, M., Ewens, P., Wang, T., Zhuang, J.D. Investigation of the Interfacial Bonding between Flax/Wool Twine and Various Cementitious Matrices in Mortar Composites. *Construction and Building Materials*. 2020. No. 239. Pp. 117833. <http://dx.doi.org/10.1016/j.conbuildmat.2019.117833>
19. El Jaouhari, A., Ben Jadi, S., El Guerraf, A., Bouabdallaoui, M., Aouzal, Z., Bazzaoui, E.A., Martins, J.I., Bazzaoui, M. Synthesis and Spectroscopic Characterization of Polypyrrole Ppy Coating on Flax Fibers and Its Behaviour toward Trimethylamine Vapor. *Synthetic Metals*. 2018. No. 245. Pp. 237–44. <http://dx.doi.org/10.1016/j.synthmet.2018.09.014>
20. Whitacre, R., Amiri, A., Ulven, C. The Effects of Corn Zein Protein Coupling Agent on Mechanical Properties of Flax Fiber Reinforced Composites. *Industrial Crops and Products*. 2015. No. 77. Pp. 232–38. <http://dx.doi.org/10.1016/j.indcrop.2015.08.056>
21. Kannan, T.G., Wu, C.M., Cheng, K.B. Influence of Laminate Lay-up, Hole Size and Coupling Agent on the Open Hole Tensile Properties of Flax Yarn Reinforced Polypropylene Laminates. *Composites Part B-Engineering*, 2014. No. 57. Pp. 80–85. <http://dx.doi.org/10.1016/j.compositesb.2013.09.042>
22. M.R., S., Siengchin, S., Parameswaranpillai, J., Jawaid, M., Pruncu, C.I., Khan, A. A comprehensive review of techniques for natural fibers as reinforcement in composites: Preparation, processing and characterization. *Carbohydrate Polymers*. 2019. 207. Pp. 108–121. DOI: 10.1016/j.carbpol.2018.11.083
23. Liu, Y., Lv, X., Bao, J., Xie, J., Tang, X., Che, J., Ma, Y., Tong, J. Characterization of silane treated and untreated natural cellulosic fibre from corn stalk waste as potential reinforcement in polymer composites. *Carbohydrate Polymers*. 2019. 218. Pp. 179–187. DOI: 10.1016/j.carbpol.2019.04.088
24. Balachandar, M., Vijaya Ramnath, B., Jagadeeshwar, P., Yokesh, R. Mechanical behaviour of Natural and Glass fiber reinforced with polymer matrix composite. *Materials Today: Proceedings*. 2019. 16. Pp. 1297–1303. DOI: 10.1016/j.matpr.2019.05.227
25. Yoddumrong, P., Rodsin, K., Katawaethwarag, S. Seismic Strengthening of Low-Strength RC Concrete Columns Using Low-Cost Glass Fiber Reinforced Polymers (Gfrps). *Case Studies in Construction Materials*, 2020. No. 13. Pp. e00383. <http://dx.doi.org/10.1016/j.cscm.2020.e00383>

Information about authors:

Xiaolian Gai,

ORCID: <https://orcid.org/0000-0002-0856-8560>

E-mail: gaixiaolian@126.com

Dongpo He,

ORCID: <https://orcid.org/0000-0003-2427-1086>

E-mail: hdp@nefu.edu.cn

Hongguang Wang, PhD

ORCID: <https://orcid.org/0000-0002-7620-614X>

E-mail: wanghongguang@zoho.com

Received 04.01.2020. Approved after reviewing 08.10.2021. Accepted 09.10.2021.



Research article

UDC 691.54

DOI: 10.34910/MCE.114.2



Fracture characteristics of high-performance concrete using nano-silica

V.T. Ngo¹ , T.T. Bui² , T.Q.K. Lam¹ , T.M.D. Do¹ , T.T.N. Nguyen³ 

¹ Mien Tay Construction University, Vinh Long, Vietnam

² University of Transport and Communications, Hanoi, Vietnam

³ University of Transport Technology, Hanoi, Vietnam

✉ lamthanhquangkhai@gmail.com

Keywords: high-performance concrete, nano-silica, fracture characteristic, fracture parameter

Abstract. High-performance concrete (HPC) using nano-silica (NS) has higher mechanical properties and durability than conventional concrete. The highly active silica ultrafine particles have improved the performance of HPC significantly. The fracture characteristics of HPC are also enhanced when using NS due to the improved quality of C-S-H gels and the interface transition zone between mortar and aggregate. The influence of NS on fracture characteristics of HPC is considered in the study as a basis for the effective application of HPC in the structure of buildings. The paper assesses the influence of NS on the strength and fracture characteristics of HPC. HPC mixes were produced by replacing Portland cement with NS at 0.5 % and 1.5 %. The fracture testing for HPC using NS was carried out based on the three-point bending test of beams with the notch. The result is the load-crack mouth opening displacement relationship curves (P-CMOD) and load-deflection (P-). Finally, fracture parameters and characteristics of HPC using NS are analyzed and calculated from the P-CMOD and P- relationship curves.

Acknowledge: Van Thuc Ngo was funded by Vingroup Joint Stock Company and supported by the Domestic Master/ PhD Scholarship Programme of Vingroup Innovation Foundation (VINIF), Vingroup Big Data Institute (VINBIGDATA), code VINIF.2020.TS.86.

Citation: Ngo, V.T., Bui, T.T., Lam, T.Q.K., Do, T.M.D., Nguyen, T.T.N. Fracture characteristics of high-performance concrete using nano-silica. Magazine of Civil Engineering. 2022. 114(6). Article No. 11402. DOI: 10.34910/MCE.114.2

1. Introduction

Many researchers have confirmed that the incorporation of nanoparticles into high-performance concrete (HPC) brings many benefits. Nanomaterials can considerably improve concrete's mechanical properties and durability [1–4]. In comparison to the use of silica fume (micrometer size), Sanchez and Sobolev determined that using nano-silica (NS) components in HPC is a new development step [5]. The NS particles aid in the formation of pozzolanic reactions by removing Ca(OH)₂ components to produce high-performance pozzolan gel products. A small amount of NS added into the mixture helps increase the performance of C-S-H gels and interface transition zone (ITZ) [6, 7], resulting in positive impacts on the mechanic properties and fracture characteristics of HPC. According to recent investigations [8–10], mechanical parameters such as compressive, tensile strength, modulus of elasticity, and stress-deformation relationship are greatly improved for HPC with nano-silica added.

For decades, the study of the fracture characteristics of high-performance concrete and high-strength concrete has received attention. Some authors claimed that the fracture of structures designed with high-

strength concrete are of high brittleness nature [11, 12]. The cause of brittle fracture in HPC is related to concrete's high strength characteristics, leading to cracks often passing through coarse aggregate instead of following the boundary of aggregate as with normal concrete. HPC has high compressive strength, high modulus of elasticity compared to normal concrete. For HPC the slope of the curve on the downside (after peak) becomes steeper. This proves that HPC is more likely to be damaged suddenly than normal concrete.

According to Van Mier [13], ultrafine material will significantly change the behavior of concrete in the fracture process. The increase of the ductility is shown by the stress-deformation (or crack mouth open displacement) curve, especially since the post-peak slope of the curves gradually decreases. The improvement of the toughness is explained by bridging cracked surfaces in the presence of ultrafine NS particles. According to the research of Ricardo et al. [11], concrete with silica fume has fracture characteristics better than concrete without it. The addition of silica fume improves the homogeneity, the structure of C-S-H gels, and the performance of the ITZ of mortar and aggregate. Fracture energy, toughness, and length characteristic are higher when using silica fume. The brittleness of HPC tends to decrease. According to Zhang et al. [14]. Increasing the density of the ITZ of mortar and aggregate with chemical and mineral admixtures in HPC causes it to affect the fracture properties of concrete.

Some studies using NS in HPC also claimed that ultrafine silica particles would provide mortar when hardened with higher performance and consistency. The fracture toughness of concrete is also significantly increased by increasing the cohesion between the cement particles and aggregates [1]. With ultrafine particles, the microstructure and the fracturing behavior of concrete is significantly enhanced. According to the researches of Quercia [15, 16], the presence of fine material substantially changes the fracture behavior of concrete. The load-deformation curve shows the increased ductility of the ultrafine concrete component. The post-peak slope of the curves is reduced compared to the concrete without fine particles. The increased toughness is explained by bridging higher cracked surfaces in the presence of ultrafine particles. Some empirical studies have also been conducted to understand the relationship between the cracking behavior of concrete and ultrafine particles. The results generally show an apparent influence of the ultrafine mineral composition on fracture parameters of concrete [7, 13].

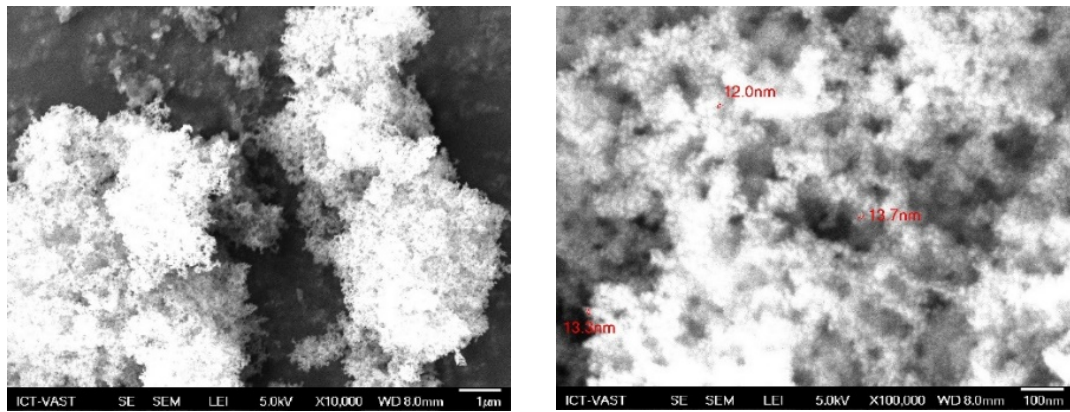
In addition, many studies have evaluated the influence of the constituent materials on the fracture characteristics of HPC, such as the study of Zang et al. assessing the effect of aggregates size on the fracture energy [17], the influence of fiber content on the fracture modes of concrete [12], the impact of silica fume on the fracture parameters of HPC [11], etc. However, there has not been any research analyzing the effects of NS composition on fracture characteristics of HPC, although they were mentioned in studies [7], [18-22].

The article's content focuses on determining parameters and fracture characteristics of HPC using NS in the form of mode I. A special testing method according to RILEM, conducted by controlling crack mouth open displacement, was applied to determine fracture parameters of HPC using NS. The three mixed proportions of HPC using NS, with the content of 0 %, 0.5 %, and 1.5 % were calculated for the component design according to ACI 211.4R-08 standards to serve for the experiments. The influence of the NS content on the fracture characteristics of the HPC was evaluated. The experimental results were analyzed according to the fracture mechanic method and used to calculate the crack extension resistance characteristics of HPC beams.

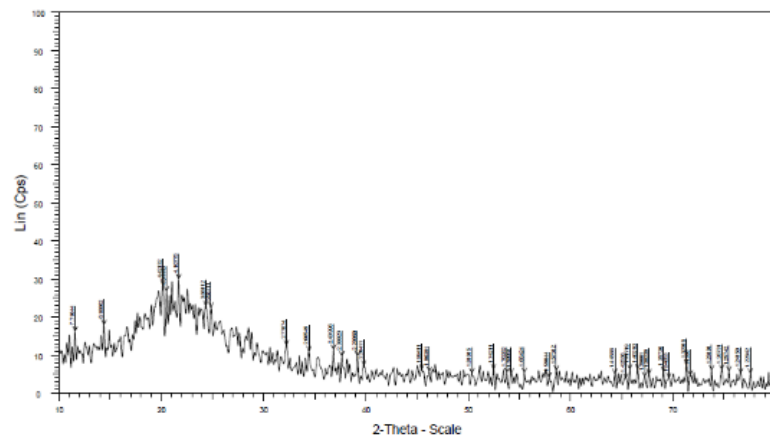
2. Materials and Methods

2.1. Materials

Materials included PC 40 cement; basalt with D_{max} 12.5 mm as coarse aggregates; fine aggregates with a module 2.7, superplasticizer, silica fume, and nano-silica. The research was conducted with Evonik chemical company NS product (Aerosil 200) of 5-50 nm dimensions with a typical 200 ± 25 m²/g surface area. Fig. 1a shows the results of SEM tests for assessing the size and form of the NS. Fig. 1a shows that the nanoparticles are on average approximately 13 nm in size. The result of XRD testing in Fig.1b, between 16° and 30°, indicates that the compounds are 100 % amorphous.



a) SEM image of nano-silica



b) XRD image of nano-silica

Figure 1. SEM and XRD image of nano-silica.

2.2. Mix proportion

The compressive strength of HPC using NS is designed by the ACI method for 70 MPa [23]. For fracture test, mixes with 0 %, 0.5 %, and 1.5 % NS ratios were prepared. By the recommendations, the percentage is selected and adjusted to the mixtures. Table 1 presents a mix of the proportion of HPC with NS:

Table 1. Mixes proportion of HPC using nano-silica

Mix code	Materials							W/B
	C	FA	CA	F	NS	SP	W	
	(kg)	(kg)	(kg)	(kg)	(%)	(l)	(l)	
NS0.0	544.2	674.6	1049.7	8.64	0.00	5.44	54.6	0.27
NS0.5	541.3	673.6	1049.7	8.64	0.50	6.53	54.6	0.27
NS1.5	535.6	671.6	1049.7	8.64	0.50	7.62	154.6	0.27

Note: C – cement; CA – coarse aggregate; FA – fine aggregate; NS – nano-silica; SF – silica fume, SP – superplasticizer, W/B – water/binder.

2.2. Preparing for experiments

Material components such as fine aggregate, coarse aggregate, cement, silica fume, superplasticizer are ready for measurement before mixing. Particularly, NS is mixed with 50 % of the required water and stirred at high speed, ensuring that NS is evenly dispersed in the mixture.

After preparing the materials, the specimen mixing process is performed according to the procedure shown in Fig. 2.

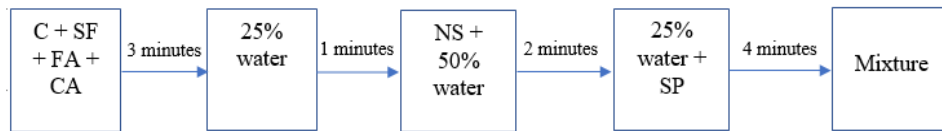


Figure 2. Mixing procedure of HPC using NS.

The beam specimens used in the fracture experiment are a 500×100×100 mm prism with a notch width of 2 mm and depth of 25 mm, as shown in Fig. 3.

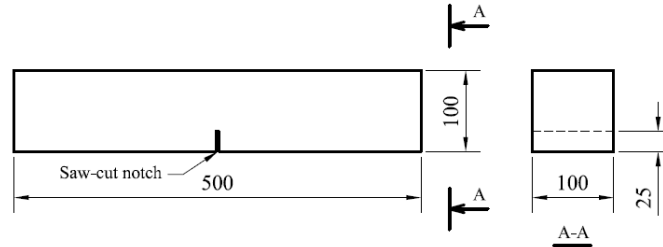
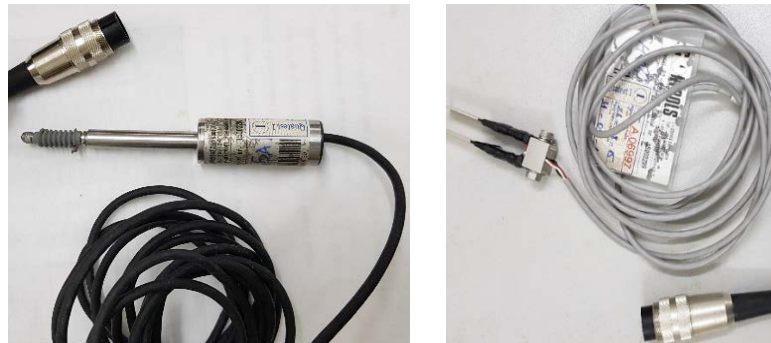


Figure 3. The specimen used in the fracture test.

According to Rilem's [15] tests on 28 day beams, the notch should be cut on the 21st day. Then, the specimens were cured up to the day of the experiment.

2.3. Experimental equipment

It is not easy to obtain a complete softening curve by the fracture test. Especially for high-strength concrete and high-performance concrete, the brittleness is very high. The equipment that controls the experiment only through the load cannot achieve the desired results. The test requires specialized equipment and very high sensitivity. A closed-loop experimental device can customize the load speed control according to the crack mouth open displacement (CMOD), and deflection will be used [24]. The linear variable differential transformer (LVTD) and the crack mouth extensometer (extensometer) are necessary to accomplish the experiment. LVTD and extensometer are shown in Fig. 4.



a) LVTD

b) Extensometer

Figure 4. LVTD and extensometer for testing.

LVTD is used to measure deflection in the middle of the test beam to obtain the load-deflection ($P-\delta$) relationship curve. LVTD has a 100 mm measuring stroke. Fig. 4b is an extensometer with high accuracy. Extensometer is specialized to measure crack mouth open displacement, with the sensitivity of 1000×10^{-6} strain/mm, the maximum measuring range is 5 mm. The load-crack mouth open displacement (P -CMOD) relationship curves are obtained using an extensometer.

2.4. Experimental method

For the experiment to be stable, the development of CMOD is controlled as a linear function of time. Their growth rate is minimal to ensure a stable experiment. The load is automatically adjusted to increase quickly or slowly or decrease depending on the structural behavior through the measuring head. In other words [25], the measuring head is an automatic device that uses a sensor core capable of two-way feedback to adjust the magnitude of the load according to the measured value. The arrangement of fracture tests of HPC specimens is shown in Fig. 5.

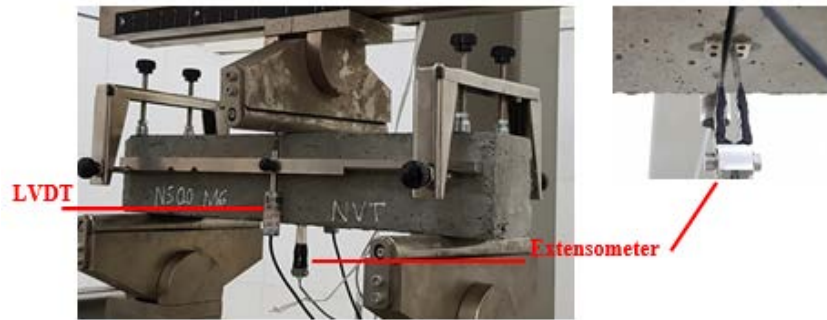


Figure 5. Three-point bending test of HPC using NS.

During the experiment, the test is kept at a certain speed by treating CMOD as a linear function of time. The experiment started at a rate of $0.04 \mu\text{m/s}$. In this test, it takes very long time for each specimen to be subject to damage, unlike in ordinary mechanical experiments.

3. Results and Discussion

3.1. Effect of nano-silica in load-deflection and load–CMOD curves of HPC

The results showed the difference of the P-CMOD curves corresponding to the beam specimens cured up to 28 days using nano-silica with ratios of 0 %, 0.5 %, and 1.5 %, as shown in Fig. 15. After reaching the peak (P_{max}), the P-CMOD curve of HPC without NS has a steep slope. When the CMOD is very small, the force value decreases quickly. When NS is added to concrete with the ratio of 0.5 % and 1.5 %, the P-CMOD curve has a significant change, especially with 1.5 % NS. The curves tend to grow the same in the early stages when the concrete is still in the elasticity limit, and the difference begins to appear when the curve is about to peak.

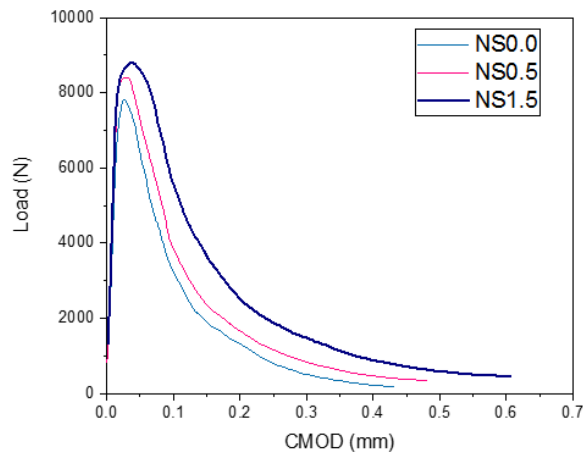


Figure 6. Effect of nano-silica in P-CMOD.

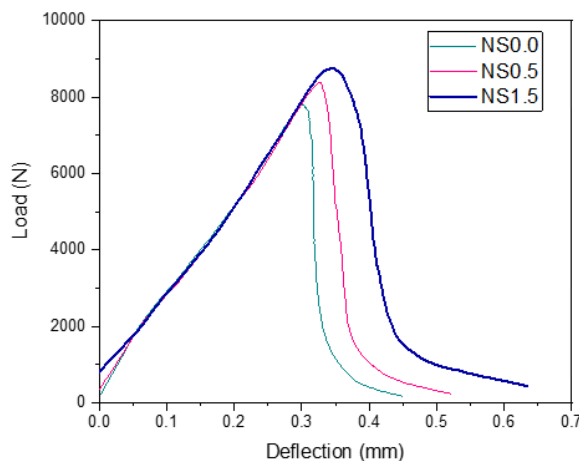


Figure 7. Effect of nano-silica on P-deflection.

In the post-peak period, the curve of HPC using NS has a slope of less than HPC without nanosilica. Fig. 6 shows that the force value decreases with the growth of the slower CMOD when comparing the same value of CMOD. The load valuation of specimens using NS remained higher than the non-NS specimens.

The load-deflection relationship curves ($P-\delta$) of HPC using NS are shown in Fig. 7. For HPC using NS, $P-\delta$ curve will be thicker, the curve's nonlinear period is longer, and the load slowly decreases.

Observations of $P-\delta$ curves in Fig. 7 show that the area under the curve (work of fracture – W_F) of the graph varies depending on the NS ratio. To calculate the area under the $P-\delta$ curves, use the integral method. As shown in Table 2, W_F increased by 21.4 % when the NS ratio was 0.5 % and by 58.71 % when the NS ratio was 1.5 %.

Table 2. Work of fracture – W_F

Mix code	P_{max} (N)	δ_{max} (mm)	W_F (N.mm)
NS0.0	7813	0.449	1454.80
NS0.5	8416	0.520	1766.42
NS1.5	8810	0.634	2308.90

Compare the P -CMOD and $P-\delta$ curves obtained by the experiment to the results of other researchers [11, 12]. The characteristics before and after the P_{max} load in Fig. 7 and Fig. 8 are very similar in shape.

3.2. Effect of NS on fracture energy (G_F)

Table 3 shows the improvement in fracture energy when the NS ratio is changed from 0 % to 0.50 % to 1.50 %. Fracture energy G_F is calculated based on the load-deflection relationship curves and is obtained from a three-point bending test. The calculation results are averaged from the results of six specimens. In comparison to concrete specimens without NS, specimens with NS had fracture energy increased by 21 % and 58 %, while the NS ratio was 0.5 %, and 1.5 %, respectively, as shown in Table 3.

Table 3. Result of fracture energy

Mix code	W_F (Nmm)	δ_0 (mm)	a_0 (mm)	A_{lig} (mm ²)	m (kg)	G_F (Nmm/mm ²)
NS0.0	1454.80	0.449	25	7500	9.82	0.200
NS0.5	1766.42	0.520	25	7500	9.84	0.242
NS1.5	2308.90	0.634	25	7500	9.84	0.316

The Effect of NS on the fracture energy of HPC is shown in Fig. 8.

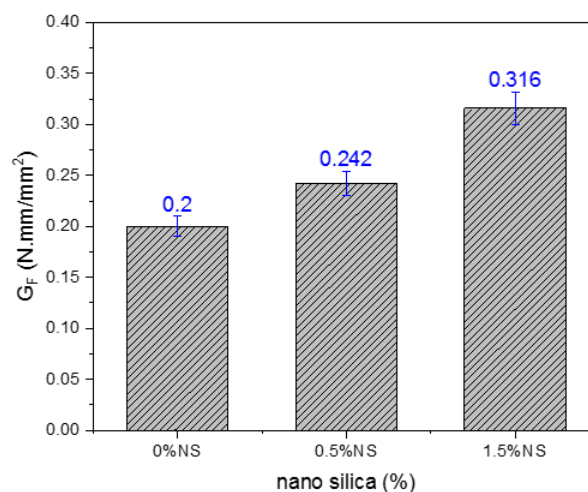


Figure 8. Effect of NS on the fracture energy.

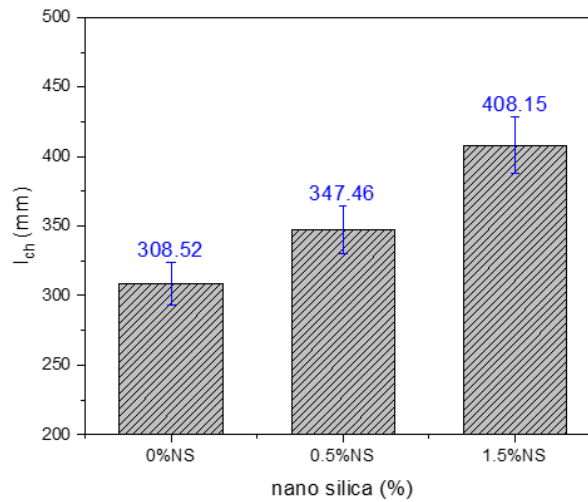


Figure 9. Effect of NS on the characteristic length.

3.3. Effect of NS on characteristic length of HPC

The characteristic length was determined based on the energy parameters of tensile strength, modulus of elasticity, and fracture energy. Tensile strength is determined indirectly through flexural strength according to the formula of CEB-FIP MC 90 [23], as shown in Table 4.

Table 4. The result of characteristic length

Mix code	E (MPa)	G_F (Nmm/mm ²)	f_t (MPa)	l_{ch} (mm)
NS0	45533	0.200	5.430	308.52
NS0.5	47620	0.242	5.760	347.46
NS1.5	50131	0.316	6.230	408.15

The effect of NS on this characteristic is presented in Fig. 9.

Based on the calculation results in Table 4 and Fig. 9, HPC with NS has a longer characteristic length than HPC without NS. This characteristic increases by 12.62 % and 32.29 % for 0.5 % NS and 1.5 % NS, respectively. It can be seen that the HPC without NS is more brittle than the one with NS.

3.4. Discussion

Through the experimental results and analysis, it can be seen that the fracture characteristics of HPC have been improved when using NS. When working in concrete, the effect of NS particles modifies the microstructure of the mortar and improves weak zones. That improves the performance of the C-S-H gels and the ITZ between the mortar and the aggregate, which enhances concrete failure characteristics. Some authors have also presented this point of view in their recent researches [7, 11, 13].

4. Conclusions

The following conclusions were obtained based on the results of the study:

1. This research determined fracture parameters and characteristics of HPC using NS in the form of mode I. The fracture parameters and characteristics of HPC using NS were determined through experiment and analysis, such as relationships between P-CMOD, load-deflection, fracture energy, and length characteristic.
2. The results show that the influence of NS content on fracture parameters and characteristics of HPC is significant. The NS ratio of 1.5 % is the most optimal in terms of use. The ductility of the HPC using NS is improved, which is shown by the fracture energy and characteristic length parameters.
3. The experimental and analysis results are similar to other researches on the fracture characteristics of high-performance concrete. Those results can be used to calculate crack extension resistance and the remaining life of HPC structures in subsequent investigations.

References

1. Chithra, S., Senthil Kumar, S.R.R., Chinnaraju, K. The effect of Colloidal Nano-silica on workability, mechanical and durability properties of High Performance Concrete with Copper slag as partial fine aggregate. *Construction and Building Materials*. 2016. 113. Pp. 794–804. DOI: 10.1016/j.conbuildmat.2016.03.119
2. Khaloo, A., Mobini, M.H., Hosseini, P. Influence of different types of nano-SiO₂ particles on properties of high-performance concrete. *Construction and Building Material*. 2016. 113. Pp. 188–201. DOI: 10.1016/j.conbuildmat.2016.03.041
3. Givi, A.N., Rashid, S.A., Aziz, F.N.A., Salleh, M.A.M. The effects of lime solution on the properties of SiO₂ nanoparticles binary blended concrete. *Composites Part B: Engineering*. 2011. 42. Pp. 562–569. DOI: 10.1016/j.compositesb.2010.10.002
4. Bastami, M., Baghbadrani, M., Aslani, F. Performance of nano-Silica modified high strength concrete at elevated temperatures. *Construction and Building Materials*. 2014. 68. Pp. 402–408. DOI: 10.1016/j.conbuildmat.2014.06.026
5. Sanchez, F., Sobolev, K. Nanotechnology in Concrete: A Review. *Construction and Building Materials*. 2010. 24. Pp. 2060–2071. DOI: 10.1016/j.conbuildmat.2010.03.014
6. Bjornstrom, J., Martinelli, A., Matic, A., Borjesson, L., Panas, I. Accelerating Effects of Colloidal Nanosilica for Beneficial Calcium-Silicate-Hydrate Formation in Cement. *Chemical Physics Letters*. 2004. 392. Pp. 242–248. DOI: 10.1016/j.cplett.2004.05.071
7. Zhang, P., Wan, J., Wang, K., Li, Q. Influence of nano-SiO₂ on properties of fresh and hardened high performance concrete: A state-of-the-art review. *Construction and Building Materials*. 2017. 148. Pp. 648–658. DOI: 10.1016/j.conbuildmat.2017.05.059
8. Ngo, V.T., Lam, T.Q.K., Do, T.M.D. Nguyen, T.C. Increased plasticity of nano concrete with steel fibers. *Magazine of Civil Engineering*. 2020. 93 (1). Pp. 27–34. DOI: 10.18720/MCE.93.3
9. Ngo, V.T., Bui, T.T., Lam, T.Q.K., Nguyen, T.T.N., Nguyen, V.H. Experimental Evaluation of Nano Silica Effects to High Performance Concrete Strength in Early Age. *IOP Conf. Series: Materials Science and Engineering*. 2020. 869 032011. DOI: 10.1088/1757-899X/869/3/032011
10. Ngo, V.T., Khai Lam, T.Q., Dung Do, T.M., Nguyen, T.C. Nano concrete aggregation with steel fibers: A problem to enhance the tensile strength of concrete. *E3S Web of Conferences*. 2019. 135 03001. DOI: 10.1051/e3sconf/201913503001
11. Ricardo, A.E., Marta, S.L.V. Fracture parameters for high-performance concrete. *Cement and Concrete*. 2006. 36. Pp. 576–583. DOI: 10.1016/j.cemconres.2005.09.004
12. Bui, T.T. Numerical simulation of Fracture in Plain and Fibre-reinforced Concrete. PhD thesis. The University of New South Wales, Sydney, Australia, 2007.
13. Van Mier, J.G.M. *Concrete Fracture: A Multiscale Approach*. New York: CRC Press. 2013.
14. Zhang, P., Zhao, Y.N., Li, Q.F., Zhang, T.H., Wang, P. Mechanical properties of fly ash concrete composite reinforced with nano-SiO₂ and steel fiber. *Current Science*. 2014. 106. Pp. 1529–1537. DOI: 10.18520/CS/V106/I11/1529-1537
15. Quercia Bianchi, G. Application of nano-silica in concrete. PhD thesis. Technische Universiteit Eindhoven, Eindhoven, 2014.
16. Quercia, G., Lazaro, A., Geus, J.W., Brouwers, H.J.H. Characterization of morphology and texture of several amorphous nano-silica particles used in concrete. *Cement and Concrete Composites*. 2013. 44. Pp. 77–92. DOI: 10.1016/j.cemconcomp.2013.05.006
17. Zang, J., Leung, C.K.Y., Xu, S. Evaluation of fracture parameters of concrete from bending test using inverse analysis approach. *Materials and Structures*. 2010. 43. Pp. 857–874. DOI: 10.1617/s11527-009-9552-5
18. Sobolev, K., Flores, I., Hermosillo, R. *Nanomaterials and nanotechnology for high-performance cement composites*. Denver: American Concrete Institute. 2006.
19. Du, H., Du, S., Liu, X. Durability performances of concrete with nano-silica. *Construction and Building Material*, 2014. 73. Pp. 705–712. DOI: 10.1016/j.conbuildmat.2014.10.014
20. Ibrahim, M., Nasir, M., Hussaini, S.R., Najamuddin, S.K., Ewebajo, A.O. Performance of structurally viable green concrete derived from natural pozzolan and nanosilica. *Magazine of Civil Engineering*. 2021. 107(7). Article No. 10710. DOI: 10.34910/MCE.107.10
21. Slavcheva, G.S., Artamonova, O.V., Shvedova, M.A., Khan, M.A. Clinkerless slag-silica binder: hydration process and hardening kinetics (part 2). *Magazine of Civil Engineering*. 2020. 97(5). Article No. 9712. DOI: 10.18720/MCE.97.12
22. Wang, Y., Zhang, X. Fracture Properties of Recycled Concrete Reinforced with Nanosilica and Steel Fibers. *Advances in Materials Science and Engineering*. 2022. Article ID 6027185. DOI: 10.1155/2022/6027185
23. Stuttgart: Task Group. Constitutive modelling Constitutive modelling high performance concrete. *Fib*. 42. 2008. 130 p.
24. RILEM. Determination of the fracture energy of mortar and concrete by means of three-point bend tests on notched beams. *Materials and Structures*. 1985. 18. Pp. 285–290. DOI: 10.1007/BF02472918
25. Tin-Loi, F., Que, N.S. Identification of cohesive crack fracture parameters by evolutionary search. *Computer methods in applied mechanics and engineering*. 2002. 191. Pp. 5741–5760. DOI: 10.1016/S0045-7825(02)00483-8

Information about authors:

Van Thuc Ngo, PhD

ORCID: <https://orcid.org/0000-0001-8101-4698>

E-mail: nvthuc34@gmail.com

Tien Thanh Bui, PhD

ORCID: <https://orcid.org/0000-0002-4001-9246>

E-mail: btthanh@utc.edu.vn

Thanh Quang Khai Lam, PhD

ORCID: <https://orcid.org/0000-0003-3142-428X>

E-mail: lamthanquangkhai@gmail.com

Thi My Dung Do, PhD

ORCID: <https://orcid.org/0000-0001-6869-8941>

E-mail: dothimydung1983@gmail.com

Thi Thu Nga Nguyen, PhD

ORCID: <https://orcid.org/0000-0002-9613-6011>

E-mail: ngantt@utt.edu.vn

Received: 28.07.2020. Approved after reviewing: 11.05.2022. Accepted: 12.05.2022.



Research article

UDC 624.131.436

DOI: 10.34910/MCE.114.3



Model of soil thermal conductivity in the form of a truncated sphere

A.V. Zakharov¹ , A.B. Ponomaryov¹ , I.V. Ofrikhter² 

¹ Saint-Petersburg Mining University, St. Petersburg, Russia

² Perm National Research Polytechnic University, Perm, Russia

✉ av_zaharov@mail.ru

Keywords: theoretical analysis, theoretical prediction model, thermal conductivity, porosity, soil, thermal conductivity model

Abstract. The model is designed for a three-phase soil system: mineral part, water, and air. The model's input parameters are porosity and water saturation coefficient, which characterize the volumetric ratio of the main components in the soil. The soil thermal conductivity model is represented as a sphere of the mineral part in the sphere of water. A cube - a unit volume, truncates both spheres. The main design parameters are the radii of the spheres of water and air. A single volume was divided into several heat flow paths with the same set of soil components, for each of which the thermal conductivity was calculated as for a multilayer wall. The total thermal conductivity was calculated by averaging, taking into account the cross-sectional areas of each of the paths. Depending on the values of the design parameters and their relationship, the model has identified three design cases. An analytical solution is obtained for each design case. Comparison of the calculation results using the developed model showed good agreement with experimental data and existing thermal conductivity models.

Funding: This research was carried out with the financial support of the Ministry of Science and Higher Education of the Russian Federation in the framework of the program of activities of the Perm Scientific and Educational Center "Rational Subsoil Use".

Citation: Zakharov, A.V., Ponomaryov, A.B., Ofrikhter, I.V. Model of soil thermal conductivity in the form of a truncated sphere. Magazine of Civil Engineering. 2022. 114(6). Article No. 11403. DOI: 10.34910/MCE.114.3

1. Introduction

Thermophysical properties play an essential role when performing calculations of energy-efficient structures of foundations of foundation soils [1]. The main thermophysical properties of the soil are usually referred to as thermal conductivity λ and heat capacity c .

The thermophysical properties of soils depend on many factors: the mineral of the soil particles, the size and shape of the particles, density, moisture content, porosity.

Solid minerals are the most heat-conducting components in the air-water-soil particles system. Therefore, they define an upper limit for thermal conductivity. The soil, consisting of different mineral substances, has different thermal conductivity [2]. Soil with a higher quartz content has a higher thermal conductivity [3].

The heat flux between soil particles is proportional to the radius of the particles. Larger particles and smaller contacts in a given volume allow one to obtain a higher thermal conductivity [2], [4]. An increase in thermal conductivity is provided by smaller particles filling the pore space between large ones [5].

An increase in soil density (constant particle size distribution) leads to a decrease in porosity, an increase in soil particles' contact area, and an increase in its thermal conductivity. The moisture content of the soil significantly affects its thermal conductivity. With increasing humidity, the thermal conductivity of the soil increases.

There are two main approaches to determining the thermal conductivity of soils. Conditionally they can be called direct and calculated.

With a direct approach, the measurement of the thermal conductivity of a particular soil sample is carried out in laboratory conditions. As a result, the thermal conductivity of the soil is determined at specific values of the physical characteristics (density, the density of dry soil, moisture, etc.).

The computational approach includes a large group of methods based on determining the thermal conductivity of the soil by calculating it from the previously established dependence of the thermal conductivity of the soil on its physical characteristics, the thermal conductivity of its components, taking into account their volume fraction.

Much research has been devoted to determining the dependence of the thermal conductivity of soil on its physical characteristics. Based on the results of which, a variety of computational models and methods have been proposed. At the same time, it is noted that new models are currently appearing, which indicates that a universal model has not been found.

The existing methods and models can be divided into three groups [6]:

- Mixing models. These models view the soil as a multiphase system composed of water, air, and soil particles. The thermal conductivity of the soil is calculated as a combination of the thermal conductivity of the volumes of individual phases (components) in an elementary volume;
- Empirical models. These models are based on the identification of empirical dependences of the thermal conductivity of the soil on its physical characteristics (density, moisture, porosity, etc.);
- Mathematical models. These models were borrowed from predictive models for other physical properties such as dielectric constant, magnetic permeability, electrical conductivity, and hydraulic conductivity.

In mixing models, the soil is most often considered a medium consisting of three main components: water, air, soil particles. Ice is added in the models for soils in a frozen state instead of or together with water.

Some of the models allow to include an unlimited number of components (for example, take into account organic inclusions). In contrast, others, on the contrary, are developed for a specific set and number of components.

The most common models are based on the classical laws of mixing (arithmetic and geometric): sequential, parallel, geometric mean model, quadratically parallel, effective mean, etc.

The simplest models are sequential ones. These models have the least amount of constraints as they do not consider the actual soil structure. The sequential model provides constant heat flux through each series-connected component so that each component has a different temperature gradient determined by its thermal conductivity.

Mixing models include Mickley (1951) [7], De Vries (1952) [8], Gemant (1952) [2], McGaw (1969) [9], many of which were later upgraded or formed the basis of new models.

Mixing models also include Gori and Corasaniti (2002) [10], Campbell (1994) [11], Gens et al. (2009) [12], Cho et al. (2001) [13], Haigh (2012) [14], Tarnawski and Leong (2016) [15], Tian et al. (2016) [16], Lu et al. (2014) [17].

One of the first empirical models for assessing thermal conductivity was the Kersten model [18]. Another of the well-known empirical methods for determining the thermal conductivity of soils is the method of Johansen (1975) [19]. This model is developed by Knutsson (1983) [20], Côté and Konrad (2005) [21], Nikoosokhan et al. [22], Zhang et al. (2017) [23], Lu et al. (2014) [17], Dharssi et al. (2009) [24], Wilson et al. (2011) [25], Róžański and Stefaniuk (2016, 2020) [26], [27].

The empirical models also include the models of McCumber and Pielke (1981) [28], Kahr and Muller-Vonmoos (1982) [29], Campbell (1985) [11], Chung and Horton (1987) [30], Becker (1992) [31], Newson et al. (2002) [32], Chen (2008) [14], Caridad et al. (2014) [33], Lu et al. (2014) [17], Yoon et al. (2018) [34].

Among the mathematical models are the models, Nimick and Leith (1992) [35], Jougnot and Revil (2010) [36].

In order to compare the various calculation methods, several assessments of the thermal conductivity of the soil have been performed. A calculation was made for sandy and clayey soil with a dry soil density $\rho_d = 1.4 \text{ g/sm}^3$, soil particle density $\rho_s = 2.65 \text{ g/sm}^3$ and varying the saturation S_r in the range $0.01 \div 1.00$. More than 60 methods were used for the calculation. The calculation results are presented on Figures 1 and 2.

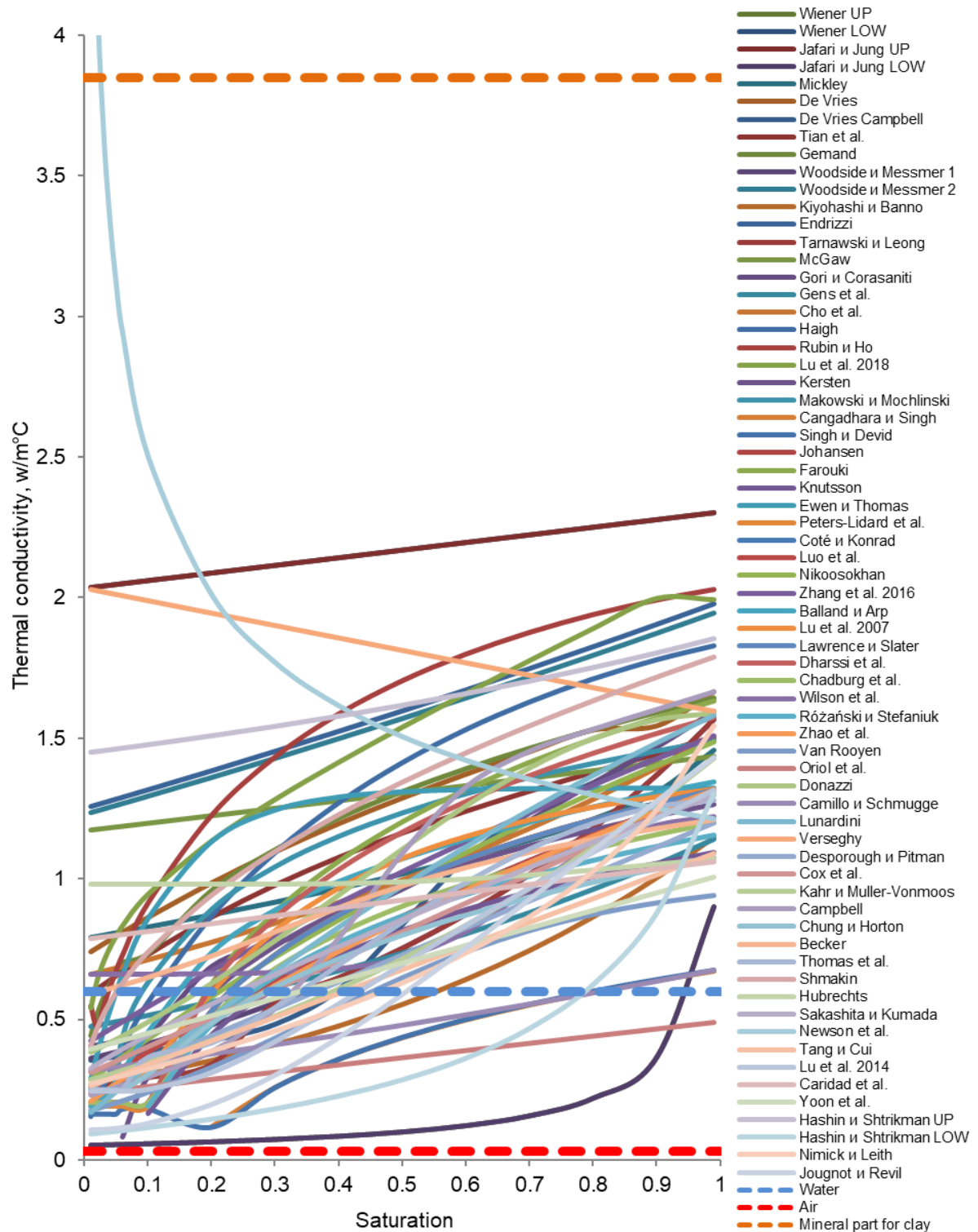


Figure 1. Thermal conductivity of clay soil ($\rho_d = 1.4 \text{ g/sm}^3$, $\rho_s = 2.65 \text{ g/sm}^3$) with a saturation from 0.01 to 1, calculated according to various models.

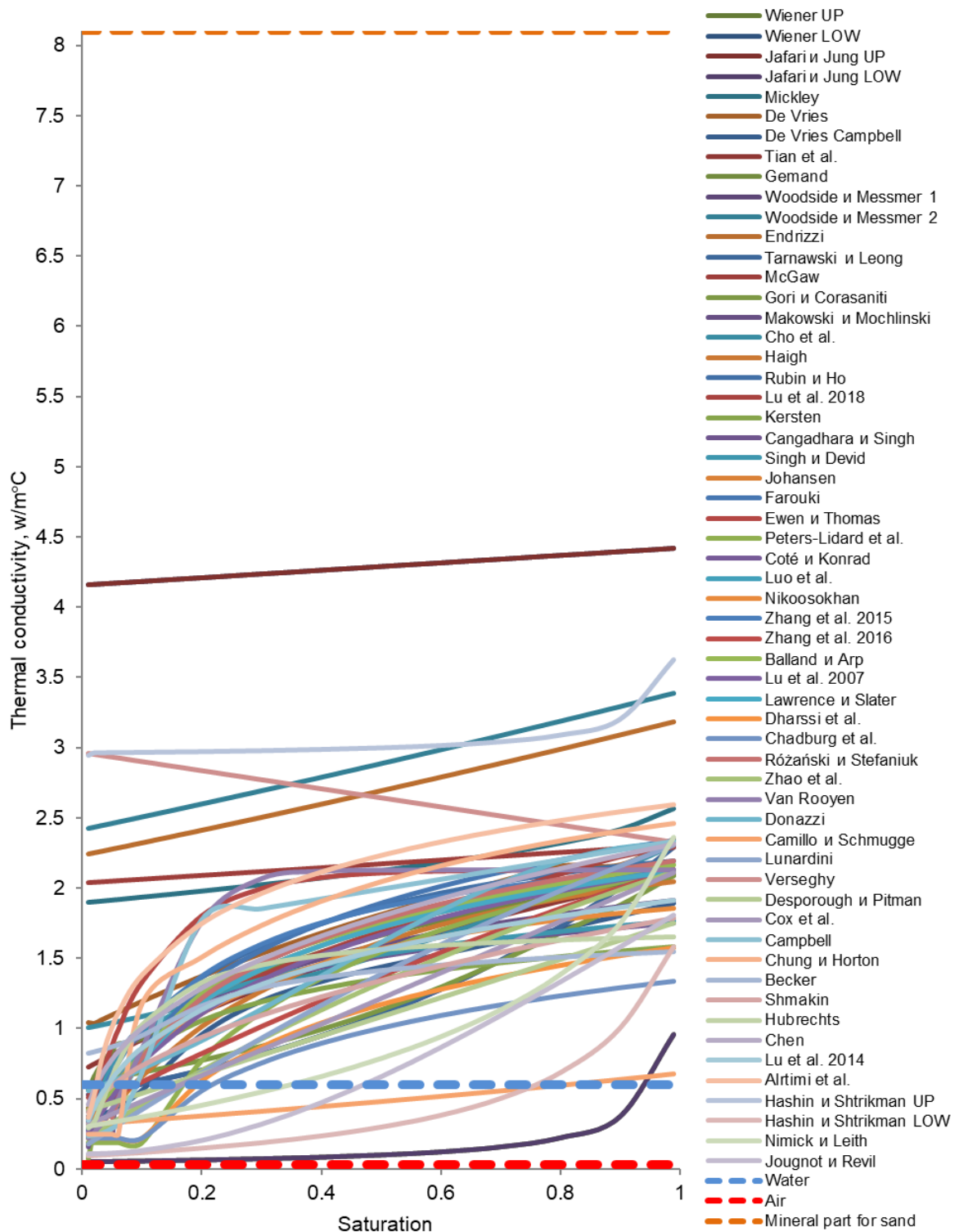


Figure 2. Thermal conductivity of sand soils ($\rho_d = 1.4 \text{ g / sm}^3$, $\rho_s = 2.65 \text{ g / sm}^3$) with a saturation from 0.01 to 1, calculated according to various models.

The analysis of the graphs showed that the considered models give a wide range of soil thermal conductivity values with the same input parameters. In this case, the obtained values lie within the Wiener boundaries (for the overwhelming number of models). A wide range of values may be due to:

- Some empirical models were developed for soils of a certain granulometric and, probably, more importantly, mineralogical composition. Since the thermal conductivity of particle minerals can differ significantly (from 2 W/m°C to 9 W/m°C). In addition, the features of the origin and composition, the presence of organic impurities (and others) in the soils, based on the tests of which empirical dependencies and empirical correction factors were obtained;

- Empirical models were developed or verified on an array of experimental studies of soils with a specific range of their physical characteristics (dry soil density, moisture content or saturation, etc.);
- Assumptions and simplifications can cause more significant errors than they supposed.

After analyzing the above studies, it can be concluded that at the moment, there is no generally accepted method for calculating the thermophysical characteristics of the soil. Existing methods give a wide range of estimates.

Empirical techniques based on experimental data give more accurate results for a specific type of soil (with certain limits of variation of its physical characteristics, grain size and mineralogical composition, etc.). Computational models (mathematical and displacement models), which attempt to describe the process mathematically conductivity in soils, give less accurate results, but have a wider field of application.

Thus, the research goal was set: the development of a non-empiric method for calculating the thermal conductivity of soil based on its physical characteristics. The following problems were solved:

- a model of soil heat transfer is proposed;
- analytical solutions of the parameters of the developed model were obtained, and a calculation method was proposed;
- laboratory studies were carried out to determine the thermal conductivity of sandy and clayey soils;
- the analysis of the convergence of the data obtained by the developed method with experimental data has been carried out.

2. Methods.

The mechanism of heat transfer between its particles is essential in describing the heat transfer process in soils. Existing researches register that heat transfer between particles occurs in several directions (Figure 3) [37].

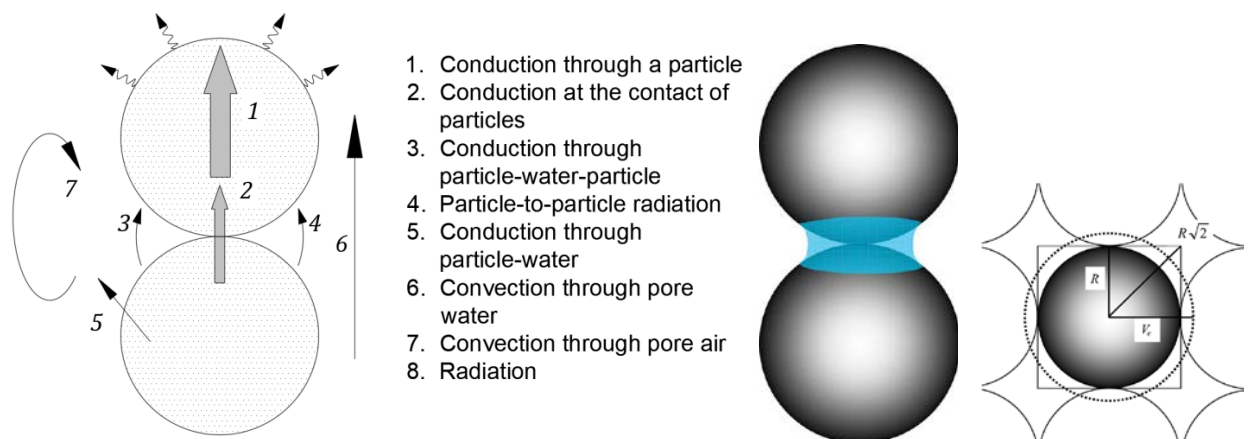


Figure 3. Scheme of heat transfer between soil particles and spherical model of soil particles [38].

At the same time, the experimental data have inconsistencies with the model of soil particles in the form of spheres. This is explained by the fact that the leading share of heat transfer is due to conductive heat transfer between particles, and the contact area of original soil particles is much higher, including due to bound water at the contact site (Figure 3).

Numerical heat transfer modeling at the contact of spherical particles considering a water lens shows a high convergence with experimental data, but only for soils with low moisture content [38]. The thermal conductivity of the soil at higher humidity is influenced by gravitational water, the position of which is not described by this model.

The proposed soil model is a sphere, truncated by the sides of a unit cube (Figure 4) to consider the increase in the contact areas of a part of the soil, the characteristics of the mineral part, and the presence of water. This model is not entirely new. Many researchers have used a spherical soil model to estimate thermal conductivity [38], [39]. Previously, the authors determined a method for refining a number of characteristics of spherical model based on laboratory tests [40]. However, in this study, it is proposed to expand the scope of the model, in comparison with existing analogues. For the proposed model, the following assumptions are made:

- Only conductive heat transfer is considered because of the possibility of experimental testing of such a model in laboratory conditions. This assumption is often used to determine the effective thermal conductivity of multiphase materials.
- It is assumed that the soils have an above-zero temperature without significant temperature gradients. Thus, heat exchange associated with a change in the state of aggregation of the liquid phase, water movement, or steam movement is ignored.
- A truncated sphere that imitates the mineral part of the soil is not related to the size of the soil particles but only expresses the volume fraction of the mineral part.
- Soil particles have contact areas with each other.

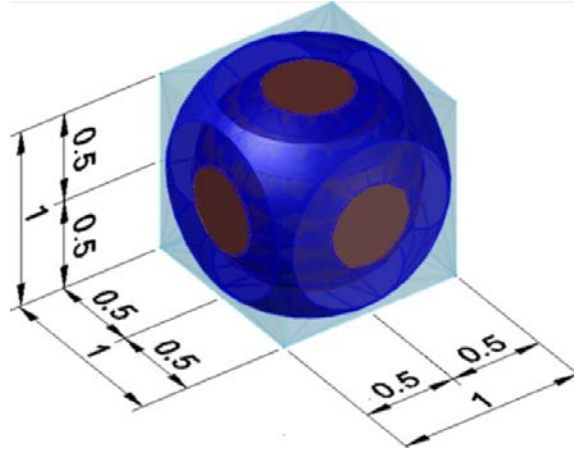


Figure 4. Geometric model of a soil particle in a unit volume.

The soil model has three main components: mineral, water, and air. The volume of each component is calculated from the porosity n and the saturation S_r , which are the model's input parameters.

$$\begin{aligned} V_s &= 1 - n; \\ V_w &= n \cdot S_r; \\ V_a &= n \cdot (1 - S_r) \end{aligned} \quad (1)$$

where V_s is the mineral volume, V_w is the water volume, V_a is the pore volume. The calculated parameters of the model are taken as R_s and R_w are radiuses of the spheres forming the volumes of the mineral part and water, respectively.

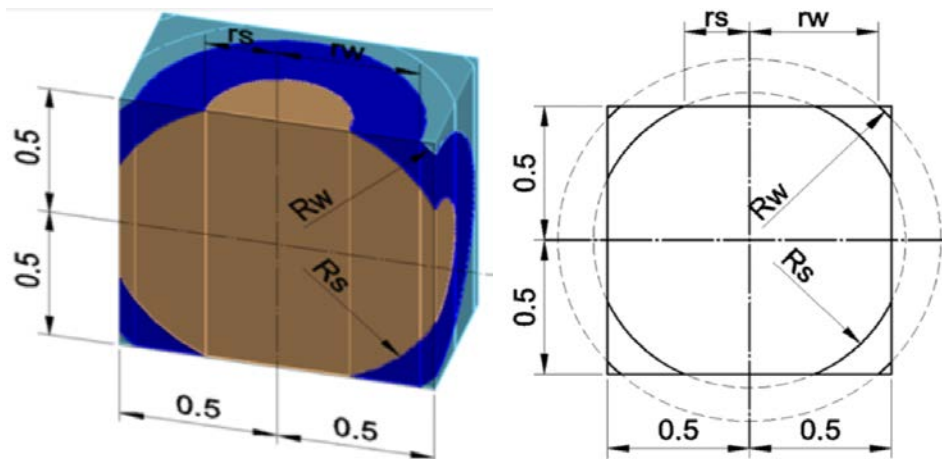


Figure 5. The design scheme of the model.

R_s is the radius of the mineral part sphere. R_w is the radius of the sphere that forms the volume of groundwater. The radius r_s of the circle formed by the intersection of the surface of the water sphere with the surface of the bounding unit volume. The radiuses r_s , r_w are found from the Pythagorean theorem:

$$\begin{aligned} r_s &= \sqrt{R_s^2 - 0.25} \\ r_w &= \sqrt{R_w^2 - 0.25} \end{aligned} \quad (2)$$

From the condition that each soil particle has at least an infinitely small area of contact with another particle, the minimum radius of the soil sphere in the model is half the size of a unit cube. The maximum radius should not exceed half the diagonal:

$$\begin{cases} R_{s,\min} = 0.5 \\ R_{s,\max} = \frac{\sqrt{2}}{2} \end{cases} \quad (1)$$

The volume of mineral particles is calculated as the volume of a sphere of radius R_s truncated by six sectors of height $R_s - 0.5$ (Figure 5, 6).

$$V_s = 1 - n = \frac{4}{3}\pi R_s^3 - 6 \cdot \frac{1}{3}\pi (2R_s^3 - 1.5R_s^2 + 0.125) \quad (2)$$

Considering porosity equation, the following equation is obtained:

$$n = 8/3\pi R_s^3 - 3\pi R_s^2 + 0.25\pi + 1 \quad (3)$$

A high-order polynomial was obtained in the interval $0.5 \geq R_s \geq \sqrt{2}/2$ to find the inverse function $R_s = f(n)$:

$$R_s = 120.69n^6 - 207.91n^5 + 144.64n^4 - 52.55n^3 + 10.972n^2 - 1.727n + 0.7553 \quad (4)$$

Further, the maximum and minimum soil porosity were obtained, for which this model is applicable:

$$\begin{cases} R_{s,\min} = 0.5 \rightarrow n_{\max} = 0.4764 \\ R_{s,\max} = \frac{\sqrt{2}}{2} \rightarrow n_{\min} = 0.0349 \end{cases} \quad (5)$$

The proposed model does not allow calculating the thermal conductivity of soil with a porosity of more than 0.4764. It should be noted that soils with a porosity of less than 0.0349 are extremely rare. Since the water is located around the soil particle, the radius of the water sphere must be greater than or equal to the radius of the soil particle. That. The boundaries of the radius of the water sphere for the model:

$$\begin{cases} R_w \geq R_s \\ R_w = 0.5 \rightarrow S_r = 0 \\ R_w = \frac{\sqrt{3}}{2} \rightarrow S_r = 1 \end{cases} \quad (6)$$

The model is divided into three design cases, to obtain an analytical solution. For each design case, the main design parameters were obtained. Design cases are highlighted due to the geometric features of the model and are determined by a set of conditions:

1. First case:

$$\begin{cases} R_{w,\min} = 0.5 \\ R_{w,\max} = \frac{\sqrt{2}}{2} \end{cases} \quad (7)$$

2. Second case:

$$\begin{cases} R_w^2 - R_s^2 \geq 0.25 \\ R_{w,\min} = \frac{\sqrt{2}}{2} \\ R_{w,\max} = \frac{\sqrt{3}}{2} \end{cases} \quad (8)$$

3. Third case:

$$\begin{cases} R_w^2 - R_s^2 \leq 0.25 \\ R_{w,\min} = \frac{\sqrt{2}}{2} \\ R_{w,\max} = \frac{\sqrt{3}}{2} \end{cases} \quad (9)$$

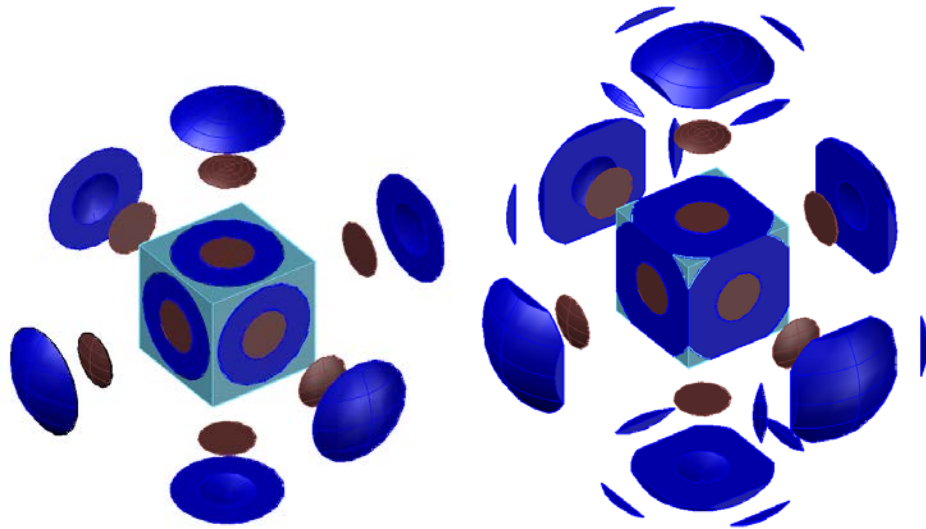


Figure 6. Scheme of truncation of the sphere of water and soil by a unit cube for first design case (left), 2 and 3 cases (right).

For the first computational case, the volume of a sphere with a radius R_w , truncated by the edges of a unit cube, includes the volumes of water and soil particles. For this case, the following expression is valid:

$$V_s + V_w = 1 - n + nS_r = \frac{4}{3}\pi R_w^3 - 6 \cdot \frac{1}{3}\pi (2R_w^3 - 1.5R_w^2 + 0.125) \quad (10)$$

From this equation, the range of admissible values of S_r for the first design case is obtained:

$$\begin{cases} R_{w,\min} = 0.5 \rightarrow (n - nS_r)_{\max} = 0.4764 \rightarrow S_r \geq 1 - \frac{0.4764}{n} \\ R_{w,\max} = \frac{\sqrt{2}}{2} \rightarrow (n - nS_r)_{\min} = 0.0349 \rightarrow S_r \leq 1 - \frac{0.0349}{n} \end{cases} \quad (11)$$

Thus, the range of permissible values of the saturation at a given porosity for the first design case is determined by the following equation:

$$S_r \leq 1 - \frac{0.0349}{n} \quad (12)$$

As $a = n - nS_r$, a polynomial for calculating the R_w parameter for the first design case through porosity and saturation is:

$$R_w = 117.55a^6 - 202.64a^5 + 141.18a^4 - 51.424a^3 + 10.784a^2 - 1.7121a + 0.754 \quad (13)$$

For the second and third calculation cases, the volume of a sphere with a radius of R_w , truncated by the edges of a unit cube, also includes the volumes of water and soil particles. The volume of the truncated sphere is calculated as the difference between a sphere with a radius R_w and six segments of the sphere with the addition of the volumes of 12 figures of the intersection of segments V_c :

$$V_s + V_w = 1 - n + nS_r = \frac{4}{3}\pi R_w^3 - \frac{6}{3}\pi(2R_w^3 - 1.5R_w^2 + 0.125) + 12V_c \quad (14)$$

The volume V_c was found by integration in cylindrical coordinates:

$$12V_c = \frac{48}{3}R_w^3 \arctan \frac{\sqrt{R_w^2 - 0.5}}{R_w} + (1 - 12R_w^2) \arctan \sqrt{4R_w^2 - 2} + \sqrt{4R_w^2 - 2} \quad (15)$$

$$n - nS_r = \frac{8}{3}R_w^3 \left(\pi - 6 \arctan \frac{\sqrt{R_w^2 - 0.5}}{R_w} \right) - 3\pi R_w^2 - \quad (16)$$

$$(1 - 12R_w^2) \arctan \sqrt{4R_w^2 - 2} - \sqrt{4R_w^2 - 2} + 0.25\pi + 1$$

From the equation, the interval of admissible values of S_r for the second and third calculated cases can be expressed:

$$\begin{cases} R_{w,\min} = \frac{\sqrt{2}}{2} \rightarrow (n - nS_r)_{\max} = 0.0349 \rightarrow S_r \geq 1 - \frac{0.0349}{n} \\ R_{w,\max} = \frac{\sqrt{3}}{2} \rightarrow (n - nS_r)_{\min} = 0.0000 \rightarrow S_r \leq 1 - \frac{0}{n} = 1 \end{cases} \rightarrow 1 - \frac{0.0349}{n} \leq S_r \leq 1 \quad (17)$$

Further, a polynomial approximation was obtained to calculate the R_w parameter for the second and third calculation cases. The equation uses porosity and saturation as input. The polynomial is split into two sections (Figure 7). The polynomials for the vertical and inclined portions of the function are obtained separately. The applicability of the model is demonstrated in Figure 7.

If $a = n - nS_r \geq 0.000233$:

$$R_w = 1592939271a^6 - 183771126.0476a^5 + 8347971.33a^4 - 190847.7004a^3 + 2375.7524a^2 - 18.6798a + 0.8315 \quad (18)$$

If $a = n - nS_r \leq 0.000233$:

$$R_w = 298924205636208000000a^6 - 426988215430283000a^5 + 235463863173120a^4 - 63097328697a^3 + 8570419.9417a^2 - 618.7835a + 0.8619 \quad (19)$$

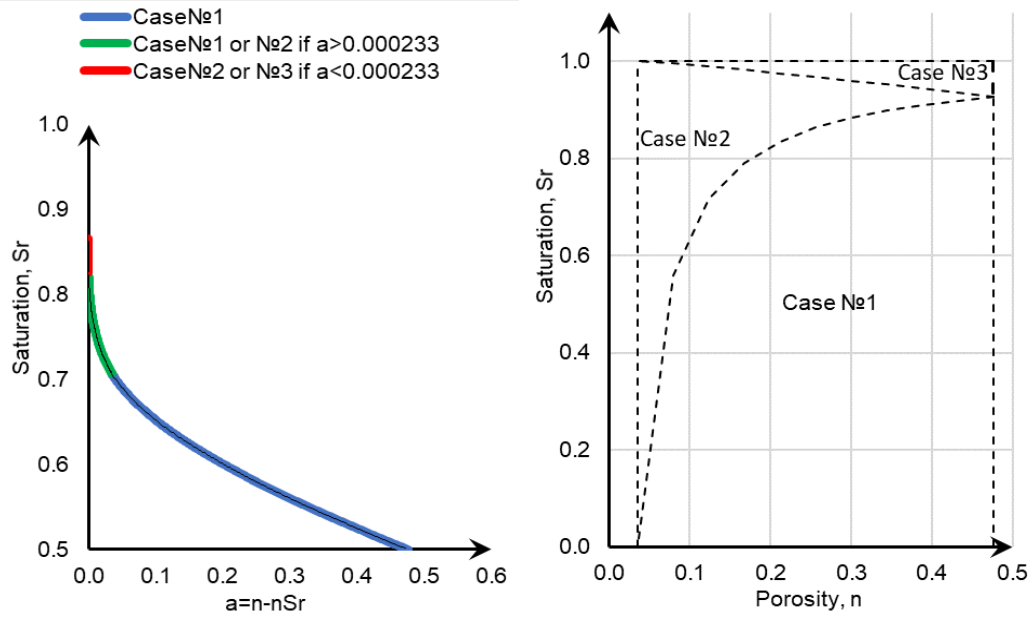
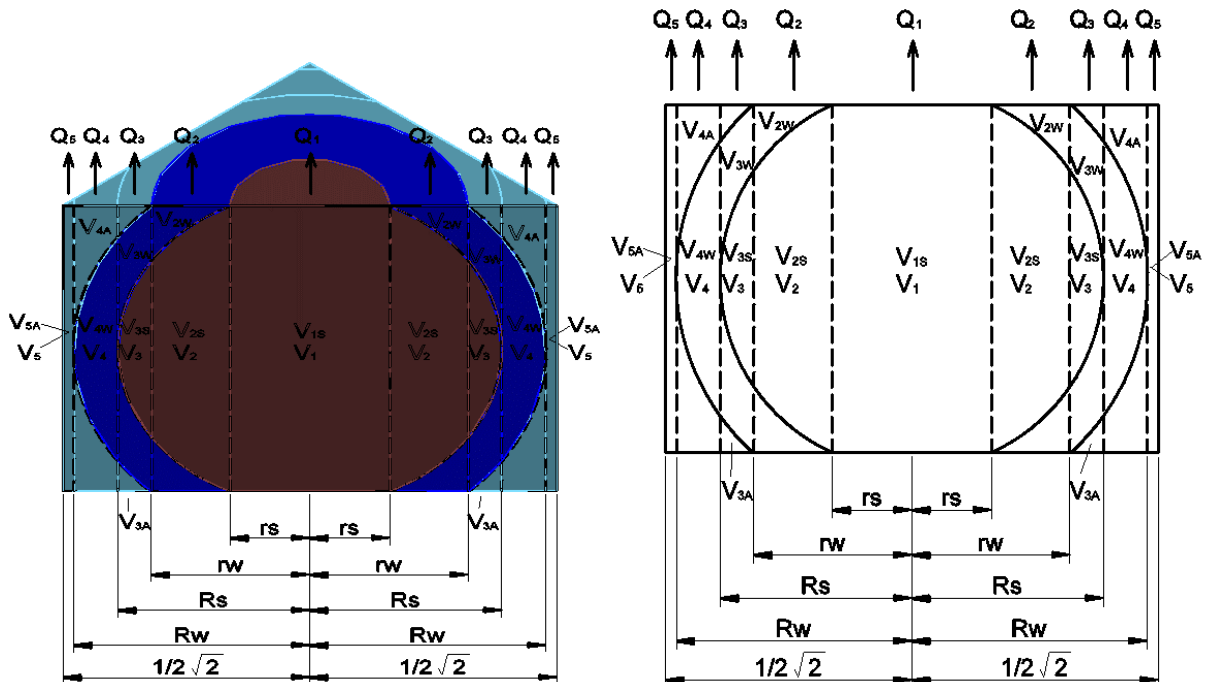


Figure 7. Scope of different cases of model applicability.

A heat flux passing through a unit volume in one direction from bottom to top was considered to derive the heat conduction equation.

The model was divided into volumes in the direction of the heat flow. All volumes have a constant set of components along the path of heat flow. For each case, a separate heat conduction equation is obtained.

For the first design case, five "paths" of the heat flux passing through a unit volume can be distinguished. Design schemes in plan and in section for deriving the desired equation are shown in the Figure 8.



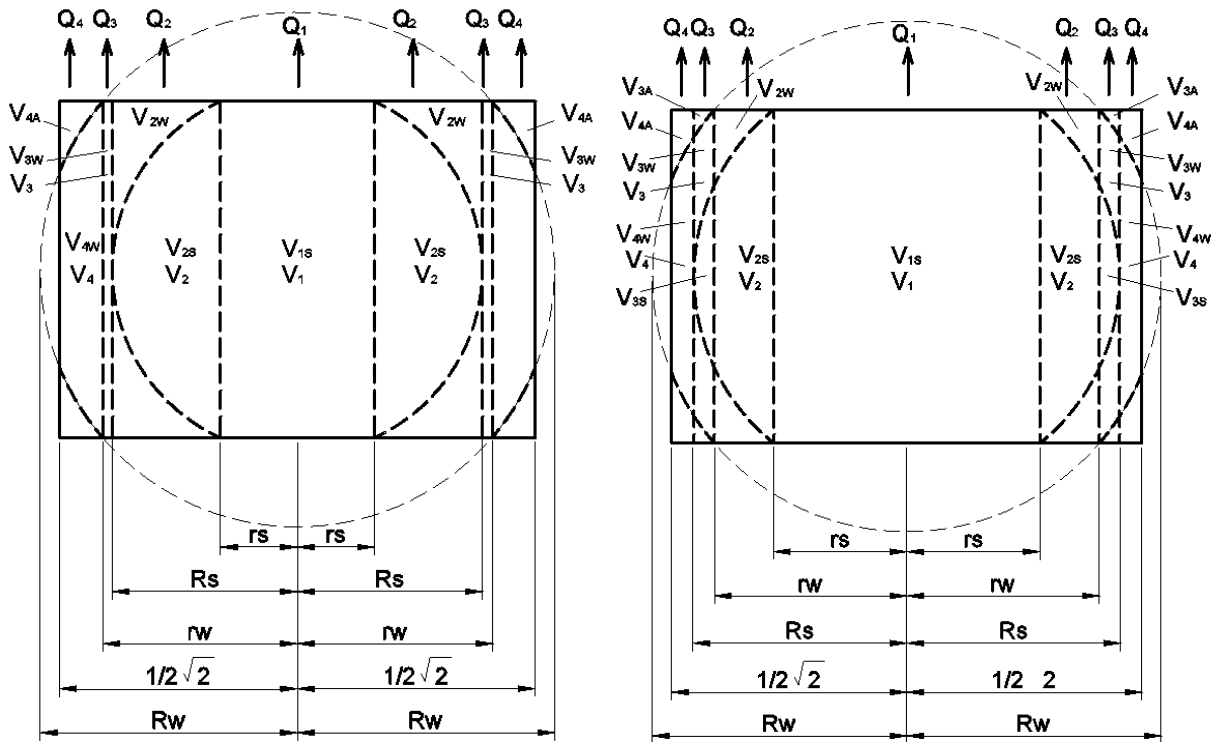


Figure 8. Diagonal section for the first, second, and third design cases.

In Figure 8, the following designations are adopted for the diagrams:

Q_1 is the heat flow passing only through the volume of the mineral part V_{1S} ;

Q_2 is the heat flow passing through the mineral part and water volumes V_{2S} и V_{2W} ;

Q_3 is the heat flow passing through the mineral part, water and air volumes V_{3S} , V_{3W} и V_{3A} ;

Q_4 is the heat flow passing through water and air volumes V_{4W} , V_{4A} ;

Q_5 is the heat flow passing through air volume V_{5A} ;

V_{1-5} is the volume through which heat flows Q_{1-5} pass ;

S_{1-5} is the horizontal sectional areas of volumes V_{1-5}

Thermal conductivity was calculated using the formula:

$$\lambda = \frac{Q}{\Delta T} = \frac{Q_1 + Q_2 + Q_3 + Q_4 + Q_5}{\Delta T} \tag{20}$$

where: ΔT is the temperature gradient, 1 is side length of a unit cube. The values of heat fluxes were found as for a multilayer wall by the formula:

$$Q = S \cdot \frac{\Delta T}{\sum_{i=1}^n \frac{\delta_i}{\lambda_i}} \tag{21}$$

where ΔT is the temperature gradient, S is the heat flow area, δ_i is the thickness of the i -th layer within the area S , λ_i is the thermal conductivity of the i -th layer. Thickness δ_i is considered unchanged within one heat flux:

$$\delta_i = \frac{V_i}{S} \tag{22}$$

With this assumption, the heat flux is written as follows:

$$Q = S^2 \cdot \frac{\Delta T}{\sum_{i=1}^n \frac{V_i}{\lambda_i}} \quad (23)$$

Next, the calculation of the power of heat flows was made for Q_{1-5} :

$$Q_1 = S_1^2 \cdot \frac{\lambda_s \cdot \Delta T}{V_{1S}} \quad (24)$$

$$Q_2 = S_2^2 \cdot \frac{\Delta T}{V_{2S} \div \lambda_s + V_{2W} \div \lambda_w} \quad (25)$$

$$Q_3 = S_3^2 \cdot \frac{\Delta T}{V_{3S} \div \lambda_s + V_{3W} \div \lambda_w + V_{3A} \div \lambda_a} \quad (26)$$

$$Q_4 = S_4^2 \cdot \frac{\Delta T}{V_{4W} \div \lambda_w + V_{4A} \div \lambda_a} \quad (27)$$

$$Q_5 = S_5^2 \cdot \frac{\Delta T}{V_{1S} \div \lambda_s} \quad (28)$$

Combining equations and (25), an expression was obtained to determine the thermal conductivity of the entire model:

$$\lambda = \frac{S_1 \lambda_s}{1} + \frac{S_2^2}{\frac{V_{2S}}{\lambda_s} + \frac{V_{2W}}{\lambda_w}} + \frac{S_3^2}{\frac{V_{3S}}{\lambda_s} + \frac{V_{3W}}{\lambda_w} + \frac{V_{3A}}{\lambda_a}} + \frac{S_4^2}{\frac{V_{4W}}{\lambda_w} + \frac{V_{4A}}{\lambda_a}} + \frac{S_5 \lambda_a}{1} \quad (29)$$

Equations of heat conductivity for second and third calculation cases were obtained in a similar way. For the second and third design cases, four "paths" of the heat flux passing through a unit volume can be distinguished.

$$\lambda = \frac{S_1 \lambda_s}{1} + \frac{S_2^2}{\frac{V_{2S}}{\lambda_s} + \frac{V_{2W}}{\lambda_w}} + \frac{S_3 \lambda_w}{1} + \frac{S_4^2}{\frac{V_{4W}}{\lambda_w} + \frac{V_{4A}}{\lambda_a}} \quad (30)$$

$$\lambda = \frac{S_1 \lambda_s}{1} + \frac{S_2^2}{\frac{V_{2S}}{\lambda_s} + \frac{V_{2W}}{\lambda_w}} + \frac{S_3^2}{\frac{V_{3S}}{\lambda_s} + \frac{V_{3W}}{\lambda_w} + \frac{V_{3A}}{\lambda_a}} + \frac{S_4^2}{\frac{V_{4W}}{\lambda_w} + \frac{V_{4A}}{\lambda_a}} \quad (31)$$

Equations were derived for the geometric parameters of the model S_i and V_i . The calculation was made by the intersection of the coordinate system and the areas of the data element (spheres, cylinder, cube). The individual parameters are calculated by integration in cylindrical coordinates.

3. Results and Discussion

The calculation of thermal conductivity according to the developed model is performed in the following sequence:

1) Preparation of input data. Initial data include saturation, porosity, the thermal conductivity of water, air, and mineral parts. Saturation and porosity can be obtained from laboratory tests. It is permissible to assign thermal conductivity of water and air $\lambda_w = 0.56 \text{ W/m}^\circ\text{C}$, $\lambda_a = 0.026 \text{ W/m}^\circ\text{C}$.

The thermal conductivity of the mineral part λ_s can be determined by carrying out one experimental measurement. When experimentally determining the thermal conductivity of a conventional mineral part, a test is required on a soil sample with a porosity of $n \leq 0.4764$.

The sample can be obtained from field test or formed in the laboratory. It is also crucial that the sample's granulometric and mineralogical composition corresponds to the soil composition for which the calculation will be made. After the experiment, the value of λ_s is selected so that the values of the experimental determination and the calculated one coincide. The found value λ_s will be suitable for calculating thermal conductivity at various values of n and S_r , provided that the mineralogical and particle size distribution is preserved.

When it is not possible to make a test, it is possible to approximately assign the thermal conductivity of the mineral part, based on the quartz content in the soil, using the calculation formulas proposed by Campbell or Johansen.

2) Checking model applicability. Porosity should be less than $n \leq 0.4764$.

3) The choice of the design case of the model according to the value of the saturation:

$$\begin{cases} S_r \leq 1 - \frac{0.0349}{n} \rightarrow \text{case1} \\ S_r \geq 1 - \frac{0.0349}{n} \rightarrow \text{case2or3} \end{cases} \quad (32)$$

4) Determination of the design parameters R_s and R_w according to the formulas of the corresponding design case. At this stage, a choice is made between the second and third design cases:

$$\begin{cases} R_w^2 - R_s^2 \geq 0.25 \rightarrow \text{case2} \\ R_w^2 - R_s^2 \leq 0.25 \rightarrow \text{case3} \end{cases} \quad (33)$$

5) Calculation of the model's parameters S_i and V_i according to the formulas of Tables 1-3 for the corresponding design case.

Table 1. Equations of thermal conductivity parameters for first a design case.

Parameters	Calculation formula
S_1	$\pi(R_s^2 - 0.25)$
S_2	$\pi(R_w^2 - R_s^2)$
S_3	$\pi(R_s^2 - R_w^2 + 0.25) - 4R_s^2 \arccos\left(\frac{0.5}{R_s}\right) + 2\sqrt{R_s^2 - 0.25}$
S_4	$1 - S_1 - S_2 - S_3 - S_5$
S_5	$1 - \pi R_w^2 + 4R_w^2 \arccos\left(\frac{0.5}{R_w}\right) - 2\sqrt{R_w^2 - 0.25}$
V_{2S}	$\frac{4}{3}\pi \left[0.125 - (R_s^2 - R_w^2 + 0.25)^{\frac{3}{2}} \right]$
V_{3S}	$\frac{4}{3}\pi \left[(R_s^2 - R_w^2 + 0.25)^{\frac{3}{2}} - 2R_s^3 + 1.5R_s^2 - 0.125 \right]$

Parameters	Calculation formula
V_{2W}	$\pi(R_w^2 - R_s^2) - \frac{4}{3}\pi \left[0.125 - (R_s^2 - R_w^2 + 0.25)^{\frac{3}{2}} \right]$
V_{3W}	$n \cdot S_r - V_{2W} - V_{4W}$
V_{4W}	$-\frac{8}{3}\pi R_w^3 + 2\pi R_w^2 - \frac{1}{6}\pi + \frac{16}{3}(R_w^2 - R_s^2)^{\frac{3}{2}} \cdot \left(\frac{\pi}{4} - \arccos \frac{1}{2R_s} \right) +$ $\frac{16}{3}R_w^3 \arctan \left(2R_w \sqrt{\frac{R_s^2 - 0.25}{R_w^2 - R_s^2}} \right) -$ $\frac{4}{3}(3R_w^2 - 0.25) \arcsin \sqrt{\frac{R_s^2 - 0.25}{R_w^2 - 0.25}} - \frac{4}{3} \sqrt{R_s^2 - 0.25} \sqrt{R_w^2 - R_s^2}$
V_{3A}	$S_3 \cdot 1$
V_{4A}	$S_4 \cdot 1$

Table 2. Equations of thermal conductivity parameters for a second design case.

Parameters	Calculation formula
S_1	$\pi(R_s^2 - 0.25)$
S_2	$0.25\pi - 4R_s^2 \arccos \left(\frac{0.5}{R_s} \right) + 2\sqrt{R_s^2 - 0.25}$
S_3	$1 - S_1 - S_2 - S_4$
S_4	$\frac{1}{4}\pi + 1 - \pi R_w^2 + 4(R_w^2 - 0.25) \arccos \left(\frac{0.5}{\sqrt{R_w^2 - 0.25}} \right) - 2\sqrt{R_w^2 - 0.5}$
V_{2S}	$S_2 \cdot 1 - V_{2W}$
V_{3S}	-
V_{2W}	$nS_r - V_{3W} - V_{4W}$
V_{3W}	$\pi(R_w^2 - R_s^2 - 0.25) - 4(R_w^2 - 0.25) \arccos \left(\frac{0.5}{\sqrt{R_w^2 - 0.25}} \right) + 4R_s^2 \arccos \left(\frac{0.5}{R_s} \right) +$ $2\sqrt{R_w^2 - 0.5} - 2\sqrt{R_s^2 - 0.25}$
V_{4W}	$S_4 \cdot 1 - V_{4A}$
V_{4A}	$n - nS_r$

Table 3. Equations of thermal conductivity parameters for a third design case.

Parameters	Calculation formula
S_1	$\pi(R_s^2 - 0.25)$
S_2	$\pi(R_w^2 - R_s^2) - 4(R_w^2 - 0.25) \arccos\left(\frac{0.5}{\sqrt{R_w^2 - 0.25}}\right) + 2\sqrt{R_w^2 - 0.5}$
S_3	$1 - S_1 - S_2 - S_4$
S_4	$1 - \pi R_s^2 + 4R_s^2 \arccos\left(\frac{0.5}{R_s}\right) - 2\sqrt{R_s^2 - 0.25}$
V_{2S}	$1 - n - V_{1S} - V_{3S}$
	$-\frac{8}{3}\pi R_s^3 + 2\pi R_s^2 - \frac{1}{6}\pi + \frac{16}{3}(R_s^2 - R_w^2 + 0.25)^{\frac{3}{2}} \cdot \left(\frac{\pi}{4} - \arccos\frac{1}{2\sqrt{R_w^2 - 0.25}}\right) +$
V_{3S}	$\frac{16}{3}R_s^3 \arctan\left(2R_s \sqrt{\frac{R_w^2 - 0.5}{R_s^2 - R_w^2 + 0.25}}\right) - \frac{4}{3}(3R_s^2 - 0.25) \arcsin\sqrt{\frac{R_w^2 - 0.5}{R_s^2 - 0.25}} -$
	$\frac{4}{3}\sqrt{R_w^2 - 0.5}\sqrt{R_s^2 - R_w^2 + 0.25}$
V_{2W}	$S_2 \cdot 1 - V_{2S}$
V_{3W}	$nS_r - V_{2W} - V_{4W}$
	$\frac{16}{3}R_w^3 \left(\arctan\left(\frac{R_w \sqrt{4R_s^2 - 1}}{\sqrt{R_w^2 - R_s^2}}\right) - \arctan\left(\frac{R_w}{\sqrt{R_w^2 - 0.5}}\right) \right) +$
V_{4W}	$\frac{1}{3}(12R_w^2 - 1) \left(\arcsin\left(\frac{1}{\sqrt{4R_w^2 - 1}}\right) - \arcsin\left(\sqrt{\frac{R_s^2 - 0.25}{R_w^2 - 0.25}}\right) \right) +$
	$\frac{2}{3} \left(\sqrt{R_w^2 - 0.5} - 2\sqrt{R_s^2 - 0.25} \sqrt{R_w^2 - R_s^2} \right) + \frac{16}{3} (R_w^2 - R_s^2)^{\frac{3}{2}} \left(\frac{\pi}{4} - \arccos\frac{0.5}{R_s} \right)$
V_{3A}	$n - nS_r - V_{4A}$
V_{4A}	$S_4 \cdot 1 - V_{4W}$

According to the proposed model, the thermal conductivity for sand and clay was calculated at various parameters of porosity and saturation. Thermal conductivity of water and air are $\lambda_w = 0.56$ W/m°C and $\lambda_a = 0.026$ W/m°C. Thermal conductivity of the mineral part $\lambda_s = 3.85$ W/m°C for clay and $\lambda_s = 8.1$ W/m°C for sand. Variation of the saturation is 0–1. The porosity varied within 0.05–0.45.

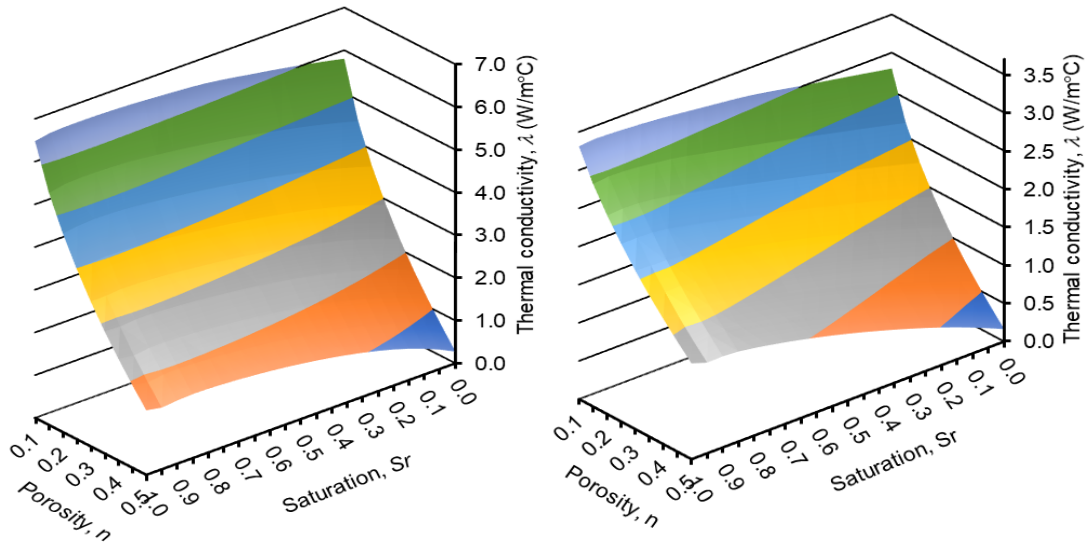
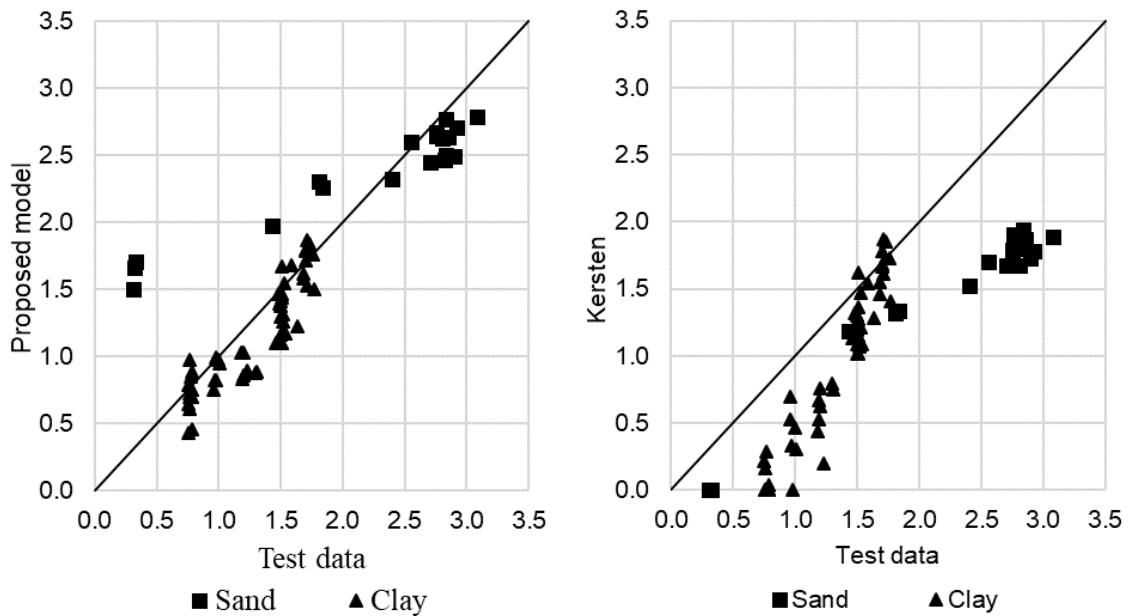


Figure 9. Thermal conductivity for sand (left) and clay (right) calculated at various parameters of porosity and saturation.

The reliability was assessed by comparing the results of the calculation of thermal conductivities according to the proposed model with experimental data and comparing the results of the calculation according to several generally accepted models.

For these purposes, an array of data on thermal conductivity of cohesive and sandy soils with varying porosity and saturation was formed. The dataset was obtained by laboratory measurements of thermal conductivity for sandy and clayey soils.

To assess the effectiveness of the proposed model, the calculation results were compared with other most popular models for assessing the thermal conductivity of the soil. For comparison, the models proposed by Kersten [18], Mickley [7], De Vries [8], Gemant [2], McGaw [9], Campbell [11], Johansen [19] were used. The comparison results are shown in Figure 10.



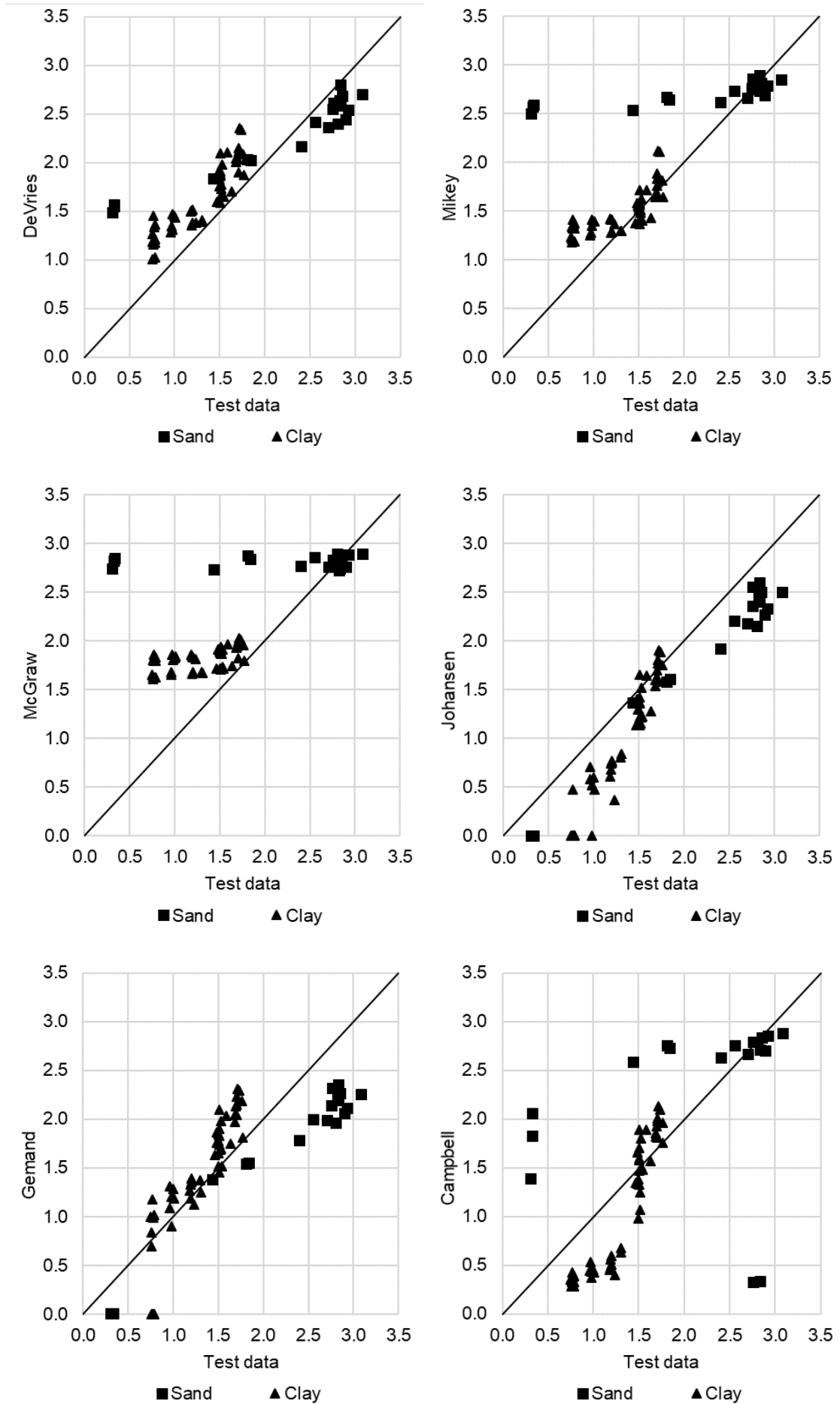


Figure 10. The comparison results.

To evaluate the performance of the proposed model, a number of statistical indicators were calculated. Pearson correlation coefficient, mean absolute percentage error and mean squared error are presented in the Table 4.

Table 4. Comparison of calculated data with experimental.

Calculation method	Sand			Clay		
	MSE	Pirson R	MAPE	MSE	Pirson R	MAPE
Kersten	0.89	0.95	32.19	0.19	0.93	22.48
De Vries	0.30	0.96	67.24	0.14	0.90	47.43
Mickley	0.93	0.81	119.00	0.09	0.76	24.51
McGraw	1.18	0.15	133.20	0.38	0.55	53.22
Johansen	0.19	0.94	15.19	0.11	0.92	21.77
Gemand	0.39	0.93	21.66	0.09	0.92	18.48
Lu et al. 2014	0.82	0.98	42.31	0.43	0.83	45.39
Campbell	0.02	0.99	19.95	0.17	0.93	30.70
Proposed model	0.34	0.97	21.78	0.05	0.90	18.05

To evaluate the performance of the proposed model, a number of statistical indicators were calculated. Pearson correlation coefficient, mean absolute percentage error and mean squared error are presented in the table.

Analysis of the above graphs and tables shows that for sandy soils, the Proposed model, the models of Johansen, Gemand and Campbell have good agreement with the experimental data and a low error.

For clayey soils, the Proposed model, the models of Johansen, Gemand and Kersten have good agreement with the experimental data and a low error.

4. Conclusion

Based on the results of the development of the model, the following conclusions were made:

1) The developed computational model for determining the thermal conductivity of the soil makes it possible to take into account the three-phase structure of the soil and the variable contact area of the mineral parts.

2) An analytical solution has been obtained, and a calculation method has been proposed, making it possible to assess the thermal conductivity of the soil based on its physical characteristics - porosity and saturation.

3) The proposed technique makes it possible to increase the convergence of the results with experimental data by determining the parameter from single laboratory determinations of the thermal conductivity of the soil.

References

1. Ponomaryov, A.B., Zakharov, A.V. Numerical Simulation of the Process of the Geothermal Low-potential Ground Energy Extraction in the Perm Region (Russia). *Procedia Engineering*. 2016. DOI: 10.1016/j.proeng.2016.07.293
2. Gemant, A. How to compute thermal soil conductivities. *Heating, Piping and Air Conditioning*. 1952. 24(1). Pp. 122–123.
3. Tarnawski, V.R., Momose, T., Leong, W.H. Assessing the impact of quartz content on the prediction of soil thermal conductivity. *Geotechnique*. 2009. 59(4). Pp. 331–338. DOI: 10.1680/geot.2009.59.4.331
4. Aduda, B.O. Effective thermal conductivity of loose particulate systems. *Journal of Materials Science*. 1996. 31(24). Pp. 6441–6448. DOI: 10.1007/BF00356246
5. Esch, D.C. Thermal analysis, construction, and monitoring methods for frozen ground 2013. 1–492 p. ISBN:9780784475485.
6. Dong, Y., McCartney, J.S., Lu, N. Critical Review of Thermal Conductivity Models for Unsaturated Soils. *Geotechnical and Geological Engineering*. 2015. 33(2). Pp. 207–221. DOI: 10.1007/s10706-015-9843-2
7. Mickley, A.S. The Thermal Conductivity of Moist Soil. *Transactions of the American Institute of Electrical Engineers*. 1951. 70(2). Pp. 1789–1797. DOI: 10.1109/T-AIEE.1951.5060631
8. De Vries D.A. The thermal conductivity of soil. *Mededeelingen van de Landbouwhogeschool te Wageningen*. Translated by Building Research Station (Library Communication No. 759). 1952. 52(1). Pp. 1–73.

9. MCGAW R. Heat Conduction in Saturated Granular Materials. Nat Acad Sciences-Nat Research Council--Highway Research Board--Special Report 103. 1969. Pp. 114–131.
10. Gori, F., Corasaniti, S. Theoretical prediction of the soil thermal conductivity at moderately high temperatures. *Journal of Heat Transfer*. 2002. 124(6). Pp. 1001–1008. DOI: 10.1115/1.1513573
11. Campbell, G.S., Jungbauer, J.D., Bidlake, W.R., Hungerford, R.D. Predicting the effect of temperature on soil thermal conductivity. *Soil Science*. 1994. 158(5). Pp. 307–313. DOI: 10.1097/00010694-199411000-00001
12. Gens, A., Sánchez, M., Guimarães, L.D.N., Alonso, E.E., Lloret, A., Olivella, S., Villar, M. V., Huertas, F. A full-scale in situ heating test for high-level nuclear waste disposal: Observations, analysis and interpretation. *Geotechnique*. 2009. 59(4). Pp. 377–399. DOI: 10.1680/geot.2009.59.4.377
13. Cho, W.J., Lee, J.O., Kwon, S. An empirical model for the thermal conductivity of compacted bentonite and a bentonite-sand mixture. *Heat and Mass Transfer/Waerme- und Stoffuebertragung*. 2011. 47(11). Pp. 1385–1393. DOI: 10.1007/s00231-011-0800-1.
14. Haigh, S.K. Thermal conductivity of sands. *Geotechnique*. 2012. 62(7). Pp. 617–625. DOI: 10.1680/geot.11.P.043
15. Tarnawski, V.R., Leong, W.H. Advanced Geometric Mean Model for Predicting Thermal Conductivity of Unsaturated Soils. *International Journal of Thermophysics*. 2016. 37(2). Pp. 1–42. DOI: 10.1007/s10765-015-2024-y
16. Tian, Z., Lu, Y., Horton, R., Ren, T. A simplified de Vries-based model to estimate thermal conductivity of unfrozen and frozen soil. *European Journal of Soil Science*. 2016. 67(5). Pp. 564–572. DOI: 10.1111/ejss.12366
17. Lu, Y., Lu, S., Horton, R., Ren, T. An Empirical Model for Estimating Soil Thermal Conductivity from Texture, Water Content, and Bulk Density. *Soil Science Society of America Journal*. 2014. 78(6). Pp. 1859–1868. DOI: 10.2136/sssaj2014.05.0218
18. Kersten, M.S. Thermal properties of soils. 30th Annual Meeting of the Highway Research Board. 1952. Pp. 161–166.
19. Johansen, O. Thermal Conductivity of Soils and Rocks. Sixth International Congress of the Foundation Francaise d'Etudes Nordiques. 1975. 2. Pp. 407–420.
20. Knutsson, S. On the Thermal Conductivity and Thermal Diffusivity of Highly Compacted Bentonite. (October)1983. 72–83 p.
21. Côté, J., Konrad, J.M. A generalized thermal conductivity model for soils and construction materials. *Canadian Geotechnical Journal*. 2005. 42(2). Pp. 443–458. DOI: 10.1139/t04-106
22. Nikoosokhan, S., Nowamooz, H., Chazallon, C. Effect of dry density, soil texture and time-spatial variable water content on the soil thermal conductivity. *Geomechanics and Geoengineering*. 2016. 11(2). Pp. 149–158. DOI: 10.1080/17486025.2015.1048313
23. Zhang, N., Wang, Z. Review of soil thermal conductivity and predictive models. *International Journal of Thermal Sciences*. 2017. 117. Pp. 172–183. DOI: 10.1016/j.ijthermalsci.2017.03.013
24. Dharssi, I., Vidale, P.L., Verhoef, A., Macpherson, B., Jones, C., Best, M. New soil physical properties implemented in the Unified Model at PS18. (528)2009. 35 pp.
25. Wilson, J., Savage, D., Bond, A., Watson, S., Bennet, D. Bentonite: A review of key properties, processes and issues for consideration in the UK context. 1(February)2011. 1–6 p.
26. Rózański, A., Stefaniuk, D. On the prediction of the thermal conductivity of saturated clayey soils: Effect of the specific surface area. *Acta Geodynamica et Geomaterialia*. 2016. 13(4). Pp. 339–349. DOI: 10.13168/AGG.2016.0016
27. Rózański, A., Kaczmarek, N. Empirical and theoretical models for prediction of soil thermal conductivity: A review and critical assessment. *Studia Geotechnica et Mechanica*. 2020. 42(4). Pp. 330–340. DOI: 10.2478/sgem-2019-0053
28. McCumber, M.C., Pielke, R.A. Simulation of the effects of surface fluxes of heat and moisture on a mesoscale numerical model. 1. Soil layer. *Journal of Geophysical Research*. 1981. 86(C10). Pp. 9929–9938. DOI: 10.1029/JC086iC10p09929
29. Kahr G., M.-V.M. Thermal conductivity of Bentonite MX 80 and Montigel using the heating wire method.
30. Chung, S. -O, Horton, R. Soil heat and water flow with a partial surface mulch. *Water Resources Research*. 1987. 23(12). Pp. 2175–2186. DOI: 10.1029/WR023i012p02175
31. Misra, A., Becker, B.R., Fricke, B.A. A Theoretical model of the thermal conductivity of idealized soil. *HVAC and R Research*. 1995. 1(1). Pp. 81–96. DOI: 10.1080/10789669.1995.10391310
32. Newson, T.A., Brunning, P., Stewart, G. Thermal conductivity of consolidating offshore clayey backfill. *Proceedings of the International Conference on Offshore Mechanics and Arctic Engineering - OMAE*. 2002. 4. Pp. 17–24. DOI: 10.1115/OMAE2002-28020
33. Caridad, V., Ortiz de Zárate, J.M., Khayet, M., Legido, J.L. Thermal conductivity and density of clay pastes at various water contents for pelotherapy use. *Applied Clay Science*. 2014. 93–94. Pp. 23–27. DOI: 10.1016/j.clay.2014.02.013
34. Yoon, S., Cho, W.H., Lee, C., Kim, G.Y. Thermal conductivity of Korean compacted bentonite buffer materials for a nuclear waste repository. *Energies*. 2018. 11(9). DOI: 10.3390/en11092269
35. Nimick, F.B., Leith, J.R. A model for thermal conductivity of granular porous media. *Journal of Heat Transfer*. 1992. 114(2). Pp. 505–508. DOI: 10.1115/1.2911302
36. Jougnot, D., Revil, A. Thermal conductivity of unsaturated clay-rocks. *Hydrology and Earth System Sciences*. 2010. 14(1). Pp. 91–98. DOI: 10.5194/hess-14-91-2010
37. Yun, T.S. Mechanical and thermal study of hydrate bearing sediments. (August)2005.
38. Ewing, R.P., Horton, R. Thermal conductivity of a cubic lattice of spheres with capillary bridges. *Journal of Physics D: Applied Physics*. 2007. 40(16). Pp. 4959–4965. DOI: 10.1088/0022-3727/40/16/031
39. Gori, F., Corasaniti, S. New model to evaluate the effective thermal conductivity of three-phase soils. *International Communications in Heat and Mass Transfer*. 2013. 47. Pp. 1–6. DOI: 10.1016/j.icheatmasstransfer.2013.07.004
40. Ofrikhter, I., Zaharov, A., Ponomaryov, A., Likhacheva, N. Modeling heat transfer process in soils. *MATEC Web of Conferences*. 2018. DOI: 10.1051/mateconf/201825102048

Information about authors:

Aleksandr Zakharov

PhD in Technical Science

ORCID: <https://orcid.org/0000-0001-7475-8779>

E-mail: av_zaharov@mail.ru

Andrey Ponomaryov

Doctor in Technical Science

ORCID: <https://orcid.org/0000-0001-6521-9423>

E-mail: andreypab@mail.ru

Ian Ofrikhter

ORCID: <https://orcid.org/0000-0002-3703-5878>

E-mail: ian.ofrikhter@gmail.com

Received 22.10.2021. Approved after reviewing 31.05.2022. Accepted 07.06.2022.



Research article

UDC 528.3

DOI: 10.34910/MCE.114.4



The method of determining the trend equation for predicting vertical displacements by the search method of nonlinear programming

G.G. Shevchenko¹ , M.Ya. Brin² , D.A. Gura^{1,3} , N.I. Khusht¹ , M.M. Tamov¹ 

¹ Kuban State Technological University, Krasnodar, Russia

² Petersburg State Transport University, St. Petersburg, Russia

³ Kuban State Agrarian University, Krasnodar, Russia

✉ gda-kuban@mail.ru

Keywords: geodetic measurements, forecasting, trend equation, time series, the adequacy of the model, search method of nonlinear programming, SDGs

Abstract. Observing the settlement of buildings and structures often gives rise to the question of their prediction. This primarily requires determining the form of the time series trend equation, which would describe by a single law all sequences of the time series compiled from geodetic data. The procedure for determining the trend equation of the time series is carried out by linear and nonlinear regression analysis. However, these methods have a number of drawbacks. In this connection, the case study of changing the benchmarks values of one of the deformation marks is considered in order to analyze the possibility to apply the search method of nonlinear programming for determining the trend equation on the basis of the geodetic measurements data. A method of constructing a trend equation for a predictive model based on geodetic data is presented, including: 1) determining the trend equation by a search method of nonlinear programming using a VBA-based search program; 2) assessment of the accuracy of determining the coefficients of the trend equations by using the search method of nonlinear programming; 3) assessment of the adequacy of trend models obtained by the search method. Based on the results of the analysis and calculations, an adequate trend model in the form of a logarithmic equation was established. The correctness of the conclusions was proved by the calculations carried out in Microsoft Excel and Statistica, which coincided with the results obtained. The predicted values of the deformation benchmarks were determined.

Acknowledge: The research was carried out using the equipment of the Research Center for Food and Chemical Technologies of KubSTU (CKP_3111) which development is supported by the Ministry of Science and Higher Education of the Russian Federation (Agreement No. 075-15-2021-679)

Citation: Shevchenko, G.G., Brin, M.Ya., Gura, D.A., Khusht, N.I., Tamov, M.M. The method of determining the trend equation for predicting vertical displacements by the search method of nonlinear programming. Magazine of Civil Engineering. 2022. 114(6). Article no. 11404. DOI: 10.34910/MCE.114.4

1. Introduction

An essential task under modern restrained urban conditions is to observe the deformations of the foundations of buildings and structures. According to Russian Code Specifications SP 22.13330.2016 and SP 305.1325800.2017, a set of works based on field observations of the behavior a newly erected structure and its foundation, including soil massif, is geotechnical monitoring. Thus, geotechnical monitoring should consider the "engineering structure – environment" system. The set of works on geotechnical monitoring

includes geodetic monitoring [1–4], which is a systematic control of the state of buildings and structures based on geodetic measurements.

However, it is important not only to control the deformation processes of buildings and structures but also to determine the upward or downward trend in the observed deformations for short- or long-term periods. In order to identify this trend, which is of prognostic character, it is necessary, first of all, to find the trend equation of functional relationships of all consecutive time series levels which is built on geodetic data. It is also worth mentioning that methods of linear and nonlinear regressive analysis are the main classic methods for equation construction. These methods, however, are not devoid of drawbacks. The object of study is evaluation of the possibility to apply the search method of nonlinear programming for determining the trend equation on the basis of the geodetic measurements data as illustrated by changing the benchmarks values of one of the deformation marks in the process of geodetic monitoring. The object under the monitoring: a hotel complex under construction in Krasnodar City and the existing buildings and utilities within the new construction influence zone.

In general, the problem of finding the trend equation and building the prognostic models in the process of geodetic monitoring of structural elements of buildings and constructions is topical and rather complicated. Its solution requires a complex and systematic approach with using the knowledge of geodesy, civil engineering, econometrics on the basis of applying the multifactor regressive analysis and nonlinear programming. It also necessary to observe the requirements of the existing legal and regulatory basis on the expediency of forecasting and prognostic modeling during the procedure of geodetic monitoring of buildings and constructions.

The review of regulatory documents showed that the requirements for the construction of predictive models based on geodetic data as a necessary part of geodetic monitoring are specified in Russian Guidance Documentation in Construction MDS 13-22.2009 “Guidelines for geodetic monitoring of the technical condition of high-rise and unique buildings and structures” and Russian Company Standards STO SRO-C 6054290 00043-2015 “Nuclear facilities. Geodetic monitoring of buildings and structures during construction and operation”. Thus, the existing regulatory documents allow work on predicting the development of deformations only for buildings and structures with a higher level of responsibility. No such requirements and recommendations apply to buildings with a normal level of responsibility.

Works [5–8] are devoted to the importance of finding a solution to this problem. In addition, it should be noted that there is a significant number of publications focusing on the issue of determining the trend equation and the construction of a predictive model correlating with it [9–13]. There are many works by Russian and foreign researchers devoted to prognostic modeling based on geodetic data. For example, Iu.P. Guliaev, A.P. Zaitsev, S.V. Marfenko, D.Sh. Mikhelev, O.N. Pozdysheva, B.A. Kharchenko, V.S. Khoroshilov, N.N. Kobeleva, N.V. Sucheva, B. Zhang, L. Qiu, Z. Zhou and others consider the problem of defining the trend equation of time series by linear and nonlinear regressive analysis [14–19]. Whereas, B.T. Mazurov and some other scientists apply numerical methods and dynamic prognostic models in solving the problem of building prognostic models. They argue that these methods give more accurate and effective results as compared to those of linear and nonlinear regressive analysis [20–22].

The aim of the present study is to develop a method for determining the trend equation on the geodetic measurements data by the search method of nonlinear programming. The values measured were elevation points obtained in the process of geodetic monitoring of the hotel complex being constructed in Krasnodar City.

To achieve this goal the following tasks were to be solved:

- a) performing an analysis of forming classical types of trend equations (linear, of logarithmic function and polynomials of various degrees);
- b) carrying out geodetic monitoring of the hotel complex being constructed in Krasnodar City and of the existing buildings and utilities by setting deformation marks on them and determining the points of the latter obtained for 11 monitoring cycles;
- c) building a prognostic model according to the obtained sample of deformation marks points, namely:
 - determining the trend equation:
 - assessing the accuracy of defining the trend equation coefficients;
 - evaluating the adequacy of trend models obtained by the search method;
 - forecasting the values of deformation mark points for several cycles ahead.

2. Methods

Linear, exponential, logarithmic functions and polynomials of various degrees are often used to build trends [11, 23, 24]. The coefficients of each of the trend equations are determined by the traditional least squares method [15], and the degree of the approximating polynomial is selected from the condition of the minimum variance of the deviations of the actually measured values from the values obtained theoretically [11]. However, the disadvantages of nonlinear regression models are the complexity of determining the type of functional dependence, as well as the complexity of determining the parameters of the model, since first, it is necessary to carry out the standard procedure for their linearization. The disadvantages of linear regression models are low adaptability and lack of ability to model nonlinear processes.

One of the problems in solving nonlinear equations is to ensure fast convergence of the computational process. This problem is discussed in [23, 25, 26].

The search method of nonlinear programming, the essence of which is an iterative search for the minimum deviations of the initial values of the time series from their experimental (theoretical) values calculated by the trend equation, is devoid of the listed disadvantages when determining the trend equation. The search for the minimum deviation of the initial values from the theoretical ones will continue until the value in the target cell – the desired deviation – decreases, i.e. in other words, the extremum of a given condition is determined, which is expressed as a specific objective function. In this case, the criteria for the termination of the program operation can be both a visual finding of the fulfillment of a given number of iterations, and compliance with the condition regarding the absence of discrepancies between the two values of the target cell at the n^{th} and $n-1^{\text{th}}$ iterations up to a certain decimal digit.

Next, we will consider the procedure for determining the trend equation by the search method of nonlinear programming based on geodetic measurements using the example of changing the elevation values of one of the deformation control benchmarks. It should be noted here that geodetic monitoring was carried out on all the twelve deformation marks (DM1–DM12), and the construction of the trend equation and the predictive model was carried out according to the marks values of the of DM6 deformation mark.

2.1. Problem statement

An obligatory stage of geotechnical monitoring of a hotel complex under construction in Krasnodar and existing buildings and communications in the zone of influence of the new construction (Fig. 1) was geodetic monitoring of settlements.

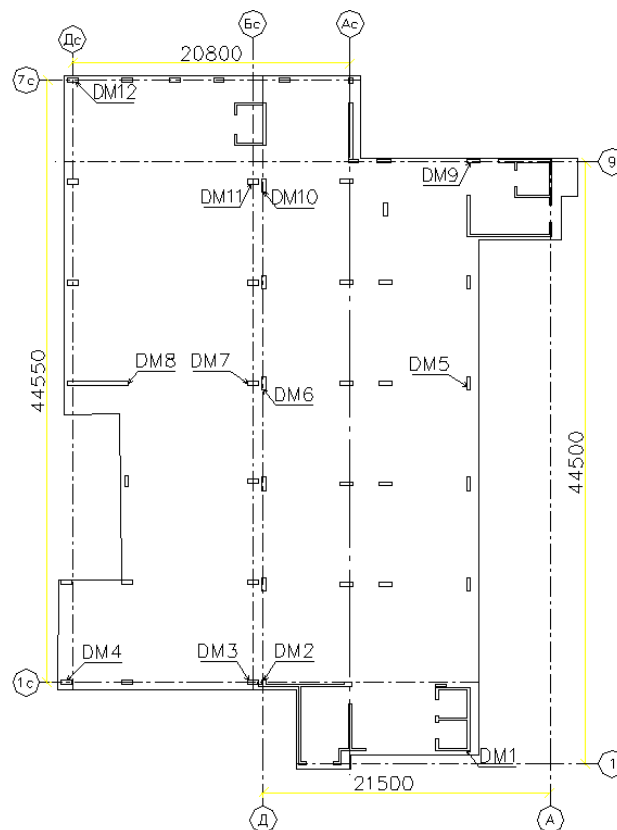
According to the project, the hotel complex under construction has one underground floor intended for parking, 8 aboveground floors in 1-9/A-D axes (hotel) and 1 aboveground floor in 1s-7s/As-Ds axes (conference hall). The shape of the building is complex in terms of its overall axial dimensions of 35.8 × 50.55 m. The structural scheme of the building is frame: the main supporting structures are monolithic reinforced concrete columns, walls and ribbed floors. In 1-9/A-D axes in the area of the walls, the foundation is designed in the form of a reinforced concrete slab with a thickness of 700 mm. The foundations of the columns in this part of the building are reinforced concrete belts located in the digital axes. In 1s-7s/As-Ds axes, the foundation is 500 mm thick slab.

The erection of the underground part of the building was carried out in a pit about 4.9 m deep. The project provides for the implementation of work to consolidate the foundation soils. To fasten the walls of the pit, a fence made of steel piles with a plank fence was arranged along its northern and western sides. The piles were immersed in 4–6 m long soil-cement elements and joined at the upper ends by a steel I-beam.

Let us consider the procedure for determining the trend equation by the search method according to the deformation control benchmarks when determining the draft of such a hotel complex. Observation of sedimentation was carried out by the method of class II geometric leveling in a conventional system of heights. Table 1 shows the deformation control benchmarks obtained during 11 observation cycles.

Table 1. The deformation control benchmarks obtained from the geodetic monitoring.

Cycle No.	1	2	3	4	5	6	7	8	9	10	11
Date	25.09	28.10	27.11	28.12	27.01	25.02	28.03	27.04	29.05	27.06	27.07
Benchmark No.	Benchmarks, m										
DM1	0.704	0.702	0.700	0.699	0.699	0.699	0.699	0.697	0.697	0.697	0.697
DM2	0.914	0.911	0.912	0.911	0.910	0.909	0.906	0.905	0.904	0.904	0.904
DM3	0.884	0.881	0.880	0.880	0.879	0.879	0.880	0.878	0.877	0.876	0.876
DM4	0.842	0.840	0.842	0.841	0.840	0.842	0.839	0.840	0.839	0.839	0.838
DM5	0.878	0.875	0.872	0.871	0.870	0.870	0.870	0.869	0.868	0.868	0.868
DM6	0.895	0.892	0.889	0.888	0.886	0.886	0.885	0.885	0.884	0.884	0.883
DM7	0.882	0.878	0.876	0.876	0.873	0.874	0.874	0.873	0.873	0.871	0.871
DM8	0.930	0.928	0.927	0.927	0.927	0.926	0.926	0.925	0.925	0.924	0.923
DM9	0.852	0.848	0.846	0.845	0.845	0.844	0.844	0.843	0.842	0.841	0.838
DM10	0.849	0.845	0.843	0.843	0.841	0.842	0.841	0.840	0.838	0.837	0.837
DM11	0.872	0.868	0.866	0.866	0.868	0.865	0.864	0.863	0.862	0.862	0.862
DM12	0.852	0.849	0.849	0.849	0.849	0.848	0.847	0.847	0.848	0.846	0.845

**Figure 1. The building plan with deformation control benchmarks locations.**

The values in Table 1 show the greatest changes in DM6, DM7, DM9 and DM10. The data in Table 1 for these four benchmarks can be presented in the form of a time series, in which the marks of the benchmark (x_i) are the levels of the series, and the cycle numbers (y_i) are the time marks (Table 2).

Table 2. Time series.

x_i	1	2	3	4	5	6	7	8	9	10	11	Benchmark
	895.00	892.00	889.00	888.00	886.00	885.50	884.50	885.00	884.00	884.00	883.00	DM6
	882.00	878.00	876.00	876.00	873.00	874.00	874.00	873.00	873.00	871.00	871.00	DM7
y_i	852.00	848.00	846.00	845.00	845.00	844.00	844.00	843.00	842.00	841.00	838.00	DM9
	849.00	845.00	843.00	843.00	841.00	842.00	841.00	840.00	838.00	837.00	837.00	DM10

Building a predictive model needs to [14]:

1. determine the trend equation;
2. evaluate the accuracy of the coefficients of the trend equations;
3. evaluate the adequacy of trend models obtained by the search method;
4. predict the values of the deformation benchmarks for several cycles ahead.

2.2. General information about the search method of nonlinear programming

As V.I. Mitskevich, D. Himmelblau [26], and other authors [27–29] note, the search method of nonlinear programming has the following advantages:

1. clarity and simplicity of the trend equation;
2. the uniformity of the applied calculation method, regardless of the desired form of the trend equation;
3. the ability to simulate both linear and nonlinear processes;
4. no need to use derivatives;
5. sufficient efficiency in preparing the problem for solution.

There are the following types of search methods:

1. Hook-Jeeves' direct search;
2. Nelder and Mead's method (search by deformable polyhedron);
3. Rosenbrock's method;
4. Davis-Svenn-Campy's method (DSC);
5. Powell's method;
6. Method of random search.

Each of the above methods, both individually and in various combinations, makes it possible to determine the extremum of a given objective function. The choice of the method is determined by the degree of relevance (adequacy to the nature of the problem being solved) and the effectiveness of solving the problem. We shall consider the procedure for determining the extremum of the objective function by a combination of the DSC and Powell algorithms.

Let the function $f(x)$ be unimodal and have a unique value x^* such that $f(x^*)$ is the minimum of $f(x)$.

Here is this algorithm (Fig. 2):

Step 1. An initial arbitrary value of the element $x^{(0)}$ is set.

Step 2. The value of the objective function $f(x^{(0)})$ is calculated.

Step 3. The variable $x^{(0)}$ is changed by the selected value Δx and $x^{(1)} = x^{(0)} + \Delta x$ is set.

Step 4. The value of the objective function $f(x^{(1)})$ is calculated.

Step 5. If $f(x^{(0)}) > f(x^{(1)})$, then the variable $x^{(1)}$ is changed by the selected value Δx and $x^{(2)} = x^{(0)} + 2\Delta x$ or $x^{(2)} = x^{(1)} + \Delta x$ is set. If $f(x^{(0)}) \leq f(x^{(1)})$, then $x^{(2)} = x^{(0)} - \Delta x$.

Step 6. The value of the objective function $f(x^{(2)})$ is calculated.

Step 7. The variable x^* is determined corresponding to the value of the minimum of the objective function $f(x)$:

$$x^* = x^{(1)} + \frac{\Delta x \left[f(x^{(0)}) - f(x^{(2)}) \right]}{2 \left[f(x^{(0)}) - 2f(x^{(1)}) + f(x^{(2)}) \right]}. \quad (1)$$

Step 8. The value of the objective function $f(x^*)$ is calculated. Thus, the minimum of the objective function $f(x)$ is achieved.

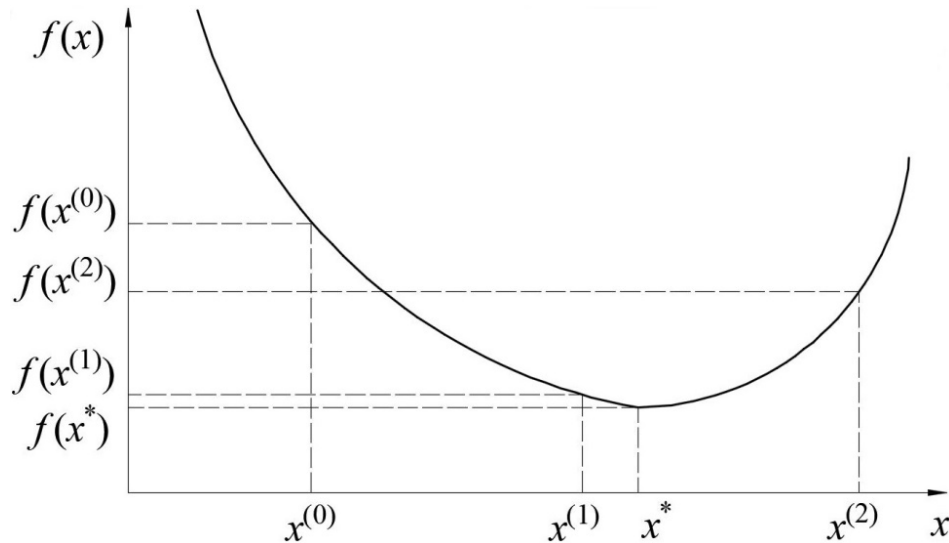


Figure 2. Geometric interpretation of minimization of the function $f(x)$ by the Powell–DSC method.

The above sequence of calculating the minimum $f(x)$ is described in general form in [27, 28]. In expression (1) the second term is a correction that is introduced into the variable $x^{(1)}$ to achieve the minimum of the objective function. Obviously, it is possible to determine the corresponding corrections for the variables $x^{(0)}$ and $x^{(2)}$, which was noted in [27].

3. Results and Discussion

3.1. Determining the trend equation by the search method of nonlinear programming in the VBA-based program

The problem of development of automated programs for processing the results of geodetic measurement has always been topical [28]. To determine the regularity of the change in the mark values of the deformation benchmarks DM6, DM7, DM9 and DM10 during automated calculations, a VBA-based program was compiled [29], which operates as a Macro in Microsoft Excel. The program implements the algorithm of the nonlinear programming search method described above. In turn, the unknown coefficients of the analyzed trend equations are also directly selected by the search method.

Thus, the following coefficients and analytical equations were obtained by the search method of nonlinear programming, presented in Table 3.

Table 3. Types of the trend equation for settlement in DM6, DM7, DM9 and DM10, obtained by the search method.

Type of trend equation	Trend equation
DM6	
linear	$y = -1.0409x + 893.1550$
logarithmic	$y = -5.0020 \cdot \ln(x) + 894.8680$
second degree polynomial (quadratic)	$y = 0.1463x^2 - 2.7962x + 896.9580$
third degree polynomial (cubic)	$y = -0.0218x^3 + 0.5379x^2 - 4.7585x + 899.3330$
DM7	
linear	$y = -0.8818x + 879.8818$
logarithmic	$y = -4.2298 \cdot \ln(x) + 881.3210$
second degree polynomial (quadratic)	$y = 0.1026x^2 - 2.1126x + 882.5486$
third degree polynomial (cubic)	$y = -0.0324x^3 + 0.6865x^2 - 5.0387x + 886.0827$
DM9	
linear	$y = -1.0618x + 850.6564$
logarithmic	$y = -4.7837 \cdot \ln(x) + 851.8969$
second degree polynomial (quadratic)	$y = 0.031x^2 - 1.4338x + 851.4719$
third degree polynomial (cubic)	$y = -0.0468x^3 + 0.8732x^2 - 5.6543x + 856.5719$
DM10	
linear	$y = -1.0273x + 847.5727$
logarithmic	$y = -4.6821 \cdot \ln(x) + 848.8589$
second degree polynomial (quadratic)	$y = 0.0583x^2 - 1.7265x + 849.0877$
third degree polynomial (cubic)	$y = -0.0258x^3 + 0.5233x^2 - 4.0569x + 851.9090$

The form of the analytical trend equations selected by the search method can be any at the operator's choice.

Further, from the obtained trend equations, the best one is selected, which characterizes the maximum change in the observed process, the settlement of deformation benchmarks.

Let us consider this and subsequent problems of choosing the best trend equation using the example of DM6. For this, empirical methods of analyzing the patterns of development of the investigated time series were used [30], such as:

- method of analysis of variance;
- calculation and analysis of the root mean square error of approximation;
- the least squares criterion of empirical and theoretical values of the levels of the time series.

The method of analysis of variance is based on the comparison of variances. The method is as follows: the total variance of the time series is divided into two parts: the variation due to the trend $V_{f(t)}$ and the random variation V_{ε} . In this case, the variation due to the tendency is defined as the difference between the total V_{total} and random variations V_{ε} [31, 32].

The total variation is defined as the sum of the squares of the deviations of the initial values of the levels of the series (y_i) from the mean level of the initial time series (\bar{y}) . The random variation is calculated as the sum of the squares of the deviations of the initial values of the time series (y_i) from the theoretical ones obtained by the trend equation (\hat{y}) [30, 31].

On the basis of these indicators of variation, the total number of elements of the initial time series n and the number of parameters of the trend equation l , various types of variance are determined: total, variance of the random component and variance of the trend.

Further, a hypothesis was put forward and passed a test whether the considered trend equation is suitable or not suitable for describing the trend of the initial time series. The hypothesis was tested on the basis of the Fischer–Snedecor F-test [30, 32]. For a given significance level α and the number of degrees of freedom ($k_1 = l - 1$, $k_2 = n - l$), the F-test is determined from the table of critical points of the Fisher–Snedecor distribution. If the calculated F-test value F_p is greater than F_t , then the trend equation is consistent with the initial data and is suitable for reflecting the trend of the initial time series [30, 32].

The choice of the best trend equation is also indicated by the value of the root mean square error of approximation [30] σ_{er} . The smaller the error value, the better the function describes the trend in the original series.

The application of the criterion of the least sum of squares of deviations of the initial and theoretical values of the levels of the time series also suggests that the trend is best described by the trend, which corresponds to the smallest value of the sum of squares of deviations.

Table 4 shows the formulas for the calculation and the results of the analysis of the trend equations obtained by the search method.

Table 4. Results of the analysis of the trend equations obtained by the search method for DM6.

Parameter	Calculation formula	Linear equation	Logarithmic equation	Second degree polynomial	Third degree polynomial
Results of analysis of variance					
Total variation V_{tot} , mm ²	$\sum_{i=1}^n (y_i - \bar{y})^2$		141.409		
Random variation V_ε , mm ²	$\sum_{i=1}^n (y_i - \hat{y}_i)^2$	22.225	2.493	3.868	0.944
Variation due to the trend $V_{f(t)}$, mm ²	$V_{o6m} - V_\varepsilon$	119.184	138.916	137.541	140.465
Total variance σ^2_{total} , mm ²	$\frac{V_{o6m}}{n-1}$		14.141		
Dispersion of the random component σ^2_ε , mm ²	$\frac{V_\varepsilon}{n-l}$	2.469	0.277	0.484	0.135
Dispersion of the trend $\sigma^2_{f(t)}$, mm ²	$\frac{V_{f(t)}}{l-1}$	119.184	138.916	68.771	46.822
Fischer–Snedecor F-test F_p	$\frac{\sigma^2_{f(t)}}{\sigma^2_\varepsilon}$	48.264	501.570	142.232	347.174
Calculation and analysis of the root mean square error of approximation					
Mean square error σ_{er} , mm	$\sqrt{\frac{\sum (y_i - \hat{y}_i)^2}{n-l-1}}$	1.667	0.558	0.743	0.397
The least squares criterion of empirical and theoretical values of the levels of the time series					
Sum of squares of deviations, mm ²	$\sum (y_i - \hat{y}_i)^2 \rightarrow \min$	22.225	2.493	3.868	0.944

The works [10, 11] note that the choice of the best trend equation is also carried out according to the values of the correlation coefficient, determination coefficient R^2 and standard approximation error σ_t . The definitions of these values of the factors for each of the trend equations obtained by the search method are shown. Also, the value of the normalized R-square, the relative approximation error E_t and the average approximation error \bar{A} was additionally calculated. The results are shown in Table 5.

Table 5. Calculation of the coefficients of regression statistics.

Coefficient	Linear equation	Logarithmic equation	Second degree polynomial	Third degree polynomial
Correlation coefficient (multiple R)	0.9181	0.9911	0.9862	0.9967
Determination coefficient R^2	0.8428	0.9824	0.9726	0.9933
Normalized R -square	0.8254	0.9804	0.9696	0.9926
Standard approximation error σ_t , mm	1.5714	0.5263	0.6953	0.3672
Relative approximation error E_t , %	0.1772	0.0593	0.0784	0.0414
Average approximation error \bar{A} , %	0.1382	0.0457	0.0530	0.0291

The closer the determination coefficient to 1,000 and the smaller the error rates are, the better the equation describes the original time series.

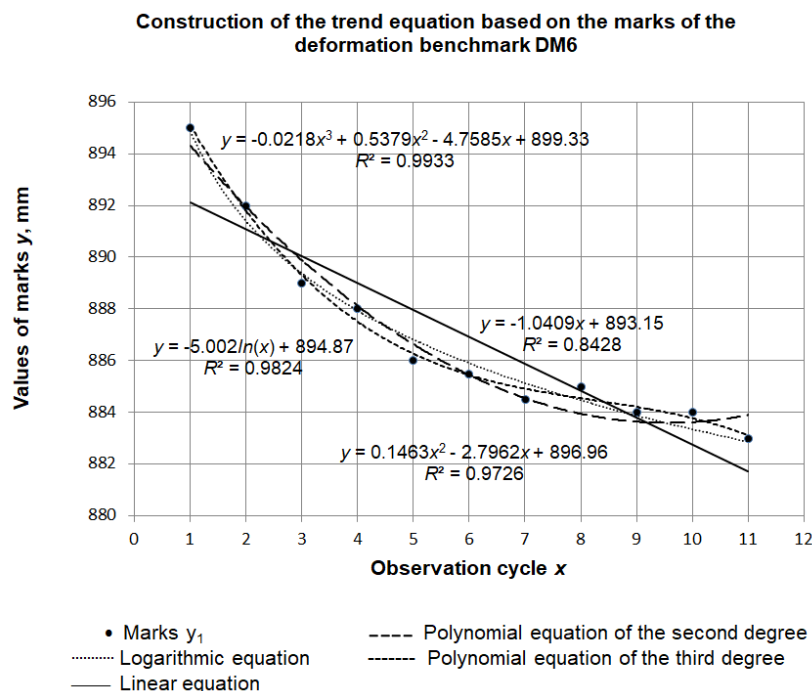
3.2. Validation of the Microsoft Excel calculations

The validation of the calculations performed and the obtained trend equations by the values of the deformation mark marks was carried out in *Microsoft Excel* using the built-in function of this program (Fig. 3).

Fig. 3 shows that the coefficients of the considered trend equations calculated by the search method and the equations obtained by the built-in function of *Microsoft Excel* completely coincide. In addition, the values of the determination coefficients R^2 , calculated in *Microsoft Excel* (Fig. 3), also coincide with the values of such a coefficient for the trend equations obtained by the search method of nonlinear programming.

The built-in functions of *Microsoft Excel* were also used to calculate the indicators of regression statistics and analysis of variance data on the example of a linear trend model. The protocol for solving the problem, drawn up in *Microsoft Excel*, confirmed the correctness of the calculations performed to determine the indicators of analysis of variance and indicators of regression statistics for the linear trend equation obtained by the search method.

We should note that *Microsoft Excel* does not provide for a similar calculation protocol for equations of the logarithmic form and polynomials of different degrees. The use of the compiled program to determine the trend equation by the search method of nonlinear programming allows calculating the necessary parameters to estimate the best trend equation in *Microsoft Excel*.



The results of regression and variance analyses with the built-in *MS Excel* package “Data analysis” for the linear trend model are shown in Fig. 4.

	A	B	C	D	E	F	G	H	I
1	Results output								
2									
3	Regression statistics								
4	Multiple R	0.9181							
5	R-square	0.8428							
6	Normalized R-square	0.8254							
7	Standard error	1.5714							
8	Observations	11							
9									
10	Variance analysis								
11		<i>df</i>	<i>SS</i>	<i>MS</i>	<i>F</i>	<i>Significance of F</i>			
12	Regression	1	119,184	119,184	48,264	6.70544E-05			
13	Remainder	9	22,225	2,469					
14	Total	10	141,409						
15									
16		<i>Coefficients</i>	<i>Standard error</i>	<i>t-statistics</i>	<i>P-values</i>	<i>Lower 95%</i>	<i>Upper 95%</i>	<i>Lower 95.0%</i>	<i>Upper 95.0%</i>
17	Y intersection	893.155	1.016	878.91001	1.627E-23	890.8557254	895.4533655	890.8557254	895.4533655
18	Variance X1	-1.0409	0.150	-6.947195	6.705E-05	-1.379851617	-0.701966565	-1.379851617	-0.701966565

Figure 4. The results of regression and variance analyses with the *MS Excel* package “Data analysis” for the linear trend model.

The results given in Fig. 4 can only be seen in *MS Excel* for the linear trend equation.

3.3. Validation of the calculations in *Statistica*

In order to additionally verify the calculations performed and the trend equations obtained from the deformation benchmarks, we carried out the equivalent calculations of coefficients for the linear and logarithmic trend equations as well as polynomial equations of the second and third degree in the software *Statistica* with adduction of corresponding statistics which characterizes the reliability of both the regression models and their particular indicators. The data obtained are given below (Fig. 5–9).

```
. regress y x
```

Source	SS	df	MS	Number of obs	=	
Model	119.184091	1	119.184091	F(1, 9)	=	48.26
Residual	22.225	9	2.46944444	Prob > F	=	0.0001
Total	141.409091	10	14.1409091	R-squared	=	0.8428
				Adj R-squared	=	0.8254
				Root MSE	=	1.5714

	y	Coef.	Std. Err.	t	P> t	[95% Conf. Interval]
	x	-1.040909	.1498316	-6.95	0.000	-1.379852 - .7019666
	_cons	893.1545	1.016207	878.91	0.000	890.8557 895.4534

Figure 5. Indicators of the linear regression trend model obtained with the software *Statistica*.

```
. generate lnx=log(x)
. regress y x x2
```

Source	SS	df	MS	Number of obs	=	
Model	137.541026	2	68.7705128	F(2, 8)	=	142.23
Residual	3.86806527	8	.483508159	Prob > F	=	0.0000
Total	141.409091	10	14.1409091	R-squared	=	0.9726
				Adj R-squared	=	0.9658
				Root MSE	=	.69535

	y	Coef.	Std. Err.	t	P> t	[95% Conf. Interval]
	x	-2.796154	.2924786	-9.56	0.000	-3.470611 -2.121697
	x2	.1462704	.0237388	6.16	0.000	.0915287 .2010121
	_cons	896.9576	.7636361	1174.59	0.000	895.1966 898.7185

Figure 6. Indicators of the linear regression trend model of a second degree polynomial obtained with the software *Statistica*.

```
. regress y x x2 x3
```

Source	SS	df	MS	Number of obs	=	11
Model	140.465035	3	46.8216783	F(3, 7)	=	347.17
Residual	.944055944	7	.134865135	Prob > F	=	0.0000
				R-squared	=	0.9933
				Adj R-squared	=	0.9905
Total	141.409091	10	14.1409091	Root MSE	=	.36724

y	Coef.	Std. Err.	t	P> t	[95% Conf. Interval]
x	-4.758547	.4488666	-10.60	0.000	-5.819948 -3.697146
x2	.5378788	.0850325	6.33	0.000	.3368088 .7389488
x3	-.021756	.0046724	-4.66	0.002	-.0328045 -.0107076
_cons	899.3333	.6503738	1382.79	0.000	897.7954 900.8712

Figure 7. Indicators of the linear regression trend model of a third degree polynomial obtained with the software Statistica.

```
. regress y lnx
```

Source	SS	df	MS	Number of obs	=	11
Model	138.916424	1	138.916424	F(1, 9)	=	501.57
Residual	2.49266693	9	.276962992	Prob > F	=	0.0000
				R-squared	=	0.9824
				Adj R-squared	=	0.9804
Total	141.409091	10	14.1409091	Root MSE	=	.52627

y	Coef.	Std. Err.	t	P> t	[95% Conf. Interval]
lnx	-5.002145	.2233522	-22.40	0.000	-5.507403 -4.496887
_cons	894.8681	.3891958	2299.27	0.000	893.9877 895.7485

Figure 8. Indicators of the logarithmic regression trend model obtained with the software Statistica.

To make the comparison of the results obtained by the search method and by the software for more convenient comparing the results *MS Excel* and *Statistica* more convenient, we developed the following table.

Table 6. Aggregate table of calculations of trend equations with statistics for DM6.

Indicator	Search method	MS Excel	Statistica
For a linear trend equation:			
- equation form	$y = -1.0409x + 893.1550$	$y = -1.0409x + 893.15$	$y = -1.0409x + 893.1545$
- determination coefficient R^2	0.8428	0.8428	0.8428
- standard error of approximation σ_t ,	1.5714	1.5714	1.5714
- normalized R-square	0.8254	0.8254	0.8254
- Fisher's test, F_p	48.264	48.264	48.26
For a logarithmic trend equation:			
- equation form	$y = -5.0020 \cdot \ln(x) + 894.8680$	$y = -5.002 \cdot \ln(x) + 894.87$	$y = -5.0020 \cdot \ln(x) + 894.8681$
- determination coefficient R^2	0.9824	0.9824	0.9824
- standard error of approximation σ_t ,	0.5263	-	0.5263
- normalized R-square	0.9804	-	0.9804
- Fisher's test, F_p	501.570	-	501.57

Indicator	Search method	MS Excel	Statistica
For a second degree polynomial trend equation:			
- equation form	$y = 0.1463x^2 - 2.7962x + 896.9580$	$y = 0.1463x^2 - 2.7962x + 896.96$	$y = 0.1463x^2 - 2.7962x + 896.9576$
- determination coefficient R^2	0.9726	0.9726	0.9726
- standard error of approximation σ_t ,	0.6953	-	0.6954
- normalized R-square	0.9696	-	0.9658
- Fisher's test, F_p	142.232	-	142.23
For a third degree polynomial trend equation:			
- equation form	$y = -0.0218x^3 + 0.5379x^2 - 4.7585x + 899.3330$	$y = -0.0218x^3 + 0.5379x^2 - 4.7585x + 899.33$	$y = -0.0218x^3 + 0.5379x^2 - 4.7585x + 899.3333$
- determination coefficient R^2	0.9933	0.9933	0.9933
- standard error of approximation σ_t ,	0.3672	-	0.3672
- normalized R-square	0.9926	-	0.9905
- Fisher's test, F_p	347.174	-	347.17

The coincidence of the statistical indicators obtained by the search method with the corresponding indicators obtained in the software MS Excel и Statistica for trend equations prove the confidence of the calculations performed.

3.4. Assessment of the accuracy of the coefficients of the trend equations by the search method of nonlinear programming

Ch.N. Zheltko [29] described the general procedure for assessing the accuracy by the search method. The work [27] presents gradually the accuracy assessment procedure by the search method using the example of assessing the accuracy of the coordinates of a determined point in a geodetic triangle.

The estimation of the accuracy of the trend line by the search method of nonlinear programming is carried out through determining the coefficients of the normal equations of the unknowns. In the considered example, the unknowns are the coefficients of the determined trend equation. For a linear trend model, the unknowns are the coefficients k and b . Taking the algorithm given in [27] as a basis, the following calculations were performed. The value of the sum of squared deviations for the linear trend model is taken as the function F_{\min} . Then, alternately setting the increments Δk_1 , Δb_1 into the corresponding determined coefficients of the linear trend model, new values of the sum of squares of deviations are calculated: the functions Fk_1 , Fb_1 are obtained, respectively. This made it possible to calculate the changes in the function $\Delta F_1 = Fk_1 - F_{\min}$ and $\Delta F_2 = Fb_1 - F_{\min}$.

Further, the increments Δk_1 and Δb_1 are simultaneously specified in the corresponding coefficients of the linear trend equation and the new value of the function Fkb_1 , is calculated, which made it possible to calculate the change in the function $\Delta F_{12} = Fkb_1 - F_{\min}$.

The determination of the coefficients of the normal equations of the unknowns is carried out by the formulas:

$$N_{11} = \frac{\Delta F_1}{\Delta k_1^2}; N_{22} = \frac{\Delta F_2}{\Delta b_1^2}; N_{12} = \frac{\Delta F_{12} - \Delta F_1 - \Delta F_2}{2\Delta k_1 \Delta b_1}. \quad (2)$$

The inverse weight matrix of the determined coefficients of the linear trend equation has been compiled:

$$Q_K = \begin{bmatrix} N_{11} & N_{12} \\ N_{21} & N_{22} \end{bmatrix}^{-1} = \begin{bmatrix} q_{k_1} & q_{k_1 b_1} \\ q_{b_1 k_1} & q_{b_1} \end{bmatrix}. \quad (3)$$

The mean square errors of the determined coefficients of the linear trend equation were calculated:

$$m_{k_1} = \mu \sqrt{q_{k_1}}; \quad m_{b_1} = \mu \sqrt{q_{b_1}}, \quad (4)$$

here q is the inverse weight of the estimated value; μ is the root mean square error (RMS) of the unit of weight, calculated by the formula

$$\mu = \sqrt{\frac{F_{\min}}{n-k}}, \quad (5)$$

where n and k are the number of performed and required measurements, respectively. It should be noted that the number of measurements performed is 11, and the number of required measurements for the linear trend model is 2.

A similar calculation procedure was applied to other types of trend models. The results of evaluating the accuracy of determining the coefficients constructed by the trend equations by the search method are presented in Table 7.

Table 7. Results of evaluating the accuracy of determining the coefficients constructed by the trend equations by the search method.

Type of trend equation	The inverse weight matrix of the determined coefficients of the linear trend equation, Q_k	RMS of the unit of weight μ	RMS of the determined coefficients of the linear trend equation m_i
Linear equation	$\begin{bmatrix} 0.009 & -0.055 \\ -0.055 & 0.418 \end{bmatrix}$	1.571	$m_{k_1} = 0.150$ $m_{b_1} = 1.016$
Logarithmic equation	$\begin{bmatrix} 0.180 & -0.286 \\ -0.286 & 0.546 \end{bmatrix}$	0.526	$m_{k_1} = 0.223$ $m_{b_1} = 0.389$
Second degree polynomial	$\begin{bmatrix} 0.001 & -0.016 & 0.036 \\ -0.016 & 0.204 & -0.491 \\ 0.036 & -0.491 & 1.399 \end{bmatrix}$	0.695	$m_{c_1} = 0.025$ $m_{d_1} = 0.314$ $m_{e_1} = 0.822$
Third degree polynomial	$\begin{bmatrix} 0.0002 & -0.003 & 0.015 & -0.018 \\ -0.003 & 0.054 & -0.277 & 0.348 \\ 0.015 & -0.277 & 1.494 & -2.013 \\ -0.018 & 0.348 & -2.013 & 3.136 \end{bmatrix}$	0.367	$m_{b_1} = 0.0047$ $m_{d_1} = 0.085$ $m_{c_1} = 0.449$ $m_{e_1} = 0.650$

It is shown that the obtained value of the mean square error in determining the coefficients of the linear trend equation corresponds to the value of the standard error of the coefficients calculated in *Microsoft Excel* as part of regression analysis. Determining the value of the standard error for equations of a different kind in *Microsoft Excel*, as noted earlier, is not possible, in contrast to the search method of nonlinear programming.

Thus, the analysis of the data in Tables 4–7 showed that the best trend equations obtained by the search method of nonlinear programming in this example are equations of the logarithmic form and the third-degree polynomial, while the worst trend equation is linear.

However, the possibility of using a trend model for analysis and forecasting can be determined only after establishing its adequacy, i.e. correspondence of the model to the investigated process [14].

3.5. Assessment of the adequacy of trend models obtained by the search method

A trend model is considered adequate if it correctly reflects the systematic components of the time series. This requirement is equivalent to the requirements for the residual component [30]:

1. randomness;
2. compliance with the normal distribution law;
3. independence of values (no autocorrelation).

Let us conduct a study on the adequacy of the obtained trend models of the logarithmic form and the third-degree polynomial.

To test the randomness of the residual component, the run test and the peak test are used [30, 32].

Deviations of the initial values from the theoretical ones were determined: $\varepsilon_i = y_i - \hat{y}_i$ for each level of the initial time series.

By arranging the obtained series ε_i in ascending order of values, the median ε_m of the obtained new series ε'_i is determined. Since the number of measurements is $n = 11$, the median is the median value. ε_i should be compared with ε_m and a sequence should be formed [14]. If $\varepsilon_i > \varepsilon_m$, then “+” is put, if $\varepsilon_i < \varepsilon_m$ then “-” is put, with $\varepsilon_i = \varepsilon_m$ – the value is omitted. A sequence of consecutive “+” or “-” is a series.

Further, the following hypothesis was tested: if deviations from the trend are random, then their alternation should be random [32]. For the sequence ε_i to be random, the length of the longest series K_{\max} should not be too long, and the number of series v should not be too small. The residual sequence is recognized as random if the following two inequalities are met at $\alpha = 0.05$:

$$K_{\max} < \lceil 3.3(\lg n + 1) \rceil, \quad (6)$$

$$v > \left\lceil \frac{1}{2} \left(n + 1 - 1.96\sqrt{n-1} \right) \right\rceil, \quad (7)$$

where n is the number of points in a row.

Square brackets on the right side of inequalities (6) and (7) denote an integer value.

The series criterion calculation is presented in:

- Table 8 for a linear trend model;
- Table 9 for a logarithmic trend model;
- Table 10 for a trend model of the second-degree polynomial;
- Table 11 for a trend model of the third-degree polynomial.

Table 8. Calculation of the criterion for the series of the linear trend model.

y_i	$f(t)$	ε_t	ε'_t	ε_m	$\varepsilon_t > \varepsilon_m$	$\varepsilon_t < \varepsilon_m$
895.00	892.11	2.89	-1.95		+	
892.00	891.07	0.93	-1.41		+	
889.00	890.03	-1.03	-1.37			-
888.00	888.99	-0.99	-1.03			-
886.00	887.95	-1.95	-0.99			-
885.50	886.91	-1.41	0.17	0.17		-

y_i	$f(t)$	ε_t	ε_t'	ε_m	$\varepsilon_t > \varepsilon_m$	$\varepsilon_t < \varepsilon_m$
884.50	885.87	-1.37	0.21			-
885.00	884.83	0.17	0.93			
884.00	883.79	0.21	1.25		+	
884.00	882.75	1.25	1.30		+	
883.00	881.70	1.30	2.89		+	

For the considered linear trend model, $K_{\max} = 5$, $\nu = 3$. Thus, according to (1) $K_{\max} < 6$, according to (2) $\nu > 2$.

For the considered linear trend model, inequalities (1) and (2) are met. This means that the hypothesis about the randomness of deviations of the time series levels from the linear trend is confirmed.

Table 9. Calculation of the criterion for the series of the logarithmic trend model.

y_i	$f(t)$	ε_t	ε_t'	ε_m	$\varepsilon_t > \varepsilon_m$	$\varepsilon_t < \varepsilon_m$
895.00	894.87	0.13	-0.82		+	
892.00	891.40	0.60	-0.63		+	
889.00	889.37	-0.37	-0.41			-
888.00	887.93	0.07	-0.37			-
886.00	886.82	-0.82	0.07			-
885.50	885.91	-0.41	0.12	0.12		-
884.50	885.13	-0.63	0.13			-
885.00	884.47	0.53	0.13		+	
884.00	883.88	0.12	0.53			
884.00	883.35	0.65	0.60		+	
883.00	882.87	0.13	0.65		+	

For the considered logarithmic trend model, $K_{\max} = 5$, $\nu = 3$. Thus, according to (1) $K_{\max} < 6$, according to (2) $\nu > 2$.

For the considered logarithmic trend model, inequalities (1) and (2) are met. This means that the hypothesis about the randomness of deviations of the time series levels from the logarithmic trend equation is confirmed.

Table 10. Calculation of the criterion for the series of the trend model of the second-degree polynomial.

y_i	$f(t)$	ε_t	ε_t'	ε_m	$\varepsilon_t > \varepsilon_m$	$\varepsilon_t < \varepsilon_m$
895.00	894.31	0.69	-0.90		+	
892.00	891.95	0.05	-0.89			
889.00	889.89	-0.89	-0.63			-
888.00	888.11	-0.11	-0.11			-
886.00	886.63	-0.63	-0.05			-
885.50	885.45	0.05	0.05	0.05		
884.50	884.55	-0.05	0.05			-
885.00	883.95	1.05	0.36		+	
884.00	883.64	0.36	0.38		+	
884.00	883.62	0.38	0.69		+	
883.00	883.90	-0.90	1.05			-

For the considered trend model of the second-degree polynomial, $K_{\max} = 3$, $\nu = 4$. Thus, according to (1) $K_{\max} < 6$, according to (2) $\nu > 3$.

For the considered trend model of the second-degree polynomial, inequalities (1) and (2) are met. This means that the hypothesis about the randomness of deviations of the time series levels from the trend of the second degree polynomial is confirmed.

Table 11. Calculation of the criterion for the series of the trend model of the third-degree polynomial.

y_i	$f(t)$	ε_t	ε'_t	ε_m	$\varepsilon_t > \varepsilon_m$	$\varepsilon_t < \varepsilon_m$
895.00	895.09	-0.09	-0.42			-
892.00	891.79	0.21	-0.31		+	
889.00	889.31	-0.31	-0.27			-
888.00	887.51	0.49	-0.21		+	
886.00	886.27	-0.27	-0.12			-
885.50	885.45	0.05	-0.09	-0.09	+	
884.50	884.92	-0.42	0.05			-
885.00	884.55	0.45	0.21		+	
884.00	884.21	-0.21	0.22			-
884.00	883.78	0.22	0.45		+	
883.00	883.12	-0.12	0.49			-

For the considered trend model of the third-degree polynomial, $K_{\max} = 1$, $\nu = 11$. Thus, according to (1) $K_{\max} < 6$, according to (2) $\nu > 3$.

For the considered trend model of the third-degree polynomial, inequalities (1) and (2) are met. This means that the hypothesis about the randomness of deviations of the time series levels from the trend of the third degree polynomial is confirmed.

According to the test for adequacy according to the series criterion, all considered trend models are recognized as adequate.

To check the peaks criterion, we determine the total number of peak points p of the ε_t , series, meeting the following condition [9, 20].

$$\varepsilon_{t-1} < \varepsilon_t < \varepsilon_{t+1} \quad \text{OR} \quad \varepsilon_{t-1} > \varepsilon_t > \varepsilon_{t+1}.$$

For the linear model, the number of turning points is 3, for the logarithmic model – 9, for the second-degree polynomial – 8, for the third-degree polynomial – 9.

Let us calculate the mathematical expectation of the number of peak points in a row and the variance using the formulas [9].

$$\bar{p} = \frac{2}{3}(n-2) = \frac{2}{3}(11-2) = 6,$$

$$\sigma^2 = \frac{16n-29}{90} = \frac{16 \cdot 11 - 29}{90} = 1.63.$$

The resulting number of turning points of the series must exceed the integer value of the equation $\left[\bar{p} - 1.96\sqrt{\sigma^2} \right]$, which, for the considered series ε_t , is equal to 3. If this criterion is met, then the investigated trend model is considered adequate.

Thus, among the studied types of trend models, according to the criterion of peaks, the linear trend model is inadequate. The best indicators of adequacy according to the criterion of peaks in the logarithmic trend model and the third-degree polynomial.

Compliance with the normal distribution law. In this case, the hypothesis is tested that deviations from the trend obey the law of normal distribution. For this, as a rule, the correspondence of the distribution of the residual component to the normal law is performed using the *RS* test.

The ratio of the range of variations R to the standard deviation S is calculated for each type of trend model under consideration.

The range of variation was calculated using the formula [30, 32]

$$R = \varepsilon_{\max} - \varepsilon_{\min}, \quad (8)$$

where ε_{\max} , ε_{\min} are the maximum and minimum values in the series ε_i , respectively.

The standard deviation was calculated by the formula

$$S = \sqrt{\frac{\sum \varepsilon_i^2}{n-1}}. \quad (9)$$

Table 12 shows the results of testing the hypothesis about the normal distribution of the residual component using the *RS* test.

Table 12. Results of the RS test calculation.

Type of trend model	Range of variations <i>R</i>	Standard deviation <i>S</i>	<i>RS</i> test
Linear model	4.89	1.49	3.28
Logarithmic model	1.47	0.49	3.00
Second degree polynomial	1.95	0.62	3.15
Third degree polynomial	0.91	0.31	2.94

For the number of elements in the series $n = 11$, the value of the *RS* test for all trend equations falls within the interval between the critical boundaries from 2.67 to 3.68, which means that the hypothesis about the normal distribution is accepted for all considered trend models.

Similar conclusions were made after checking the correspondence of the distribution of the residual component to the normal law using the indices of asymmetry and kurtosis.

Independence of values (no autocorrelation). To check the autocorrelation in the levels of the series, various criteria are used, including the Durbin–Watson d-test, the calculated value of which is determined by the formula [30, 32]:

$$d = \frac{\sum_{i=2}^n (\varepsilon_i - \varepsilon_{i-1})^2}{\sum_{i=1}^n \varepsilon_i^2}. \quad (10)$$

According to the results of calculations for the logarithmic equation, the d-test was 1.782, for the third-degree polynomial – 3.585.

Further, according to special tables, the critical values of the Durbin–Watson d-test are determined for a given number of observations, the number of independent variables of the model and the level of significance [31].

Comparing the calculated values of the d-criterion of trend models with tabular data, the following results were obtained:

- the logarithmic trend model does not have autocorrelation, which means it can be recognized as adequate;
- the trend model of the third-degree polynomial has autocorrelation and cannot be recognized as adequate.

Thus, according to the results of the performed assessment of the adequacy of the two types of trend models obtained by the search method of nonlinear programming, the logarithmic trend model was recognized the best.

3.6. Comparison of predicted deformation benchmarks with their actual values

To confirm the conclusions about the best form of the trend model obtained by the search method, the predicted values of the marks of the deformation benchmark DM6 were compared with the actual ones measured during observations of the stability of the building.

According to the requirements of STO SRO-S 6054290 00043-2015, according to geodetic monitoring data, forecasting can be carried out only to a depth of no more than 20–25 % of the length of the time series. Thus, Table 13 shows the actual marks of the deformation benchmarks and the predicted marks of this benchmark obtained for 12–14 observation cycles according to the studied trend models.

Table 13. Comparison of the predicted and actual values.

Names of elements of compared models		Cycle No.		
		12	13	14
Actual marks H_{calc} , m		0.8800	0.8816	0.8810
Predictive marks H_{predict} , m	Linear model	0.8807	0.8796	0.8786
	Logarithmic model	0.8824	0.8820	0.8817
	Second degree polynomial	0.8845	0.8853	0.8865
	Third degree polynomial	0.8821	0.8809	0.8784
Prediction errors Δ , mm	Linear model	-0.7	+2.0	+2.4
	Logarithmic model	-2.4	-0.4	-0.7
	Second degree polynomial	-4.5	-3.7	-5.5
	Third degree polynomial	-2.1	+0.7	+2.6

Table 13 shows that the logarithmic trend model has the smallest forecast error.

After correcting the obtained predictive marks [30] according to STO SRO-S 6054290 00043-2015 of the deformation benchmark DM6, considering the actual state of marks according to the data of 12–14 cycles, new (corrected) trend equations were determined. Once again, the predicted value of the mark was extrapolated one cycle ahead for all the trend equations. The obtained predicted value of the mark, considered deformation mark, was compared with the actual mark for cycle 15. The logarithmic trend equation again showed the smallest predictive error.

Thus, the validity of the earlier conclusion that the logarithmic trend model obtained by the search method of nonlinear programming is the best form of the trend model for the example under consideration is confirmed.

With a view to comparing the research results with similar scientific publications devoted to the application of nonlinear programming methods for solving geodetic problems, it should be noted that, despite their large number and variability, few of them highlight the possibility of combinative convergence of Powell and DSC algorithms for solving nonlinear programming problems. Thus, a consistent application of the Powell and DSC methods, which is close in nature to this work, declared as a single "parabola method" and aimed at solving nonlinear optimization problems, is given in the scientific works of A.V. Zubova and N.N. Eliseeva [33, 34], Ch.N. Zheltko [29]. However, in this case, there is no possibility of direct comparison of research results due to the different nature of applied and scientific problems, the solution of which was aimed at a combination of the above search methods of nonlinear programming.

4. Conclusion

The authors developed a method for constructing a trend equation for a predictive model using a search method of nonlinear programming based on geodetic data, including:

- determining the trend equation by the search method of nonlinear programming in the VBA-based program;
- assessing the accuracy of the coefficients of the trend equations by the search method of nonlinear programming;
- assessing the adequacy of trend models obtained by the search method.

This technique was used to calculate the construction of a predictive model based on geodetic data using a search method of nonlinear programming for various types of trend equations. The obtained calculation results were confirmed by calculations in *Microsoft Excel*, using the example of a linear trend model. In addition, the computation results were confirmed by the calculations performed in the *Statistica* program for all the four trend equations.

The use of the search method of nonlinear programming to assess the accuracy of determining the coefficients of the equations of trend models made it possible to obtain the inverse weight matrix of the vector of coefficients, the root-mean-square error of the unit of weight and the root-mean-square error of each determined coefficient of the trend equation.

Comparison of the predicted values of the marks of the deformation benchmark with the actual marks is carried out. The correctness of the choice of the trend equation in the form of a logarithmic model for the considered example has been confirmed.

References

1. Bryn, M.J., Afonin, D.A., Bogomolova, N.N. Geodetic Monitoring of Deformation of Building Surrounding an Underground Construction. *Procedia Engineering*. 2017. 189. Pp. 386–392. DOI: 10.1016/J.PROENG.2017.05.061
2. Gura, D.A., Shevchenko, G.G., Gura, A.Y. Development research methodology elastic deformation total station. *Journal of Engineering and Applied Sciences*. 2016. 11 (13). Pp. 2885–2888. DOI: 10.3923/JEASCI.2016.2885.2888
3. Mustafin M.G., Kazantsev A.I., Valkov V.A. Monitoring of Deformation Processes in Buildings and Structures in Metropolises. *Procedia Engineering*. 2017. No. 189. Pp. 729–736.
4. Gubaidullina, R.A. Features of using the method of aerial topographic survey in deformation monitoring. Trends in the development of science and education. *SRC L-Journal*. 2018. 45. Pp. 386–391. (rus)
5. Li, D., Yan, C. Building deformation prediction based on ground surface settlements of metro-station deep excavation. *Advances in Civil Engineering*. 2018. 2018. DOI: 10.1155/2018/6050353
6. Shardakov, I., Barayakh, A., Yepin, V., Tsvetkov, R., Glot, I. Control of surface subsidence based on building deformation monitoring data. *MATEC Web of Conferences*. 2019. 265. Pp. 05026. DOI: 10.1051/MATECONF/201926505026
7. Huang, M.Q., Zhou, L., Qi, L.X., Huang, H.Y., Tang, M.Y., Shi, Y.J. Multi-factor building deformation analysis and prediction model based on multi-source data. *International Archives of the Photogrammetry, Remote Sensing and Spatial Information Sciences - ISPRS Archives*. 2020. 42(3/W10). Pp. 193–198. DOI: 10.5194/ISPRS-ARCHIVES-XLII-3-W10-193-2020
8. Degtyarev, G.V., Dats'O, D.A. The seasonal regulation basin dam basis deformation forecast. *IOP Conference Series: Materials Science and Engineering*. 2019. 698(2). DOI: 10.1088/1757-899X/698/2/022013
9. Bazilevskiy, M. Analytical dependences for some adequacy criteria of deming regression model. *Proceedings of Irkutsk State Technical University*. 2016. 117 (10). Pp. 81–89. DOI: 10.21285/1814-3520-2016-10-81-89
10. Makarova, I.L., Ignatenko, A.M. Determination coefficient for nonlinear regression. *Yevraziyskoye Nauchnoye Obyedineniye*. 2018. 3 (37). Pp. 161–163. (rus)
11. Skvortsov, V.V. Study methods of the tendency of the temporary rows in economic researches. *Social-Economic Phenomena and Processes*. 2008. 2(10). Pp. 75–78. (rus)
12. Espinosa-Garza, G., Loera-Hernández, I. Proposed model to improve the forecast of the planned value in the estimation of the final cost of the construction projects. *Procedia Manufacturing*. 2017. 13. Pp. 1011–1018. DOI: 10.1016/J.PROMFG.2017.09.103
13. Huang, Z., Tu, Y., Meng, S., Bagge, N., Nilimaa, J., Blanksvärd, T. Validation of a numerical method for predicting shear deformation of reinforced concrete beams. *Engineering Structures*. 2019. 197. DOI: 10.1016/J.ENGSTRUCT.2019.109367
14. Gulyaev YU.P. Prognozirovaniye deformatsiy sooruzhenij na osnove rezul'tatov geodezicheskikh nablyudenij [Forecasting deformations of structures based on the results of geodetic observations]. Novosibirsk: SGGa, 2008. 256 p.
15. Zajcev A.K., Marfenko S.V., Mihelev D.SH. i dr. Geodezicheskie metody issledovaniya deformatsiy sooruzhenij [Geodetic methods for studying deformations of structures]. Nedra, Moskva, 1991. 272 p.
16. Pozdysheva, O.N. Forecasting of deformations of building structures according to the results of geodetic observation. 2017. (No 02 (56). Part 2). Pp. 56–58. DOI: 10.23670/IRJ.2017.56.058. (rus)
17. Kharchenko, B.A. Analysis and prediction of the buildings deformations using the geodetic data are based on the program product the Mathcad-15. *Interexpo Geo-Sibir*. 2015. 1 (1). Pp. 21-27 (rus)
18. Khoroshilov, V.S., Kobeleva, N.N., Sycheva, N.V. Mathematical modeling of the high-rise buildings deformation development process in Moscow (Voststania square). *IOP Conference Series: Materials Science and Engineering*. 2019. 698 (4). Pp. 044004. DOI: 10.1088/1757-899X/698/4/044004.
19. Zhang, B., Qiu, L., Zhou, Z. Prediction Analysis for Building Deformation Based on Multiple Linear Regression Model. *IOP Conference Series: Earth and Environmental Science*. 2020. 455(1). DOI:10.1088/1755-1315/455/1/012047.
20. Bronstein, V.I., Groshev, M.E. Numerical modeling of the stress-strain state of high dams. *Hydrotechnical construction*. 2002. No. 6. Pp. 2–11. (rus)
21. Salazar, F., Morán, R., Toledo, M.Á., Oñate, E. Data-Based Models for the Prediction of Dam Behaviour: A Review and Some Methodological Considerations. *Archives of Computational Methods in Engineering*. 2015. 24(1). Pp. 1–21. DOI: 10.1007/S11831-015-9157-9.
22. Mazurov B.T., Pankrushin V.K., Seredovich V.A. Matematicheskoe modelirovaniye i identifikatsiya napryazhenno-deformirovannogo sostoyaniya geodinamicheskikh sistem v aspekte prognoza prirodnykh i tekhnogennykh katastrof [Mathematical modeling and identification of the stress-strain state of geodynamic systems in the aspect of predicting natural and man-made disasters]. *Vestnik SGGa*. 2004. No. 9. Pp. 30–35. (rus)
23. Lebega, O., Vytvitsky, Y. Use of correlation-regression analysis for estimation of prospects of natural gas extraction of shale rocks. *EUREKA: Social and Humanities*. 2017. 4 (4). Pp. 37–43. DOI: 10.21303/2504-5571.2017.00383.
24. Seredovich, V.A., Ekhigiator-Irughe, R., Ekhigiator, O.M., Oriakhi, H. Prognoz deformatsiy s ispol'zovaniem funktsiy pokazatel'nogo mnogochlena [Deformation prediction using exponential polynomial functions]. *Interexpo Geo-Sibir*. 2012. VIII Mezhdunar. nauch. kongr.: Mezhdunar. nauch. konf. «Geodeziya, geoinformatika, kartografiya, markshejderiya»: sb. materialov v 3 t. (Novosibirsk, 10-20 aprelya 2012 g.). -Novosibirsk: SGGa, 2012. T. 1. Pp. 148-155.
25. Degtyarev, V.G., Khodakovskiy, V.A. Probabilistic and deterministic methods to find solutions of nonlinear equations and systems. *System analysis and analytics*. 2017. 1 (2). Pp. 4-12 (rus)
26. David M. Himmelblau Applied nonlinear programming. Mir, Moscow, 1975. 536 p. (rus)
27. Shevchenko, G.G. Using search methods for leveling and assessing the accuracy of elementary geodetic constructions. *Geodezia i Kartografiya*. 2019. 952 (10). Pp. 10–20. DOI: 10.22389/0016-7126-2019-952-10-10-20
28. Shevchenko, G.G., Bryn, M.J., Afonin, D.A., Gura, D.A. Experimental researches in defining deformations by free station method and results processing by search method. *Lecture Notes in Civil Engineering*. 2020. 50. Pp. 163–175. DOI: 10.1007/978-981-15-0454-9_17
29. Zheltko, Ch.N., Shevchenko, G.G., Gura, D.A., Pastukhov, M.A. Universal'naya programma opredeleniya trekhmernykh koordinat tochek cherez obrabotku izmerenij gorizontalnykh, vertikal'nykh uglov i rasstoyanij poiskovym sposobom [Universal program for determining three-dimensional coordinates of points through the processing of measurements of horizontal, vertical angles and distances by the search method]. Certificate of state registration of a computer program: copyright holder: Kuban State Technological University. Reg. No. RU 2015617205 dated 03.07.15. Rospatent, Moscow, 2015. (rus)

30. Sadovnikova, N.A., Shmojllova, R.A. Analiz vremennyh ryadov i prognozirovanie [Time series analysis and forecasting]. Universitet «Sinergiya», Moscow, 2016. 152 p. (rus)
31. Krasina, I.B., Danovich, L.M. Statistical methods for processing of experimental data. Publishing house of the Kuban State Technological University, Krasnodar, 2015. 244 p. (rus)
32. Tatarenko, S.I. (comp.) Metody i modeli analiza vremennyh ryadov [Methods and models of time series analysis]. Publishing house of Tambov State Technical University, Tambov, 2008. 32 p. (rus)
33. Zubov, A.V., Eliseeva, N.N. Software suite for determining the tilts of tower-type structures according to terrestrial laser scanning. Geodezia i Kartografiya. 2020. 961 (7). Pp. 2–7. DOI: 10.22389/0016-7126-2020-961-7-2-7
34. Eliseeva, N.N., Zubov, A.V. The application of search methods for solving optimization problems. Topical Issues of Rational Use of Natural Resources 2019. 2019. 1. Pp. 346–352. DOI: 10.1201/9781003014577-43.

Information about authors:

Grittel Shevchenko,

PhD in Technical Science

ORCID: <https://orcid.org/0000-0003-1849-4718>

E-mail: grettel@yandex.ru

Mikhail Brin,

Doctor in Technical Science

ORCID: <https://orcid.org/0000-0002-4722-9289>

E-mail: 3046921@mail.ru

Dmitry Gura,

PhD in Technical Science

ORCID: <https://orcid.org/0000-0002-2748-9622>

E-mail: gda-kuban@mail.ru

Nafset Khusht,

ORCID: <https://orcid.org/0000-0001-5405-3798>

E-mail: nafset-khusht@yandex.ru

Murat Tamov,

PhD in Technical Science

ORCID: <https://orcid.org/0000-0001-8235-2314>

E-mail: murat.tamov@gmail.com

Received 23.09.2020. Approved after reviewing 07.04.2022. Accepted 12.04.2022.



Research article

UDC 528.01:004.428:519.816

DOI: 10.34910/MCE.114.5



AHP-TOPSIS hybrid decision support system for dam site selection

S. Rodriguez Vazquez , N. Mokrova 

National Research Moscow State Civil Engineering University, Moscow, Russia

✉ solrusita85@gmail.com

Keywords: river basins, selection of areas, dams, multicriterial analysis, decision making, AHP, TOPSIS

Abstract. Inadequate selection of an area for the location of dams brings about social and economic disadvantages due to the non-fulfillment of its objective, as well as causes significant damage to the ecosystem of the river basin. This type of selection depends on a set of different criteria and variables, so it is necessary to develop a tool to support decision-making that allows reducing the collateral damage that a project of this type entails and increasing the project effectiveness. This paper proposes the development of a hybrid method of multicriterial analysis using the hierarchical analysis technique (AHP) and the technique for the order of preferences by similarity to the ideal solution (TOPSIS) with a specific focus on the selection of sites for dams. Modifications to traditional methods were established by eliminating the decision-maker as an evaluator of alternatives. The proposed method is based on the hierarchical ordering of alternatives taking into account the subjective judgments of decision-makers when considering the uncertainties of the selection process. The ordering of the alternatives is preceded by the analysis of a series of hydrological, geological, topographic and land use parameters extracted from a digital elevation model. According to the results obtained, it was possible to order hierarchically (better-worse) each of the river basins evaluated according to the established parameters.

Citation: Rodriguez Vazquez, S., Mokrova, N. AHP-TOPSIS hybrid decision support system for dam site selection. Magazine of Civil Engineering. 2022. 114(6). Article No. 11405. DOI: 10.34910/MCE.114.5

1. Introduction

The social and economic contributions of dams in most cases outweigh the damages and costs provided by the construction of dams worldwide. The selection of the best location for the construction of a dam is one of the most complex and controversial decisions in water supply management [1]. Just as optimal site selection can improve reservoir safety and groundwater regeneration in a region, poor site selection can undermine them. A well-selected site will not only provide direct benefits, but its careful design can also provide the additional benefit of a recreation area surrounding the reservoir. Conversely, a poorly selected site could cause harmful influences such as negative biophysical, socio-economic and geopolitical impacts, often through the loss of ecosystem services provided by fully functioning aquatic systems [2–5]. Therefore, for the selection of dam sites, it is necessary to conduct an accurate study of the area of interest considering the factors affecting this selection. However, this procedure is expensive and time-consuming. With advances in Informatics and Information Technologies, the determination of competitive solutions in terms of cost, time and a variety of other objective variables is greatly facilitated.

A powerful tool that plays a notable role in this process is the Geographic Information System (GIS) and its applications in hydrology. In addition to GIS, Multi-Criteria Decision Making (MCDM) helps decision makers select from alternative solutions, in this case sites for dam construction, where there are many criteria [6]. Two of the most commonly used MCDM techniques are known as analytical hierarchy process (AHP) [7] and technique for order of preference by similarity to the Ideal solution (TOPSIS) [8–11]. The integration of MCDM and other data analysis tools such as GIS have been commonly used by previous

researchers, particularly in dam site selection studies [12–15]. It should be noted that GIS is powerfully used in the selection of dam sites [16–18]; however, its capacity in a certain region may differ from other locations. The AHP approach is an effective tool for System Analysis and solves decision problems by reducing complex decisions to a series of peer comparisons. AHP is an effective multi-criteria decision-making technique that has been used to solve decision problems in a variety of fields [19–20]. In addition, the AHP includes an effective technique for checking the consistency of the decision maker's assessments, thus decreasing the bias in the decision-making process [21]. The TOPSIS method is based on the idea that the best alternative has the shortest distance from the ideal solution and the furthest distance from the negative ideal solution. The ideal solution is assumed to be an alternative that has the best values for all criteria considered, while the negative ideal solution is identified as a hypothetical alternative that has the worst criteria values [8]. Many articles have been published in the field of dam site selection using MCDM techniques to choose a viable location to build a dam. However, the authors of the present research are not aware of any studies using TOPSIS and AHP as a hybrid method to solve dam site selection problems.

A wide range of risk or performance analysis studies have been conducted in multiple watersheds, dams or tunnels around the world with various hydroclimatological regimes [22–26]. Piadeh F. et al. (2012) carried out a study to prioritize the best locations for irrigation with treated wastewater (TWW) in Tunisia [26]. Potential viable locations were identified based on resource conflicts, cost-effectiveness, land suitability, social acceptance and environmental factor. Several researchers have applied fuzzy systems in decision-making methods [27–30]. Using fuzzy AHP combined with GIS, they were able to map and prioritize appropriate sites for different purposes. Reliable data and advanced technologies are two necessary elements for efficient classification management based on its overall performance using the TOPSIS technique. Kim et al. (2012) used the TOPSIS method in a diffuse environment to classify the best of ten sites for treated wastewater (TWW) in an urban Basin of South Korea [27]. They considered four main criteria, including technical, social, economic and environmental criteria. Uncertainty of weighting values and input data were considered using triangular fuzzy numbers, and data were collected through individual interviews.

Zyoud et al. (2016) used AHP and TOPSIS methods within a diffuse environment to create a framework for Water Loss Management in developing countries [29]. They proposed a hierarchical structure of the decision problem consisting of four levels: overall objective; main criteria; evaluation criteria; and options. In this study, the weightings of the criteria were determined by AHP fuzzy, and TOPSIS fuzzy was also used to rank the options in terms of their potential to meet the overall goal based on the assessments and preferences of decision makers. The most important option was supposed to be a pressure management and control strategy. In addition, the use of advanced techniques and the establishment of District measurement areas were identified as the second and third most important, respectively. In addition, based on the results of the sensitivity analysis, the stronger and weaker options were less sensitive to changes in the weightings of the evaluation criteria. Özcan et al. (2017) applied the AHP and TOPSIS methods for the selection of maintenance strategies in hydropower plants in Turkey [31]. In their study, a combined AHP-TOPSIS methodology was used to choose the most critical equipment. Nine units critical for hydropower plants were identified. A goal programming (GP) model was proposed to obtain combinations of maintenance strategies for the team. The results showed that there was a 77.1 % improvement in the frequency of plant failures as a result of employing an incorrect maintenance strategy on critical equipment compared to the period when the model was not used. Önüt and Soner (2018) conducted a comparison between AHP and TOPSIS techniques to select an optimal transshipment site in Istanbul, Turkey [32]. They used fuzzy sets to account for uncertainties in different criteria and derived criteria weightings based on a peer comparison using the AHP method. Mulliner et al. (2016) conducted a comprehensive analysis of five different MCDM techniques, including TOPSIS and AHP, to assess sustainable housing affordability using different economic, social and environmental criteria in Liverpool, UK [33]. Their results show that the overall classification of alternatives varies from method to method, and there is no perfect technique for this problem. Therefore, when possible, applying a selection of different methods to the same problem is ideal. Balioti et al. (2018) applied the AHP and TOPSIS methods with fuzzy logic to select the optimal type of Spillway on a dam in northern Greece [34]. They concluded that these tools are necessary to take into account additional parameters beyond technical and construction costs. Table 1 shows a quick review of a recent research study on dam site selection using AHP and TOPSIS techniques.

Table 1. The optimal dam site selection using a group decision-making method through fuzzy TOPSIS model [35].

Reference	Year	Site Selection for	Applied Method
[36]	2012	Underground Dam	AHP
[37]	2013	Dam	AHP
[38]	2013	Dam	TOPSIS
[39]	2013	Underground Dam	AHP
[39]	2014	Subsurface dams	AHP
[40]	2015	Small underground dams	AHP
[41]	2015	Dam	AHP
[18]	2016	Dam	AHP
[42]	2017	Dam	AHP
[43]	2018	Dam	AHP
[1]	2018	Dam	TOPSIS

In order to prevent the damage caused by floods and intense rains due to climatic phenomena Cuba has proposed to build new dams and reservoirs. In addition, the stages of drought deprive that part of the population of the necessary and continuous supply of water. The construction of new dams in strategic locations can contribute to improving these aspects. This article presents a study based on the selection of suitable dam sites in Manicaragua municipality, Villa Clara, Cuba. Therefore, a study on two MCDM models (TOPSIS and AHP) in the GIS environment is applied to determine the proposed locations for dam construction. For this, based on the literature and similar research experiences, several criteria were used in the selection procedure. Therefore, the main objectives of this study are as follows:

- Propose several factors that affect the selection of the dam site in Manicaragua municipality, Villa Clara province, Cuba, based on previous experiences around the world.
- Integrate MCDM and GIS into the study area for the purpose of selecting the dam site.
- Consider topographic and morphological conditions in the selection of the dam site.
- Assist decision makers in the construction of new dams in the area of interest.

The present research is organized as follows. At the beginning, the hybrid method and the way of combining the AHP and TOPSIS techniques to choose the best locations for dam construction is described. Subsequently, the results of the implementation of the proposed hybrid method are discussed and finally the conclusions obtained from the validation of the AHP-TOPSIS hybrid method are provided.

2. Methods

The hybrid method used in this study is based on the integration of hierarchical ordering methods AHP and TOPSIS. First, the AHP method is applied in order to determine what are the criteria and sub-criteria that should be taken into account and the weight that these should have when evaluating possible alternatives. Following this, the TOPSIS method is applied in order to select the closest solution to the ideal before all possible alternatives that exist, making use of a similarity index that is constructed by combining the proximity to the positive ideal and the distance from the negative ideal. Decision making in this integrated method involves several essential steps.

Step 1: Structure the problem as a hierarchy

The first step of the AHP method is to model the decision problem that is intended to be solved as a hierarchy. In this step, the effective criteria for locating the dam site are determined by using a thorough review of the literature and expert opinions. The hierarchy is then modeled as a graphical representation of a complex problem in which the objectives, criteria and alternatives are at the highest, intermediate and lowest levels, respectively (Fig. 1).

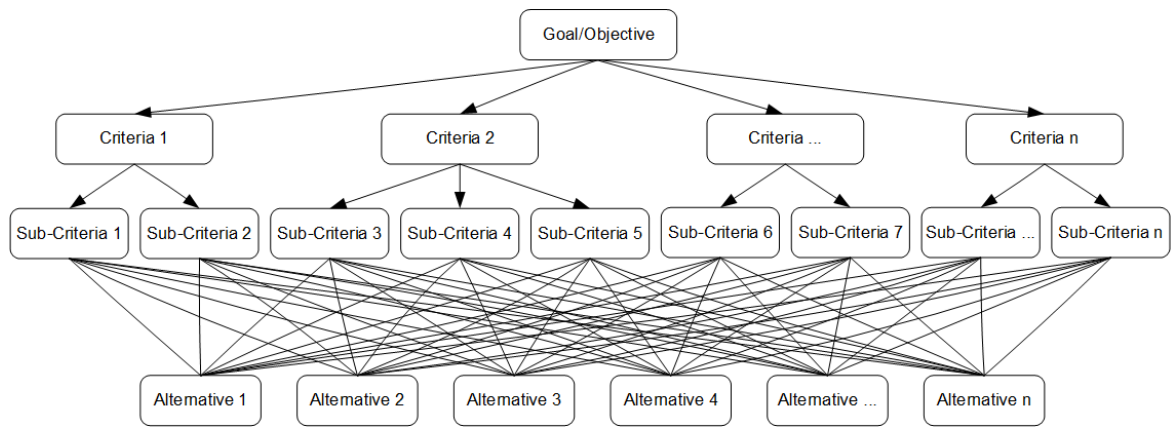


Figure 1. Outline of the AHP analysis regarding the context of the research.

Step 2: Prioritization among criteria

The fundamental idea of this study is to facilitate the work of the experts so the proposal in this step by the author is that the experts should only evaluate the criteria according to their opinion and not weigh each of the criteria in correspondence with the rest of the criteria. For this purpose, the author proposes to use two comparison scales, one that will be used by the expert to evaluate the criteria (Table 2) and another so that the GIS system itself creates the peer comparison matrix using the criteria established by the expert. The latter scale corresponds to the scale proposed by Saaty [7] (Table 3).

Table 2. Scale proposal for the direct assignment made by the expert.

<i>Qualitative assessment</i>	<i>Quantitative valuation</i>
Very Low Importance	1
Low Importance	3
Moderately important	5
Strong importance	7
Highest importance	9

Table 3. Fundamental paired comparison scale.

FUNDAMENTAL PAIRED COMPARISON SCALE		
Numerical scale	Verbal comparison scale	Explaining
1	Equal importance	Two activities contribute equally to the objective
3	Moderate importance of one element over another	Experience and judgment are in favor of one element over another
5	Strong importance of one element over another	One element is strongly favored
7	Very strong importance of one element over another	One element is very dominant
9	Extreme importance of one element over another	An element is favored by at least an order of magnitude difference

In order to establish priorities between the elements at each level, a measurement methodology proposal is made that allows connecting the scale proposed in Table 2 (expert assessments) and the scale proposed by Saaty in Table 3 for the paired comparison. For this the methodology is aided by 2 fundamental steps:

Step 2.1. The expert determines the importance of each criteria with respect to the objective and the sub-criteria with respect to each criteria. This is done by making use of Table 2.

Step 2.2. An intermediate value scale (Table 4) is created using Table 2 and 3. This scale will be used by the GIS system internally and will allow to know the values that are obtained from the paired comparison between the valuations given by the expert to each of the criteria. (These values are used to complete paired comparison arrays).

Table 4. Value comparison scale using Tables 2 and 3. (Source: Author's creation).

Comparison scales of the values assigned by the expert	Values obtained by comparison	Comparison scales of the values assigned by the expert	Values obtained by comparison
(1) to (n)	$\frac{1}{n}; (n = 1, 3, 5, 7, 9)$	(n) to (1)	$n; (n = 1, 3, 5, 7, 9)$
(3) to (5)	$\frac{1}{3}$	(5) to (3)	3
(5) to (7)		(7) to (5)	
(7) to (9)		(9) to (7)	
(3) to (7)	$\frac{1}{5}$	(7) to (3)	5
(5) to (9)		(9) to (5)	
(3) to (9)	$\frac{1}{7}$	(9) to (3)	7

On the basis of the information collected with the measurement methodology outlined above, we construct a matrix R of dimension $m \times n$ (Eq. (1)), where r_{ij} represents the priority between factor i and factor j , and the values of the lower half with respect to the diagonal values (reciprocal) correspond to the inverse values of the upper half $\left(r_{ij} = \frac{1}{r_{ji}} \right)$, being $r_{ij} = 1$, when $i = j$.

$$R = \begin{bmatrix} 1 & r_{12} & \cdots & r_{1n} \\ r_{21} & 1 & \cdots & r_{2n} \\ \vdots & \vdots & \ddots & \vdots \\ r_{n1} & r_{n2} & \cdots & 1 \end{bmatrix}. \quad (1)$$

In the comparison matrix R , the columns represent the relative weights of each factor with respect to the others. To determine the factor of greatest preference, for a certain criterion, the values are normalized by dividing each element of column j by the sum of all elements of that column (Equation (2)) and then, estimating a vector of weights $\vec{w} = [w_1, w_2, \dots, w_n]$. This weight vector is obtained by averaging each row of the normalized matrix (Equation (3)) and its value indicates the relative importance of each factor in a range between 0 and 1.

$$x_{ij} = \frac{r_{ij}}{\sum_{i=1}^n r_{ij}}, \quad (2)$$

$$w_i = \sum_{j=1}^n \frac{x_{ij}}{n}. \quad (3)$$

Subjective valuations may cause inconsistencies. Because of this it becomes necessary to measure the consistency of the paired comparison matrix. If a matrix is consistent it must be verified that, if the judgments are consistent, the matrix R would have a single eigenvalue $\lambda = n$, but since it is not possible for a person to be perfectly consistent then inconsistency will always exist. The important thing is that a certain permissible limit is not exceeded.

The above implies that the paired comparison matrix will have more than one eigenvalue λ_i . The maximum eigenvalue (λ_{\max}) allows us to estimate the degree of consistency of the paired comparison matrix using the consistency index (CI) (Eq. (6)).

To obtain the value of λ_{\max} first of all it is necessary to multiply the comparison matrix, row R by the vector of priorities \vec{w} (Equation (4)) to obtain a vector of consistency $\vec{\lambda w} = [\lambda w_1, \lambda w_2, \dots, \lambda w_n]$. If the matrix R were perfectly consistent, the sum of the elements of the obtained vector should be equal to n . The situation above does not usually happen, so to determine the degree of inconsistency it is necessary to divide each element of the consistency vector $\vec{\lambda w}$ by its vector \vec{w} corresponding in the priority and in this way all possible values λ_i , are obtained. Then to finally obtain λ_{\max} we proceed to perform Eq. (5):

$$\begin{bmatrix} r_{11} & r_{12} & r_{13} \\ r_{21} & r_{22} & r_{23} \\ r_{31} & r_{32} & r_{33} \end{bmatrix} \times \begin{bmatrix} w_1 \\ w_2 \\ w_3 \end{bmatrix} = \begin{bmatrix} \lambda w_1 \\ \lambda w_2 \\ \lambda w_3 \end{bmatrix}, \quad (4)$$

$$\lambda_{\max} = \sum_{i=1}^n \frac{\lambda_i}{n}, \quad (5)$$

$$CI = \frac{\lambda_{\max} - n}{n - 1}. \quad (6)$$

Then to check if the degree of consistency is permissible, a Random Consistency Index (RI) is used as a reference (Table 5) [44, 45].

Table 5. Random Consistency Index (RI) as a function of the dimension (n) of the matrix.

n	1	2	3	4	5	6	7	8
RI	0	0	0.525	0.882	1.115	1.252	1.341	1.404
n	9	10	11	12	13	14	15	16 ≤
RI	1.452	1.484	1.513	1.535	1.555	1.570	1.583	1.595

The consistency ratio (CR) measures the degree of inconsistency of the paired comparison matrix and is calculated as follows:

$$CR = \frac{CI}{RI}. \quad (7)$$

If $CR = 0$ then the matrix is consistent, if $CR \leq 0.10$ the matrix has an allowable inconsistency, which means that it is considered consistent and therefore the vector of weights w is also accepted as valid. But if $CR > 0.10$, the inconsistency is inadmissible and it is advisable to review the assessments made.

Step 3: Establishing local priorities among sub-criteria

In the modeling of the decision problem as a hierarchy, the decomposition of all criteria into sub-criteria has been considered. The procedure is the same as that described in the previous step, but in this case paired comparisons between sub-criteria should be made to determine their relative importance with respect to the criteria immediately higher in the hierarchy.

Step 4: Setting local and global priorities among alternatives

The procedure is the same as explained in step 2, but this time the priority level of one alternative over another is established taking the degree of compliance or satisfaction of each criteria or sub-criteria as a basis of comparison.

$$\bar{n}_{ij} = \frac{x_{ij}}{\sqrt{\sum_{j=1}^m (x_{ij})^2}}, \quad i = 1, \dots, m; \quad j = 1, \dots, n. \quad (9)$$

Step 5: Creation of weighted normalized decision matrix

The weighted normalized value \bar{v}_{ij} of the weighted normalized decision matrix $V = [\bar{v}_{ij}]_{m \times n}$ is calculated as:

$$\bar{v}_{ij} = w_j \otimes \bar{n}_{ij}, \quad i = 1, \dots, m; \quad j = 1, \dots, n, \quad (10)$$

where w_j is such that $1 \in \sum_{j=1}^n w_j$ is the weight of the j^{th} attribute or criteria.

Step 6: Definitions of the positive ideal solution (PIS) and negative ideal solution (NIS)

The positive ideal solution minimizes cost criteria and benefit criteria; conversely, the negative ideal solution maximizes cost criteria and minimizes benefit criteria. The set of positive ideal values \bar{A}^+ and the set of negative ideal values \bar{A}^- are determined as:

$$\bar{A}^+ = \left\{ \bar{v}_1^+, \dots, \bar{v}_n^+ \right\} = \left\{ \left(\max_i \bar{v}_{ij}, j \in J \right) \left(\min_i \bar{v}_{ij}, j \in J' \right) \right\}; i = 1, 2, \dots, m, \quad (11)$$

$$\bar{A}^- = \left\{ \bar{v}_1^-, \dots, \bar{v}_n^- \right\} = \left\{ \left(\min_i \bar{v}_{ij}, j \in J \right) \left(\max_i \bar{v}_{ij}, j \in J' \right) \right\}; i = 1, 2, \dots, m, \quad (12)$$

where J is associated with the profit criteria and J' is associated with the cost criteria.

Step 7: Determination measures of distances between positive and negative ideal alternatives and solutions

In this step, the separation of each alternative from the positive ideal solution and the negative ideal solution is calculated and then two different GIS layers \bar{A}^+ and \bar{A}^- are created, similar findings are found in [49–51].

The separation of each alternative from the positive ideal solution \bar{A}^+ is given as:

$$d_i^+ = \left\{ \sum_{j=1}^n \left(\bar{v}_{ij} - \bar{v}_{ij}^+ \right)^2 \right\}^{\frac{1}{2}}; \quad i = 1, \dots, m. \quad (13)$$

And the separation of each alternative of the negative ideal solution \bar{A}^- is as follows:

$$d_i^- = \left\{ \sum_{j=1}^n \left(\bar{v}_{ij} - \bar{v}_{ij}^- \right)^2 \right\}^{\frac{1}{2}}; \quad i = 1, \dots, m. \quad (14)$$

In this case the Euclidean m-multidimensional distance is used.

Step 8: Calculation of the performance of each alternative

The relative proximity of \bar{R}_i to the ideal solution can be expressed as follows:

$$\bar{R}_i = \frac{\bar{d}_i^-}{\bar{d}_i^+ + \bar{d}_i^-}; i = 1, \dots, m, \quad (15)$$

- If $\bar{R}_i = 1 \rightarrow A_i = \bar{A}^+$
- If $\bar{R}_i = 0 \rightarrow A_i = \bar{A}^-$

The closer the value of \bar{R}_i is to 1, it implies a higher priority of the i^{th} alternative.

Step 9: Ranking alternatives

In the last step, the values of the layer (the relative proximity to the positive ideal solution) created in step 7 are determined for the selected sites based on topographic conditions. The set of sites can now be sorted by the descending order of the value of \bar{R}_i . The best sites are those that have higher \bar{R}_i values and as they are closer to the positive ideal solution, they are preferable and should be chosen as is the case of the outputs obtained in [50].

3. Result and Discussion

The case study focuses on the selection of suitable sites for the construction of dams in the municipality of Manicaragua, Cuba. The objectives for the construction of these dams can be: support for the development of agriculture and industry, drinking water supply, power generation, fishing.

The municipality of Manicaragua has a surface area of 1064.4 km², of which 309 km² constitute a mountain area with limitations for habitat development, due to various risk factors that this area has. Only the mountainous area of the municipality represents approximately 29 % of the territorial total, standing out within the provincial statistics of Villa Clara. It is bordered to the north by the municipalities of Santa Clara, Ranchuelo and Placetás; to the South by the provinces of Cienfuegos and Sancti Spíritus; to the East by the province of Sancti Spíritus; and to the West by the municipality of Ranchuelo and the province of Cienfuegos.

Its relief is characterized by a fluvial plain and slightly dissected pre-mountain heights, the highest above mean sea level is the Pico Tuerto, with 919 meters, which in turn is the highest elevation of the province. Brown soils with carbonates, grayish brown and leached red ferralites prevail.

Within its hydrographic characteristics it can be commented that it presents a group of areas considered to be at risk for flooding, highlighting the area included within the Jibacoa Valley, which occupies an area of 12 km². Here, intense rains alone cause the incommunication of the area affecting 176 homes with a total of 486 people having to evacuate. Two more areas, popular councils of Las Cajas and Nicaragua I, are also subject to some significant damage, albeit not as severe as the popular council of Jibacoa.

In the first step, to determine the effective factors in the selection of an appropriate site for the construction of dams in the municipality of Manicaragua, an exhaustive review of the literature [52–56] was carried out. The most important criteria were selected and used in the current research. Below is a brief explanation of the selected criteria and the sub-criteria associated with each of them.

Hydrology (C_1): main stream length (C_{11}), mainstream slope (C_{12}), time of concentration (C_{13}), maximum flow estimate (C_{14}), runoff coefficient (C_{15}), rainfall intensity (C_{16}), real evapotranspiration (C_{17}), average annual rainfall of the basin (C_{18}), sinuosity of water currents (C_{19}), average annual rainfall volume of the basin (C_{110}), constant stability of the river (C_{111}), order of rivers (C_{112}), torrential coefficient (C_{113}), calculation of runoff coefficient (C_{114}).

Topography (C_2): basin area (C_{21}), compactness index (C_{22}), form factor (C_{23}), middle slope of the basin (C_{24}), drainage density (C_{25}), average elevation of the basin (C_{26}), watershed width (C_{27}), elongation index (C_{28}).

Geology (C_3): coefficient of massiveness of the basin (C_{31}), orographic coefficient (C_{32}).

Land Use (C_4): delimitation of areas suitable for location (C_{41}).

After collecting and evaluating the required information based on the selected criteria (mentioned above), 29 feasible alternatives were proposed for the dam site in Manicaragua. Three of them A_1, A_4, A_{28} , were not be included within the alternatives to be evaluated: A_1 turned out to be a false positive, while the analysis showed that the area of A_4 and A_{28} did not include tributaries of rivers. The locations of the proposed alternatives are show in Fig. 2 and are identified by numbers. Each of these alternatives represents the basins present in the municipality. This way the best area would be evaluated along with the best locations in each of these areas.

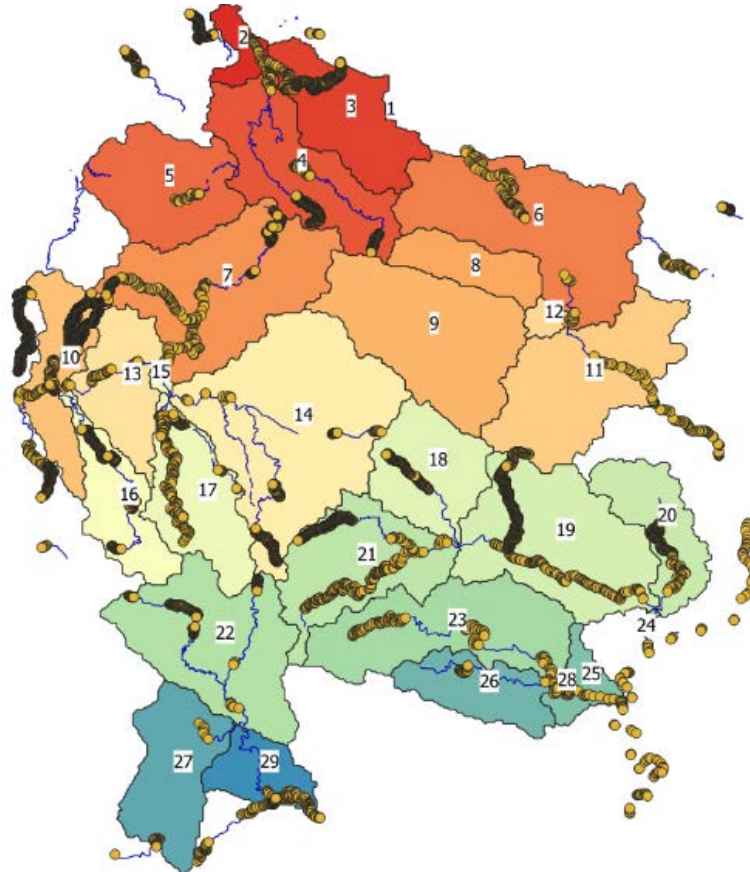


Figure 2. Alternatives for the site of the dam in the municipality of Manicaragua, Cuba.

After selecting the criteria for locating the dam site and considering alternatives (Fig. 2), the combination of AHP and TOPSIS methods for paired comparison was applied to select the best site. Fig. 3 shows the problem of site selection of the Manicaragua dam using a hierarchical structure. The structure has four levels: Objective (location of the dam site), criteria (C_1 to C_4), sub-criteria (C_{11} to C_{114} , C_{21} to C_{28} , C_{31} to C_{32} , C_{41}) and alternatives (A_1 to A_{29}).

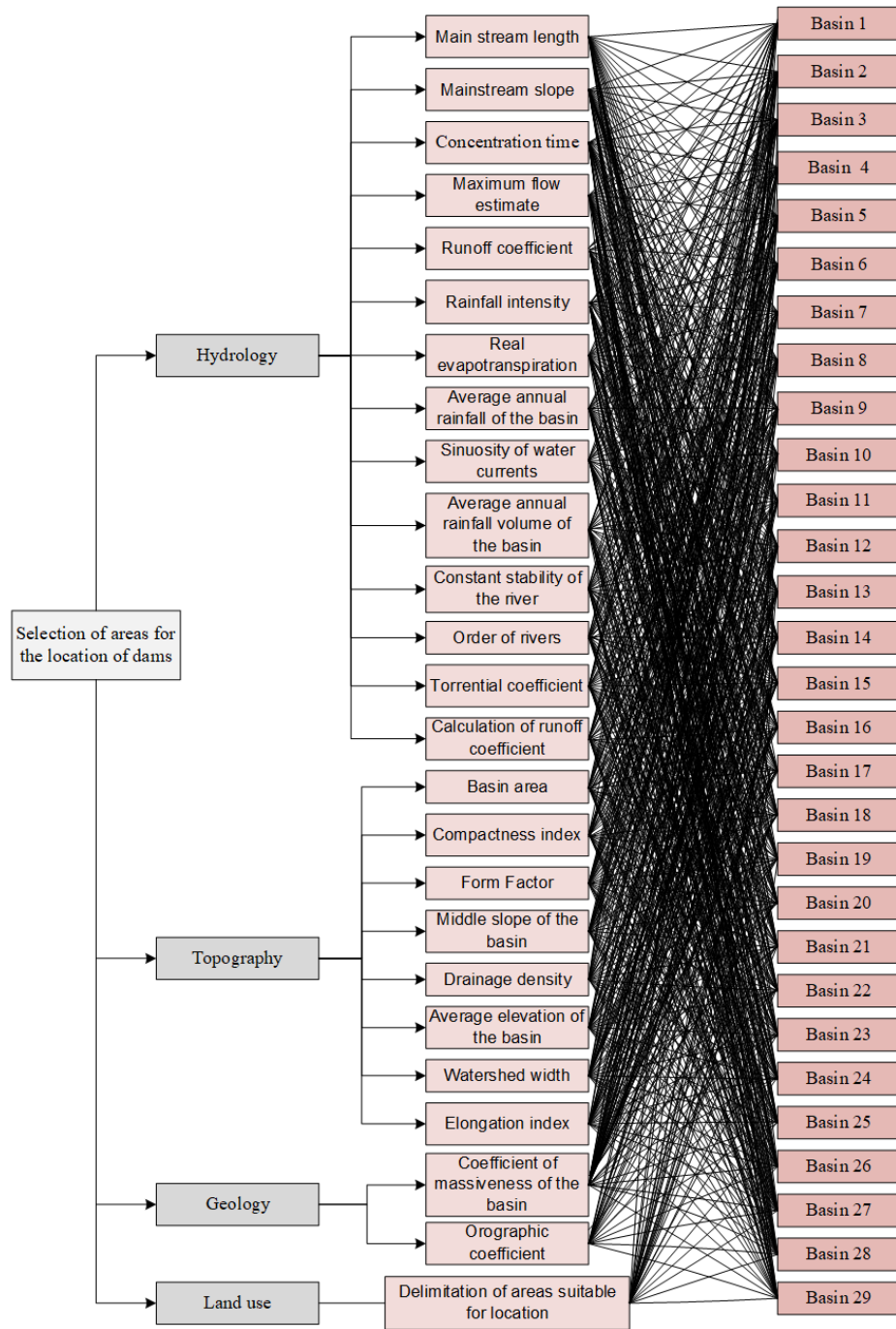


Figure 3. Selection of the dam site of the municipality of Manicaragua using a hierarchical structure.

To evaluate the relevance of the criteria incorporated in the AHP method, a questionnaire was developed, and an E_1 expert, involved in the dam construction project, was asked to express the importance of each criterion using linguistic variables established in Table 2. Then, a pair comparison matrix was formed to determine the weights of the criteria according to the description made in step 2. Once the paired comparison matrices are obtained and the local and global priorities for each of the criteria, sub-criteria and alternatives are established, the weighted normalized decision matrix is constructed, obtaining the distribution of values according to the graphs shown in Fig. 4.

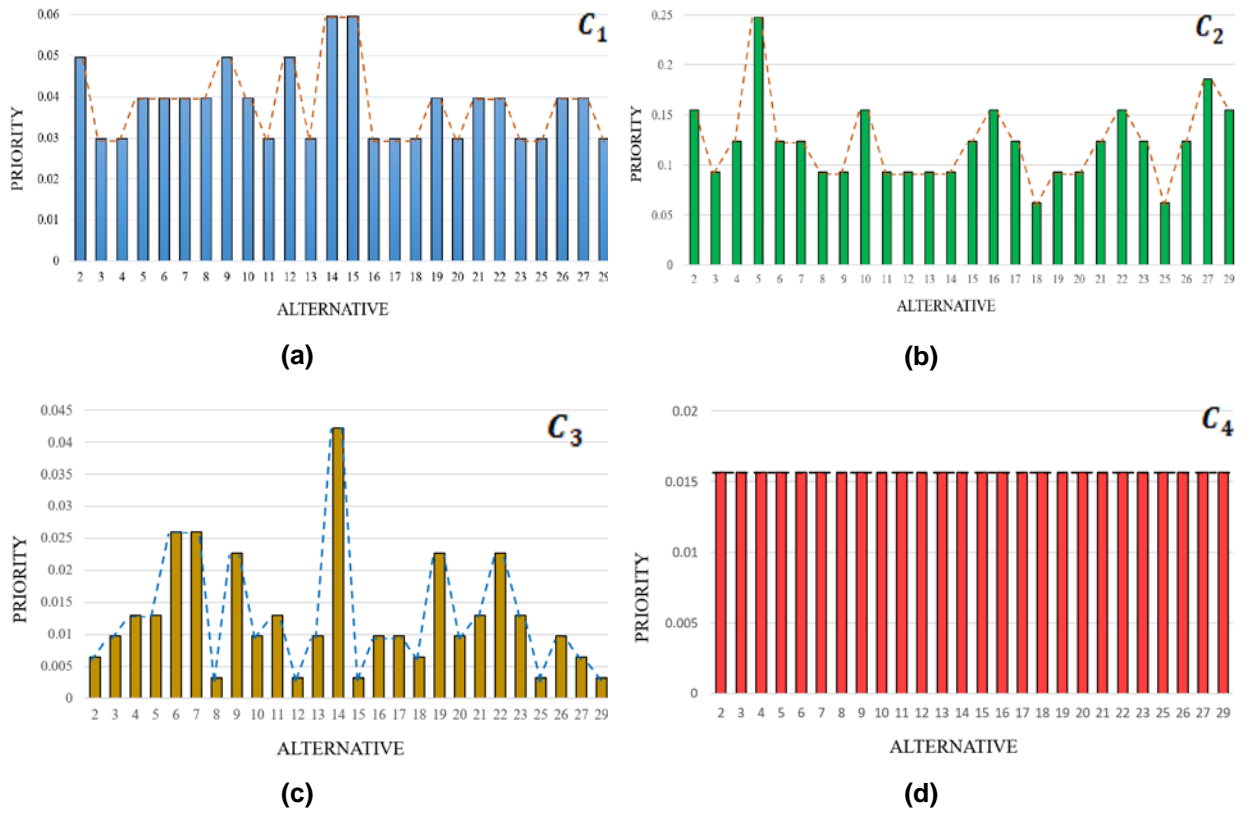


Figure 4. Prioritization of the weights of the alternatives according to the criteria in the normalized matrix. a) Criteria C_1 , b) Criteria C_2 , c) Criteria C_3 , d) Criteria C_4 .

The distances between alternatives and ideal positive and negative solutions are subsequently determined. The Euclidean distance is calculated for the best ideal value (\bar{d}_i^+) and for the worst ideal value (\bar{d}_i^-) , Fig. 5. Then the relative proximity \bar{R}_i to the ideal solution is calculated, Fig. 6.

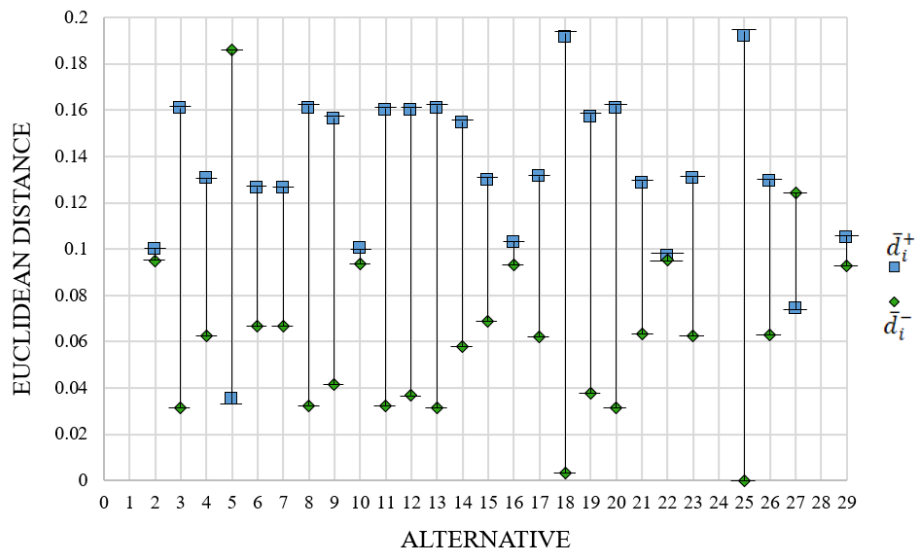


Figure 5. Best ideal value (\bar{d}_i^+) and worst ideal value (\bar{d}_i^-) of each alternative.

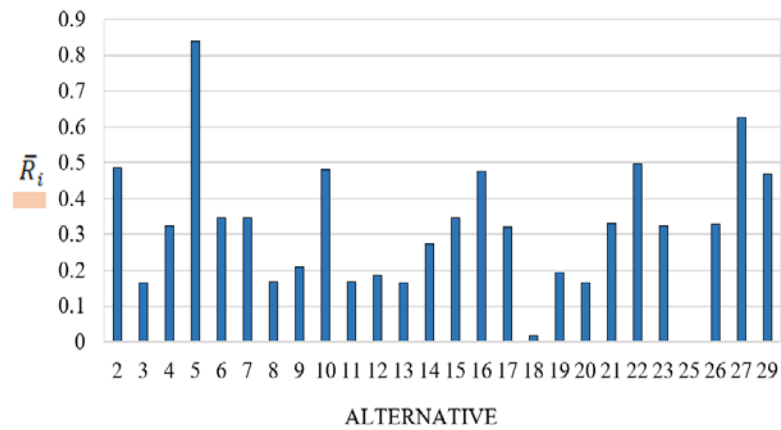


Figure 6. Graph of the relative proximity \bar{R}_i to the ideal solution.

Finally, the best alternatives are sorted according to \bar{R}_i in descending order.

Table 7. Hierarchical order of the alternatives evaluated.

Alternative	Weight	Ranking	Alternative	Weight	Ranking
A_5	0.8401	1	A_{23}	0.3241	14
A_{27}	0.6259	2	A_{17}	0.3213	15
A_{22}	0.4959	3	A_{14}	0.2729	16
A_2	0.4871	4	A_9	0.2104	17
A_{10}	0.4825	5	A_{19}	0.1943	18
A_{16}	0.4751	6	A_{12}	0.1869	19
A_{29}	0.4691	7	A_{11}	0.1683	20
A_{15}	0.346	8	A_8	0.1681	21
A_6	0.3453	9	A_3	0.1642	22
A_7	0.3453	10	A_{13}	0.1642	23
A_{21}	0.33	11	A_{20}	0.1642	24
A_{26}	0.3272	12	A_{18}	0.0167	25
A_4	0.3241	13	A_{25}	0	26

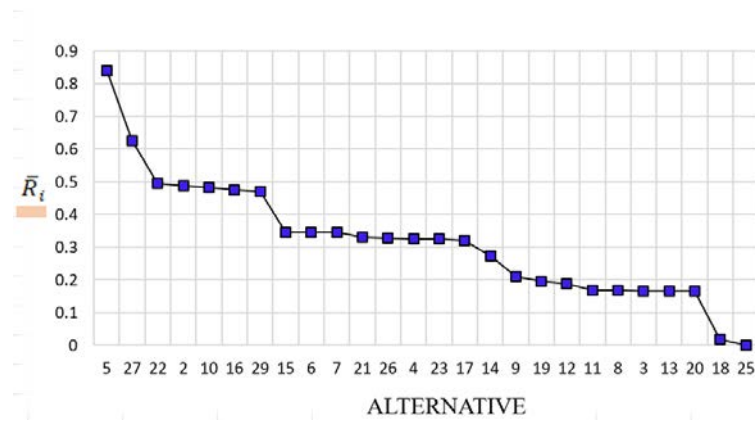


Figure 7. Hierarchical order of the alternatives evaluated.

As a result of using the proposed hybrid system, it was obtained that the best evaluated basin or its alternative turned out to be basin number 5, while the worst evaluated one was basin number 25. It is very important in all this type of research that the assessment of the expert(s) on each of the criteria and sub-criteria is correctly performed because a change or mistake in said assessment will change the results obtained. Taking into account the results of the conducted analysis and local surveys, the experts involved in the design of the dam confirmed the robustness of the research methodology and findings.

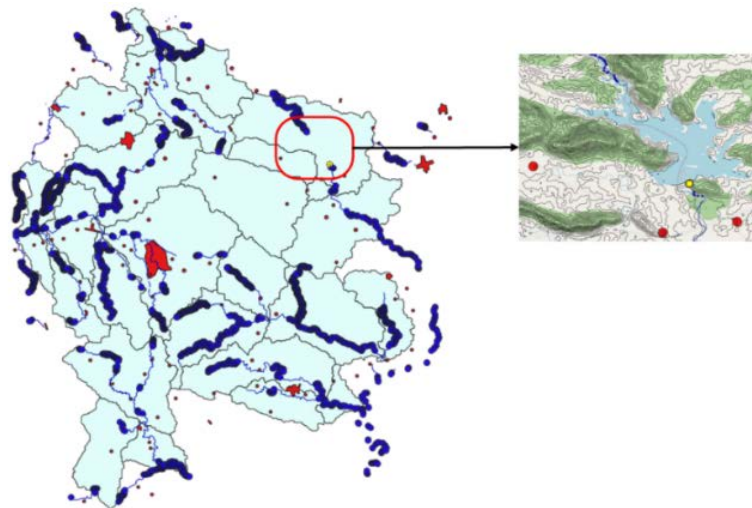


Figure 8. Analysis of one of the points determined by the model as a possible area for the location of dams.

4. Conclusion

This research presents the application of an AHP-TOPSIS hybrid method, integrating GIS, in the selection of dam sites in the Manicaragua municipality of the province of Villa Clara, Cuba. Based on the review of recent studies on dam site selection using MCDM, it can be commented that many researchers have mainly used AHP and TOPSIS in the application of dam site selection, but independently. Therefore, a method was implemented that worked with the advantages offered by each one in a study area in Cuba to evaluate its capacity for the selection of dam sites in a new local context. Based on previous experience and literature, several factors (criteria) were presented, including geology, land use, hydrology and topography. Once this hybrid method was implemented in the GIS environment, relatively suitable sites for dam construction were located in the area of interest. Finally, to verify the results obtained, the actual location of the dams built was used as a study area. The main conclusions of this study can be drawn as follows:

- The results show that the proposed hybrid method AHP-TOPSIS, as well as the modifications made for the adaptation of these methods to this type of problem is suitable for the selection of areas for the location of the dam with respect to the study area.
- A methodology has been proposed to take into account the blurred preferences of decision-makers when using the AHP-TOPSIS method based on the establishment of relationship intervals when assessing the importance of criteria and subcriteria. A quantitative indicator has been proposed that reflects the trend of decision makers in assessing criteria by translating utility (value) estimates

of criteria and sub-criteria into estimates of relative importance. This reduces the number of assessments by the decision maker by completing matrices of peer comparisons and ensures consistency.

- A procedure for comparing alternatives has been developed through the analysis of the subcriteria and subsequent construction of paired matrices eliminating the decision-maker as an evaluator object, something that is not contemplated within the standard methods.
- The use of MCDM provides an overview of the initial calculations to reduce expenses and arrive at a thorough study of the selection of the dam site; however, there is an evident need to collect accurate data to provide a correct assessment by the method implemented.
- To corroborate and verify the results obtained, an area in which there are dams built in advance was used as a study area.
- Correctly choosing the location of dams provides economic, social and ecological benefits. The economic benefits include a decrease in the costs allocated for direct studies on the areas, to the staff employed, as well as in services to other institutions or the purchase of support tools. The social benefits are evidenced by the improvement of the services provided by the dam being located in a hydrologically beneficial area. In addition, the construction of these dams in strategic areas allows the collection of water and the prevention of economic, social and environmental damage caused by floods. On the other hand, the ecosystem is benefited through the soil use criterion that is responsible for offering only areas of analysis that do not belong to the set of protected areas (cities, forests, industries, etc.) according to the laws of the country.

5. Recommendations for future research

1. Comparison of the results of the implementation of fuzzy TOSIS and fuzzy AHP with the results obtained in this investigation.
2. Collect more accurate reports on the selection of the dam site to improve and update the criteria and sub-criteria.
3. Consideration of more complete criteria can lead to more accurate results.

References

1. Noori, A., Bonakdari, H., Morovati, K., Gharabaghi, B. The optimal dam site selection using a group decision-making method through fuzzy TOPSIS model. *Environment Systems and Decisions*. 2018. 38 (4). Pp. 471–488. DOI: 10.1007/s10669-018-9673-x.
2. Beck, M.W., Claassen, A.H., Hundt, P.J. Environmental and livelihood impacts of dams: common lessons across development gradients that challenge sustainability. *International Journal of River Basin Management*. 2012. 10 (1). Pp. 73–92. DOI: 10.1080/15715124.2012.656133.
3. Fearnside, P.M. Environmental and Social Impacts of Hydroelectric Dams in Brazilian Amazonia: Implications for the Aluminum Industry. *World Development*. 2016. 77. Pp. 48–65. DOI: 10.1016/J.WORLDDEV.2015.08.015.
4. Shafieardekani, M., Hatami, M. Forecasting Land Use Change in suburb by using Time series and Spatial Approach; Evidence from Intermediate Cities of Iran. *European Journal of Scientific Research*. 2013. 116 (2). Pp. 199–208. URL: https://www.researchgate.net/publication/324215686_Forecasting_Land_Use_Change_in_suburb_by_using_Time_series_and_Spatial_Approach_Evidence_from_Intermediate_Cities_of_Iran
5. Mulatu, C., Crosato, A., Moges, M., Langendoen, E., McClain, M. Morphodynamic Trends of the Ribb River, Ethiopia, Prior to Dam Construction. *Geosciences*. 2018. 8 (7). Pp. 255. DOI: 10.3390/geosciences8070255.
6. Belton, V., Stewart, T.J. *Multiple Criteria Decision Analysis: An Integrated Approach*. Springer US, 2002.
7. Saaty, T.L. *The Analytic Hierarchy Process: Planning, Priority Setting, Resource Allocation*. McGraw-Hill International Book Co, 1980.
8. Hwang, C.-L., Yoon, K. *Methods for Multiple Attribute Decision Making. Methods and Applications A State-of-the-Art Survey*. Springer, Berlin, Heidelberg, 1981. Pp. 58–191.
9. Tsolaki-Fiaka, S., Bathrellos, G., Skilodimou, H. Multi-Criteria Decision Analysis for an Abandoned Quarry in the Evros Region (NE Greece). *Land*. 2018. 7 (2). Pp. 43. DOI: 10.3390/land7020043.
10. Rahman, M.A., Jaumann, L., Lerche, N., Renatus, F., Buchs, A.K., Gade, R., Geldermann, J., Sauter, M. Selection of the Best Inland Waterway Structure: A Multicriteria Decision Analysis Approach. *Water Resources Management*. 2015. 29 (8). Pp. 2733–2749. DOI: 10.1007/s11269-015-0967-1.
11. Afshari, A., Vatanparast, M., Cockalo, D. Application of multi criteria decision making to urban planning: A review. *Journal of Engineering Management and Competitiveness*. 2016. 6 (1). Pp. 46–53. DOI: 10.5937/jemc1601046A.
12. Mollalo, A., Alimohammadi, A., Shirzadi, M.R., Malek, M.R. Geographic information system-based analysis of the spatial and spatio-temporal distribution of zoonotic cutaneous leishmaniasis in Golestan Province, north-east of Iran. *Zoonoses and public health*. 2015. 62 (1). Pp. 18–28. DOI: 10.1111/zph.12109.
13. Mollalo, A., Sadeghian, A., Israel, G.D., Rashidi, P., Sofizadeh, A., Glass, G.E. Machine learning approaches in GIS-based ecological modeling of the sand fly *Phlebotomus papatasi*, a vector of zoonotic cutaneous leishmaniasis in Golestan province, Iran. *Acta tropica*. 2018. 188. Pp. 187–194. DOI: 10.1016/j.actatropica.2018.09.004.
14. Theilen-Willige, B., Aher, S., Gawali, P., Venkata, L. Seismic Hazard Analysis along Koyna Dam Area, Western Maharashtra, India: A Contribution of Remote Sensing and GIS. *Geosciences*. 2016. 6 (2). Pp. 20. DOI: 10.3390/geosciences6020020.

15. Nsanziyera, A., Rhinane, H., Oujaa, A., Mubea, K. GIS and Remote-Sensing Application in Archaeological Site Mapping in the Awsard Area (Morocco). *Geosciences*. 2018. 8 (6). Pp. 207. DOI: 10.3390/geosciences8060207.
16. Koohbanani, H., Barati, R., Yazdani, M., Sakhdari, S., Jomemanzari, R. Groundwater recharge by selection of suitable sites for underground dams using a GIS-based fuzzy approach in semi-arid regions. *Progress in River Engineering & Hydraulic Structures*. International Energy and Environment Foundation. Najaf, Iraq, 2018. Pp. 11–38.
17. Jamali, A.A., Randhir, T.O., Nosrati, J. Site Suitability Analysis for Subsurface Dams Using Boolean and Fuzzy Logic in Arid Watersheds. *Journal of Water Resources Planning and Management*. 2018. 144 (8). Pp. 04018047. DOI: 10.1061/(ASCE)-WR.1943-5452.0000947.
18. Dai, X. Dam Site Selection Using an Integrated Method of AHP and GIS for Decision Making Support in Bortala, Northwest China. Lund University, Lund, Sweden, 2016.
19. Tung, S.L., Tang, S.L. A comparison of the Saaty's AHP and modified AHP for right and left eigenvector inconsistency. *European Journal of Operational Research*. 1998. 106 (1). Pp. 123–128. DOI: 10.1016/S0377-2217(98)00353-1.
20. Atiq, M.Z., Arslan, M., Baig, Z., Ahmad, A., Tanveer, M.U., Akhtar, A., Naeem, K., Mahmood, S.A. Dam Site Identification Using Remote Sensing and GIS (A case study Diامر Basha Dam Site). *International Journal of Agriculture & Sustainable Development*. 2019. 1 (4). Pp. 168–178. DOI: 10.33411/ijst/2019010412.
21. Abdullah, T., Ali, S., Al-Ansari, N., Knutsson, S. Possibility of Groundwater Pollution in Halabja Saidadiq Hydrogeological Basin, Iraq Using Modified DRASTIC Model Based on AHP and Tritium Isotopes. *Geosciences*. 2018. 8 (7). Pp. 236. DOI: 10.3390/geosciences8070236.
22. Nikvar Hassani, A., Katibeh, H., Farhadian, H. Numerical analysis of steady-state groundwater inflow into Tabriz line 2 metro tunnel, northwestern Iran, with special consideration of model dimensions. *Bulletin of Engineering Geology and the Environment*. 2016. 75 (4). Pp. 1617–1627. DOI: 10.1007/s10064-015-0802-1.
23. Nikvar Hassani, A., Farhadian, H., Katibeh, H. A comparative study on evaluation of steady-state groundwater inflow into a circular shallow tunnel. *Tunnelling and Underground Space Technology*. 2018. 73. Pp. 15–25. DOI: 10.1016/J.TUST.20-17.11.019.
24. Sadoughi, A., Kibert, C., Sadeghi, F.M., Jafari, S. Thermal performance analysis of a traditional passive cooling system in Dezful, Iran. *Tunnelling and Underground Space Technology*. 2019. 83. Pp. 291–302. DOI: 10.1016/J.TUST.2018.09.024.
25. Piadeh, F., Alavi Moghaddam, M.R., Mardan, S. Present situation of wastewater treatment in the Iranian industrial estates: Recycle and reuse as a solution for achieving goals of eco-industrial parks. *Resources, Conservation and Recycling*. 2014. 92. Pp. 172–178. DOI: 10.1016/J.RESCONREC.2014.06.004.
26. Piadeh, F., Alavi-moghaddam, M.R., Mardan, S. Assessment of sustainability of a hybrid of advanced treatment technologies for recycling industrial wastewater in developing countries: Case study of Iranian industrial parks. *Journal of Cleaner Production*. 2018. 170. Pp. 1136–1150. DOI: 10.1016/J.JCLEPRO.2017.09.174.
27. Kim, Y., Chung, E.-S., Jun, S.-M., Kim, S.U. Prioritizing the best sites for treated wastewater instream use in an urban watershed using fuzzy TOPSIS. *Resources, Conservation and Recycling*. 2013. 73. Pp. 23–32. DOI: 10.1016/J.RESCON-REC.2012.12.009.
28. Şengül, Ü., Eren, M., Eslamian Shiraz, S., Gezder, V., Şengül, A.B. Fuzzy TOPSIS method for ranking renewable energy supply systems in Turkey. *Renewable Energy*. 2015. 75. Pp. 617–625. DOI: 10.1016/J.RENENE.2014.10.045.
29. Zyoude, S.H., Kaufmann, L.G., Shaheen, H., Samhan, S., Fuchs-Hanusch, D. A framework for water loss management in developing countries under fuzzy environment: Integration of Fuzzy AHP with Fuzzy TOPSIS. *Expert Systems with Applications*. 2016. 61. Pp. 86–105. DOI: 10.1016/J.ESWA.2016.05.016.
30. Lahijanian, B., Zarandi, M.H.F., Farahani, F.V. Proposing a model for operating room scheduling based on fuzzy surgical duration. 2016 Annual Conference of the North American Fuzzy Information Processing Society (NAFIPS). IEEE, 2016. Pp. 1–5.
31. Özcan, E.C., Ünlüsoy, S., Eren, T. A combined goal programming – AHP approach supported with TOPSIS for maintenance strategy selection in hydroelectric power plants. *Renewable and Sustainable Energy Reviews*. 2017. 78. Pp. 1410–1423. DOI: 10.1016/J.RSER.2017.04.039.
32. Önüt, S., Soner, S. Transshipment site selection using the AHP and TOPSIS approaches under fuzzy environment. *Waste Management*. 2008. 28 (9). Pp. 1552–1559. DOI: 10.1016/J.WASMAN.2007.05.019.
33. Mulliner, E., Malys, N., Maliene, V. Comparative analysis of MCDM methods for the assessment of sustainable housing affordability. *Omega*. 2016. 59. Pp. 146–156. DOI: 10.1016/J.OMEGA.2015.05.013.
34. Balioti, V., Tzimopoulos, C., Evangelides, C. Multi-Criteria Decision Making Using TOPSIS Method Under Fuzzy Environment. Application in Spillway Selection. *Proceedings*. 2018. 2 (11). Pp. 637. DOI: 10.3390/proceedings2110637.
35. Jozaghi, A., Alizadeh, B., Hatami, M., Flood, I., Khorrami, M., Khodaei, N., Ghasemi Tousi, E. A Comparative Study of the AHP and TOPSIS Techniques for Dam Site Selection Using GIS: A Case Study of Sistan and Baluchestan Province, Iran. *Geosciences*. 2018. 8 (12). Pp. 494. DOI: 10.3390/geosciences8120494.
36. Esavi, V., Karami, J., Alimohammadi, A., Niknezhad, S.A. Comparison the AHP and FUZZY-AHP Decision Making Methods in Underground DAM Site Selection in Taleghan Basin. *Journal of Geoscience*. 2012. 22 (85). Pp. 27–34. DOI: 10.22071/GSJ.2012.54018.
37. Yasser, M., Jahangir, K., Mohmmad, A. Earth dam site selection using the analytic hierarchy process (AHP): a case study in the west of Iran. *Arabian Journal of Geosciences*. 2013. 6 (9). Pp. 3417–3426. DOI: 10.1007/s12517-012-0602-x.
38. Tzimopoulos, C., Balioti, V., Evangelides, C. Fuzzy multi-criteria decision making method for dam selection. *Proceedings of the 13th International Conference on Environmental Science and Technology, Athens, Greece 2013*. Pp. 5–7.
39. Rezaei, P., Rezaie, K., Nazari-Shirkouhi, S., JamalzadehTajabadi, M.R. Application of Fuzzy Multi-Criteria Decision Making Analysis for evaluating and selecting the Best Location for Construction of Underground Dam. *Acta Polytechnica Hungarica*. 2013. 10 (7). Pp. 187–205. DOI: 10.12700/aph.10.07.2013.7.13
40. Barkhordari, J. The pre-selection of suitable sites for small underground dams in arid areas using GIS (A case study in Yazd_Ardakan watershed). *International Geoinformatics Research and Development Journal*. 2015. 6 (1). Pp. 18–27.
41. Minatour, Y., Khazaei, J., Ataei, M., Javadi, A.A. An integrated decision support system for dam site selection. *Scientia Iranica, Transactions A: Civil Engineering*. 2015. 22 (2). Pp. 319–330.
42. Choo, T.H., Ahn, S.H., Yang, D.U., Yun, G.S. A Study on the Estimating Dam Suitable Site based on Geographic Information using AHP. 6th International Conference on Developments in Engineering and Technology (ICDET-2017) 2017. Pp. 50–56.
43. Njiru, F.M., Siriba, D.N., Njiru, F.M., Siriba, D.N. Site Selection for an Earth Dam in Mbeere North, Embu County—Kenya. *Journal of Geoscience and Environment Protection*. 2018. 06 (07). Pp. 113–133. DOI: 10.4236/gep.2018.67009.

44. Aguarón, J., Moreno-Jiménez, J.M. The geometric consistency index: Approximated thresholds. *European Journal of Operational Research*. 2003. 147 (1). Pp. 137–145. DOI: 10.1016/S0377-2217(02)00255-2.
45. Tutygin, A.G., Korobov, V.B., Menshikova, T.V. Problems of consistency of expert judgments in the method of hierarchy analysis. *Bulletin of civil engineers*. 2019. 76 (5). Pp. 291–297. DOI: 10.23968/1999-5571-2019-16-5-291-297.
46. Djenadic, S., Jovančić, P., Ignjatović, D., Miletic, F., Jankovic, I. Analysis of the application of multi-criteria methods in optimizing the selection of hydraulic excavators on open-cast coal mining. *Tehnika*. 2019. 74 (3). Pp. 369–377. DOI: 10.5937/TEHNIKA1903369D.
47. Ibrahim, G.R.F., Rasul, A., Hamid, A.A., Ali, Z.F., Dewana, A.A. Suitable site selection for rainwater harvesting and storage case study using Dohuk governorate. *Water (Switzerland)*. 2019. 11 (4). DOI: 10.3390/w11040864
48. Xiao, Q., Shan, M., Xiao, X., Rao, C. Evaluation Model of Industrial Operation Quality Under Multi-source Heterogeneous Data Information. *International Journal of Fuzzy Systems*. 2020. 22 (2). Pp. 522–547. DOI: 10.1007/s40815-019-00776-x.
49. Konstantinos, I., Georgios, T., Garyfalos, A. A Decision Support System methodology for selecting wind farm installation locations using AHP and TOPSIS: Case study in Eastern Macedonia and Thrace region, Greece. *Energy Policy*. 2019. 132. Pp. 232–246. DOI: 10.1016/J.ENPOL.2019.05.020.
50. Katarzhina, H. Selecting a technology using the method TOPSIS. *Foresight and STI Governance*. 2020. 14 (1). Pp. 85–96. DOI: 10.17323/2500-2597.2020.1.85.96.
51. Kazazi Darani, S., Akbari Eslami, A., Jabbari, M., Asefi, H. Parking Lot Site Selection Using a Fuzzy AHP-TOPSIS Framework in Tuyserkhan, Iran. *Journal of Urban Planning and Development*. 2018. 144 (3). Pp. 04018022. DOI: 10.1061/(asce)up.1943-5444.0000456.
52. Moges, G., Bhole, V. Morphometric Characteristics and the Relation of Stream Orders to Hydraulic Parameters of River Goro: An Ephemeral River in Dire-dawa, Ethiopia. *Universal Journal of Geoscience*. 2015. 3(1). Pp. 13–27. DOI: 10.13189/ujg.2015.030102.
53. Shumie, M.C. River Slope and Roughness Impact on Downstream Hydraulic Structures. *Journal of Earth Science & Climatic Change*. 2018. 9 (11). Pp. 1–7. DOI: 10.4172/2157-7617.1000500.
54. Solodovnikov, A.B. Methods of estimating the time of concentration in small watersheds. Design of development of regional railway network: journal of science. 2018. (6). Pp. 32–57. URL: https://elibrary.ru/download/elibrary_36408133_12154366.pdf
55. Solodovnikov, A.B. Description of rational method of calculation of rain drain. Design of development of regional railway network: journal of science. 2014. (2). Pp. 93–101. URL: <https://www.elibrary.ru/item.asp?id=22706011>
56. Ponkina, E., Rossova, A., Herpsumer, K., Bondarovich, A., Schmidt, G., Illiger, P. Approaches to the assessment of potential evapotranspiration. *Proceedings of the seminar on Geometry and Mathematical Modeling*. 2019. (5). Pp. 125–133. URL: <http://journal.asu.ru/psgmm/article/view/7251>

Information about authors:

Solangel Rodriguez Vazquez,

ORCID: <https://orcid.org/0000-0001-6250-1108>

E-mail: solrusita85@gmail.com

Natalia V. Mokrova,

Doctor in Technical Science

ORCID: <https://orcid.org/0000-0002-8444-2935>

E-mail: natali_vm@mail.ru

Received 04.02.2021. Approved after reviewing 24.01.2022. Accepted 16.02.2022.



Research article

UDC 624.042

DOI: 10.34910/MCE.114.6



Forced vibrations of a box element of a multi-story building under dynamic impact

M.K. Usarov¹, G.I. Mamatisaev², G.T. Ayubov³

¹ Institute of Mechanics and Seismic Stability of Structures, Tashkent, Uzbekistan

² Fergana Polytechnic Institute, province Fergana, Ferpi, Uzbekistan

³ Institute of Seismic Stability of Structures AS RUz, Tashkent, Uzbekistan

✉ umakhamatali@mail.ru

Keywords: buildings, box- like structure, dynamic calculation, displacement, stress, deformation, equation of motion, boundary conditions, contact conditions.

Abstract. The article is devoted to the dynamic calculations of the elements of the box-shaped structure of buildings for seismic resistance, taking into account the spatial work of the elements of the box under the action of dynamic influences set by the movement of their lower part according to the sinusoidal law. The equations of motion are given for each of the plate and beam elements of the box-shaped structure of the building on the basis of the Kirchhoff-Love theory. Expressions are given for the forces, moments and stresses of the plate elements that equalize the movement of the box elements, and the boundary conditions, as well as the conditions for full contact in terms of displacements and force factors in the contact zones of plate and beam elements. The general solution of the problem is constructed by the method of decomposition of the movement of the elements of the box according to their own forms using the method of finite differences. The calculation results were obtained in the form of diagrams over the height of the box of bending moments, plate elements working in bending, as well as shear stresses of plate elements.

Citation: Usarov, M.K., Mamatisaev, G.I., Ayubov, G.T. Forced vibrations of a box element of a multi-story building under dynamic impact. Magazine of Civil Engineering. 2022. 114(6). Article No. 11406. DOI: 10.34910/MCE.114.6

1. Introduction.

The theory of beams, slabs and shells is widely used in the field of structural dynamics when calculating structural elements of buildings and structures. In [1-4], the spatial vibrations of a structure made of rod elements interacting with the surrounding soil under seismic influences are considered.

In [5], the problem of protecting a building or a group of buildings using a seismic barrier from seismic waves is considered. Various types of seismic barriers are available depending on the nature of the seismic waves.

In [6,7], the dynamic characteristics and vibrations of elements of various designs are considered, taking into account the dissipative properties of materials.

In calculations on earthquake resistance of underground and aboveground structures, an important role is played by consideration of physically nonlinear properties of the structure elements material and the soil base and the structure-soil interaction. Such studies include the works of the authors [8–10], who investigated the elastic-plastic behavior of structural materials under complex loading conditions, the studies in [11-14] devoted to the determination of elastic-plastic law of state of soils and soil structures.

In works [15-18], the problems of forced vibrations of boxes of a large-panel building and cells of frame buildings were solved, taking into account the interaction of their elements, and also a spatial box

with a pinched lower end is considered as a design scheme. On the basis of the finite difference method, the numerical results of the stress and displacement in the box elements are obtained.

In a scientific study [19], oriented particle board (OSB) is considered as an element of a pitched roof structure with a soft roof, under the action of a vertical load from snow. The reasons for uneven deflections in OSB joints in the structures of inclined roofs and vertical walls are revealed, and recommendations for eliminating these reasons are justified.

The article [20] considers the impact of earthquakes of various intensity and frequency character on the seismic resistance of a wooden building. A computational and theoretical assessment of the frame building was carried out on simple and complex models under the influence of different intensities and frequency composition. It has been established that the frequency composition of the seismic effect significantly affects the seismic resistance of frame buildings.

The article [21] proposes methods for solving dynamic problems of the dynamics of soils and earth structures, as well as underground structures interacting with the soil.

Using the method of initial functions (ISF), a multilayer basic model was developed and the spatial problem of the theory of elasticity of compression of an isotropic layer by a normal load uniformly distributed over a bounded region of the boundary was solved [22].

In [23], the influence of displacements, fractures of the axes of wall panels during their installation on the operation of a large-panel structure is considered. A comparative analysis of design schemes, taking into account different types of installation errors, has been carried out. In the process of calculating structures, taking into account the installation error of parts, efforts were obtained in the structural elements that exceeded the permissible values prescribed in the regulatory documentation.

In [24], a multi-storey reinforced concrete frame-braced frame with prestressed girders is considered, subject to emergency impact in the form of a sudden removal of a column of the outermost row on the first floor of the building. Using the finite element method, a nonlinear quasi-static analysis of deformation and failure was carried out under the structure in the form of a two-storey two-span frame, separated from the building frame by the decomposition method.

In [25], the analysis of the process of changing the initial geometric parameters of the elements of the design scheme in the erection mode with various methods of installation of structures is carried out. Proposals are presented for performing a computational analysis within a computational experiment for a situation of structural degradation associated with various reasons (wear, corrosion, micro- and macro-destruction under load, etc.).

The purpose and task of the study is the dynamic calculation of elements of a box-shaped structure of buildings for seismic resistance, taking into account the spatial work of the elements of a box under the action of dynamic influences set by the movement of their lower part. according to the sinusoidal law.

2. Methods

This article deals with the problem of forced vibrations of elements of a spatial box-shaped structure of buildings, consisting of rectangular plate and beam elements, as shown in Fig. 1. It is believed that the bottom of the box is firmly pressed against the base.

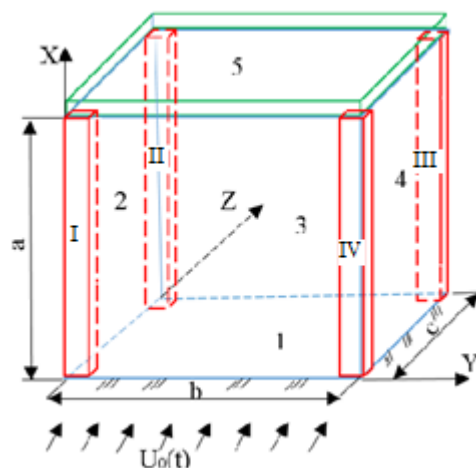


Figure 1. Building space box [15, 16].

The dynamic problem of oscillation of the building box is considered, the base of which oscillates according to the law:

$$U_0 = A_0 \sin \omega_0 t, \quad (1)$$

where A_0 and ω_0 are amplitude, and frequency of forced oscillations.

Assume that the load-bearing walls of the building (plate elements 1. and 3.) are located perpendicular to the direction of seismic action and work only for lateral dynamic bending. The deflection function of the plate elements are denoted by $W(x, y, t)$. Parallel plate elements 2. and 4. in the direction of the external impact are subjected only to shear in the OXZ plane. The functions for moving plate elements, working on shear, are denoted $u(x, z, t)$, $v(x, z, t)$.

The overlap (plate elements 5.) is also considered deformable. The law of motion of its points is determined in accordance with the deformation forms of the upper edges of the vertical contacting plate elements.

Let us introduce the following designations for the plate elements of the spatial box-shaped structure of the building: E_b , ρ_b , h_b and ν_b are the modulus of elasticity, density, width, thickness and Poisson's ratio of bent plate elements, E_c , ρ_c , h_c and ν_c are the modulus of elasticity, density, width, thickness and Poisson's ratio of panels working in shear. E_n , ρ_n , h_n and ν_n are modulus of elasticity, density, thickness and Poisson's ratio of the slab, G_n is slab shear modulus $G_n = \frac{E_n}{2(1+\nu_n)}$. Box height (dimensions of all plate elements and beams are the same) is a . The cross-sections of all the beam elements of the space box have a rectangular cross-section with the sizes h_b , h_c of the same material, with the same moduli of elasticity E and shear G , and Poisson's ratio ν and density ρ . J and I_{kr} are moments of inertia of the beam section during bending and torsion.

Plate elements of the frame are rigidly connected to the beam elements, therefore, the beam elements are subjected to bending and torsion. The deflection functions and torsion angles of the beams are denoted $W^{(i)}(x, t)$ and $\alpha^{(i)}(x, t)$, where: i : I, II, III, IV (number of beams).

Let us introduce the forces and moments arising in the elements of the box and their butt joints.

The expressions for the bending and torque moments of the bending panels M_{xx} , M_{yy} and M_{xy} will be introduced by the formulas:

$$\begin{aligned} M_{xx} &= -D \left(\frac{\partial^2 W}{\partial x^2} + \nu_b \frac{\partial^2 W}{\partial y^2} \right), \quad M_{yy} = -D \left(\nu_b \frac{\partial^2 W}{\partial x^2} + \frac{\partial^2 W}{\partial y^2} \right), \\ M_{xy} &= -D \frac{(1-\nu_b)}{2} \frac{\partial^2 W}{\partial x \partial y}, \end{aligned} \quad (2)$$

where: $D = \frac{E_b h_b^3}{12(1-\nu_b^2)}$ is cylindrical stiffness in transverse bending.

The expressions for the longitudinal and tangential forces of the plate elements working in shear can be represented as:

$$\begin{aligned} P_z &= B \left(\frac{\partial U}{\partial z} + \nu_c \frac{\partial V}{\partial x} \right), \quad P_x = B \left(\frac{\partial V}{\partial x} + \nu_c \frac{\partial U}{\partial z} \right), \\ P_{zx} &= B \frac{1-\nu_c}{2} \left(\frac{\partial V}{\partial z} + \frac{\partial U}{\partial x} \right), \end{aligned} \quad (3)$$

where $B = \frac{E_c h_c}{1-\nu_c^2}$ is the cylindrical stiffness of the panels in tension and compression.

Write the bending and torque moments of the beams in the form:

$$M^{(i)} = -EJ \frac{\partial^2 W^{(i)}}{\partial x^2}, \quad M_{kr}^{(i)} = EI_{kr} \frac{\partial \alpha^{(i)}}{\partial x}, \quad (4)$$

where EI_{kr} is the torsional stiffness of the beam, EJ is the bending stiffness of the beam.

Write the expressions for bending moment and the reactive shear forces, the bending plate elements and the longitudinal force of the panel in the zone of joint between plate and beam elements as follows:

$$\begin{aligned} M_{yy}^b &= (M_{yy})_{y=b} = -D \left[\nu_b \frac{\partial^2 W}{\partial x^2} + \frac{\partial^2 W}{\partial y^2} \right]_{y=b}, \\ R_y^b &= (R_y)_{y=b} = -D \frac{\partial}{\partial y} \left[\frac{\partial^2 W}{\partial y^2} + (2 - \nu_b) \frac{\partial^2 W}{\partial x^2} \right]_{y=b}, \\ R_x^a &= (R_x)_{x=a} = -D \frac{\partial}{\partial x} \left[\frac{\partial^2 W}{\partial x^2} + (2 - \nu_b) \frac{\partial^2 W}{\partial y^2} \right]_{x=a}, \\ P_z^c &= (P_z)_{z=0} = B \left(\frac{\partial U}{\partial z} + \nu_c \frac{\partial V}{\partial x} \right)_{z=0}. \end{aligned} \quad (5)$$

An analytical-numerical method is proposed for solving the problem of oscillation of the building box, taking into account spatial deformations with full contact conditions in the zones of butt joints of plate and beam elements of the building box.

Based on representation (1), we will rewrite the kinematic laws of movement of the points of the plate elements. The general kinematic law of movement of the box is presented as the sum of the function of displacement of the base $U_0(t)$ and the relative displacements of the plate elements:

$$\begin{aligned} u_3 &= U_0(t) + W(x, y, t), \\ u_1 &= U_0(t) + u(x, y, t), u_2 = v(x, z, t), \\ u_3^i &= U_0(t) + W^{(i)}(x, t). \end{aligned} \quad (6)$$

Write down the displacements of plate and beam elements as follows:

$$\begin{aligned} W &= W(x, y) \sin(\omega_0 t), \\ u &= u(x, z) \sin(\omega_0 t), v = v(x, z) \sin(\omega_0 t), \\ W^{(i)} &= W^{(i)}(x, y) \sin(\omega_0 t), \alpha^{(i)} = \alpha^{(i)}(x, y) \sin(\omega_0 t). \end{aligned} \quad (7)$$

Consider the theoretical calculation of the box of a large-panel building under dynamic action, taking into account the spatial work of transverse and longitudinal walls.

As the equation of motion of the bending panel, Based on the findings/relations/formulations in [7, 8], and taking into account of (1), the equation of motion of the bending panel can be written in the form:

$$D \left(\frac{\partial^4 W}{\partial x^4} + 2 \frac{\partial^4 W}{\partial x^2 \partial y^2} + \frac{\partial^4 W}{\partial y^4} \right) + \rho h_b \ddot{W} = \rho h_b A_0 \omega_0^2 \sin \omega_0 t. \quad (8)$$

Two dimensional equations can be written as shown in [7,8]:

$$\begin{aligned} B \left(\frac{\partial^2 u}{\partial z^2} + \frac{1 + \nu_c}{2} \frac{\partial^2 v}{\partial x \partial z} + \frac{1 - \nu_c}{2} \frac{\partial^2 u}{\partial x^2} \right) &= \rho h_c \ddot{u} - \rho h_c A_0 \omega_0^2 \sin \omega_0 t, \\ B \left(\frac{\partial^2 v}{\partial x^2} + \frac{1 + \nu_c}{2} \frac{\partial^2 u}{\partial x \partial z} + \frac{1 - \nu_c}{2} \frac{\partial^2 v}{\partial z^2} \right) &= \rho h_c \ddot{v}. \end{aligned} \quad (9)$$

The equation of bending and torsional vibrations of beams will be written as:

$$\frac{\partial^2}{\partial x^2} \left(EJ \frac{\partial^2 W^{(i)}}{\partial x^2} \right) + \rho F \ddot{W}^{(i)} = R_y^b - P_z^c - \frac{h_b}{2} \frac{\partial P_{zx}^c}{\partial x} - \rho F \ddot{U}_0, \quad (10)$$

$$\frac{\partial}{\partial x} \left(GI_{kr} \frac{\partial \alpha^{(i)}}{\partial x} \right) = \rho I_{kr} \ddot{\alpha}^{(i)} + M_{yy}^b + \frac{h_c}{2} R_y^b,$$

where GI_{kr} is the torsional stiffness of the beam.

Write the boundary conditions at the base of the building box ($x=0$) as for rigid clamping. The lower part of the building moves with the base and there is no turn

$$u_1 = u_3 = u_3^{(i)} = U_0(t), u_2 = 0, \frac{\partial W}{\partial x} = 0, \frac{\partial W^{(i)}}{\partial x} = 0, \alpha^{(i)} = 0. \quad (11)$$

Boundary conditions (11) with allowance for (6) will be rewritten as:

$$W = 0, \frac{\partial W}{\partial x} = 0, u = 0, v = 0, W^{(i)} = 0, \frac{\partial W^{(i)}}{\partial x} = 0, \alpha^{(i)} = 0. \quad (12)$$

The boundary conditions at the upper ends of the building box elements at $x=a$ are the following contact conditions between these elements and the floor.

Contact conditions in the zones of butt joints (at) beam and plate elements working in shear will be written in the form:

$$u(x, z, t) = W^{(i)}(x, t), v(x, z, t) = \pm \frac{h_b}{2} \frac{\partial W^{(i)}(x, t)}{\partial x}, \quad (13)$$

$$W(x, y, t) = W^{(i)}(x, t), \left(\frac{\partial W(x, y, t)}{\partial y} \right) = -\alpha^{(i)},$$

The displacements of the top points of beam and plate elements operating bending and shear are denoted by:

$$W_a(y, t) = W(a, y, t), u_a(y, t) = u(a, z, t), v_a(z, t) = v(a, z, t). \quad (14)$$

Based on the notation (13), the distribution law of the displacement of overlap points will be given by:

$$u_n(z, y, t) = W_a(y, t) + u_a(z, t) - W^{(i)}(a, t) \quad (15)$$

$$v_n(z, y, t) = v_a(z, t).$$

The contact conditions at the joints of the floor and the wall working in bending have the form:

$$-R_x^a + \eta_0 \rho_n h_b h_n \left(\ddot{W}_a + W^{(i)}(a, t) \right) = h_b h_n \frac{\partial \tau_{zy}^n}{\partial y} - \eta_0 \rho_n h_b h_n \ddot{U}_0, \quad (16)$$

$$M_{xx} = 0,$$

where $\tau_{zy}^n = G_n \left(\frac{\partial W_a}{\partial y} \right)$ is the tangential stress of the floor at its edge $z = a$, $\eta_0 = \frac{2(bh_b + ch_c)}{bc}$.

The contact conditions at the joints of the floor and the wall working in shear, with respect to the contact tangential and normal stresses, will be written in the form:

$$\begin{aligned}
 -ch_c \tau_{zx}^c + \eta_0 m_{mc} \ddot{u}_a &= ch_c h_n \frac{\partial \sigma_{zz}^n}{\partial z} - \eta_0 m_{nc} \ddot{U}_0, \\
 -ch_c \sigma_{xx}^c + \eta_0 m_{nc} \ddot{u}_a &= ch_c h_n \frac{\partial \sigma_{xz}^n}{\partial z}
 \end{aligned} \quad (17)$$

where $\sigma_{zz}^n = E_n \left[\frac{\partial u_a}{\partial z} \right]$, $\sigma_{zx}^n = G_n \left[\frac{\partial v_a}{\partial z} \right]$ are normal and shear stresses of the floor at its edge $y = b$,
 $\sigma_{xx}^c = E_c \left[\frac{\partial v}{\partial x} + \nu_c \frac{\partial u}{\partial z} \right]_{x=a}$, $\tau_{zx}^c = G_c \left[\frac{\partial v}{\partial z} + \frac{\partial u}{\partial x} \right]_{x=a}$ are normal and shear stresses of the shear plate elements at its upper edge $x = a$.

Set the boundary conditions on the contour of the window opening as for the free edge (Figure. 2):

$$M_{xx} = 0, R_x = 0, \text{ at } x = \text{const}, \text{ (on the AB and CD circuit)}, \quad (18)$$

$$M_{yy} = 0, R_y = 0, \text{ at } y = \text{const}, \text{ (on the AC and BD circuit)}. \quad (19)$$

At each interior corner points of the opening A, B, C, D, we have five boundary conditions:

$$M_{xx} = 0, R_x = 0, M_{yy} = 0, R_y = 0, M_{xy} = 0, \text{ at } x = \text{const}, y = \text{const} \quad (20)$$

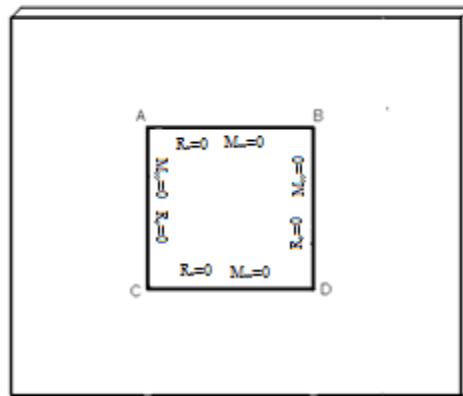


Figure. 2. Bending plate element with cut out.

The initial conditions of the problem are taken to be zero.

The vibration modes (7) must satisfy the equations of motion (8–10), boundary conditions (12), contact conditions (13) and (16–20).

The general solution to the problem of forced vibrations of the bending box plate element is described by a function represented as the sum of the solution to the problem of forced and natural vibrations:

$$W(x, y, t) = A_0 W_v(x, y) \sin \omega_0 t + \sum_{i=1}^N C_i W_i(x, y) \sin p_i t, \quad (21)$$

The solution to the problem of forced vibrations of bending plate elements are expressed through the main vibration modes:

$$W_v(x, y) = \sum_{i=1}^N A_i W_i(x, y), \quad (22)$$

where $A_i (i = 1.2.3...)$ expansion coefficients.

In the calculations, it was enough to restrict ourselves to the one-term approximation. The general solution to the equation of bending vibrations of the panels is:

$$W(x, y, t) = A_0 W_v(x, y) \sin \omega_0 t + C_1 W_1(x, y) \sin p_1 t, \quad (23)$$

Let express the solution to the problem of forced vibrations in terms of the main vibration mode:

$$W_v(x, y) = A_1 W_1(x, y), \quad (24)$$

where p_1 is the first natural frequency, $W_v(x, y)$ is the form of forced oscillations, C_1 is constant to be determined.

A_1 is the decomposition coefficient, the value of which is obtained by the formula.

$$A_1 = \frac{\iint f_0(x, y) f_1(x, y) dx dy}{\iint f_1^2(x, y) dx dy} = 0.1739.$$

Here $f_0(x, y)$ and $f_1(x, y)$ are the forced and main natural modes of oscillations.

Substituting (24) into (23) and subjecting to zero initial conditions, we obtain $C_1 = -A_0 A_1 \frac{\omega_0}{p_1}$.

By virtue of this expression and taking into account (24), we obtain a general solution to the problem for a bending plate element in the form [15-16]:

Solution method. The general solution given by previous studies [17, 18] is:

$$W(x, y, t) = A_0 \left(\sin \omega_0 t - \frac{\omega_0}{p_1} \sin p_1 t \right) W_v(x, y). \quad (25)$$

The expressions for moving the shear plate elements are:

$$\begin{aligned} u(x, z, t) &= A_0 \left(\sin \omega_0 t - \frac{\omega_0}{p_1} \sin p_1 t \right) u_v(x, z), \\ v(x, z, t) &= \left(\sin \omega_0 t - \frac{\omega_0}{p_1} \sin p_1 t \right) v_v(x, z). \end{aligned} \quad (26)$$

The kinematic functions of the beams are written as:

$$\begin{aligned} W^{(i)}(x, t) &= A_0 \left(\sin \omega_0 t - A_1 \frac{\omega_0}{p_1} \sin p_1 t \right) W_v^{(i)}(x), \\ \alpha^{(i)}(x, t) &= A_0 \left(\sin \omega_0 t - A_1 \frac{\omega_0}{p_1} \sin p_1 t \right) \alpha_v^{(i)}(x). \end{aligned} \quad (27)$$

The problem of determining the unknown coordinate functions in expressions (25–27) was solved using the “fortran” software by the finite difference method.

Represent the frequency of forced oscillations in the form:

$$\omega_0 = \frac{\beta}{H^2} \sqrt{\frac{D}{\rho h_b}},$$

where β is the frequency parameter of the external influence.

In the problems being solved, with the values of the frequency parameter of the external influence $\beta = 2.0$ then the frequency and amplitude of external influence were obtained as $\omega_0 = 81.03 \text{sec}^{-1}$ and $A_0 = 2.0 \text{cm}$.

3. Results and Discussion

The following parameters are set as the initial data [7–9]. The ratio of the height to the width of the bending plate elements $H/b = 3.25/6.0$, the ratio of the height to the width of the shear plate elements $H/c = 3.25/6.0$. The ratio of the thickness to the width of the bending plate element $h_b/b = 0.5/6.0$

, and the ratio of the thickness of the bending plate element to the thickness of the shear plate element $h_c / h_b = 0.25 / 0.5$.

Moduli of elasticity of flexible and shear plate elements $E_c = 7500\text{Mpa}$ and $E_b = 20000\text{Mpa}$. Poisson's ratio of plate element materials is $\nu_b = \nu_c = \nu_n = 0.3$.

Figure 3 shows a graph of the change in the bending moment M_{yy} on the upper and lower parts of bending plate elements, from the middle of the plate element to one of its edges. As you can see, the moments of the panels increase as they approach the edge of the plate element (at $A_0 = 2.0\text{cm}$).

In the figures, the blue lines represent the values obtained when solving stationary problems. The red lines show the numerical results obtained taking into account the window openings.

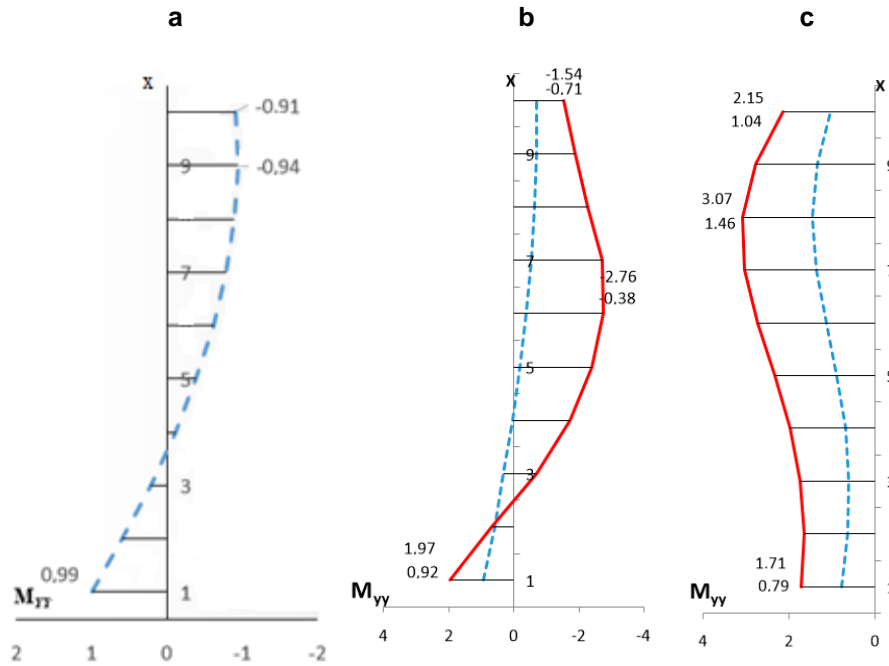


Figure. 3. Changes in the bending moment M_{yy} of bending plate element.
a) edge opening b) middle c) panel edges.

Calculations show that the bending moment M_{yy} values in the middle of the plate elements are less than at the edges of the plate element. The maximum value of the bending moment M_{yy} is found in the middle of the second half of the contact zone of the bending plate and beam elements. Note that at the contact zones of the plate element, the bending moment M_{yy} twists the beams and plays the role of the torque.

In Fig. 4 the graphs of the vertical change of the dimensionless maximum bending moment of the plate element working in bending are shown.

The maximum values of the bending moment (Fig. 4.a) are achieved at the lowest points of the bending plate elements.

In Fig. 4 it can be seen that the bending moment of the vertical edge of the bending plate element is several times greater than the moment of the middle part, since the edges of the plate elements are held by transverse plate elements that work in shear.

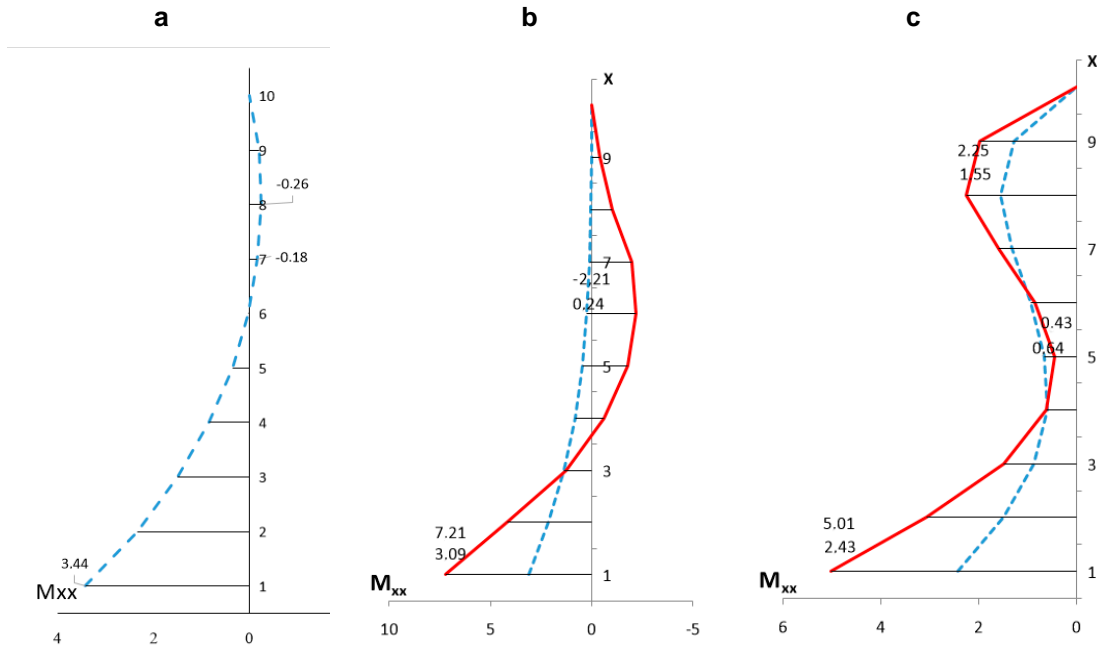


Figure 4. Changes in the bending moment along the height of the plate element operating in bending) of the edge of the opening b) the middle c) the edge of the plate element.

In Fig. 5 graphs are presented that characterize the changes in the maximum normal stress in the lower vertical sections of plate elements and in the zones of butt joints of plate and beam elements. Consequently, in plate element working in bending, the middle of the plate element is compressed and the edges of the plate elements are stretched.

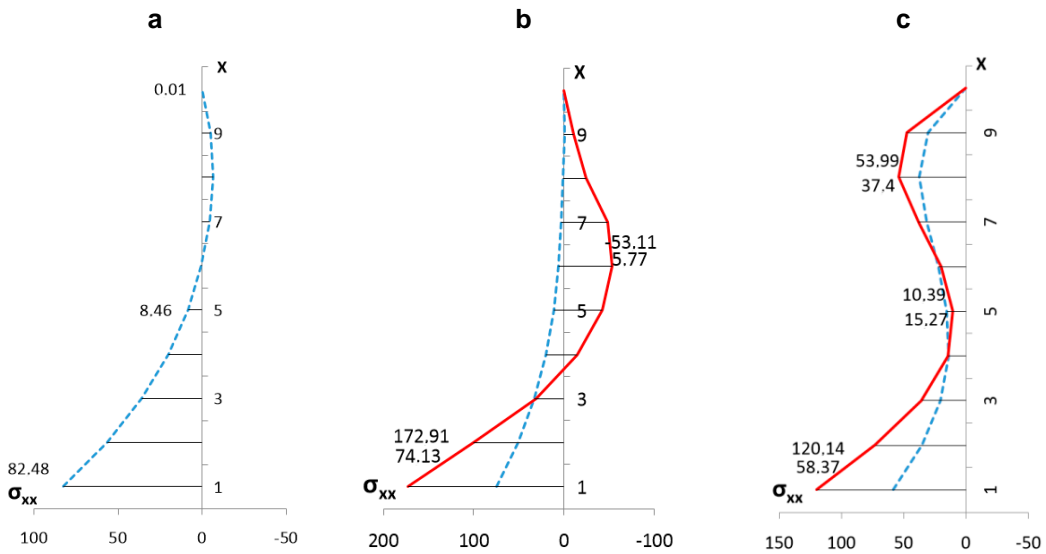


Figure 5. Changes in the stresses of bending plate elements: a) the edge of the window opening; b) middle; c) plate element edge.

Figure 6 shows the diagrams of the maximum compressive and tensile stresses of bending panels. The maximum stress values are found at the top of the bending panel. In the contact zones of the panel, the stresses are tensile.

The maximum value of the normal stress in plate elements operating in bending without taking into account the window opening is obtained equal to: $-\sigma_{yy} = -7.37\text{MPa}$.

The method for calculating the box-shaped structure of a building proposed in the article makes it possible to estimate the maximum stresses in the internal transverse and external longitudinal bearing panels, as well as in the butt joints of these elements. This means that our proposed method for calculating

the box-like structure complements the calculation method developed within the framework of the continuous plate model [17, 18].

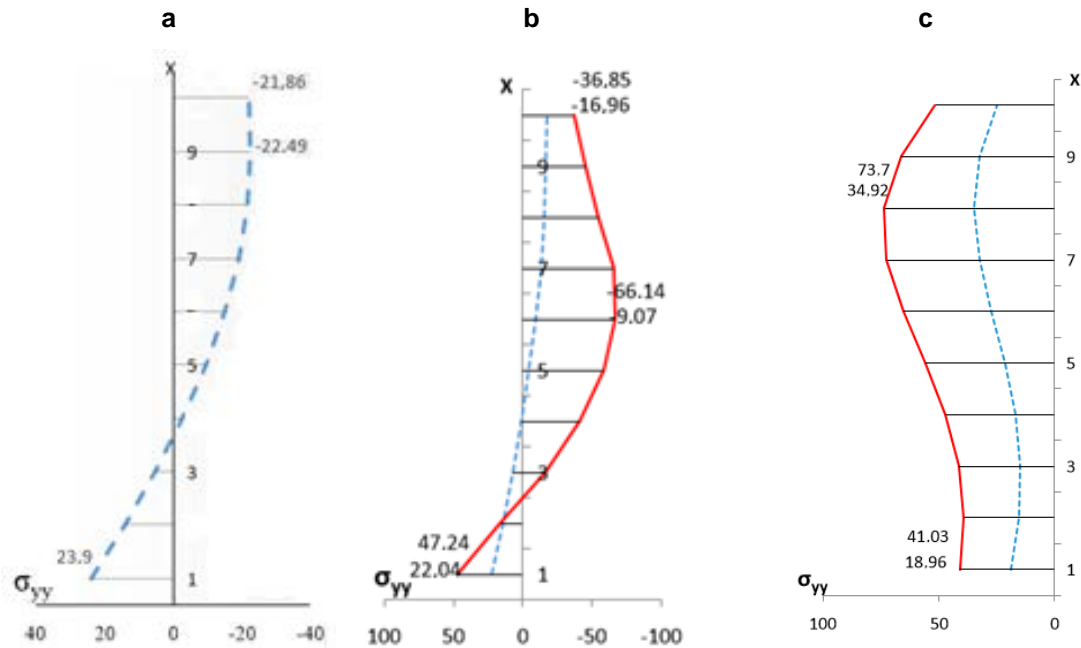


Figure 6. Changes in the stress of panels working in bending in height: a) the edge of the window opening; b) middle; c) panel edge.

4. Conclusions

1. The method of dynamic calculation of the box-shaped structure of buildings under dynamic influences has been developed. Equations of motion of points of plate and beam elements, boundary and contact conditions of the box of buildings of the problem of forced vibrations are constructed.

2. Within the framework of the finite-difference method, a method for dynamic calculation of the bending moments of plate elements of box-shaped structures of buildings has been developed.

3. The laws of change in the maximum values of moments and stresses in the characteristic sections of plate elements with and without window openings are graphically presented.

4. From the graphs it can be seen that the maximum values of the normal stress when taking into account the window openings are obtained by 25–30% more than the values of the normal stress obtained when solving the problem without taking into account the window openings.

References

1. Nishonov, N., Bekmirzaev, D., An, E., Urazmukhamedova, Z., Turajonov, K. Behaviour and Calculation of Polymer Pipelines under Real Earthquake Records. IOP Conference Series: Materials Science and Engineering. 2020. DOI: 10.1088/1757-899X/869/5/052076.
2. Rashidov, T.R., Bekmirzaev, D.A. Seismodynamics of Pipelines Interacting with the Soil. Soil Mechanics and Foundation Engineering. 2015. 52(3). Pp. 149–154. DOI: 10.1007/s11204-015-9321-0.
3. Khojmetov, G., Mirzaev, I., Yuvmitov, A., Mirzahmedov, M. On influence of linear and nonlinear models of foundation-base interaction on vibrations of multi-storey buildings at seismic impacts. AIP Conference Proceedings. 2022. 2432. 030071. DOI: 10.1063/5.0089506
4. Mirzaev, I., Yuvmitov, A., Turdiev, M., Shomurodov, J. Influence of the Vertical Earthquake Component on the Shear Vibration of Buildings on Sliding Foundations. E3S Web of Conferences. EDP Sciences. 2021. Vol. 264. Pp. 02022.
5. Bratov, V., Ilyashenko, A., Morozov, N., Rashidov, T. Seismic barriers: Theory and numerical simulations. E3S Web of Conferences. 2019. 97. 03005. DOI: 10.1051/e3sconf/20199703005
6. Mirsaidov, M.M., Toshmatov, E.S. Spatial stress state and dynamic characteristics of earth dams. Magazine of Civil Engineering. 2019. 89(5). Pp. 3–15. DOI: 10.18720/MCE.89.1.
7. Mirsaidov, M.M., Khudainazarov, Sh.O. Spatial natural vibrations of viscoelastic axisymmetric structures. Magazine of Civil Engineering. 2020. 96(4). Pp. 118–128. DOI: 10.18720/MCE.96.10
8. Babamuratov, K.S., Abirov, R.A. On physical reliability in the theory of plasticity. Strength of Materials. 2001. DOI:10.1023/A:1010478208161.
9. Abirov, R.A. On the physical reliability and taking complex loading into account in plasticity. Materials Science. 2008. 44(4). Pp. 512–516. DOI:10.1007/s11003-009-9114-6.
10. Abirov, R.A. Allowance for complex loading in transversely isotropic solids. Journal of Applied Mechanics and Technical Physics. 2009. 50(1). Pp. 107–111. DOI:10.1007/s10808-009-0015-0.

11. Khusanov, B., Rikhsieva, B. Thickness dimensions of the contact layer of soil-rigid body interaction. E3S Web of Conferences. 2019. DOI:10.1051/e3sconf/20199704040.
12. Khusanov, B., Khaydarova, O. Stress-strain state of earth dam under harmonic effect. E3S Web of Conferences. 2019. DOI:10.1051/e3sconf/20199705043.
13. Sultanov, K., Khusanov, B., Rikhsieva, B. Elastic wave propagation in a cylinder with external active friction. Journal of Physics: Conference Series. 2021. 1901. 012125. 10.1088/1742-6596/1901/1/012125.
14. Rashidov, T.R., Nishonov, N.A. Seismic Behavior of Underground Polymer Piping with Variable Interaction Coefficients. Soil Mechanics and Foundation Engineering. 2016. 53. Pp. 196–201. DOI: 10.1007/s11204-016-9385-5.
15. Usarov, M., Mamatisaev, G. Calculation on seismic resistance of box-shaped structures of large-panel buildings IOP Conf. Series: Materials Science and Engineering. 2020. 971. 032041. DOI: 10.1088/1757-899X/971/3/032041
16. Usarov, M., Usarov, D., Mamatisaev, G. Calculation of a Spatial Model of a Box-Type Structure in the LIRA Design System Using the Finite Difference Method. Lecture Notes in Networks and Systems. 2022. Vol. 403. Springer, Cham. DOI: 10.1007/978-3-030-96383-5_141
17. Mirsaidov, M., Usarov, M., Mamatisaev, G. Calculation methods for plate and beam elements of box-type structure of building oscillations based on a plate model. E3S Web of Conferences. 2021. 264. 03030. DOI: 10.1051/e3sconf/202126403030
18. Usarov, M., Ayubov, G., Usarov, D., Mamatisaev, G. Spatial Vibrations of High-Rise Buildings Using a Plate Model. In: Vatin, N., Roshchina, S., Serdjuks, D. (eds) Proceedings of MPCPE 2021. Lecture Notes in Civil Engineering. 2022. Vol 182. Springer, Cham. DOI: 10.1007/978-3-030-85236-8_37
19. Gavrilov, T.A., Kolesnikov, G.N. Oriented particle boards: effect of the tangential load component. Magazine of Civil Engineering. 2017. No. 74(6). Pp. 33–42. DOI: 10.18720/MCE.74.3.
20. Belash, T.A., Ivanova, Zh.V. Timber frame buildings with efficient junction designs for earthquake-prone areas. Magazine of Civil Engineering. 2019. 92(8). Pp. 84–95. DOI: 10.18720/MCE.92.7
21. Bekmirzaev, D.A., Kishanov, R.U. Assessment of the Effect of Inertia Forces in Problems of Underground Pipeline Seismodynamics. International Journal of Innovative Technology and Exploring Engineering. 2020. 9(3). Pp. 500–503. DOI: 10.35940/ijtee.C8526.019320.
22. Shirunov, G.N. Method of initial functions in model of compression linearly deformable layered foundation under normal local load. Magazine of Civil Engineering. 2015. 53(1). Pp. 91–96. DOI: 10.5862/MCE.53.9.
23. Vatin, N.I., Kuznetsov, V.D., Nedviga, E.S. Installation errors in calculating large-panel buildings. Magazine of Civil Engineering. 2011. 24(6). Pp. 35–40. DOI: 10.5862/MCE.24.3.
24. Kolchunov, V.I., Fedorova, N.V., Savin, S.Yu., Kovalev, V.V., Iliushchenko, T.A. Failure simulation of a RC multi-storey building frame with prestressed girders. Magazine of Civil Engineering. 2019. 92(8). Pp. 155–162. DOI: 10.18720/MCE.92.13
- Kabantsev, O.V., Tamrazian, A.G. Allowing for changes in the calculated scheme during the analysis of structural behaviour. Magazine of Civil Engineering. 2014. 49(5). Pp. 15–26. DOI:10.5862/MCE.49.2.

Information about authors

Makhamatali Usarov,

Doctor of Physical and Mathematical sciences

E-mail: umakhamatali@mail.ru

Giyosiddin Mamatisaev

E-mail: gmamatisaev@gmail.com

Gayratjon Ayubov

E-mail: ayubov.1984@mail.ru

Received 29.09.2020. Approved after reviewing 28.09.2021. Accepted 29.09.2021.



Research article

UDC 624.01

DOI: 10.34910/MCE.114.7



Bond testing of salty-sand concrete reinforced with different rebars

R. Bostel¹ , A.C.P. dos Santos¹ , J.B.O. Lopes² , F.L. Willrich² , R.L.O. Basso¹ , M.G. Honnicke¹ 

¹ Universidade Federal da Integração Latino-Americana, Foz do Iguaçu, Brazil

² Itaipu Binacional, Foz do Iguaçu, Brazil

✉ marcelo.honnicke@unila.edu.br

Keywords: concrete structures, chloride-induced corrosion, bond stress, FRP, pull-out resistance

Abstract. In this work, reinforced concrete (RC) test specimens, cast with different rebars (CA-50 Steel, Basalt Fiber Reinforced Polymer – BFRP and Glass Fiber Reinforced Polymer – GFRP) and different concrete mixtures (salty-sand and unsalty sand), were submitted to the pull-out tests in order to follow the bonding behavior between the concrete and the rebar. The use of salty-sand in concrete mixtures for building construction has grown, especially in places where regular sand is scarce. However, the salinity attacks the steel rebar in RC structures, resulting in corrosion problems, which can be strongly reduced by using composite material rebars which shows, similar or superior, mechanical strength, when compared to steel rebars. Conformance testing, including X-ray powder diffraction (XPD), scanning electronic microscopy (SEM) and tensile tests, were performed on the rebars, with the aim to check the conformity of the physical, chemical and mechanical properties. Standard cylindrical test specimens (diameter of 100 mm and a height of 200 mm) and RC test specimens were prepared for compression and pull-out tests performed at 63, 217 and 315 days, after casting. The results showed a bonding loss for the RC test samples molded with CA-50 steel rebar and salty-sand concrete. On the other hand, bonding loss was not detected for test samples molded with BFRP and GFRP rebars. In conclusion, the BFRP and GFRP rebars showed to be the proper ones to be used for salty-sand concrete mixtures, however, even having higher traction resistance, their use in the RC structures will demand higher anchor lengths.

Funding: This work was supported by Fluxo Continuo/Fundacao Araucaria (302/2013) and CNPq/UNIVERSAL (479404/2013-5).

Acknowledge: The authors acknowledge the management support of both UNILA and Itaipu Binacional for the co-operation agreement. The authors grateful acknowledge Composite Chelyabinsk Group LLC for providing the BFRP and GFRP rebars.

Citation: Bostel, R., dos Santos, A.C.P., Lopes, J.B.O., Willrich, F.L., Basso, R.L.O., Honnicke, M.G. Bond testing of salty-sand concrete reinforced with different rebars. Magazine of Civil Engineering. 2022. 114(6). Article No. 11407. DOI: 10.34910/MCE.114.7

1. Introduction

Long term bond testing was carried out on reinforced concrete (RC – concrete + rebar) test specimens cast with salty-sand and unsalty-sand concrete mixtures reinforced with steel and Fiber Reinforced Polymer (FRP) rebars.

RC strengths depend on the specific deformations of the rebar (steel or composite materials) and of the concrete as well as the bonding between them [1–2]. In general, the adhesion between the rebar and

concrete can be described by a chemical and a physical contribution. The last one is provided by the frictional forces arising from the roughness of the interface between the rebar and the surrounding concrete and, also, by the mechanical interlocking of the rebar surface textures [3].

The use of marine sands (salty-sand) in construction have been evaluated in different countries [4–7]. The salinity in marine sands (basically composed of sodium chloride – NaCl) attacks the steel rebars, causing corrosion problems [8] which affects the mechanical properties (and, consequently, the durability) of the RC structure. The salty-sand concrete mixtures present higher strengths at early ages compared to specimens using unsalty-sand concrete mixtures [7, 9–10]. The bonding strength decreases as the corrosion level increases [11–14]. However, for corrosion levels lower than ~ 4 %, the adhesion resistance increases proportionally to the corrosion level, which can be attributed to the deposition of oxides in the region around the rebar that increases the superficial friction [11–14]. One of the ways to evaluate the bonding between concrete and rebar, in RC, is through the pull-out tests [15] carried out on standard laboratory sample models (RC test specimens). The methodology of the pull-out test considers a tensile force applied to the rebar to pull it out of the RC concrete specimen. The pulling force permits to infer the bonding strength between concrete and rebar [16].

Fiber Reinforced Polymer (FRP) rebars [17–27] are an alternative to steel rebars in RC. They have some advantages over steel such as higher corrosion resistance, lower electrical conductivity, higher tensile strength per unit of mass and lower specific gravity [20–23].

In this work, salted and unsalted RCs cast with three different materials rebars (steel; basalt fiber rebar and; fiberglass) were comparatively investigated. The pull-out tests were performed at 63, 217 and 315 days after casting. Compressive strength tests were performed, at the same ages, in standard cylindrical salted and unsalted test specimens. The introduction of kitchen salt (sodium chloride – NaCl) into the concrete mixture had the aim to simulate the use of marine sands (salty-sand). Conformance testing, including, X-ray powder diffraction (XPD), scanning electronic microscopy (SEM) analysis (image and spectroscopy) and tensile tests, were also performed on the rebars, with the aim to check the conformity of the physical, chemical and mechanical properties of these materials.

2. Methods

2.1. Rebars conformance testing

In the process of casting the RC test specimens, rebars with three different materials were employed: i) CA-50 steel rebar; (ii) Basalt Fiber Reinforced Polymer (BFRP) rebar and; (iii) Glass Fiber Reinforced Polymer (GFRP) rebar. The physical and mechanical properties of the CA-50 steel rebars are described by the Brazilian standard ABNT NBR 7480, while the physical and mechanical properties of the composite rebars (BFRP and GFRP) are described by the Russian standard ISC GOST 31938-2012. In order to check the rebars conformance we have characterized them with few different tests: (i) X-ray powder diffraction (XPD), (ii) Scanning Electronic Microscopy (SEM) including Energy Dispersive X-ray Spectroscopy (EDS) and; (iii) tensile tests.

2.1.1. X-ray powder diffraction

The crystallographic structure of the materials employed in the different rebars was investigated by X-ray powder diffraction (XPD) measurements. They were carried out in the Bragg-Brentano geometry in a $\theta - \theta$ diffractometer (Panalytical Empyrean) by using a Cu target X-ray tube at 40 kV x 20 mA. To limit the X-ray beam area on the surface sample, 5 mm (horizontally) x 0.5 mm (vertically) crossed slits were employed. Also, in order to assure that most of the radiation is CuK α (~ 8 keV) a Ni filter was employed. Firstly, pieces (5 mm long by ~ 6 mm in diameter) of the different rebar types (CA-50 steel, BFRP and GFRP) were prepared in a home-made cold mounting resin for the XPD measurements. To further characterize the FRP rebars we decided to grind them until get a homogeneous powder (particle size between 1 μ m and 6 μ m) and repeat the XPD measurements.

2.1.2. Scanning electron microscopy

The scanning electronic microscopy (SEM) measurements [including energy dispersive X-ray spectroscopy (EDS)] were carried out with a Zeiss EVO MA10 electronic microscope. Again, cross section pieces (5 mm long by ~ 6 mm in diameter) of the different rebar types (CA-50 steel, BFRP and GFRP) were prepared. Also, in order to try to measure only the fibers and not only the FRP resins, longitudinal section pieces (5 mm long) were also prepared. In the process of cutting the different FRP section pieces, one BFRP rebar sample was unraveled, showing up the basalt fibers. This sample was also used for the SEM images. The sectioned samples were lapped and polished. All the samples (sections and the unraveled) were cleaned with isopropanol and then coated, by sputtering deposition, with palladium (Pd) for the SEM analysis. The samples were then mounted in the SEM reel table.

2.1.3. Tensile tests

In order to confirm compliance with the specifications and standards, the different rebar types (CA-50 steel, BFRP and GFRP) were also submitted to tensile tests. The tests were performed in an universal testing machine (TimeGroup WAW1000C). The operation of the universal testing machine is made by a software that acquires the loading data as function of time. For consistency check, the tests, carried out with the CA-50 steel rebars, were also measured with a strain gauge (displacement indicator), attached to the test machine.

2.2. Concrete specimens design and preparation

Standard cylindrical test specimens (diameter of 100 mm and a height of 200 mm), for compression tests, and RC test specimens, for pull-out tests, were prepared. The procedure for assembling the RC test specimens and for executing the pull-out tests are reported in the ASTM standard C234-91a. In this work, the RC test specimens were cast in standard cylindrical molds (diameter of 150 mm and a height of 300 mm) however, slightly modified, by inserting a small cylindrical section, set on the top of the RC test specimens, as described in a previous work [28]. The small cylindrical section was included in the mold in order to reduce the RC test specimens thickness to be able to carry out in-situ X-ray inspection during the pull-out tests [28]. Nevertheless, this methodology did not showed to be efficient for RC test specimens with BFRP and GFRP rebars since the density of the rebars are very close to the concrete density then producing no contrast in the acquired in-situ X-ray images. To solve this problem, in-situ phase contrast X-ray inspection [29] is envisaged. The challenge is to mount such an experiment in the universal testing machine especially due to the size of the radiation shielding, since the sample to detector distance needs to be increased to ~ 1 m.

Coming back to the RC test specimens design, the bonding embedment length (anchorage length) between the concrete and the rebars (CA-50 steel, BFRP and GFRP) was kept to a length of 70 mm on the longitudinal axis, including the section with the reduced diameter. In order to avoid contact between the concrete and the steel rebar along the remaining length (180 mm), a flexible polyvinyl chloride tube with an internal diameter of 8 mm was placed around the rebar and sealed at the ends with ethylene vinyl acetate glue.

Normal (unsalty-sand) and salty-sand concrete mixtures (Table 1) were made up with Portland cement with a high initial strength (Ciplan CPV Extra Forte). The salty-sand concrete mixtures were prepared with unsalted sand, however, adding kitchen salt (sodium chloride – NaCl) to the mixture with the same salt concentration of sea sands reported in the literature [23]. All the concrete mixtures were prepared in order to have an initial compressive strength of 30 MPa (theoretically estimated). The slump test (in accordance with the Brazilian standard ABNT NBR NM 67), measured just before casting the test specimens, was found to be in the range of 35 mm to 75 mm for unsalty-sand concrete mixtures and in the range of 55 mm to 160 mm for the salty-sand concrete mixtures. The sand comes from regional natural river extraction (Foz do Iguacu, Brazil) and the coarse aggregate is made from the basaltic rock. Both are in accordance with the Brazilian standard ABNT NBR 7211, i.e., maximum diameters of 2.4 mm (sand) and 9.5 mm (coarse aggregate).

Table 1. Concrete mixture specifications used for casting the RC test specimens (pull-out tests) and the standard cylindrical test specimens (compression tests) for a theoretically estimated compressive strength value of 30 MPa

Material	Unsalty-sand concrete mixture mass (kg)	Salty-sand concrete mixture mass (kg)
Cement	25.50	25.50
Sand	74.97	74.97
Gravel	85.00	85.00
Water	17.00	17.00
Salt	–	0.4335

The water was provided by the local water supply company (Sanepar). The concrete was mixed in an electric mixer with a capacity of 300 l. 72 RC test specimens were cast for each different rebar type (CA-50 steel, BFRP and GFRP) in two different dozen sets (unsalty-sand and salty-sand concrete mixtures) (Fig. 1 and Table 2). As previously mentioned, at the same time, standard cylindrical test specimens (72 in total with a diameter of 100 mm and a height of 200 mm), one dozen for each different set, were also cast (Fig. 1 and Table 2). The aim to do that is to carry out compression tests and pull-out tests at the same time in order to determine both, the concrete compressive strength and the bond strength. For the RC test specimens, the concrete was cast in four layers. The first layer filled the 35 mm diameter region. The other

three layers were equally divided along the height of the specimen. For the standard cylindrical test specimens the concrete was cast in three layers of ranging from ~ 60 mm to ~ 70 mm each. For the concrete compaction; the specimens were repeatedly tamped (25 times for each layer, in accordance with the Brazilian standard ABNT NBR 5738), using a metal rod to avoid the formation of large voids and aggregate segregations inside the specimen. The specimens were demolded 48 h after casting and were placed in a humid chamber until the test dates.

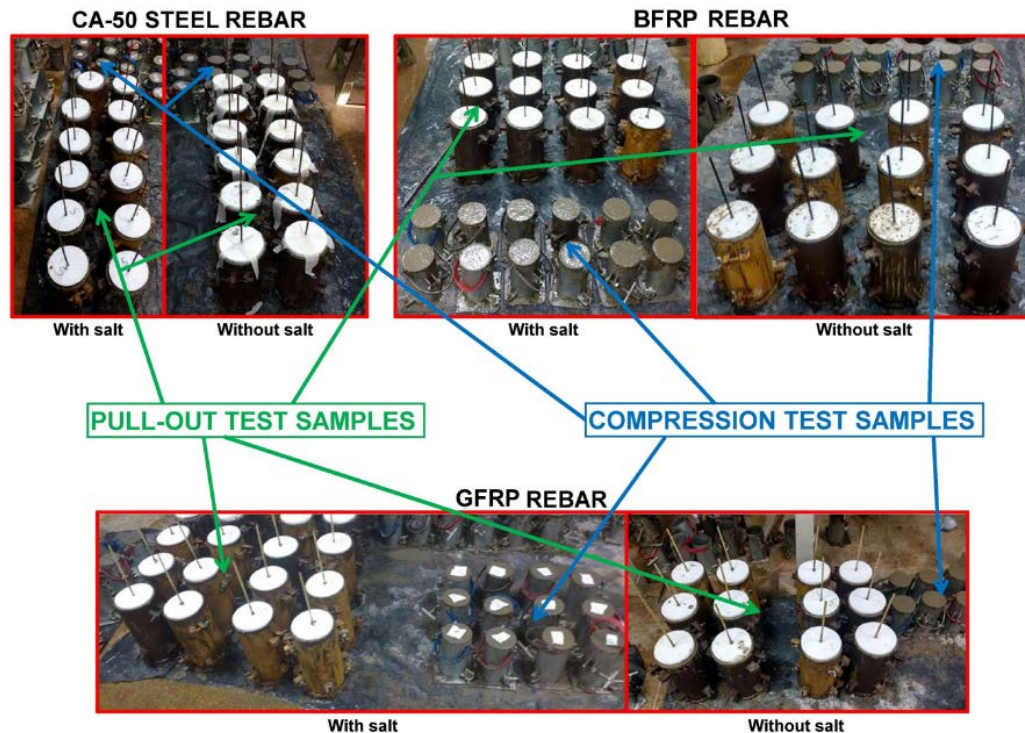


Figure 1. Cast samples for the pull-out (Reinforce Concrete – RC test specimens) and compression tests (standard cylindrical test specimens). Salty-sand and unsalty-sand samples and unsalted samples.

Table 2. RC test specimens (pull-out tests) and the standard cylindrical test specimens (compression tests) inventory

Rebar type	Unsalty-sand RC test specimens (unit)	Salty-sand RC test specimens (unit)	Unsalty-sand standard cylindrical test specimens (unit)	Salty-sand standard cylindrical test specimens (unit)
<i>Steel</i>	12	12	12	12
<i>BFR</i>	12	12	12	12
<i>GFR</i>	12	12	12	12

2.3. Pull-out and compression tests

The pull-out tests on the RC test specimens and the compression tests on the standard cylindrical test specimens were carried out at the universal testing machine (TimeGroup WAW1000C) at 63, 217 and 315 days after casting. For the pull-out tests (Fig. 2) we have designed a metal cradle (carbon steel) for holding the RC test specimens, as described in a previous work [28]. Two different concrete mixtures (unsalty-sand and salty-sand) and three different rebar types (CA-50 steel, BFRP and GFRP) were studied.

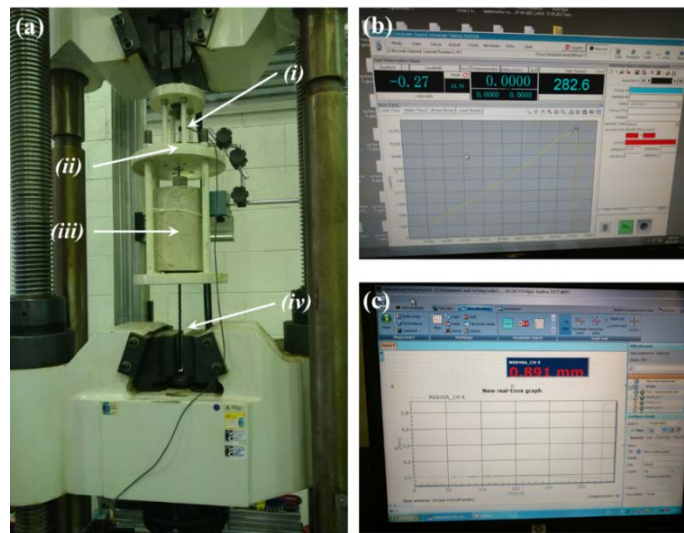


Figure 2. (a) Setup for the pull-out test mounted on the universal testing machine: (i) Displacement indicator; (ii) Metallic cradle; (iii) Reinforced concrete (RC) test specimen and; (iv) Detail of the rebar (in this a BFRP) fixed in the universal testing machine clamps. (b) Picture of the computer screen showing the software that controls the operation of the machine and stores the loading data versus time. (c) Picture of the computer screen showing the software that stores the displacement versus time data, as measured by the displacement indicator.

3. Results and Discussion

3.1. Conformance testing

For the CA-50 steel rebar the XPD results (represented by the diffractogram in Fig. 3) show the main X-ray diffraction peaks of 0.95Fe0.05Mn alloy (indexed by JCPDS no. 98-010-3521), as expected. Also, X-ray diffraction peaks of the cold mounting resin were detected. For the XPD measurements carried out on the BFRP and on the GFRP rebars, only the cold mounting resin X-ray diffraction peaks were found (results not presented here). For this reason, the FRP rebars were grind and further characterized by XPD.

For the grind FRP rebars, few X-ray diffraction peaks were found and they look similar (same angular position) for both samples (BFRP and GFRP) (Fig. 4). Since the diffraction peaks are angularly broad, which is characteristic of low range cristallinity materials (such as paraffin wax, polypropylene, etc.) [30, 31], we attributed them to the FRP resins. However, we were not able to get the diffractogram indexed. Then, at last, we decided to proceed with spectroscopy analysis in order to check the main components (chemical elements) of each FRP rebar. This was made by scanning electronic microscopy (SEM) including energy dispersive X-ray spectroscopy (EDS).

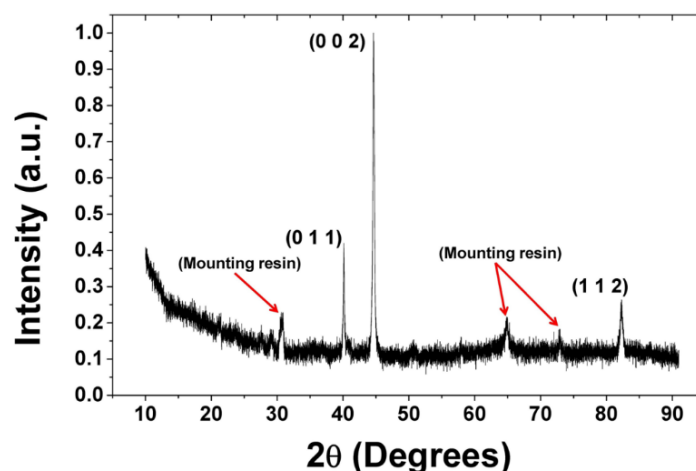


Figure 3. Diffractogram for the CA-50 steel rebar. The three main diffraction peaks were indexed to be 0.95Fe0.05Mn alloy (JCPDS no. 98-010-3521). Each diffraction peak represents the X-ray diffraction by a different crystallographic plane, indicated between the brackets, by the Miller indices. Diffraction peaks of the mounting resin are also present.

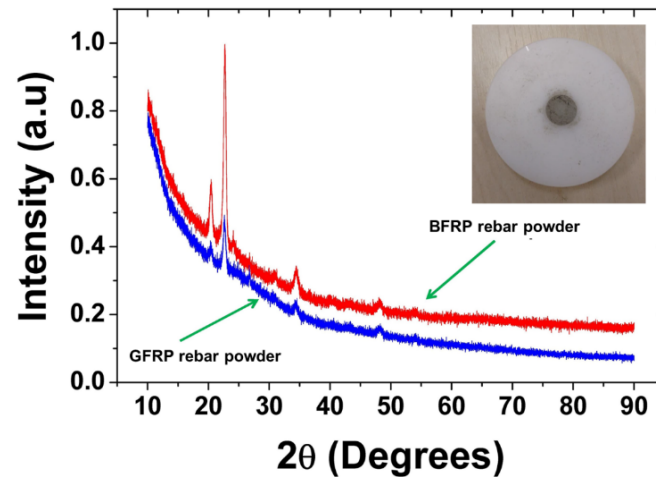


Figure 4. Diffractograms of the BFRP and GFRP rebar powders. As an example, in the inset, is shown the GFRP powder prepared in a polyamide sample holder for the XPD measurements.

The SEM images of the basalt fiber and the glass fiber themselves, are shown Fig. 5. Diameter sizes of $17\ \mu\text{m}$ and $18\ \mu\text{m}$, respectively, were measured. In Fig. 6 and 7 are shown the EDS analysis for the different sections of BFRP and GFRP, respectively. The results show the presence of oxygen (O), silicon (Si), iron (Fe), calcium (Ca), magnesium (Mg), sodium (Na) and potassium (K) for the BFRP fibers and; oxygen (O), silicon (Si), calcium (Ca) and aluminum (Al) for the GFRP fibers, in accordance with other data presented in the literature [32]. Some measurements show also the presence of carbon (C), gold (Au) and palladium (Pd). The first occurs because some of the measured fibers can still be embedded in the FRP resin. Au and Pd are present as a consequence of the coating material used for SEM analysis. In some results they were electronically filtered and did not showed up.

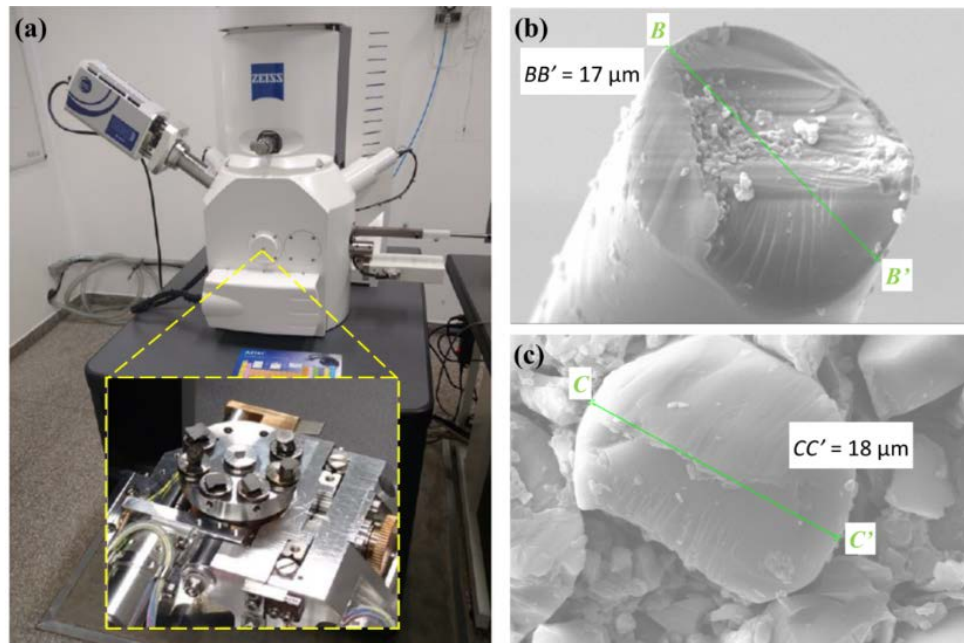


Figure 5. (a) Scanning electron microscope (SEM). In the inset it is shown, mounted in the reel table, inside the SEM vacuum chamber, all the samples (sectioned FRP and the unraveled sample) already coated with palladium. (b) SEM image of the basalt fiber. (c) SEM image of the glass fiber.

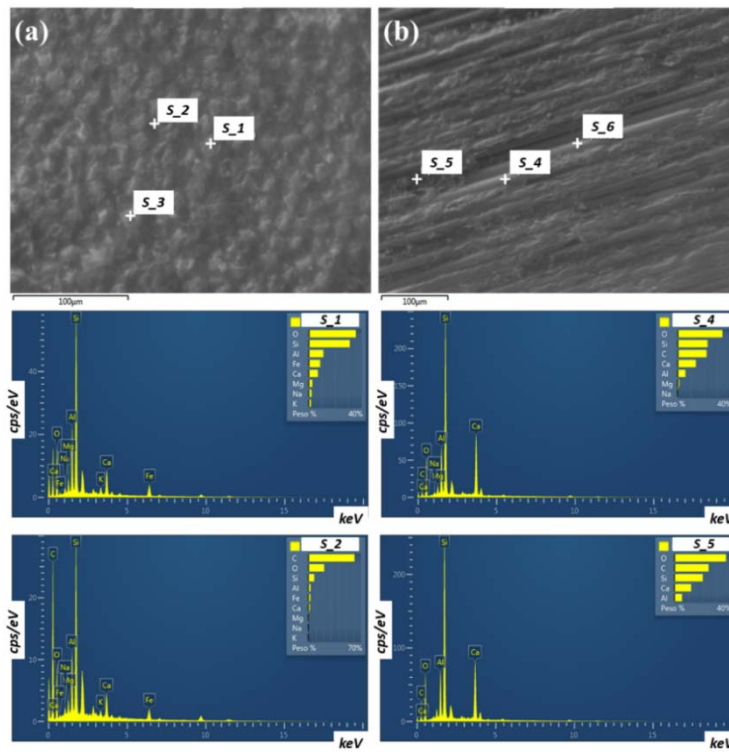


Figure 6. SEM / Energy Dispersive X-ray Spectroscopy (EDS) measurements on the sections of the BFRP rebar. (a) Cross section and (b) Longitudinal section. Results on the different points where de EDS was performed were chosen to show here: s1, s2, s4 and s5. They correspond to areas with the fiber (s1 and s4) and areas with FRP resin (s2 and s4). Carbon (C) was also present in the s4 area, indicating that the basalt fiber is still embedded in the FRP resin.

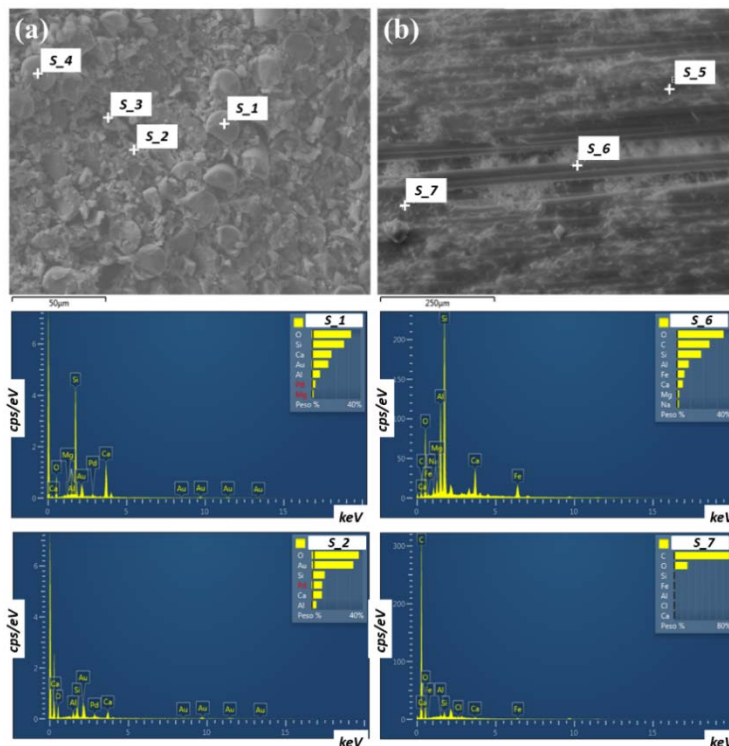


Figure 7. SEM / EDS measurements on the sections of the GFRP rebar. (a) Cross section and (b) Longitudinal section. Results on the different points where de EDS was performed were chosen to show here: s1, s2, s6 and s7. They correspond to areas with the fiber (s1 and s4) and, in principle, areas with FRP resin (s2 and s7). Gold (Au) and Palladium (Pd), not electronically filtered in these measurements, were found in s1 and s2. Carbon (C) was not found in s2, indicating that there is no FRP resin in that area. However, Carbon (C) was in the s6 area, indicating that the glass fiber is still embedded in the FRP resin.

The tensile test results for the CA-50 steel rebars are presented in Fig. 8. For the BFRP and GFRP rebars, firstly, they were fixed as the CA-50 steel rebars, i.e. directly to the clamps of the universal testing machine [Fig. 9(a) and 9(b)]. This methodology was not the most appropriate due to the characteristics of BFRP and GFRP rebars. When the applied load increases, a slippage occurs in the contact region between the rebars and the clamps even before reaching the yield strength limit. This damaged the tested rebars [Fig. 9(c)]. To solve this problem, the rebars extremities were embedded in resin-filled (in our case, polyester putty) steel tubes (sleeves) [Fig. 9(d)] in a methodology similar to the recommended by the Russian standard ISC GOST 31938-2012. Using such a methodology, the universal testing machine clamps will be in contact with the steel tubes (sleeves) and not in direct contact with the rebars, thus preventing the rebars slippage in the clamps region when pulled. As an example, Fig. 9(e) shows a GFRP rebar with the resin filled steel tubes mounted in the universal testing machine previously to the tensile test. Even with that, the tests showed to be unsuccessful, because, during load application, the steel tube (sleeve) was crushed, most probably, due to some void inside the steel tube. This leads to a loss of adhesion between the hardened resin and the steel tube. Consequently, the rebars, together with the hardened resin, were torn out from the steel tube, thus not allowing the test to be completed. However, the rebar manufacturer (Composite Chelyabinsk Group LLC) indicates that the tensile strength of both BFRP rebar and GFRP rebar is ~ 1000 MPa. In the case of the rebar used in this work, which have diameter of 6 mm, this is equivalent to a maximum force of 28.3 kN. In pull-out tests that will be further presented, the maximum applied force never exceeded 20 kN, which safely moves away from possibility of breaking off the BRPR and GRPR rebars before reaching the ultimate bonding strength.

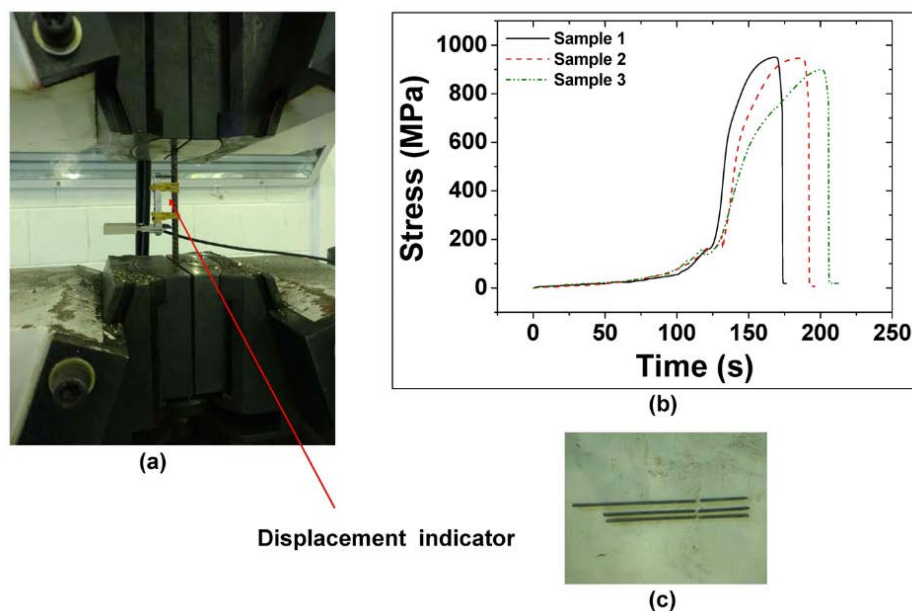


Figure 8. Tensile tests for the CA-50 steel rebar. (a) CA-50 Steel rebar fixed in the clamps of the universal testing machine. Use of strain gauge (displacement indicator) installed in contact with CA-50 steel rebar. (b) Stress (MPa) x time (s) results for the three different the CA-50 steel rebar samples. (c) CA-50 steel rebar samples after the tensile test.

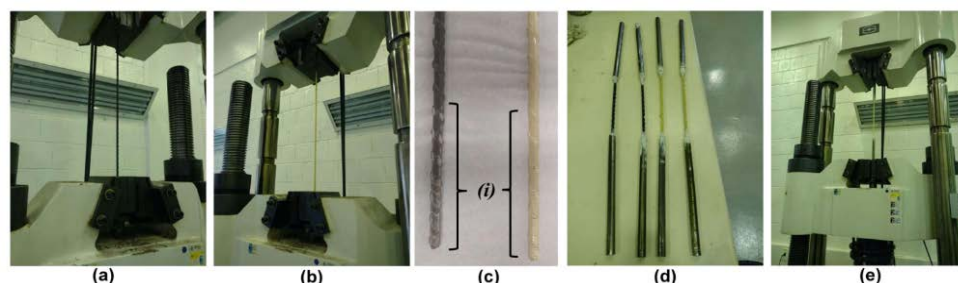


Figure 9. Tensile tests for the FRP rebars. BFRP rebar (a) and GFRP rebar (b) directly fixed into the clamps of the universal testing machine. (c) BFRP rebar (left) and GFRP rebar (right) after tensile tests showing the damage in the rebars (i) due to the slipping in the universal testing machine clamps. (d) Samples of BFRP rebar (left) and GFRP rebar (right) embedded in resin filled steel tubes (sleeves). (e) GFRP rebar with the resin filled steel tubes mounted in the universal testing machine for the tensile test.

3.2. Compression and bond strengths

The results are summarized in Tables 3-14. A total of 18 sets of pull-out tests were carried out on 36 RC test specimens and a total of 18 sets of compression tests were done on 60 standard cylindrical test samples. The results for the average bond strength values (acquired with the pull-out tests) for the different rebar types with different concrete mixtures at different ages (Tables 3, 5, 7, 9, 11 and 13), for better comparison, are summarized in the Fig. 10, 11 and 12.

Table 3. Results for the pull-out tests on unsalty-sand RC test specimens with CA-50 steel rebar.

Specimen #	Time after molding (days)	Bond strength (MPa)	
		Per specimen	Average
POT-AC-SS-01	63	19.24	18.10
POT-AC-SS-02		16.96	
POT-AC-SS-03	217	16.21	16.47
POT-AC-SS-04		16.74	
POT-AC-SS-05	315	18.87	19.06
POT-AC-SS-06		19.25	

Table 4. Results for the compression tests on the unsalty-sand standard cylindrical test specimens molded at the same time with the unsalty-sand RC test specimens with CA-50 steel rebar. The result for the specimen RC-AC-SS-04 was excluded since its value is 5% (or more) greater than the average.

Specimen #	Time after molding (days)	Compressive strength (MPa)	
		Per specimen	Average
RC-AC-SS-01	63	33.10	33.16
RC-AC-SS-02		33.25	
RC-AC-SS-03	217	33.12	42.63
RC-AC-SS-04		36.47	
RC-AC-SS-05	315	43.00	42.13
RC-AC-SS-06		41.96	
RC-AC-SS-07	315	41.92	42.13
RC-AC-SS-08		43.62	
RC-AC-SS-09	315	40.20	42.13
RC-AC-SS-10		44.05	

Table 5. Results for the pull-out tests on salty-sand RC test specimens with CA-50 steel rebar.

Specimen #	Time after molding (days)	Bond strength (MPa)	
		Per specimen	Average
POT-AC-CS-01	63	18.93	17.99
POT-AC-CS-02		17.06	
POT-AC-CS-03	217	15.30	15.69
POT-AC-CS-04		16.08	
POT-AC-CS-05	315	14.23	14.00
POT-AC-CS-06		13.77	

For the RC test specimens with CA-50 steel rebars and salty-sand concrete mixtures there is a reduction in the bond strength along the time (~ 20 % when comparing to the measured bond strengths in 315 days and 63 days and ~ 26 % when compared with the RC test specimens with CA-50 steel rebars and unsalty-sand concrete mixture) (Fig. 10, Table 3 and 5). This can be attributed to the initial corrosion stages in the CA-50 steel rebars due to the higher salinity of the concrete mixture.

For the RC tests specimens with BFRP rebars and unsalty-sand concrete mixture, there is a reduction in the bond strength along the time (Fig. 11, Table 7). However, since this difference, at 315 days, is only 9 % for the specimens with different concrete mixtures (salty-sand and unsalty-sand), one can say that, within the error bars, the bond strengths are, approximately, the same. On the other hand, for the RC test specimens with BFRP rebars and salty-sand concrete mixtures there is an increase in the bond strength along the time (Fig. 11, Table 9), this can be related to the hydration of the cementitious matrix, reflected on the higher compressive strength (Table 10).

Table 6. Results for the compression tests on the salty-sand standard cylindrical test specimens molded at the same time with the salty-sand RC test specimens with CA-50 steel rebar. The result for the specimen RC-AC-CS-08 was excluded since its value is 5% (or more) smaller than the average.

Specimen #	Time after molding (days)	Compressive strength (MPa)	
		Per specimen	Average
RC-AC-CS-01	63	35.74	35.68
RC-AC-CS-02		35.62	
RC-AC-CS-03		34.97	
RC-AC-CS-04		36.37	
RC-AC-CS-05		39.56	
RC-AC-CS-06	217	40.11	39.58
RC-AC-CS-07		39.06	
RC-AC-CS-08		35.74	
RC-AC-CS-09	315	42.06	42.50
RC-AC-CS-10		42.94	

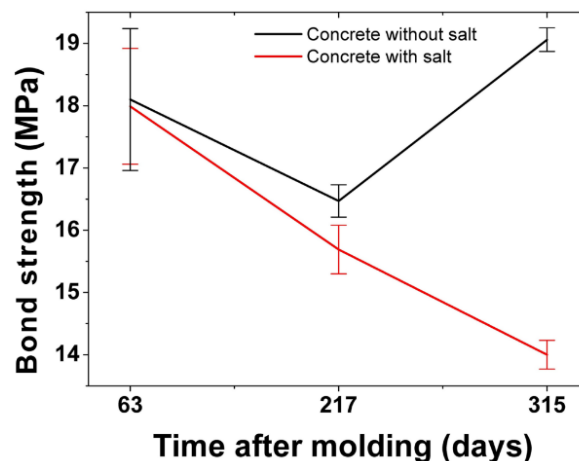


Figure 10. Temporal evolution of the average bond strength values for the RC test specimens with CA-50 steel rebars with different concrete mixtures (salty-sand and unsalty-sand). The error bars are the standard deviations.

Table 7. Results for the pull-out tests on unsalty-sand RC test specimens with BFRP rebar. The result for the specimen POT-FB-SS-01 was discarded due to a slippage of the BFRP rebar in the clamps of universal testing machine. The slippage occurred before the maximum bond strength between the BFRP rebar and the concrete.

Specimen #	Time after molding (days)	Bond strength (MPa)	
		Per specimen	Average
POT-FB-SS-01	63	10.38	14.33
POT-FB-SS-02		14.33	
POT-FB-SS-03		15.10	
POT-FB-SS-04	217	15.16	15.13
POT-FB-SS-05		12.36	
POT-FB-SS-06	315	13.19	12.78

Table 8. Results for the compression tests on the unsalty-sand standard cylindrical test specimens molded at the same time with the unsalty-sand RC test specimens with BFRP rebar.

Specimens #	Time after molding (days)	Compressive strength (MPa)	
		Per specimen	Average
RC-FB-SS-01	63	27.20	27.34
RC-FB-SS-02		26.75	
RC-FB-SS-03		26.63	
RC-FB-SS-04		28.78	
RC-FB-SS-05		36.37	
RC-FB-SS-06	217	36.97	36.74
RC-FB-SS-07		36.92	
RC-FB-SS-08		36.70	
RC-FB-SS-09	315	29.73	30.05
RC-FB-SS-10		30.38	

Table 9. Results for the pull-out tests on salty-sand RC test specimens with BFRP rebar

Specimen #	Time after molding (days)	Bond strength (MPa)	
		Per specimen	Average
POT-FB-CS-01	63	12.39	12.33
POT-FB-CS-02		12.27	
POT-FB-CS-03		12.83	
POT-FB-CS-04	217	13.84	13.33
POT-FB-CS-05		12.87	
POT-FB-CS-06	315	15.21	14.04

Table 10. Results for the compression tests on the salty-sand compression test specimens molded at the same time with the salty-sand RC test specimens with BFRP steel rebar. The result for the specimen RC-FB-CS-08 was excluded since its value is 5% (or more) smaller than the average.

Specimen #	Time after molding (days)	Compressive strength (MPa)	
		Per specimen	Average
RC-FB-CS-01	63	32.05	31.80
RC-FB-CS-02		31.50	
RC-FB-CS-03		32.63	
RC-FB-CS-04		31.03	
RC-FB-CS-05		36.65	
RC-FB-CS-06	217	37.40	37.20
RC-FB-CS-07		37.57	
RC-FB-CS-08		34.33	
RC-FB-CS-09	315	33.97	33.74
RC-FB-CS-10		33.50	

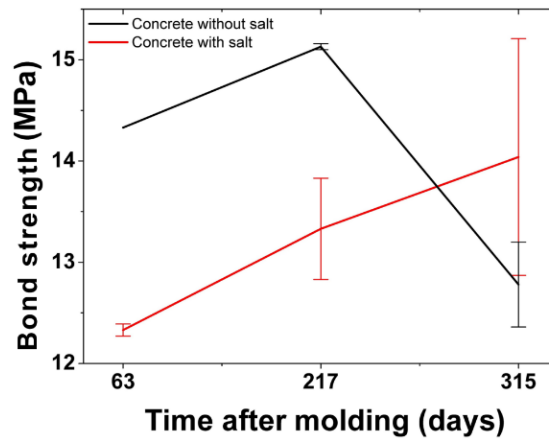


Figure 11. Temporal evolution of the average bond strength values for the RC test specimens with BFRP rebar with different concrete mixtures (salty-sand and unsalty-sand). The error bars are the standard deviations.

For the RC test specimens with GFRP rebar the measured bond strengths, for all the concrete mixtures (salty-sand and unsalty-sand) and all the ages, were very similar (Fig. 12, Table 11 and 13).

In summary, the bond strength results showed that BFRP and GFRP rebar can be successfully used in salty-sand concrete mixtures. However, the BFRP and GFRP rebar showed, in all the reported measurements (Table 3, 5, 7, 9, 11, 13 and Fig. 10–12), bond strengths smaller than the bond strengths for the CA-50 steel rebar. Then, even the BFRP and GFRP rebar having higher tensile strength than the CA-50 steel rebar, their use in the RC structures will demand higher anchorage lengths, as already reported in the literature [3, 33]. This is attributed to the difference in the surface deformations of the FRP rebar and steel rebar [33].

Table 11. Results for the pull-out tests on unsalty-sand RC test specimens with GFRP rebar.

Specimen #	Time after molding (days)	Bond strength (MPa)	
		Per specimen	Average
POT-FV-SS-01	63	13.20	14.50
POT-FV-SS-02		15.79	
POT-FV-SS-03	217	12.56	12.43
POT-FV-SS-04		12.30	
POT-FV-SS-05	315	13.63	12.95
POT-FV-SS-06		12.26	

Table 12. Results for the compression tests on the unsalty-sand standard cylindrical test specimens molded at the same time with the unsalty-sand RC test specimens with GFRP rebar.

Specimen #	Time after molding (days)	Compressive strength (MPa)	
		Per specimen	Average
RC-FV-SS-01	63	35.87	36.27
RC-FV-SS-02		36.20	
RC-FV-SS-03		36.75	
RC-FV-SS-04		36.27	
RC-FV-SS-05	217	42.09	41.74
RC-FV-SS-06		40.87	
RC-FV-SS-07		42.92	
RC-FV-SS-08		41.09	
RC-FV-SS-09	315	41.09	41.99
RC-FV-SS-10		42.89	

Table 13. Results for the pull-out tests on salty-sand RC test specimens with GFRP rebar. The result for the specimen POT-FV-CS-04 was discarded due to a crack in the in the small cylindrical section during to the pull-out test which prevented us to determine the bond strength between GFRP rebar and the concrete.

Specimen #	Time after molding (days)	Bond strength (MPa)	
		Per specimen	Average
POT-FV-CS-01	63	15.18	14.68
POT-FV-CS-02		14.19	
POT-FV-CS-03	217	13.95	13.95
POT-FV-CS-04		9.23	
POT-FV-CS-05	315	14.07	12.71
POT-FV-CS-06		11.35	

Table 14. Results for the compression tests on the salty-sand standard cylindrical test specimens molded at the same time with the salty-sand RC test specimens with GFRP steel rebar.

Specimen #	Time after molding (days)	Compressive strength (MPa)	
		Per specimen	Average
RC-FV-CS-01	63	37.27	37.10
RC-FV-CS-02		36.85	
RC-FV-CS-03		36.32	
RC-FV-CS-04		37.95	
RC-FV-CS-05		41.67	
RC-FV-CS-06	217	42.37	42.35
RC-FV-CS-07		42.24	
RC-FV-CS-08		43.12	
RC-FV-CS-09	315	40.89	39.87
RC-FV-CS-10		38.85	

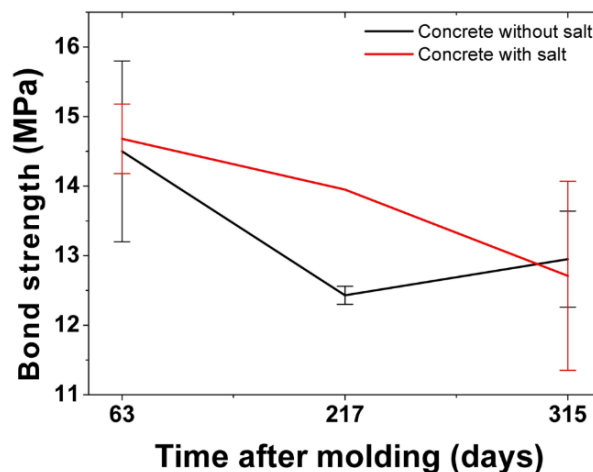


Figure 12. Temporal evolution of the average bond strength values for the RC test specimens with GFRP rebars. with different concrete mixtures (salty-sand and unsalty-sand). The error bars are the standard deviations.

4. Conclusion

Long term pull-out tests were carried out in Reinforced Concrete (RC) test specimens with CA-50 steel rebars, Basalt Fiber Reinforced Polymer (BFRP) rebars and Glass Fiber Reinforce Polymer (GFRP) rebars with salty-sand and unsalty-sand concrete mixtures. For different ages (up to 315 days after casting) pull-out tests and compression tests were performed. Conformance testing, including X-ray powder

diffraction (XPD), Scanning Electronic Microscopy (SEM) and tensile tests, were carried out on the rebars previously to the pull-out and compression tests.

Our results showed that all the tested RC test specimens cast with different rebar types (CA-50 steel, BFRP and GFRP) and unsalty-sand concrete mixtures did not show expressive changes in the measured bond strengths along the time. However, for the RC test specimens cast with salty-sand concrete mixtures, the results were different. For the RC test specimens molded with BFRP and GFRP rebars also no expressive changes in the measured bond strengths along the time were found. Although for the RC test specimens cast with CA-50 steel rebars, a reduction in the bond strength along the time was detected (~20 % when comparing the measured strengths in 315 days and 63 days and 26 % when compared with the RC test specimens with CA-50 steel rebars and unsalty-sand concrete mixture). This can be attributed to the initial corrosion stages in the CA-50 steel rebars (not detected in the BFRP and GFRP rebars) due to the higher salinity of the concrete mixtures.

At last, the BFRP and GFRP rebars showed to be the proper rebars to be used for salty-sand concrete mixtures. However, since their bond strengths are smaller than the bond strengths for the CA-50 steel rebars in all the reported measurements, their use in the RC structures, will demand higher anchor lengths even having higher traction resistance.

References

1. Fanella, D.A. Reinforced Concrete Structures: Analysis and Design. 1st ed. New York, McGraw-Hill, 2010. 652 p.
2. Wight, J., Macgregor, J. Reinforced Concrete: Mechanics and Design: International Edition. New Jersey, Pearson Education, 2012. 1176 p.
3. Quayyum, S. Bond behaviour of Fibre Reinforced Polymer (FRP) rebars in concrete. University of British Columbia, 2010. 190 p.
4. Yin, H., Li, Y., Lv, H., Gao, Q. Durability of sea-sand containing concrete: Effects of chloride ion penetration. Mining Science and Technology. 2011. 21 (1). Pp. 123–127. DOI: 10.1016/j.mstc.2010.07.003
5. Apostolopoulos, C.A., Demis, S., Papadakis, V.G. Chloride-induced corrosion of steel reinforcement - Mechanical performance and pit depth analysis. Construction and Building Materials. 2013. 38. Pp. 139–146. DOI: 10.1016/j.conbuildmat.2012.07.087
6. Kog, Y.C. High-performance concrete made with dune sand. Magazine of Concrete Research. 2020. 72 (20). Pp. 1036–1046. DOI: 10.1680/jmacr.18.00073
7. Wegian, F.M. Effect of seawater for mixing and curing on structural concrete. The IES Journal Part A: Civil & Structural Engineering. 2010. 3 (4). Pp. 235–243. DOI: 10.1080/19373260.2010.521048
8. Tuutti, K. Corrosion of steel in concrete. Swedish Cement and Concrete Research Institute, 1982. 468 p.
9. Olutoge, F.A., Amusan G.M. The Effect of Sea Water on Compressive Strength of Concrete. International Journal of Engineering Science Invention. 2014. 3 (7). Pp. 23–31.
10. Nagabhushana, D.R., Hebbal, D., Akash, N., Deepak, S., Kumar, M. Effect of salt water on compressive strength of concrete. International Research Journal of Engineering and Technology. 2017. 4 (5). Pp. 2687–2690.
11. Fang, C., Lundgren, K., Chen, L., Zhu, C. Corrosion influence on bond in reinforced concrete. Cement and Concrete Research. 2004. 34 (11). Pp. 2159–2167. DOI: 10.1016/j.cemconres.2004.04.006
12. Fang, C., Lundgren, K., Plos, M., Gylltoft, K. Bond behaviour of corroded reinforcing steel bars in concrete. Cement and Concrete Research. 2006. 36 (10). Pp. 1931–1938. DOI: 10.1016/j.cemconres.2006.05.008
13. Lundgren, K. Effect of corrosion on the bond between steel and concrete: an overview. Magazine of Concrete Research. 2007. 59 (6). Pp. 447–461. DOI: 10.1680/macrc.2007.59.6.447
14. Yalciner, H., Eren, O., Sensoy, S. An experimental study on the bond strength between reinforcement bars and concrete as a function of concrete cover, strength and corrosion level. Cement and Concrete Research. 2012. 42 (5). Pp. 643–655. DOI: 10.1016/j.cemconres.2012.01.003
15. Watstein, D. Bond Stress in Concrete Pullout Specimens. ACI Journal Proceedings. 1941. 38. Pp. 37–52. DOI: 10.14359/8586
16. Nawy, E.G. Reinforced Concrete: a Fundamental Approach. New Jersey, Pearson, 2008. 944 p.
17. Teng, J.G., Chen, J.F., Smith, S.T., Lam, L. Behaviour and strength of FRP-strengthened RC structures: a state-of-the-art review. Proceedings of the Institution of Civil Engineers – Structures and Buildings. 2003. 156 (1). Pp. 51–62. DOI: 10.1680/stbu.2003.156.1.51
18. Yuan, H., Teng, J.G., Seracino, R., Wu, Z.S., Yao, J. Full-range behavior of FRP-to-concrete bonded joints. Engineering Structures. 2004. 26 (5). Pp. 553–565. DOI: 10.1016/j.engstruct.2003.11.006
19. Okelo, R., Yuan, R.L. Bond Strength of Fiber Reinforced Polymer Rebars in Normal Strength Concrete. Journal of Composites for Construction. 2005. 9 (3). Pp. 203–213. DOI: 10.1061/(ASCE)1090-0268(2005)9:3(203)
20. Karbhari, V.M. Durability of Composites for Civil Structural Applications. Pennsylvania, Woodhead Publishing, 2007. 944 p.
21. Lau, D., Pam, H.J. Experimental study of hybrid FRP reinforced concrete beams. Engineering Structures. 2010. 32 (12). Pp. 3857–3865. DOI: 10.1016/j.engstruct.2010.08.028
22. Kara, I.F., Ashour, A.F., Koroğlu, M.A. Flexural behavior of hybrid FRP/steel reinforced concrete beams. Composite Structures. 2015. 129. Pp. 111–121. DOI: 10.1016/j.compstruct.2015.03.073
23. Dong, Z., Wu, G., Xu, Y. Experimental study on the bond durability between steel-FRP composite bars (SFCBs) and sea sand concrete in ocean environment. Construction and Building Materials. 2016. 115. Pp. 277–284. DOI: 10.1016/j.conbuildmat.2016.04.052
24. Lee, J.-Y., Lim, A.-R., Kim, J., Kim, J. Bond behaviour of GFRP bars in high-strength concrete: bar diameter effect. Magazine of Concrete Research. 2017. 69 (11). Pp. 541–554. DOI: 10.1680/jmacr.15.00403

25. Dong, Z., Wu, G., Xu, B., Wang, X., Taerwe, L. Bond performance of alkaline solution pre-exposed FRP bars with concrete. Magazine of Concrete Research. 2018. 70 (17). Pp. 894–904. DOI: 10.1680/jmacr.17.00027
26. Yang, Y., Wu, G. Evaluation of fatigue performance of ballastless track slabs reinforced with basalt-FRP and steel-FRP composite bars. Magazine of Concrete Research. 2020. 72 (1). Pp. 43–54. DOI: 10.1680/jmacr.18.00179
27. Chai, L., Guo, L., Chen, B., Ding, C. Bond behaviour of bars embedded in ecological high-ductility cementitious composites. Magazine of Concrete Research. 2020. 72 (3). Pp. 122–133. DOI: 10.1680/jmacr.18.00160
28. Bostel, R., Dos Santos, A.C.P., Lopes, J.B., Willrich, F.L., Hönnicke, M.G. Watching the bonding between steel rebar and concrete with in situ X-ray imaging. Magazine of Concrete Research. 2020. 72 (15). Pp. 768–777.
29. Sarapata, A., Ruiz-Yaniz, M., Zanette, I., Rack, A., Pfeiffer, F., Herzen, J. Multi-contrast 3D X-ray imaging of porous and composite materials. Applied Physics Letters. 2015. 106 (15). Pp. 154102. DOI: 10.1063/1.4918617
30. Clark, G.L., Smith, H.A. X-Ray Diffraction Study of Fractionated Paraffin Waxes. Industrial and Engineering Chemistry. 1931. 23 (6). Pp. 697–701. DOI: 10.1021/ie50258a025
31. Farrow, G. The measurement of crystallinity in polypropylene fibres by X-ray diffraction. Polymer. 1961. 2 (C). Pp. 409–417. DOI: 10.1016/0032-3861(61)90046-5
32. Wei, B., Cao, H., Song, S. Tensile behavior contrast of basalt and glass fibers after chemical treatment. Materials and Design. 2010. 31 (9). Pp. 4244–4250. DOI: 10.1016/j.matdes.2010.04.009
33. Tighiouart, B., Benmokrane, B., Gao, D. Investigation of bond in concrete member with fibre reinforced polymer (FRP) bars. Construction and Building Materials. 1998. 12 (8). Pp. 453–462. DOI: 10.1016/S0950-0618(98)00027-0

Information about authors:

Rudney Bostel,

ORCID: <https://orcid.org/0000-0003-4354-3040>

E-mail: rudney.bostel@unila.edu.br

Ana Carolina Parapinski dos Santos, D.Eng.

ORCID: <https://orcid.org/0000-0002-4359-8714>

E-mail: ana.santos@unila.edu.br

Joao Bernardino de Oliveira Lopes,

ORCID: <https://orcid.org/0000-0001-8370-0616>

E-mail: joaobol@itaipu.gov.br

Fabio Luiz Willrich,

ORCID: <https://orcid.org/0000-0003-0215-6044>

E-mail: fabiolw@itaipu.gov.br

Rodrigo Leonardo de Oliveira Basso, D.Sc.

ORCID: <https://orcid.org/0000-0001-9815-1592>

E-mail: rodrigo.basso@unila.edu.br

Marcelo Goncalves Honnicke, D.Sc.

ORCID: <https://orcid.org/0000-0003-3276-4323>

E-mail: marcelo.honnicke@unila.edu.br

Received 10.03.2021. Approved after reviewing 16.12.2021. Accepted 16.12.2021.



Research article

UDC 691-408.66

DOI: 10.34910/MCE.114.8



Influence of electromagnetic field on characteristics of crushed materials

R.A. Ibragimov¹ , E.V. Korolev² 

¹ Kazan State University of Architecture and Engineering, Kazan, Russia

² Saint Petersburg State University of Architecture and Civil Engineering, Saint Petersburg, Russia

✉ rusmag007@yandex.ru

Keywords: cements, energy efficiency, specific surface area, electromagnetic field

Abstract. This paper describes the findings of a study into the impact of the magnitude of induction and the frequency of rotation of an electromagnetic field on the properties of materials (Portland cement, gypsum plaster, limestone), which are treated in the vortex layer machines. The effects were assessed based on the following criteria: 1) the location of the maximum values of the specific surfaces in the factor space as determined by the Tovarov method based on the BET method and the temperature of the model powders following treatment in a vortex layer machine; 2) the symbasis of the change in the values of the specific surface as determined by the BET method and the temperature of the powders following activation. Theoretical and experimental studies have been used as a basis for putting forward the concept of treatment in vortex layer machines. The essence of the concept lies in boosting the defectiveness of particles (i.e. accumulation of defects) followed by defects emerging and particles dispersing. The maximum values of specific surfaces and of the temperature of powder upon activation can be obtained at an electromagnetic field rotation frequency of 66 Hz while the material being treated is mechanically activated at an electromagnetic field induction value of 0.21 T with Portland cement, 0.22 T with gypsum plaster and 0.23 T with limestone. A classification to define the susceptibility of the mineral component to treatment inside vortex layer machines has been proposed.

Citation: Ibragimov, R.A., Korolev, E.V. Influence of electromagnetic field on characteristics of crushed materials. Magazine of Civil Engineering. 2022. 114(6). Article No. 11408. DOI: 10.34910/MCE.114.8

1. Introduction

Materials science in the domain of construction states that a variety of mills, dispersants, disintegrators and other kinds of devices are employed to obtain mineral components of the needed dispersed composition or specific surface [1–3].

A material is destroyed under the action of various physical forces such as impact, abrasion or a combination of them. Grinding bodies are propelled by gravity, or by centrifugal forces [4, 5].

Grinding media move at different rates depending on the type of machine used. It is well-known that materials behave quite differently under quasi-static and dynamic loadings. When loaded at a high rate, a material is able to withstand a significantly higher load provided a corresponding static impact is applied [6–7].

Recently, electromagnetic disintegrating machines have found widespread use [8]; a vortex layer machine being one of them. The electromagnetic field generated by an electromagnetic disintegrating machine sets in motion ferromagnetic bodies inside the chamber in a chaotic order [9]. Determinations of the quantitative properties of disintegrating machines normally take into account the impact force, the time

of grinding, and the energy intensity of the process while the effect which the electromagnetic field produces on the substance is absolutely ignored [10–12].

It was established that a weak magnetic field with $B \approx 1$ T induction barely affects the structure and properties of non-magnetic solid bodies [13]. With that said, the magnetic field has been found to affect the mobility of dislocations in the absence of an external mechanical load at $B < 1$ Tl on NaCl single crystals [14]. While investigating the mobility of edge dislocations in NaCl and LiF crystals, the authors [15] witnessed a 4.5 – fold decrease in the dynamic inhibition coefficient of dislocations under the action of an electron beam (pulsed magnetic field). The effect of a magnetic field reduces micro-hardness in NaCl single crystals. However, this process is reversible with a relaxation time of up to 18 hours [16].

The paper [17] indicates that by varying the parameters of the electromagnetic field during a grinding process one can set not only the average size of the particles but also the degree of uniformity of the powder.

An equation has been proposed to outline the elastic precursor of an elastic-plastic wave which forms under pulsed action in the paper [18, 19]. The equation reads as follows:

$$\sigma_y = \sigma_* + (\rho c v_p - \sigma_*) \exp(-2A\mu_0 S(x/c)) \quad (1)$$

(here x is the coordinate; c is the longitudinal velocity of sound; σ_* is the dynamically equilibrium value of the Hugoniot elastic limit; $A = b^2 N_0 / B$; $S = 2\mu_0 / 3\rho c^2$; μ_0 is the initial modulus of elasticity; ρ is the density of matter; b is the Burgers vector; N_0 is the initial density of mobile dislocations; B is the retardation constant of dislocations an analysis of which shows that with all other things being equal the decay rate of the elastic precursor goes down as the B coefficient decreases:

$$\frac{d\sigma_y}{dB} = -\frac{2\sigma_* b^2 N_0 \mu_0 S(x/c)}{x^2 \exp(2A\mu_0 S(x/c))}. \quad (2)$$

The analysis of research and development information shown here suggests that vortex layer machine treatments must demonstrate effects which reveal the contributions of the electromagnetic field to grinding of material along with resulting physical limitations which impair the efficiency of vortex layer machine treatments.

This paper aims to determine the effect which electromagnetic field properties produce on the degree of change in the specific surface of treated materials. This is achieved by mathematical planning of experiments.

2. Methods, materials and equipment used in this study

2.1. Materials and objects of research

The following materials have been selected as models:

1. Portland cement I 42.5 produced by the Novotroitsky cement plant. The product meets the requirements under Russian State Standard GOST 31108-2016. The Portland cement in question features the following mineralogical composition: $C_3S - 64-65\%$, $C_2S - 11-13\%$, $C_3A - 5-6\%$, $C_4AF - 14-15\%$;
2. Limestone from the Bondyuzhsky deposit (Mendeleevsk, Republic of Tatarstan);
3. Gypsum plaster (brand G-5 BII) (β -semihydrate) produced by ZAO "Samara Gypsum Plant". The product conforms to Russian State Standard GOST 125-2018.

The specific surface of the initial Portland cement was 375.5 ± 16.75 m²/kg (as per Tovarov) and 1015 ± 20.3 m²/kg (under the BET method) with an average particle size of 5.15 ± 0.21 microns.

Limestone was ground with material with a fraction of 0.315–0.63 mm picked for the study. The specific surface of the fraction was 6.4 ± 0.3 m²/kg (as per Tovarov) and 21.4 ± 1 m²/kg (under the BET method) with an average particle size of 380 ± 10 microns.

The specific surface of the gypsum plaster was 260 ± 11.75 m²/kg (as per Tovarov) and 754 ± 15.1 m²/kg (under the BET method) with an average particle size of 8.7 ± 0.26 microns.

Portland cement, gypsum plaster and limestone underwent treatment in a vortex layer machine manufactured by OOO "Regionmettrans"; model 297. The paper [20, 21] presents a typical vortex layer machine design.

The specific surface was determined by relying on the air permeability method using a PSH-9 device and the BET method (Nova 1200e Quantachrome analyzer).

The magnetic field induction was determined by a magnetometer with a Hall sensor.

A TemPro 300 pyrometer was used to measure the temperature of materials treated in the vortex layer machine. The device operates in a measurement range of 32 to 350 °C and offers a measurement accuracy of ± 1.5 °C.

The duration of treatment by the vortex layer machine was assumed to be the same and amounted to five minutes in the case of Portland cement and limestone and three minutes in the case of gypsum plaster.

The effects observed as the materials were being treated in the vortex layer machine were assessed based on two criteria:

- location of the maximum values $S_{ud,T}$, $S_{ud,BET}$ and T_{max} in the factor space which determines the intensity of vortex layer machine treatment ($S_{ud,T}$ is the specific surface determined under the Tovarov method; $S_{ud,BET}$ is the specific surface determined by the BET method; T_{max} is the maximum heating temperature of material powder after having been treated in a vortex layer machine). The magnetic field induction (X_1) and the electromagnetic field rotation frequency (X_2) were the factors which determined the material treatment mode in the vortex layer machine;
- symbiosis of the change $S_{ud,BET}(X_1, X_2)$ and $T_{max}(X_1, X_2)$.

3. Results and Discussion

The criteria have been selected based on the following scientific hypothesis. In the process of electromagnetic mechanical activation, the treated substance is affected by both the mechanical shock effects of ferromagnetic particles and electromagnetic forces (the Lorentz force and the effect of electromagnetic field strength). However, a certain intensity may make the mechanical action of ferromagnetic bodies cause various defects which naturally results in the area of the phase interface growing. Given the specificity of the resulting defects, a change like this in the phase interface can be recorded through the specific surface area based on the BET method. The mechanical action which comes next causes defects, cracks and the destruction of particles in the material being treated. This naturally leads to increasing dispersion which can be recorded through the specific surface area based on the Tovarov method.

A material being treated in a vortex layer machine sees an increase in temperature. This impacts the effects which occur when an electromagnetic field is being applied to the substance of a material. In the case of dielectrics, an increase in temperature leads to a disruption in the orientation of the dipoles [22, 23], while crystals are exposed to a Peierls-Nabarro effect which consists in inhibited movement of dislocations [24–26]. Still, the contribution of the aforementioned effect is significant at low temperatures only. It is clear that the impact of temperature will be of extreme nature. A point of extremum reached should be followed a decrease in the level of defectiveness of the material being treated characterized by $S_{ud,BET}$. A change in the treatment mode (factors X_1 and X_2) should naturally lead to a virtually linear increase in the temperature of the material. It appears from the foregoing that certain values of the factors $X_{1,S}$ and $X_{2,S}$ cause a disruption in the symbiosis of the way in which $S_{ud,BET}(X_1, X_2)$ and $T_{max}(X_1, X_2)$ divert from the variable factors. This point of the factor space once achieved means that the competing processes of the effects of the electromagnetic field and of the temperature on the defectiveness of the material have reached the same intensity.

The increasing effects of competing processes caused by temperature as a material is being treated in the vortex layer machine will indicate that the following condition has been fulfilled:

$$\frac{dS_{ud,BET}(X_1, X_2)}{dX_i} < \frac{dT_{max}(X_1, X_2)}{dX_i} \quad (3)$$

The concept of vortex layer machine material treatment – an increase of particle defectiveness (up to $S_{ud,BET}(X_1, X_2) = \max$) → development of defects and dispersion of particles of the material being treated (up to $S_{ud,T}(X_1, X_2) = \max$) – indicates that an optimal mode of vortex layer machine material treatment ensuring its mechanical activation should be in the interval between the specified points of the factor space.

A two-factor composite (rotatable) plan is has been designed to test the concept with a quadratic model used:

$$Y(X_1, X_2) = b_0 + b_1X_1 + b_2X_2 + b_{12}X_1X_2 + b_{11}X_1^2 + b_{22}X_2^2, \quad (4)$$

where b_i are the parameters of the experimental-statistical model.

The variable parameters included the magnetic field induction in the working chamber of the vortex layer machine (X_1) with a parameter boundary of 0.06 T to 0.24 T, a variation interval of 0.09 T. The frequency of rotation of the electromagnetic field (X_2) had a parameter boundary of 30 to 110 Hz and a variation interval of 40 Hz.

Under this concept the responses turned out to be $S_{ud,T}$, $S_{ud,BET}$ and T_{max} .

An experiment planning matrix which shows the desired responses for model materials under examination is given in Table 1.

Table 1. Planning matrix and experiment results.

Plan point	Factor		Specific surface, m ² /kg (under the Tovarov method)	Specific surface area, m ² /kg (BET)	Average particle size, microns	Powder temperature after treatment, °C
	X_1	X_2				
Portland cement						
1	0.06	30	460±22.0	1255±21.0	4.22±0.17	85
2	0.24	30	505±24.0	1405±24.0	3.90±0.17	90
3	0.06	110	385±18.0	1055±18.0	5.11±0.20	80
4	0.24	110	415±20.0	1160±19.5	4.69±0.18	82
5	0.02	70	550.0±26.0	1780±28.5	3.43±0.16	110
6	0.28	70	610.0±29.0	2075±37.2	3.09±0.12	120
7	0.15	13.43	410±20.0	1125±19.0	4.73±0.18	55
8	0.15	126.57	395±19.0	1095±18.5	5.28±0.21	45
9	0.15	70	580.0±28.0	1930±32.6	3.17±0.14	115
Gypsum plaster						
1	0.06	30	326±13.0	984±19.0	6.81±0.2	73
2	0.24	30	387±15.3	1124±22.5	5.85±0.17	79
3	0.06	110	265±10.6	792±15.8	8.55±0.25	67
4	0.24	110	295±11.8	904±18.1	7.67±0.23	72
5	0.02	70	439±17.6	1599±31.9	5.16±0.15	101
6	0.28	70	571±22.8	2132±42.6	3.96±0.12	111
7	0.15	13.43	286±11.4	859±17.2	7.92±0.23	49
8	0.15	126.57	275±11.0	832±16.6	8.23±0.25	41
9	0.15	70	505±20.2	1851±37.1	4.48±0.13	106
Limestone						
1	0.06	30	160±6.5	545±11.0	14.1±0.56	76
2	0.24	30	190±7.5	660±13.0	11.9±0.47	82
3	0.06	110	130±5.0	435±8.5	17.5±0.7	71
4	0.24	110	145±6.0	500±10.0	15.9±0.64	74

Plan point	Factor		Specific surface, m ² /kg (under the Tovarov method)	Specific surface area, m ² /kg (BET)	Average particle size, microns	Powder temperature after treatment, °C
	X_1	X_2				
5	0.02	70	215±8.5	885±17.5	10.8±0.43	103
6	0.28	70	280±11.0	1180±23.5	8.2±0.33	109
7	0.15	13.43	140±5.5	475±9.5	16.3±0.65	47
8	0.15	126.57	135±5.5	460±9.0	17.1±0.68	40
9	0.15	70	245±10.0	1025±20.5	9.3±0.37	107

Values of the parameters of the experimental and statistical models (4) are given in Table 2.

Table 2. Coefficients of the parameters of the obtained experimental and statistical models.

Property	Model parameter					
	b_0	b_1	b_2	b_{12}	b_{11}	b_{22}
Portland cement						
Specific surface area under the Tovarov method, m ² /kg	580	20	-23.3	-3.8	-12.5	-101.3
Specific surface under the BET method, m ² /kg	1935	85.1	-60.3	-11.3	-74.2	-487.3
Average particle diameter, microns	3.2	-0.1	0.3	-0.03	0.1	1
Powder temperature after treatment, °C	115	2.6	-3.4	-0.8	0.4	-32
Gypsum plaster						
Specific surface area under the Tovarov method, m ² /kg	505	34.7	-21.1	-7.8	-18.6	-130.9
Specific surface under the BET method, m ² /kg	1851	132.2	-56	-6.5	-92.1	-602.1
Average particle diameter, microns	4.5	-0.4	0.5	0.02	0.2	2
Powder temperature after treatment, °C	106	3.1	-3	-0.3	-0.7	-31.2
Limestone						
Specific surface area under the Tovarov method, m ² /kg	245	17.1	-10.3	-3.8	-7.8	-62.8
Specific surface under the BET method, m ² /kg	1025	74.7	-36.4	-12.5	-50	-332.5
Average particle diameter, microns	9.3	-0.9	1	0.1	0.5	4.1
Powder temperature after treatment, °C	107	2.2	-2.9	-0.8	-0.3	-31.5

The analysis given in Table 2 shows that in the case of all of the materials under examination, the maximum values $S_{ud,T}$, $S_{ud,BET}$ and T_{max} are in the factor space on the same line at $X_2 = 66$ Hz.

Typical graphs $S_{ud,BET} = f(X_1)$, $S_{ud,T} = f(X_1)$ and $T_{max} = f(X_1)$ are shown in Fig. 1 (at $X_2 = 66$ Hz) which also shows the location of the maximum values of these dependencies with their actual values presented in Table 3. The coordinate $X_{1,s}$ is the boundary X_1 which when surpassed leads to a disruption in the symbiosis of the change of $S_{ud,BET} = f(X_1)$ and $T_{max} = f(X_1)$ has been determined based on the following formula:

$$X_{1,s} = \frac{2b_{11}}{b_1 + b_{12}X_2} \quad (5)$$

and the condition (3) can be converted to appear as follows:

$$\frac{k_s X_1 + 1}{k_T X_1 + 1} \leq 1, \tag{6}$$

where $k_i = 2b_{11,i} / (b_{1,i} + b_{12,i} X_2)$; indexes "s" and "T", respectively, for $S_{ud,BET} = f(X_1)$ and $T_{max} = f(X_1)$; $X_2 = \text{const}$.

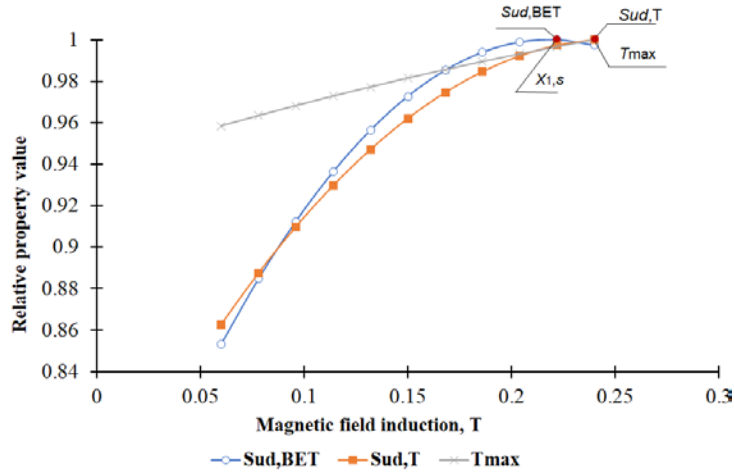


Figure 1. A typical graph of dependencies of $S_{ud,BET} = f(X_1)$, $S_{ud,T} = f(X_1)$ and $T_{max} = f(X_1)$.

The data shown in Fig. 1 and Table 3 support the validity of the concept of vortex layer machine material treatment: the temperature of the material powder goes up in the process of treatment; the dependency $T_{max} = f(X_1)$ is rectilinear; accumulation of defects is of extreme nature caused by development of defects resulting in an increase in the dispersion of the powder of the material being treated. This is also evidenced by the location of the maximum values $S_{ud,BET}$ and $S_{ud,T}$:

$$|X_1|_{S_{ud,T}} > |X_1|_{S_{ud,BET}} . \tag{7}$$

Table 3. Coordinates of points in the factor space.

Material	Coordinates of points in the factor space								
	Properties								
	$S_{ud,BET}$		$S_{ud,T}$		T_{max}		$X_{1,S}$	$X_{2,S}$	Condition (3)
	X_1, T	X_2, Hz	X_1, T	X_2, Hz	X_1, T	X_2, Hz	T	Hz	
Portland cement	0.204	66	0.222	66	0.24	66	0.230		+
Gypsum plaster	0.213	66	0.24	66	0.24	66	0.231	66	+
Limestone	0.222	66	0.24	66	0.24	66	0.233		+

The analysis of experimental and statistical models demonstrates that the condition (3) is fulfilled. The mechanically activated mineral component requires that two conditions be fulfilled: an increase in the dispersion (1) and the defectiveness (2) of the particles of the powder being treated. Under the concept, these conditions correspond to the equality:

$$S_{ud,BET}(X_1) = S_{ud,T}(X_1). \tag{8}$$

The equality (8) for Portland cement is met at $X_{1,opt} = 0.21 T$, for gypsum plaster – at $X_{1,opt} = 0.22 T$, and for limestone at $X_{1,opt} = 0.23 T$.

An analysis of the effect of the mode selected on accumulation of defects $S_{ud,BET} = f(X_1)$ allows the susceptibility parameter which is calculated by the formula:

$$K_{ac} = \frac{S_{ud,BET}(X_{1,min})}{S_{ud,BET,max}}, \quad (9)$$

($S_{ud,BET,max}$ is the maximum value of the specific surface area as determined by the BET method) to arrange the mineral components in question in the following order:

Limestone > gypsum plaster > Portland cement.

This classification differs from the other classifications which are based on:

- the criteria of iron ion content and/or magnetic susceptibility;
- the criterion of grind ability.

Under the first classification the materials in question can be arranged in the following order based on their properties (Table 4):

Portland cement > Gypsum plaster > Limestone,

under the second classification:

Gypsum plaster > Limestone > Portland cement.

Table 4. Some properties of the materials under examination

Material name	Type of substance	The content of iron ions in fixed form	Magnetic susceptibility, χ
Portland cement	Paramagnetic	+	$45 \cdot 10^{-5}$
Gypsum plaster	Paramagnetic	–	$12 \cdot 10^{-5}$
Limestone	Diamagnetic	–	$-300 \cdot 10^{-5}$

Note. The "+" symbol indicates presence, the "-" symbol indicates absence or the need for further research.

The classification difference shown here serves to confirm once again that the electromagnetic field and the temperature produce a mutual effect when materials are being treated in a vortex layer machine.

4. Conclusion

1. The paper proposes and justifies a concept of material treatment by vortex layer machines which consists in a consistent increase in the defectiveness of particles (up to $S_{ud,BET}(X_1, X_2) = \max$) with subsequent development of defects and dispersion of particles in the material being treated (up to $S_{ud,T}(X_1, X_2) = \max$). However, the temperature of material powder when it is being treated rises almost linearly accompanied by extreme kinetics of defect accumulation resultant from development of defects which gives rise to an increase in the dispersion of the powder of the material being treated. The electromagnetic field and temperature have been confirmed to have competing effects in the range of vortex machine treatment parameters under examination.

2. The effects of the magnitude of the induction value and the frequency of rotation of the electromagnetic field on the specific surface and the temperature of the powders of Portland cement, gypsum plaster and limestone after being treated in a vortex layer machine have been determined. It has established that the highest values of the specific surface are achieved at a frequency of rotation of electromagnetic field of 66 Hz while the conditions to increase the dispersion and defectiveness of the particles of the powder being treated are fulfilled at a value of electromagnetic field induction of 0.21 T with Portland cement; 0.22 T – with gypsum plaster and 0.23 T with limestone.

3. The paper proposes a classification of the susceptibility of mineral components to treatment in vortex layer machines (per criterion $S_{ud,BET}$ in decreasing order): Limestone > gypsum plaster > Portland cement.

References

1. Mucsi, G. A review on mechanical activation and mechanical alloying in stirred media mill. 148. Institution of Chemical Engineers, 01-08-2019.
2. Acar, I., Acisli, O. Mechano-chemical surface modification of calcite by wet-stirred ball milling. Applied Surface Science. 2018. 457. Pp. 208–213. DOI: 10.1016/j.apsusc.2018.06.247

3. Boldyreva, E. Mechanochemistry of inorganic and organic systems: What is similar, what is different? *Chemical Society Reviews*. 2013. 42 (18). Pp. 7719–7738. DOI: 10.1039/c3cs60052a. URL: <https://pubmed.ncbi.nlm.nih.gov/23864028/> (date of application: 20.03.2021).
4. Trejbal, J. Mechanical properties of lime-based mortars reinforced with plasma treated glass fibers. *Construction and Building Materials*. 2018. 190. Pp. 929–938. DOI: 10.1016/j.conbuildmat.2018.09.175
5. Arizzi, A., Cultrone, G. Comparing the pozzolanic activity of aerial lime mortars made with metakaolin and fluid catalytic cracking catalyst residue: A petrographic and physical-mechanical study. *Construction and Building Materials*. 2018. 184. Pp. 382–390. DOI: 10.1016/j.conbuildmat.2018.07.002
6. Morozov, V.A., Petrov, Y.V., Sukhov, V.D. Experimental Evaluation of Structural and Temporal Characteristics of Material Fracture Based on Magnetic Pulse Loading of Ring Samples. *Technical Physics*. 2019. 64 (5). Pp. 642–646. DOI: 10.1134/S1063784219050165
7. Atroshenko, S.A., Morozov, V.A., Kats, V.M., Gribov, D.A., Petrov, Y. V. Rupture of copper rings by a magnetic-pulse method over a wide range of loading times. *Procedia Structural Integrity*. 2018. 13. Pp. 1373–1377. DOI: 10.1016/j.prostr.2018.12.287
8. Khaydarov, B., Suvorov, D., Pazniak, A., Kolesnikov, E., Gorchakov, V., Mamulat, S., Kuznetsov, D. Efficient method of producing clinker-free binding materials using electromagnetic vortex milling. *Materials Letters*. 2018. 226. Pp. 13–18. DOI: 10.1016/j.matlet.2018.05.016
9. Ibragimov, R.A., Korolev, E.V., Deberdeev, T.R., Leksin, V.V. Efficient complex activation of Portland cement through processing it in the vortex layer machine. *Structural Concrete*. 2019. 20 (2). Pp. 851–859. DOI: 10.1002/suco.201800008
10. Ibragimov, R.A., Korolev, E.V., Kayumov, R.A., Deberdeev, T.R., Leksin, V.V., Sprince, A. Efficiency of activation of mineral binders in vortex-layer devices. *Magazine of Civil Engineering*. 2018. 82 (6). Pp. 191–198. DOI: 10.18720/MCE.82.17
11. Calus, D., Makarchuk, O. Analysis of interaction of forces of working elements in electromagnetic mill. *Przeglad Elektrotechniczny*. 2019. 95 (12). Pp. 64–69. DOI: 10.15199/48.2019.12.12
12. Ogonowski, S., Ogonowski, Z., Pawelczyk, M. Multi-objective and multi-rate control of the grinding and classification circuit with electromagnetic mill. *Applied Sciences (Switzerland)*. 2018. 8 (4). DOI: 10.3390/app8040506
13. Davydov, V.N., Karankevich, O.A. Application of the Onsager Principle to the Polar-axial Phenomena in Crystal Physics. *Russian Physics Journal*. 2019. 61 (10). Pp. 1922–1932. DOI: 10.1007/s11182-019-01619-w
14. Zhigachev, A.O., Rodaev, V.V., Umrikhin, A.V., Golovin, Y.I. The effect of silica content on microstructure and mechanical properties of calcia-stabilized tetragonal zirconia polycrystalline ceramic. *Ceramics International*. 2019. 45 (1). Pp. 627–633. DOI: 10.1016/j.ceramint.2018.09.220
15. Darinskaya, E.V., Koldaeva, M.V., Alshits, V.I., Voloshin, A.E., Pritula, I.M. Threshold Effects of the Magnetic Influence on the Microhardness of KDP Crystals. *JETP Letters*. 2019. 110 (4). Pp. 279–283. DOI: 10.1134/S0021364019160045
16. Alshits, V.I., Darinskaya, E.V., Koldaeva, M.V., Petrzhih, E.A. Paradoxes of the influence of small Ni impurity additions in a NaCl crystal on the kinetics of its magnetoplasticity. *Journal of Experimental and Theoretical Physics*. 2016. 122 (1). Pp. 118–130. DOI: 10.1134/S1063776115130014
17. Egorov, I.N., Egorova, S.I., Kryzhanovsky, V.P. Particle size distribution and structural state analysis of mechanically milled strontium hexaferrite. *Materials Science Forum*. 2019. 946 MSF. Pp. 293–297. DOI: 10.4028/www.scientific.net/MSF.946.293
18. Morozov, V., Kats, V., Savenkov, G., Lukin, A. Mechanisms of fracture of ring samples made of FCC metals on loading with magnetic-pulse method. *AIP Conference Proceedings*. 2018. 1959. DOI: 10.1063/1.5034753
19. Zaychenko, O.K., Morozov, V.A. Building a stress calculation model for dynamic deformation of metal rings under magnetic loads. *Journal of Physics: Conference Series*. 2019. 1203 (1). DOI: 10.1088/1742-6596/1203/1/012018
20. Wołosiewicz-Głab, M., Foszcz, D., Ogonowski, S. Design of the electromagnetic mill and the air stream ratio model. *IFAC-PapersOnLine*. 2017. 50 (1). Pp. 14964–14969. DOI: 10.1016/j.ifacol.2017.08.2554. URL: www.sciencedirect.com (date of application: 20.03.2021).
21. Ogonowski, S., Wołosiewicz-Głab, M., Ab, Ogonowski, Z., Foszcz, D., Pawelczyk, M. minerals Comparison of Wet and Dry Grinding in Electromagnetic Mill. 2018. DOI: 10.3390/min8040138. URL: www.mdpi.com/journal/minerals (date of application: 20.03.2021).
22. Poplavko, Y.M. Dielectrics. *Electronic Materials*. Elsevier, 2019. Pp. 287–408.
23. Poplavko, Y., Yakymenko, Y. Physical nature of crystal internal polarity. *Functional Dielectrics for Electronics*. Elsevier, 2020. Pp. 1–49.
24. Edagawa, K., Kamimura, Y., Iskandarov, A.M., Umeno, Y., Takeuchi, S. Peierls stresses estimated by a discretized Peierls–Nabarro model for a variety of crystals. *Materialia*. 2019. 5. Pp. 100218. DOI: 10.1016/j.mta.2019.100218
25. Boldyrev, V.V. Mechanochemical processes with the reaction-induced mechanical activation. *Chemo-mechanochemical effect*. 67 (6). Springer, 01-06-2018.
26. Stroganov, V., Sagadeev, E., Ibragimov, R., Potapova, L. Mechanical activation effect on the biostability of modified cement compositions. *Construction and Building Materials*. 2020. 246. Pp. 118506. DOI: 10.1016/j.conbuildmat.2020.118506

Information about authors:

Ruslan Ibragimov,

PhD in Technical Science

ORCID: <https://orcid.org/0000-0001-8879-1190>

E-mail: rusmag007@yandex.ru

Evgeny Korolev,

Doctor in Technical Science

ORCID: <https://orcid.org/0000-0003-0815-4621>

E-mail: korolev@nocnt.ru

Received 31.03.2021. Approved after reviewing 23.11.2021. Accepted 26.11.2021.



Research article

UDC 624.31

DOI: 10.34910/MCE.114.9



Bolted connections stiffness of steel trusses for bridge superstructures

D.A. Valiullin , S.V. Chizhov 

St. Petersburg State Transport University, St. Petersburg, Russia

✉ damirvall@rambler.ru

Keywords: connection stiffness, semi-rigid connection, steel truss, railway bridge, finite-element analysis, Ansys Mechanical

Abstract. The article assesses stiffness of main trusses bolted connections in the railway bridges metal superstructures. The generally accepted approach for trusses of bridge structures analysis is to replace joints with hinges. This technique simplifies finding the forces in structure elements, but reduces the reliability of the design model. In this study, the finite element method implemented in the Ansys Mechanical software package is used. The process of determining the stiffness of the high-strength bolts joint connection is described in detail. The paper proposes formulas to determine rotation angles of the truss elements joint sections according to the finite element model analysis results. For two joints of a standard design, superstructure stiffness was determined: $kN_2 = 107183.06 \text{ kN}\cdot\text{m}/\text{rad}$, $kN_3 = 137605.56 \text{ kN}\cdot\text{m}/\text{rad}$. Graphs of bending moment on the rotation angle dependence were also made. It was concluded that the beam model of the structure shows underestimated values of the joints stiffness, and the difference with the stiffness determined for the detailed finite element model can reach 5.635.

Citation: Valiullin, D.A., Chizhov, S.V. Bolted connections stiffness of steel trusses for bridge superstructures. Magazine of Civil Engineering. 2022. 114(6). Article No. 11409. DOI: 10.34910/MCE.114.9

1. Introduction

Nowadays, when designing new and reconstructing existing bridge structures on the Russian Federation territory, engineers are guided by the SP 35.13330.2011 "Bridges and Pipes" code specification, which allows replacing rigid joints in connections with hinges when analyzing lattice trusses, if the structure remains unchanged and the ratio of the truss element section height to its length is ensured to be not more than 1:15. If the last condition is not met, when analyzing the strength and fatigue behavior of the lattice trusses elements with high-strength bolts connections, it is necessary to take into account the joints stiffness, and the elements longitudinal forces can be determined according to the hinge scheme. However, there are no direct instructions on how to take into account the connections stiffness in the code specification. Note here, that this approach to the lattice trusses analysis can be found in all specification documents of the USSR since 1938: in TUPM-38 (Technical conditions for the design of bridges and pipes), in TUPM-47, in 1955 additions and changes to TUPM-47, as well as in SN 200-62. Therefore, it can be argued that the question of how to take into account the connection stiffness and its effect on the reliability and durability of the structure has not yet been finally answered.

However, there are publications on this topic that need to be mentioned here to represent the level of knowledge on this issue.

First, let us turn to foreign specification documents. According to the fourth edition of the AASHTO LRFD, a truss can be analyzed as hinged structure when loads are applied to the panel nodes. European norms introduce a classification of nodes according to two criteria: stiffness and strength. Note, however,

that although Eurocode 1993-2-2009 refers to Eurocode 1993-1-8 in terms of connections modeling, the provisions given here are applicable more to the field of building design.

As shown in [1], a number of outstanding scientists of the second half of the 19th century were engaged in the elimination of the lattice trusses stress-strain state with rigid connections at the joints: Manderla, Engesser, Azimont, Winkler, Ritter and Landsberg, Müller-Breslau, Mor. At the beginning of the 20th century, the works of national researchers appeared – E.O. Paton, E.V. Zotikov, G.P. Peredery, K.M. Dubyaga, N.V. Nekrasov. But the obtained results contradicted each other in many ways, therefore, subsequently, this area practically did not develop.

The works [2–5] are devoted to the necessity of considering the connections as semi-rigid joints in the analysis of the wooden trusses state. Some methods of taking into account the real characteristics of connections are given, which show a good approximation to real structures.

Detailed analysis of joints of metal beams and columns of buildings have been carried out [6–12]. The obtained results indicate that the reliability and bearing capacity of the joints is influenced by a whole set of factors: the geometric dimensions of the joined elements, the configuration of the attachment unit, the bolts diameter.

The detailed stress-strain state analysis of four different systems taking into account the connection joints stiffness was carried out in [13]. Taking the stiffness of the hinge connection as 0, and the stiffness of an absolutely rigid connection as 100 %, the authors showed the presence of a relationship between the values of internal forces and displacements and the degree of restraint in the connection. Some continuation of this study can be found in [14], where the analysis of the relationship between the dynamic characteristics of railway bridge superstructure and the connections rotational stiffness was made.

As shown in [15–17], the most important characteristic of the joint connection is the graph with the "Angle of rotation" – "Moment" axes. In general, this is a curve that characterizes the dependence of the bending moment arising in the joint on the angle of rotation; the tangent of the slope of this curve to the abscissa axis characterizes the joint stiffness, which is expressed by the formula:

$$K_s = \frac{M}{\theta}, \quad (1)$$

where M is the bending moment, expressed in kN, and θ is rotation angle, expressed in radians.

Eurocode 1993-1-8 allows simplification of the non-linear relationship between the rotation angle and the bending moment; thus, bilinear approximation has become widespread (dashed line in Fig. 1).

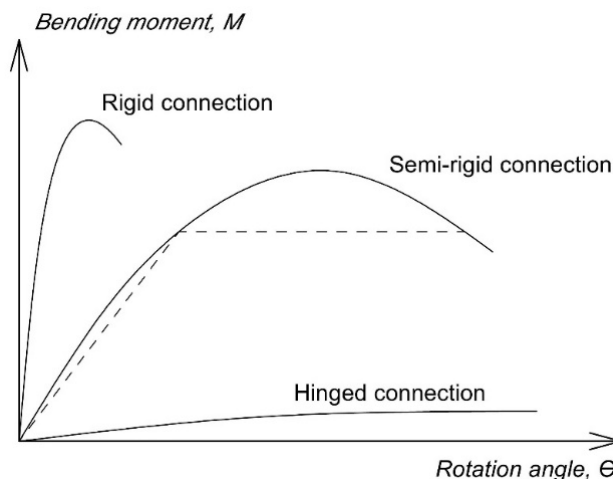


Figure 1. Dependence of the bending moment on the rotation angle at the joint.

The Eurocode approach to the truss joints classification has some drawbacks: firstly, stiffness and strength criteria are considered separately, what can lead to difficulties in the choice of a specific category. Secondly, the possibility of joint category changing at different stages of loading is not taken into account. In this regard, the need for development of a different classification system devoid of the indicated inaccuracies arises. The article [18] is devoted to this issue.

Articles [19–21] are devoted to the study of various aspects of the work of gusset plates as part of bridge trusses and building frames. Analysis of the gussets joints dimensions assigning approaches was made. A nonlinear model to take them into account when analyzing frame structures and assessed the stiffness of the attached elements, initial imperfections, eccentricity of load application impact on the stress-strain state of gussets was proposed.

According to [22, 23], detailed modeling of bridge structures makes it possible to identify reserves of bearing capacity, as well as alternative ways of forces distributing in case of bearing elements failure.

Works [24–27] describe various approaches of taking into account the joint connections stiffness when analyzing the frames of buildings. The authors paid great attention to the mathematical substantiation of the proposed procedures, and also gave specific examples of structural analysis.

Works [28–31] are devoted to the finite element method application in the study of the operation of joint connections for various purposes structures. Comparison of the results obtained by experimental and numerical methods is performed. It is shown that numerical modeling makes it possible to assess the stress-strain state of a structure with the required degree of accuracy; moreover, data become available that is not possible to obtain experimentally.

Connections of lattice structures of power transmission line supports were investigated in works [32, 33]. It is shown that bolted joints have a great influence on the deformed state of this type of structures.

Based on the performed review of scientific publications, we can conclude the following: in world practice, an approach to the consideration of bolted connections of building frames as semi-rigid joints has become widespread. At the same time, the concept of a semi-rigid connection is practically not used in the design of metal trusses for transport structures. Despite the external similarity of the aforementioned structures, the conditions of their operation are fundamentally different: while the columns and beams of buildings work mainly on static loads (compressive longitudinal force and bending moment, respectively), the elements of the bridge structures trusses experience a complex dynamic effect from the circulating moving loads with a predominance of longitudinal compressive and tensile forces. At the same time, as noted in [34, 35], the joint connection stiffness has an insignificant effect on the results of the static analysis of structures, but the dependence of their dynamic characteristics on the joints properties is much greater. The problem of correct determination of the bridge structures dynamic characteristics is becoming especially urgent now, with the advent of high-speed railways.

The connections of the bridge superstructures main trusses elements have a very complex composition. For through bridges, this connection, as shown in Fig. 2, represents the area of braces, chords, stands and crossbeams intersection. The elements are joined by overlapping with gusset plates, followed by the installation of high-strength bolts. Obviously, such a connection is neither hinged nor absolutely rigid; it has some intermediate properties, and therefore received the name "*semi-rigid connection*".

Moreover, there is no doubt that the stiffness of such assemblies depends on many factors: the connected elements geometry, the thickness and dimensions of the gusset plates, the number and degree of tension of high-strength bolts. Therefore, the problem of determining the stiffness of bridge superstructures metal trusses joints is practically insoluble from the point of view of structural analysis approaches.

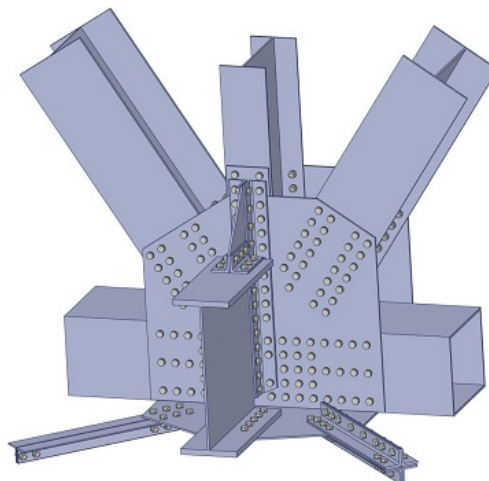


Figure 2. Joint of a standard design railway bridge superstructure.

In our opinion, the only possible way to solve the original problem is the finite element method implemented in software packages such as Ansys. With a certain degree of detail, the created mathematical model will make it possible to assess the influence of all the above factors on the joint properties.

When writing this article, we set a goal of assessing the bolted connections stiffness of main trusses for bridge steel superstructures. For this, the following tasks are being solved:

- a detailed finite element model of a fragment of the analyzed railway bridge lattice superstructure is being developed;
- stiffness of the main truss joint connections are determined;
- a comparative analysis of the superstructure beam and detailed finite element models are performed.

2. Methodology of numerical experiment

2.1. General information

Since the use of software packages implementing the finite element method in the investigation of complex detailed models requires large computational resources, it was decided to analyze the structure in two steps:

1. Beam model analysis. This stage is necessary to assess the general stress-strain state of the structure and to check the correctness of the assignment of general parameters, such as material properties, sections of elements, support fixings.
2. Within the framework of the beam model, the investigated elements are modeled in detail using shell finite elements.

2.2. Description of the superstructure under study

The structure under study is a metal superstructure with through trusses, manufactured according to standard design No. 3.501-30/75. The span of this single-track railway bridge is 55 m. The main elements of the superstructure are made of 15KhSND low-alloy steel. Lattice truss elements are welded as box-shaped and H-shaped sections with field connections on high-strength bolts. Box-shaped elements have a perforated bottom chord, perforation dimensions are 270 × 600 mm, the distance between perforation centers is 1200 mm. The chords connections are aligned with the main trusses joints and are located at 11 m intervals.

The main trusses are connected by top and bottom braces in the plane of the chords, portal frames in the plane of the outside braces and struts in the plane of the stands (Fig. 3).

Field connections are made on high-strength bolts with a diameter of 22 mm. All contact surfaces of the joints and connections are sandblasted before assembly. The standard tension force of a high-strength bolt is taken equal to 20 tons.

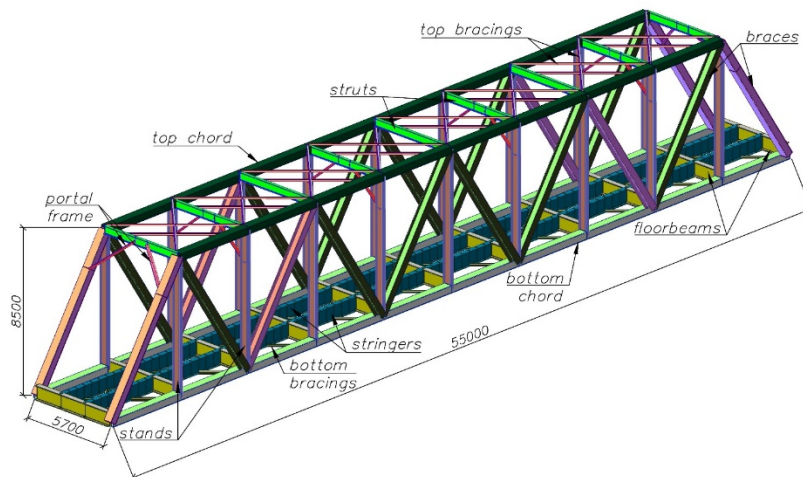


Figure 3. Superstructure beam model.

2.3. Beam model

General view of the superstructure model is shown in Fig. 3.

The analysis was carried out taking into account the linear work of the material, the elastic modulus and Poisson's ratio were set as $E = 2.0 \times 10^5$ MPa and $\mu = 0.3$, respectively. The specific gravity of steel was taken equal to $\rho = 76.98$ kN/m³.

Each element of the beam model has its own type of cross-section with dimensions taken from standard design project. All joint connections are rigid. Supports are installed at the joints of the extreme

braces and the lower chords intersections: fixed supports on one side and supports with displacements along the axis of the bridge on the other side.

Dead loads from the self-weight of the superstructure and the weight of the bridge deck and moving loads from passing trains were applied to the structure.

As a result of the structure analysis, the displacement values of the superstructure finite element model nodes were obtained for the position of the passing trains, at which the biggest longitudinal forces arise in the element under consideration. Optimization of the moving load position was performed in the Midas Civil software package.

2.4. Detailed model

In this work, the stiffness of the joints $N2$ and $N3$ of the lower chord of the superstructure main truss is assessed (Fig. 4).

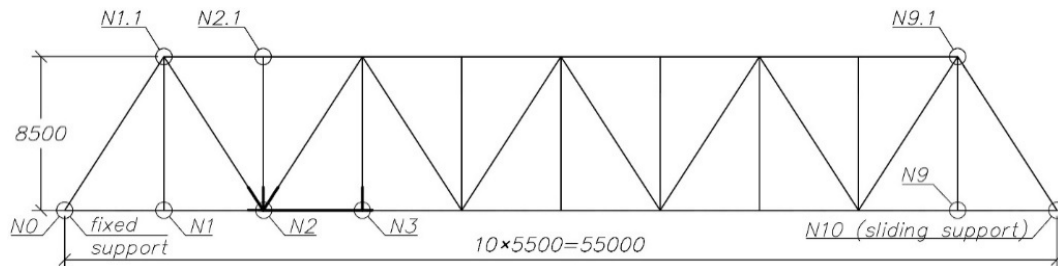


Figure 4. Main truss scheme.

As noted earlier, the actual joint connections of railway bridge trusses are complex assemblies of main elements and high-strength bolts. Therefore, to perform an accurate analysis, it is necessary to carry out a detailed modeling of the truss bottom chord panel between joints $N2$ and $N3$, in which all the components that influence the behavior of the structure will be presented in an explicit form (Fig. 5). At the same time, the study of the stress state of the bolts themselves is not the purpose of this work; therefore, in the analysis they will be represented by equivalent beams, to which a tension force is applied. The main elements of the truss and elements of longitudinal bracings, as well as gussets and angles, are approximated by shell elements. Thus, the stress-strain state of the bottom chord section $N2$ - $N3$ depends only on the properties of the contiguous joints.

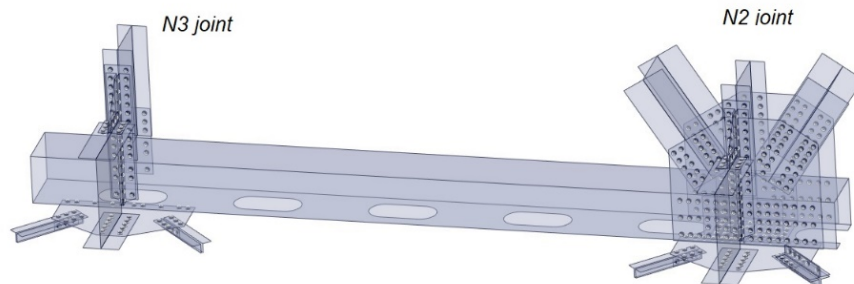


Figure 5. Fragment of the detailed analysis model in Ansys Mechanical.

For the structure material Bilinear Isotropic Hardening property was set with the following characteristics: Yield Strength $\sigma_Y = 345$ MPa and Tangent Modulus $\sigma_T = 696.2$ MPa. The material of high-strength bolts is 40Ch steel with Yield Strength $\sigma_Y = 785$ MPa and Tangent Modulus $\sigma_T = 2029.7$ MPa. All the contacts between elements are Frictional type; + Friction Coefficient is set equal to 0.58.

Truss bottom chord panel with $N2$ and $N3$ contiguous joints attached to the beam part of the model by Fixed Joints. All bolts are tensioned with 196.12 kN Preload force. The total number of high strength bolts in this model is 454 pcs.

The "Face Sizing" option has been applied to the shell elements with a finite element size of 6 mm. Total task size is 809748 nodes and 785004 elements.

2.5. Determination of the joint connections stiffness

As shown earlier, the numerical value of the joint stiffness is the quotient of dividing the bending moment by the angle of rotation of the section. To determine the latter, let us turn to Fig. 6, which shows the vertical displacements of a bottom chord panel between joints N2 and N3. The solid line corresponds to the case of a hinged connection at the truss joints; since in this case only a longitudinal tensile force acts on the element, this line is straight. The dotted line corresponds to the case of a semi-rigid connection with real joint characteristics; this line has a certain curvature, which is due to the presence of fixing in the connections. The angle between the straight and dotted lines is the angle of the section rotation from the action of the bending moment in the plane of the truss (Fig. 7).

The data for the selected cross-sections required for calculating the stiffnesses of the joints, as well as the final result are shown in Table 1.

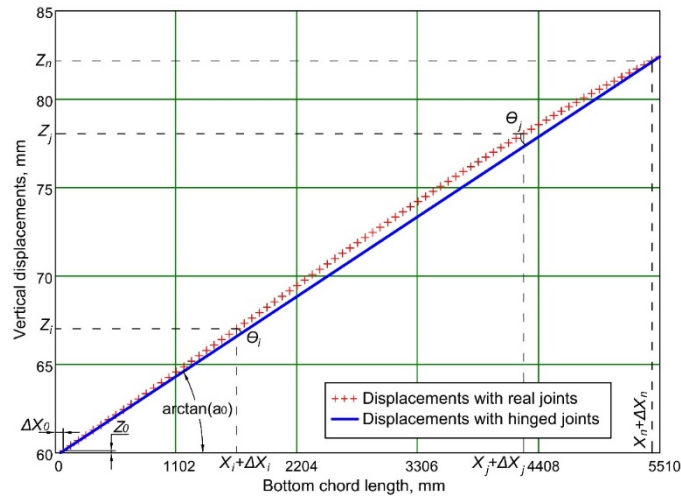


Figure 6. Vertical displacements of the N2-N3 bottom chord panel.

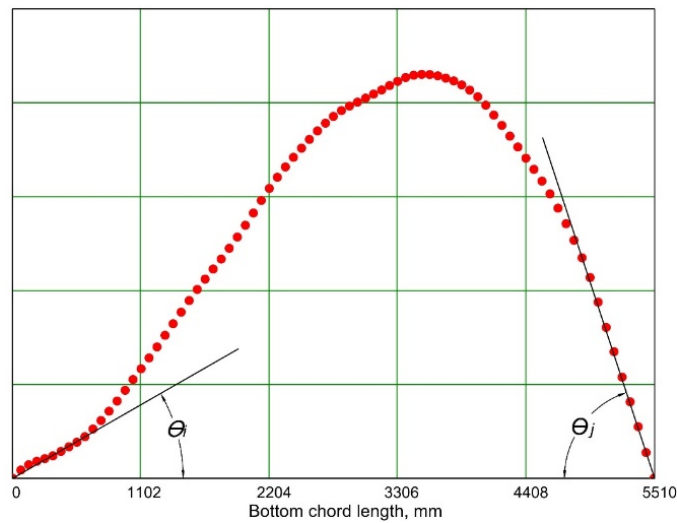


Figure 7. Scheme for determining the angles of rotation.

The angles of rotation θ_i and θ_j are determined based on the analysis of the curve in Fig. 6 using the formulas:

$$\theta_i = \arctan\left(\frac{Z_i - Z_0}{X_i + \Delta X_i - \Delta X_0}\right) - \arctan(a_0); \tag{2}$$

$$\theta_j = \arctan(a_0) - \arctan\left(\frac{Z_n - Z_j}{X_n + \Delta X_n - X_j - \Delta X_j}\right), \tag{3}$$

where Z_0, Z_n, Z_i, Z_j are the coordinates along the vertical axis of the first, end, i^{th} and j^{th} points of the curve, X_n, X_i, X_j are the initial coordinates along the horizontal axis of the end, i^{th} and j^{th} points of the curve, $\Delta X_0, \Delta X_n, \Delta X_i, \Delta X_j$ are displacements of the first, end, i^{th} and j^{th} points of the curve, obtained as a result of deformation from the action of applied loads, a_0 is the slope of the straight line connecting the first and end points of the curve on the graph.

Table 1. Data for determining the stiffness of joint connections

Joint	Angle of rotation, radians	Angle of rotation, degrees	Bending moment, kNxm	Joint stiffness, kNxm/rad
N2	0.0001406726	0.0080599478	15.078	107183.06
N3	0.0007581663	0.0434397292	104.328	137605.56

Note: rotation angle θ_i corresponds to N2 joint, θ_j corresponds to N3 joint.

3. Results and Discussion

Data on the stiffness of joints N2 and N3 is shown in Table 1. However, of greater interest are the dependence graphs of the bending moment and the angle of rotation in the joint, which clearly demonstrate the change in the connection stiffness depending on the magnitude of the applied loads. The graphs in Fig. 8 and 9 are derived from the structure load history analysis in Ansys Mechanical.

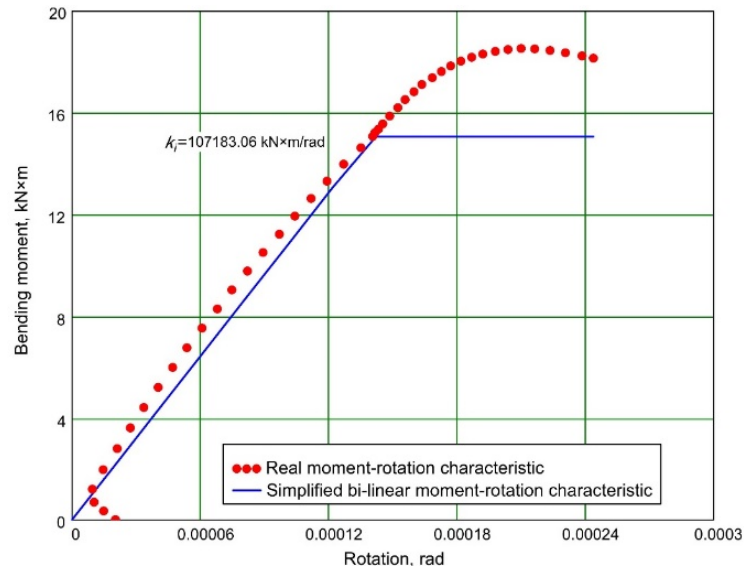


Figure 8. Graph of the N2 joint stiffness.

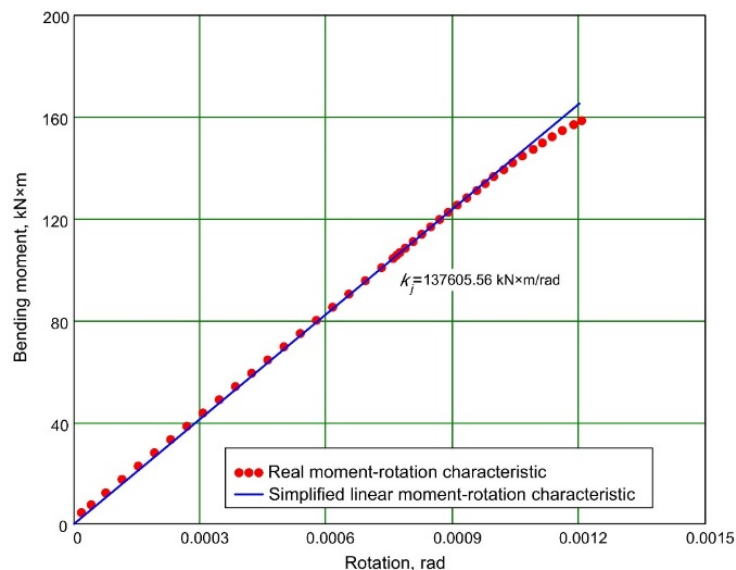


Figure 9. Graph of the N3 joint stiffness.

Let us remark here that the graph of the stiffness of the $N2$ joint has the same form as the curves obtained in [24, 25, 28, 29, 36, 37]. However, despite the indicated external similarity, the obtained values are very different. Comparing the rotation angles of $N2$ joint, shown in Fig. 8, and the values obtained in [28] for the Specimen SC7, we see that the beam-column connection of buildings steel frames are more flexible – the maximum rotation angles obtained within a numerical experiment differ by 250 times. The curve corresponding to joint $N3$ requires further study as part of a separate finite element model.

Conspicuous is the fact that the $N3$ joint stiffness is 1.284 times higher than the $N2$ joint stiffness. The greater flexibility of $N2$ joint can be explained by the fact that it is aligned with the truss lower chord connection, while in $N3$ joint the lower chord is continuous.

An interesting question is how accurate the result on the joint connections stiffness can be obtained from the beam model analysis. Data on the stiffness of beam model joints $N2$ and $N3$ is shown in Table 2.

Table 2. Joint connections stiffness in beam model.

Joint	Angle of rotation, radians	Angle of rotation, degrees	Bending moment, kNxm	Joint stiffness, kNxm/rad
$N2$	0.0003222700	0.0184647119	6.13	19021.32
$N3$	0.0006856034	0.0392821833	50.05	73001.38

In this case, $N3$ joint stiffness is also greater than $N2$ joint stiffness, and the stiffness ratio is equal to 3.838.

At the same time, the stiffness of the $N2$ joint for the case with detailed models of connections is 5.635 times higher than the corresponding characteristic for the case with a full beam model. For $N3$ joint this ratio is equal to 1.885. Such a difference in the obtained results can be explained by the fact that the beam model does not consider the complex stress-strain state in the truss joint. It can also be concluded that the more complex the construction joint, the less accurate results obtained from the analysis of the beam model. Based on the above, we can argue that the beam model of the structure is not able to give an adequate assessment of the complex joint connections stiffness.

Let us note the difference in the graphs of the analyzed joints stiffness. For node $N2$, two stages of work are clearly traced: linear, up to the value of the rotation angle $\theta_i = 0.0001406726$ radian, and nonlinear afterwards. For $N3$ joint the stiffness is linear for all values obtained as a result of a numerical experiment.

4. Conclusions

1. This work presented an assessment of bolted connections stiffness in steel trusses of bridge superstructures. In the Ansys Mechanical software package it was analyzed a detailed finite element model of the truss bottom chord panel as part of the entire structure. This approach makes it possible, without additional constructions, to determine the joints stiffness when calculating the entire superstructure.

2. In the process of writing this work, formulas were obtained analytically to determine the angles of rotation θ_i and θ_j of the truss elements joint sections according to the finite element model analysis results.

3. After analysis of the created finite element model, the stiffness values of two connection joints were determined: $k_{N2} = 107183.06$ kNxm/rad, $k_{N3} = 137605.56$ kNxm/rad. The obtained results allow us to conclude that the continuity of the element itself in the connection has a great influence on its rigidity.

4. By comparing the analysis results of the beam and detailed finite element models, we can conclude that the beam model of the structure shows underestimated values of the joints stiffness. At the same time, the values of the joints stiffness for the two indicated cases may differ by a factor of 5.635.

5. Based on the analysis of the dependence of the bending moment on the angle of rotation, the graphs of the stiffness were made for the joints $N2$ and $N3$ of the superstructure under consideration. Linear and bilinear approximations of the obtained data were proposed.

6. Taking into account all the above, we can conclude the following: the connection stiffness is the joint generalized characteristic, largely dependent on its composition. With an increase in the joint complexity, the difference between the stiffness of the real connection and the stiffness determined for a beam model with absolutely rigid connections increases. Therefore, joint connections must be considered semi-rigid. The question of correct stiffness assessment of the bridge superstructures steel trusses connections is becoming especially urgent at the present time, with the appearance and development of

the high-speed railway system. However, in the existing standard documents there are no direct instructions on the method of determining stiffness of these structures joint connections, especially with respect to static and dynamic analysis. Therefore, further development of this area of knowledge is necessary.

References

1. Valiullin, D.A., Chizhov, S.V. Analysis of assessment methods of stress-strain state of lattice trusses with rigid connections in nodal joints. *Vestnik Grazhdanskikh Inzhenerov [Bulletin of Civil Engineers]*. 2019. 75 (4). Pp. 38–43. DOI: 10.23968/1999-5571-2019-16-4-38-43
2. Leichti, R.J., Hyde, R.A., French, M.L., Camillos, S.G. The continuum of connection rigidity in timber structures. *Wood and Fiber Science*. 2000. 32 (1). Pp. 11–19.
3. Masse, D.I., Salinas, J.J. Analysis of timber trusses using semi-rigid joints. *Canadian Agricultural Engineering*. 1988. 30 (1). Pp. 111–124.
4. Mam, K., Douthe, C., Le Roy, R., Consigny, F. Shape optimization of braced frames for tall timber buildings: Influence of semi-rigid connections on design and optimization process. *Engineering Structures*. 2020. 216. Pp. 1–15. DOI: 10.1016/j.engstruct.2020.110692
5. Sawata, K., Yasumura, M. Estimation of yield and ultimate strengths of bolted timber joints by nonlinear analysis and yield theory. *Journal of Wood Science*. 2003. 49 (5). Pp. 383–391. DOI: 10.1007/s10086-002-0497-3
6. Li, Z., Su, Y., Zhang, K. Numerical Analysis Of The T-stub Beam-to- Column Hysteretic Behavior Affected By Beam Height. The 2016 International Conference on Advances in Energy, Environment and Chemical Science. 2016. Pp. 0373–0376. DOI: 10.2991/aeecs-16.2016.70
7. Gomes, V., Silva, A.T., de Lima, L.R.O., Vellasco, P.C.G. da S. Numerical investigation of semi-rigid connection ultimate capacity. *Revista Escola de Minas*. 2018. 71 (4). Pp. 505–512. DOI: 10.1590/0370-44672018710031
8. Madjour, A., Soltani, M.R., Harkati, E.H. Numerical investigation into the ultimate strength of steel cellular beams with semi-rigid connections. *Periodica Polytechnica Civil Engineering*. 2018. 62 (2). Pp. 517–532. DOI: 10.3311/PPci.11304
9. Aydin, A.C., Ardalani, A., Maali, M., Kiliç, M. Numeric modelling of innovative semi-rigid connections under cyclic loading. *Steel Construction*. 2020. 13. Pp. 1–13. DOI: 10.1002/stco.201900037
10. Tushina, V.M. Semi-rigid steel beam-to-column connections. *Magazine of Civil Engineering*. 2017. 73 (5). Pp. 25–39. DOI: 10.18720/MCE.73.3
11. Vatin, N., Bagautdinov, R., Andreev, K. Advanced Method for Semi-Rigid Joints Design. *Applied Mechanics and Materials*. 2015. 725–726. Pp. 710–715. DOI: 10.4028/www.scientific.net/amm.725-726.710
12. Babu, S.S., Sreekumar, S. A Study on the Ductility of Bolted Beam- Column Connections. *International Journal of Modern Engineering Research*. 2012. 2 (5). Pp. 3517–3521.
13. Kartal, M.E., Başağa, H.B., Bayraktar, A., Muvafik, M. Effects of semi-rigid connection on structural responses. *Electronic Journal of Structural Engineering*. 2010. 10. Pp. 22–35.
14. Patil, M., Pandey, A.D. Influence of Semirigid joints on fatigue life of steel truss railway bridge. *International Journal of Civil and Structural Engineering*. 2012. 3 (1). Pp. 44–56. DOI: 10.6088/ijcser.201203013005
15. Faridmehr, I., Tahir, M.M., Lahmer, T. Classification system for semi-rigid beam-to-column connections. *Latin American Journal of Solids and Structures*. 2016. 13 (11). Pp. 2152–2175. DOI: 10.1590/1679-78252595
16. van Keulen, D.C., Nethercot, D.A., Snijder, H.H., Bakker, M.C.M. Frame analysis incorporating semi-rigid joint action: Applicability of the half initial Secant stiffness approach. *Journal of Constructional Steel Research*. 2003. 59 (9). Pp. 1083–1100. DOI: 10.1016/S0143-974X(03)00031-2
17. Weynand, K., Jaspert, J.-P., Steenhuis, M. The stiffness model of revised annex j of eurocode 3. *Connections in Steel Structures III1996*. Pp. 441–552.
18. Nethercot, D.A., Li, T.Q., Ahmed, B. Unified classification system for beam-to-column connections. *Journal of Constructional Steel Research*. 1998. 45 (1). Pp. 39–65. DOI: 10.1016/S0143-974X(97)00064-3
19. Crosti, C., Duthinh, D. A nonlinear model for gusset plate connections. *Engineering Structures*. 2014. 62–63. Pp. 135–147. DOI: 10.1016/j.engstruct.2014.01.026
20. Crosti, C., Duthinh, D. Instability of steel gusset plates in compression. *Structure and Infrastructure Engineering*. 2014. 10 (8). Pp. 1–11. DOI: 10.1080/15732479.2013.786102
21. Court-Patience, D., Garnich, M. Buckling analysis of gusset plates with bolted connections using finite element modeling. *Journal of Constructional Steel Research*. 2021. 176. Pp. 1–15. DOI: 10.1016/j.jcsr.2020.106420
22. Butler, M.A., Swanson, J.A., Rassati, G.A., Dues, E.F. High Resolution Modeling and Modeling of Connections in Pony-Truss Bridges. *Transportation Research Record*. 2018. 2672 (41). Pp. 186–195. DOI: 10.1177/0361198118792126
23. Buitrago, M., Bertolesi, E., Calderón, P.A., Adam, J.M. Robustness of steel truss bridges: Laboratory testing of a full-scale 21-metre bridge span. *Structures*. 2021. 29. Pp. 691–700. DOI: 10.1016/j.istruc.2020.12.005
24. Ngo-Huu, C., Nguyen, P.C., Kim, S.E. Second-order plastic-hinge analysis of space semi-rigid steel frames. *Thin-Walled Structures*. 2012. 60. Pp. 98–104. DOI: 10.1016/j.tws.2012.06.019
25. Nguyen, P.C., Kim, S.E. An advanced analysis method for three-dimensional steel frames with semi-rigid connections. *Finite Elements in Analysis and Design*. 2014. 80. Pp. 23–32. DOI: 10.1016/j.finel.2013.11.004
26. Zlatkov, D., Zdravkovic, S., Mladenovic, B., Stojic, R. Matrix formulation of dynamic design of structures with semi-rigid connections. *Facta universitatis – series: Architecture and Civil Engineering*. 2011. 9 (1). Pp. 89–104. DOI: 10.2298/fuace-1101089z
27. Sagirolu, M., Aydin, A.C. Design and analysis of non-linear space frames with Semi-rigid connections. *Steel and Composite Structures*. 2015. 18 (6). Pp. 1405–1421. DOI: 10.12989/scs.2015.18.6.1405
28. Shi, G., Shi, Y., Wang, Y., Bradford, M.A. Numerical simulation of steel pretensioned bolted end-plate connections of different types and details. *Engineering Structures*. 2008. 30 (10). Pp. 2677–2686. DOI: 10.1016/j.engstruct.2008.02.013
29. Girão Coelho, A.M. Rotation capacity of partial strength steel joints with three-dimensional finite element approach. *Computers and Structures*. 2013. 116. Pp. 88–97. DOI: 10.1016/j.compstruc.2012.10.024

30. Wang, G., Ding, Y. The interface friction in the friction-type bolted joint of steel truss bridge: Case study. *Baltic Journal of Road and Bridge Engineering*. 2020. 15 (1). Pp. 187–210. DOI: 10.7250/bjrbe.2020-15.467
31. Omar, R., Rani, M.N.A., Yunus, M.A. Finite Element Modelling and Updating of a Bolted Structure Using Elements Representing the Stiffness Members, Bolts and Affected Areas of the Joints. *Journal of Physics: Conference Series*. 2019. 1262 (1). Pp. 1–10. DOI: 10.1088/1742-6596/1262/1/012005
32. Jiang, W.-Q., Liu, Y.-P., Chan, S.-L., Wang, Z.-Q. Direct Analysis of an Ultrahigh-Voltage Lattice Transmission Tower Considering Joint Effects. *Journal of Structural Engineering*. 2017. 143 (5). Pp. 1–14. DOI: 10.1061/(asce)st.1943-541x.0001736
33. Baran, E., Akis, T., Sen, G., Draisawi, A. Experimental and numerical analysis of a bolted connection in steel transmission towers. *Journal of Constructional Steel Research*. 2016. 121. Pp. 253–260. DOI: 10.1016/j.jcsr.2016.02.009
34. Tran-Ngoc, H., Khatir, S., De Roeck, G., Bui-Tien, T., Nguyen-Ngoc, L., Abdel Wahab, M. Model updating for nam O bridge using particle swarm optimization algorithm and genetic algorithm. *Sensors (Switzerland)*. 2018. 18 (12). Pp. 1–20. DOI: 10.3390/s18124131
35. Luong, H.T.M., Zabel, V., Lorenz, W., Rohrmann, R.G. Vibration-based Model Updating and Identification of Multiple Axial Forces in Truss Structures. *Procedia Engineering*. 2017. 188. Pp. 385–392. DOI: 10.1016/j.proeng.2017.04.499
36. Frye, M.J., Morris, G.A. Analysis of flexibly connected steel frames. *Canadian Journal of Civil Engineering*. 1976. 3 (2). Pp. 280–291. DOI: 10.1139/l76-034
37. Krolo, P., Grandić, D., Bulić, M. The Guidelines for Modelling the Preloading Bolts in the Structural Connection Using Finite Element Methods. *Journal of Computational Engineering*. 2016. 2016. Pp. 1–8. DOI: 10.1155/2016/4724312

Information about authors:

Damir Valiullin,

ORCID: <https://orcid.org/0000-0002-1961-2942>

E-mail: damirvall@rambler.ru

Sergei Chizhov,

PhD in Technical Science

ORCID: <https://orcid.org/0000-0001-7613-8848>

E-mail: sergchizh@yandex.ru

Received 01.04.2021. Approved after reviewing 21.12.2021. Accepted 17.01.2022.



Research article

UDC 691.624

DOI: 10.34910/MCE.114.10



Functional indium oxide-based thin-film coatings with variable light transmission

D.A. Strekalovskaya , L.P. Baturova , A.V. Semencha , E.K. Aleksandrova 

Peter the Great St. Petersburg Polytechnic University, St. Petersburg, Russia

✉ darya.strek@gmail.com

Keywords: electrochromic properties, optically active glazing material, transparent-reflective switchable, ITO films, smart glass coating, thin-film coatings, magnetron sputtering, transmittance, smart windows, switchable glass, glazing systems

Abstract. One of the directions of energy-saving technologies development in the public works construction is associated with the engineering of glazing materials that allow regulating light and heat flux passing through them. Known solutions are associated with the use of multilayer materials with special optical thin-film electrochromic coatings. This work presents the results of the functional properties study of single-layer transparent conductive thin-film coatings based on tin-doped indium oxide (ITO films), formed on a glass substrate by magnetron sputtering. It is shown that, under conditions of cathodic treatment in a potentiodynamic mode at certain threshold potentials E_p in aqueous and aqueous-ethanol solutions, the introduction of hydrogen atoms into surface layers is observed, leading to a decrease in the transmittance T_x to ~10% and the transition of ITO films to a colored state. It was found that the introduction of hydrogen atoms is accompanied by the formation of hydrogen-indium bronzes with the general formula $H_xIn_2O_3$, the composition of which depends on the pH of the solution. Indium bronzes formed in a neutral 3% NaCl solution are characterized by a low value of the x index, high conductivity and reversibility of the coloration-discoloration processes, i.e. have electrochromic properties. Indium bronzes formed in 1M aqueous and aqueous-ethanol KOH solutions have higher values of the x index, low conductivity and irreversibility of the coloring process. Increase bronzes conductivity due to the introduction of carbon nanoparticles into the outer layers of ITO films does not affect the reversibility of the coloration-discoloration processes. The results obtained can serve as a basis for the creation of a wide range of modern improved glass and double-glazed windows with an adjustable value of light transmittance.

Funding: Ministry of Science and Higher Education of the Russian Federation as part of World-class Research Center program: Advanced Digital Technologies (contract No. 075-15-2020-934 dated of 17.11.2020)

Citation: Strekalovskaya, D.A., Baturova, L.P., Semencha, A.V., Aleksandrova, E.K. Functional indium oxide-based thin-film coatings with variable light transmission. Magazine of Civil Engineering. 2022. 114(6). Article No. 11410. DOI: 10.34910/MCE.114.10

1. Introduction

One of the urgent tasks in modern energy-efficient buildings construction is to create conditions for protection from environmental influences [1]–[3]. It is often necessary to reduce the excess thermal solar radiation (TSI) penetrating into living spaces through glazing elements [4]–[6]. To reduce the TSI value and to have the ability to control the degree of illumination in a room, glazing materials must have a set of properties capable of directionally changing their parameters: transmitting a light flux in a discoloration state or inhibiting the transmission intensity in a coloration state. Usually multilayer transparent thin-film coatings

with special properties are used to impart desired functional properties to the glazing materials [7], [8]. An integral part of such coatings is the presence of an electrochromic layer formed on a conductive transparent substrate (current-conductive layer), capable of reversibly changing optical properties (transmission) during alternating polarization. Thus, the use of glazing materials with multilayer electrochromic coatings, which reversibly change the light transmission coefficient, makes it possible to reduce energy costs for cooling, heating or room lighting [9]–[11].

Thin-film coatings based on transition metal oxides (TMO) exhibit electrochromic properties and, due to their high optical transparency in the visible wavelength range and electrical conductivity, are widely used in various fields of electronic and microsystem engineering [12]–[15]. The thin films functional properties are determined primarily by their composition and structure [16]–[18]. Upon contact of thin-film coatings based on transition metal oxides with an electrolyte under conditions of cathodic polarization, adsorbed hydrogen atoms H_{ads} formed during the discharge of water molecules: $H_2O + e \rightarrow H_{ads} + OH^-$, can accumulate on the surface and be intercalated into the oxide. The introduction of adsorbed hydrogen atoms into a transparent oxide can lead to the formation of compounds of various nonstoichiometric compositions with a general formula $H_xM_yO_z$ and cause a change in its electrical and optical properties [19]–[21]. If the process of intercalation proceeds reversibly in the film, then upon changing the direction of polarization the film can restore its original properties. As materials with reversible properties, of particular interest are coatings based on indium-tin oxide (Indium Tin Oxide - ITO), which are widely used as a transparent conductive sublayer in the creation of various indicator systems, monitoring sensors, electrochromic devices with variable optical density, etc. [22]–[25].

The object of the study was transparent electrically conductive thin films of tin-doped indium oxide in a ratio of 90% indium oxide In_2O_3 and 10% tin oxide SnO_2 (ITO-films) laid on a glass substrate by magnetron sputtering. The research purpose was to study the optical properties of thin ITO films in aqueous and aqueous-ethanol solutions with different pH values in a wide range of potentials and to determine the factors leading to a change in its functional properties. In this work, we used solutions characterized by different values of hydrogen evolution overvoltage in which the dissolution of ITO films is minimized. For this purpose, analysis of Pourbaix diagrams for In- H_2O and Sn- SnO_2 systems was preliminary performed and pH interval was found in which In_2O_3 and SnO_2 oxides are thermodynamically stable in aqueous media [19], [24]. The objectives of the study were the deposition of indium tin oxides-based thin films, electrochemical measurements by linear anodic and cyclic polarization, modification of indium oxide-based coatings, and evaluation of thin film coating optical properties – transmission coefficient. The obtained results make it possible to determine the prospects of using ITO films for glazing materials.

2. Methods

Thin-film coatings based on indium-tin oxides with a ratio of In_2O_3 -90% and SnO_2 -10% oxides were settled-down on transparent glass substrates by magnetron sputtering using the industrial vacuum spraying plant "Aspira-150" (Research and manufacturing complex "Polytech"). The transmission coefficient T_0 of the initial ITO films with a thickness of 0.21 μm with a uniformity of $\pm 0.4\%$ was 83%.

The current-voltage characteristics of ITO films were compared in aqueous and aqueous-ethanol solutions with different pH values. Cyclic voltage curves (CVC) were taken in a potentiodynamic mode using the IPC-PRO M potentiostat of the Volta company with a computer system for recording and processing data. The potential sweep rate V_p was 1 $mV \cdot s^{-1}$. The reference electrode was a saturated silver chloride electrode (all values of potentials E are given relatively to standard hydrogen electrode (SHE)). Ethyl alcohol had the reagent grade qualification.

The installation allowed to take absorption spectra of ITO films at different potentials simultaneously with electrochemical measurements, without removing the sample from the solution. For this purpose, a compact USB-650 Red Tide spectrometer was used. It was fixed in such a way that the illuminator's light beam passed through the cell, the electrolyte solution and the working thin-film electrode. The reference electrode was located outside the cell in a separate vessel with a saturated potassium chloride solution and connected to the system using a micro electrochemical key. Transmission coefficients $T(\lambda)$ were determined in the wavelength range from 150 to 1000 nm at a wavelength $\lambda = 550$ nm.

During studying the elemental composition of ITO films surface after cathodic treatment in a potentiostatic mode in a 1M KOH solution, containing hydroxylated water-soluble derivatives of fullerenes – fullereneol $C_{60}(OH)_{24}$, two-layer films were used, obtained by alternating the ITO layer and the nickel oxide (II) layer. The NiO layer was applied by chemical deposition from the gas phase in an argon-oxygen medium with small ozone additives ($Ar + 5 \text{ vol.}\% O_2 + 0.1 \text{ vol.}\% O_3$) at temperature of 330°C, using a horizontal quartz reactor with "hot walls" equipped with a gas inlet system, a furnace with a thermostat, a vacuum meter in a gas medium [16]. The elemental composition of the ITO films outer layers was studied

by X-ray photoelectron spectroscopy (XPS) using the Nano-FAB 25 installation jointly produced by NT-MDT (Russia) and SPECS (Germany). The analyzer sensitivity is 0.1%, the penetration depth during the analysis reached 10 nm, the analysis area is 0.1 mm². The analysis of X-ray photoelectronic spectra and their decomposition was carried out using special Casa XPS software (version 2.3.18, Casa Software Ltd, 2020 [26]).

3. Results and Discussion

Thin-film devices typically use ion-conducting electrolytes with a wide range of electrochemical stability. The ITO films behavior under polarization conditions was studied in aqueous and aqueous-ethanol 1M KOH solution, as well as in 3% NaCl solution, in which indium oxide is thermodynamically stable. Fig. 1, Curve 1 shows the cathode branch of the ITO-film voltage curve obtained in an aqueous 1M KOH solution in the potential range from initial E_{in} to -1.85 V.

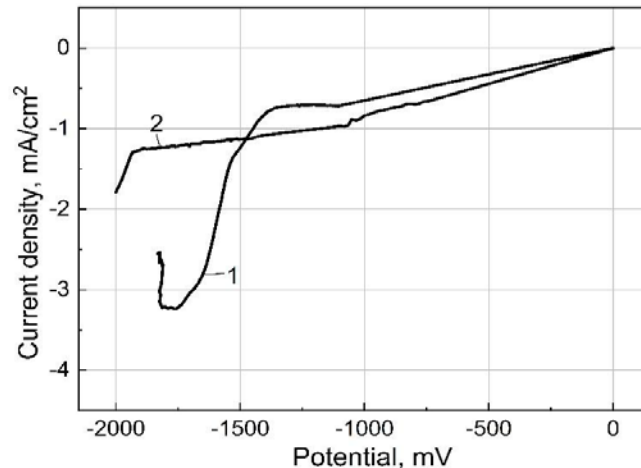


Figure1. Cathode branches of voltage curves obtained on an ITO film in an aqueous (1) and aqueous-ethanol (2) 1M KOH solution.

At a potential of -1.45 V, an increase in the cathode current is observed on the polarization curve, due to the hydrogen release process beginning due to the discharge of water molecules and a change in the ITO film optical absorption. ITO films turn into a dark brown colored state. At a potential of -1.8 V, the current reaches its maximum value. A further potential shift in the negative direction leads to a decrease in the rate of the hydrogen release process due to an increase in the resistance of the film due to the process solid-phase diffusion difficulties. In accordance with this, it was not possible technically to obtain the ITO films anode branch in the painted state. The obtained results have demonstrated that after switching off polarization in an open circuit, ITO films retain their properties in the colored state. The transmission coefficient does not change for a long time (up to a day or more), i.e. ITO films have an "optical memory effect" and are characterized by non-volatility. The ITO films storage time in the air also does not affect the transmittance value. This made it possible to determine the ITO films transmittance coefficients in the colored state at different potentials under open circuit conditions. Figure 2, a shows the transmission coefficient spectrum obtained on an ITO film in the staining state at a potential of -1.85 V.

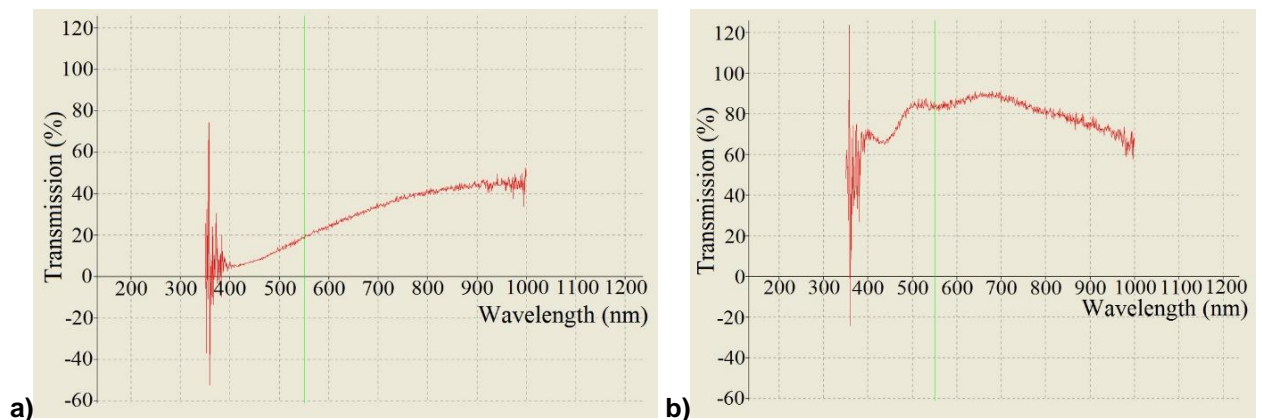


Figure 2. Transmission spectra of ITO films obtained after record of volt-ampere curves (VAC) in aqueous (a) and ethanol (b) 1M KOH solution.

The transmission T_x coefficient, determined at the wavelength $\lambda = 550$ nm, was 18.4%. Figure 3, Curve 1 shows the dependence of the transmission coefficient T_x (%) of ITO films on the value of the potential E , obtained in 1M KOH solution in a wide range of potentials.

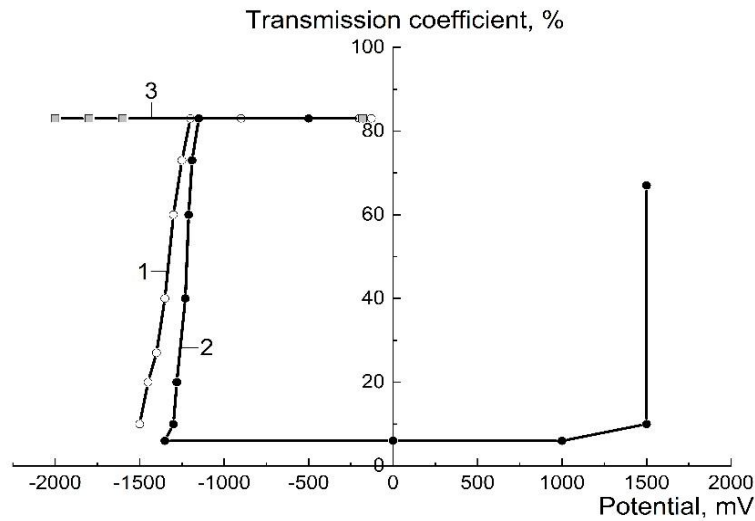


Figure 3. Dependences of the ITO films transmittance on the potential obtained in various solutions: 1 – 1M KOH solution; 2 – 3% NaCl solution; 3 – 1M KOH solution in ethanol.

As can be seen, the ITO films staining beginning potential (the potential of the transmission reduction coefficient beginning) is -1.45 V, which coincides with the potential of the VAC cathode current branch growth beginning. The transition from the discolored state to the state of complete ITO films staining in 1M KOH solution occurs in a fairly narrow range of potentials of the 50 mV order.

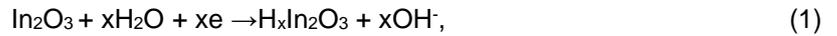
The cathode branch record of the voltampere curve on an ITO film in an anhydrous 1M KOH solution in ethanol (conditionally anhydrous solution containing no more than 0.5 wt% H₂O) shows that there is no peak cathode current on the polarization curve in the studied potential range and a small limiting current associated with the reduction of dissolved oxygen is observed. Figure 2, b shows the transmission coefficient spectrum obtained on an ITO film with a final sweep potential of -2.0 V. The ITO film transmission coefficient, determined at a wavelength of $\lambda = 550$ nm, was 83% (Figure 3, curve 3), which corresponds to the transmission coefficient of the original ITO films. This indicates that in the 1M KOH solution in ethanol, ITO films in a wide range of potentials are not electrochemically active by themselves and the transition from aqueous alkaline media to ethanol leads to their electrochemical stability window expansion.

When 5 wt% H₂O is added into a 1M KOH solution in ethanol, a section associated with the hydrogen evolution process appears on the cathode branch of the VAC at potentials $E \leq -1.8$ (Fig. 1, curve 2) and the ITO film staining in a dark brown color is observed (Fig. 4). The potential for staining beginning E_{stb} in an ethanol 1M KOH solution containing 5 wt% H₂O is -1.8 V and shifts in comparison with an aqueous 1M KOH solution to the cathode side by 350 mV. This is due to the fact that the transition from aqueous alkaline media to ethanol media with a low water content is accompanied by an increase in the overvoltage of hydrogen release and a change in the nature of the delayed stage. So, if in an aqueous 1M KOH solution, the speed of the process is determined by the delayed stage of discharge of water molecules, then in ethanol with small water additives – by the recombination stage of adsorbed hydrogen atoms [27]–[29]. This leads to an increase in the degree of surface filling with adsorbed hydrogen H_{ads} contributing to the transition of H_{ads}→H_{ab} and the addition of hydrogen into the ITO film surface layer. The T_x transmission coefficient, determined at a potential of -1.8 V in an ethanol solution containing 5 wt% H₂O, decreases by about 2.5 times compared to an aqueous 1M KOH solution and reaches 7.6%.



Figure 4. ITO film deposited on a transparent glass substrate in a colored state.

Thus, under conditions of ITO films cathodic polarization in 1M KOH solution, a change in their optical and electrical properties is observed in the region of hydrogen release potentials: an intense dark brown film color appears and electrical conductivity decreases. A strong modification of ITO films properties in the region of hydrogen release potentials is due to the fact that the resulting atomic hydrogen, penetrating into ITO films surface layer, participates in the heterogeneous process of indium oxide reduction In_2O_3 with the formation of hydrogen indium bronze with the general formula $\text{H}_x\text{In}_2\text{O}_3$:



where x - is the stoichiometric coefficient varying in the interval $0 < x < 1$. During the hydrogen ion discharging process, the thickness of the indium bronze layer increases, a film with a "sandwich structure" is formed and ITO film sequential transition from a state with high electrical conductivity to a state with low one is observed. When the structural transformations, occurring during the bronze synthesis in the film end, the film goes into a stable state characterized by high insulating properties.

The reversibility of the staining-discoloration process of ITO films is determined by the hydrogen deintercalation degree from the indium bronze $\text{H}_x\text{In}_2\text{O}_3$ layer in the process of recording the voltampere curve (VAC) anode branch. An increase in the electrochemical activity of indium bronze layers formed under conditions of the VAC cathode branch recording can be carried out by modifying their properties by introducing impurities of various elements into them.

The work investigates the carbon injection effect on the ITO films kinetic characteristics. The carbon was added into the thin-film systems outer layers by cathodic deposition in a solution containing a water-soluble form of fullerene derivatives (C_{60}) is polyhydroxylated fullerene, called fulleranol-d, obtained by direct heterogeneous-catalytic oxidation of fullerene and corresponding to the conditional formula $\text{C}_{60}(\text{OH})_{24}$ [30]–[32]. In cathodic polarization conditions in potentiostatic or potentiodynamic modes, fulleranol ions $[\text{C}_{60}(\text{OH})_{23}]^+$ are capable of receiving electrons by introducing a carbon film or fulleranol particles into the matrix.

To study the elemental composition of the films outer layers after cathodic treatment in the potentiostatic mode, two-layer ITO/NiO (II) films were used. Figure 5 shows an overview XPS spectrum of the two-layer ITO/NiO (II) film surface layer after cathodic treatment at a potential of -800 mV for 30 s in a 2M KOH solution containing 0.2% $\text{C}_{60}(\text{OH})_{24}$.

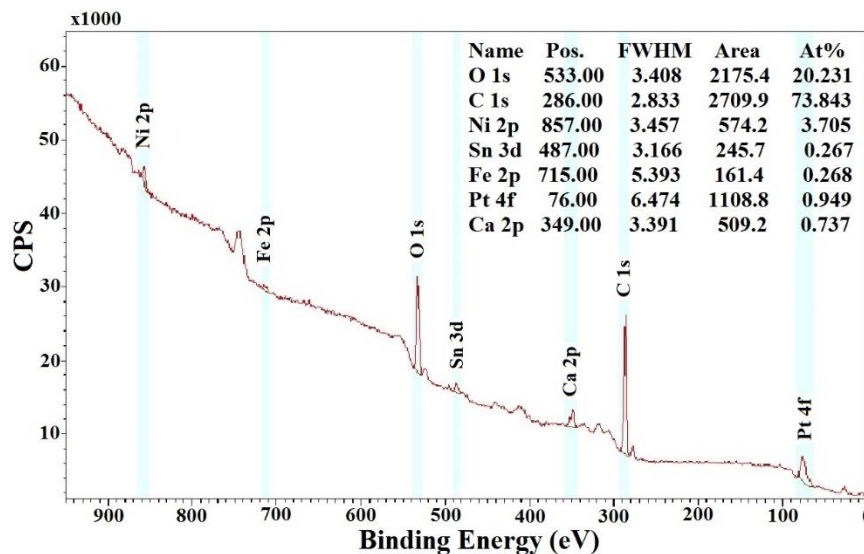


Figure 5. Overview X-ray spectrum of a two-layer ITO/NiO film after cathodic treatment in a KOH solution containing 0.2% fulleranol $\text{C}_{60}(\text{OH})_{24}$.

According to X-ray photoelectron spectroscopy, the following elements were detected in the film outer layers: Ni (3.7%), O (20.2%), C (73.8%), the rest ones to be Sn, Pt, Fe and Ca. The carbon (carbon-containing particles) proportion in the ITO film outer layers during cathodic treatment can reach about 80%.

Figure 6 shows a cyclic voltage curve obtained on ITO films in a 1M KOH solution containing 0.2% $\text{C}_{60}(\text{OH})_{24}$. The carbon intrusion into the ITO films outer layers during cathodic polarization does not affect the indium bronze formation. Thus, the VAC cathode branch shape, the potentials of the cathode current growth beginning and the film transition to the colored state in the presence and absence of fulleranol-d in the 1M KOH solution coincide and amount to -1.45V. Increasing the indium bronze layers conductivity made it possible to obtain the VAC anode branch. As can be seen, currents characteristic peaks are observed on it. However, the ITO film transition to a discolored state did not occur in the studied potential range. This

indicates that indium bronzes formed during the ITO films cathodic polarization in a 1M KOH solution containing 0.2% $C_{60}(OH)_{24}$, are characterized by irreversible properties and there is no electrochromic effect in them.

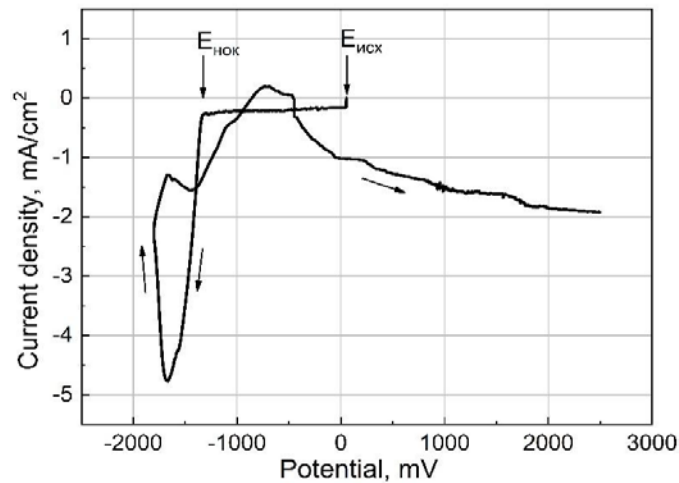


Figure 6. Cyclic voltage curve obtained on ITO films in 1M KOH solution containing 0.2% fullerene $C_{60}(OH)_{24}$.

Apparently, indium bronzes formed in 1M KOH solutions are characterized by a sufficiently high value of the stoichiometric coefficient x in the general formula of bronze $H_xIn_2O_3$. The 1M solution of KOH fullerene-d addition leads to a decrease in the transmittance of T_x ITO films in the colored state to 9.8%.

The properties of hydrogen indium bronzes formed under conditions of cathodic polarization in ITO films in a neutral 3% NaCl solution are investigated. Figure 7 shows the cathode and anode branches of the cyclic voltampere curve (VAC) obtained on an ITO film in a neutral 3% NaCl solution in the potential range from -1360 to 2500 mV.

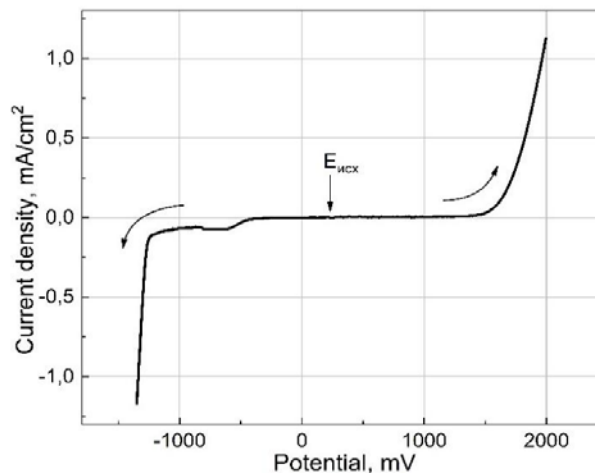


Figure 7. Voltamper curve cathode and anode branches obtained on ITO films in 3% NaCl solution.

As can be seen, in a neutral 3% NaCl solution, the potential for hydrogen release beginning and ITO film staining in dark brown is observed at a more positive potential than in the 1M KOH solution and is -1.28 V (Fig. 3, curve 2). As the potential shifts in the negative direction to -1360 mV, the intensity of ITO film staining increases. The transmittance T_x , determined at a wavelength $\lambda = 550$ nm of ITO films in the staining state at a potential $E = -1.360$ V in a 3% NaCl solution was 6.8%, and the contrast ratio (transmittance index) $CR = T_x/T_0$, representing the transmittance ratio in the colored and unpainted states, relatively, was 8.12%. When the potential was deployed in the opposite anode direction, and the anode HAC branch was recorded, it was found that the colored ITO-plates state remained almost up to 1.48 V. At a potential of 1.48V, an increase in the anode current is observed on the VAC anode branch, and the ITO film moves into a discolored state.

Figure 3, Curve 2 shows (in a wide range of potentials) the dependence of ITO-strips transmittance on the potential in the processes of discoloration staining in a 3% NaCl solution. As can be seen, the

process of ITO film electrochromic staining in a 3% NaCl solution occurs in a narrow range of potentials and is characterized by asymmetry during discoloration in relation to the potential axis. The ITO film transmittance in the discoloration state at a potential of 2.0 V in a 3% NaCl solution was 64.4%, i.e. under these conditions, the ITO film is not completely discolored. Thus, the switching efficiency, denoting the proportion of electrochromic material, going from the colored state, when changing the redox process direction to the unpainted state, is 76%.

Thus, indium bronzes formed in ITO films in a neutral 3% NaCl solution are characterized by high conductivity (as well as the original ITO films) and a sufficiently small value of the stoichiometric coefficient x in the general formula of bronze $H_xIn_2O_3$ and are capable of reversibly changing light transmission when voltage is applied, i.e. they have electrochromic properties.

4. Conclusions

As a result, it was found that in aqueous solutions at certain threshold potential E_p , depending on the solution pH, and more negatively, the modification of the optical and electrical properties of ITO films is observed. The properties modification is determined by the kinetics of hydrogen intercalation into the film with the formation of hydrogen-indium bronzes $H_xIn_2O_3$. The conductivity and electrochromic properties of the resulting bronzes are determined by the stoichiometric coefficient x value in the general formula of bronzes.

The results showed that indium bronzes formed in a neutral 3% NaCl solution with a low x index value were characterized by high conductivity and reversible dark brown coloration-discoloration of the film, i.e. had electrochromic properties. Under open circuit conditions, ITO films retained a colored state for a long time (up to a day or more), i.e. ITO films had an "optical memory effect" and were non-volatile. These bronzes could be used for premises protection from the environmental factors effects.

The results showed that indium bronzes formed in aqueous and water-ethanol 1M KOH solutions were characterized by a rather high value of the stoichiometric coefficient x , low conductivity and irreversibility of the ITO films coloring process. The increase in the bronzes conductivity due to the carbon intercalation into the ITO film did not affect the reversibility of its coloration-discoloration process.

References

1. Nguyen, T.D., Yeo, L.P., Ong, A.J., Zhiwei, W., Mandler, D., Magdassi, S., Tok, A.I.Y. Electrochromic smart glass coating on functional nano-frameworks for effective building energy conservation. *Materials Today Energy*. 2020. 18. Pp. 100496. DOI: 10.1016/j.mtener.2020.100496.
2. Cannavale, A., Ayr, U., Fiorito, F., Martellotta, F. Smart Electrochromic Windows to Enhance Building Energy Efficiency and Visual Comfort. *Energies*. 2020. 13(6). Pp. 1449. DOI: 10.3390/en13061449.
3. Evecan, D., Zayim, E. Highly uniform electrochromic tungsten oxide thin films deposited by e-beam evaporation for energy saving systems. *Current Applied Physics*. 2019. 19(2). Pp. 198–203. DOI: 10.1016/j.cap.2018.12.006.
4. Oh, M., Roh, S., Jang, M., Park, J. Evaluation of heating and cooling load according to applying electrochromic glass to office building envelope in south Korea. *International Journal of Sustainable Building Technology and Urban Development*. 2018. 9(3). Pp. 158–169. DOI: 10.22712/susb.20180015.
5. Gutai, M., Kheybari, A.G. Energy consumption of hybrid smart water-filled glass (SWFG) building envelope. *Energy and Buildings*. 2021. 230. Pp. 110508. DOI: 10.1016/j.enbuild.2020.110508.
6. Pugliese, M., Bisconti, F., Rizzo, A., Colella, S., Prontera, C.T., Gigli, G., Maiorano, V., Cossari, P. Highly Efficient All-Solid-State WO₃-Perovskite Photovoltachromic Cells for Single-Glass Smart Windows. *ACS Applied Energy Materials*. 2020. 3(11). Pp. 10453–10462. DOI: 10.1021/acsaem.0c01442.
7. Phan, G.T., Pham, D. Van, Patil, R.A., Tsai, C.-H., Lai, C.-C., Yeh, W.-C., Liou, Y., Ma, Y.-R. Fast-switching electrochromic smart windows based on NiO-nanorods counter electrode. *Solar Energy Materials and Solar Cells*. 2021. 231. Pp. 111306. DOI: 10.1016/j.solmat.2021.111306.
8. Park, B.R., Hong, J., Choi, E.J., Choi, Y.J., Lee, C., Moon, J.W. Improvement in Energy Performance of Building Envelope Incorporating Electrochromic Windows (ECWs). *Energies*. 2019. 12(6). Pp. 1181. DOI: 10.3390/en12061181.
9. Piccolo, A., Marino, C., Nucara, A., Pietrafesa, M. Energy performance of an electrochromic switchable glazing: Experimental and computational assessments. *Energy and Buildings*. 2018. 165. Pp. 390–398. DOI: 10.1016/j.enbuild.2017.12.049.
10. Tong, S.W., Goh, W.P., Huang, X., Jiang, C. A review of transparent-reflective switchable glass technologies for building facades. *Renewable and Sustainable Energy Reviews*. 2021. 152. Pp. 111615. DOI: 10.1016/j.rser.2021.111615.
11. Brzezicki, M. A Systematic Review of the Most Recent Concepts in Smart Windows Technologies with a Focus on Electrochromics. *Sustainability*. 2021. 13(17). Pp. 9604. DOI: 10.3390/su13179604.
12. Colby Evans, R., Ellingworth, A., Cashen, C.J., Weinberger, C.R., Sambur, J.B. Influence of single-nanoparticle electrochromic dynamics on the durability and speed of smart windows. *Proceedings of the National Academy of Sciences*. 2019. 116(26). Pp. 12666–12671. DOI: 10.1073/pnas.1822007116.
13. Yamazoe, N., Shimano, K. New perspectives of gas sensor technology. *Sensors and Actuators B: Chemical*. 2009. 138(1). Pp. 100–107. DOI: 10.1016/j.snb.2009.01.023.
14. Tajima, K., Yamada, Y., Bao, S., Okada, M., Yoshimura, K. Electrochemical evaluation of Ta₂O₅ thin film for all-solid-state switchable mirror glass. *Solid State Ionics*. 2009. 180(6–8). Pp. 654–658. DOI: 10.1016/j.ssi.2008.12.034.

15. Kovalev, M., Alekseeva, E., Shaposhnikov, N., Povyshev, A. Predicting the durability of zinc coatings based on laboratory and field tests. E3S Web of Conferences. 2019. 121. Pp. 01008. DOI: 10.1051/e3sconf/201912101008.
16. Kondrateva, A.S., Alexandrov, S.E. Fundamental physicochemical regularities of the chemical vapor deposition of nickel oxide layers. Russian Journal of Applied Chemistry. 2016. 89(9). Pp. 1402–1408. DOI: 10.1134/S1070427216090032.
17. Luzanov, V.A. Specific features of the formation of oblique texture in aluminum nitride films. Journal of Communications Technology and Electronics. 2017. 62(10). Pp. 1182–1183. DOI: 10.1134/S1064226917090157.
18. Kovalev, M., Shakhmatov, A., Alhimenko, A. Electrochemical studies of welded joints corrosion resistance made from stainless steels. Materials Today: Proceedings. 2020. 30. Pp. 501–505. DOI: 10.1016/j.matpr.2020.01.034.
19. Krylov, P.N., Zakirova, R.M., Fedotova, I.V. Optical properties of ITO films obtained by high-frequency magnetron sputtering with accompanying ion treatment. Semiconductors. 2013. 47(10). Pp. 1412–1415. DOI: 10.1134/S1063782613100175.
20. Luzanov, V.A. Features of Indium Tin Oxide Film Deposition by Magnetron Sputtering. Journal of Communications Technology and Electronics. 2020. 65(3). Pp. 290–291. DOI: 10.1134/S1064226920030110.
21. Golubev, I.A., Suprun, I.K. Application of magnetic units for intensification of water treatment. IOP Conference Series: Materials Science and Engineering. 2020. 862(6). Pp. 062051. DOI: 10.1088/1757-899X/862/6/062051.
22. Ito, Y., Abe, Y., Kawamura, M., Kim, K.H., Kiba, T. Influence of substrate cooling on ion conductivity of tantalum oxide thin films prepared by reactive sputtering using water vapor injection. Thin Solid Films. 2020. 710. Pp. 138276. DOI: 10.1016/j.tsf.2020.138276.
23. Chen, P.-W., Chang, C.-T., Ali, M.M., Wu, J.-Y., Li, Y.-C., Chen, M.-H., Jan, D.-J., Yuan, C.-T. Tantalum oxide film deposited by vacuum cathodic arc plasma with improved electrochromic performance. Solar Energy Materials and Solar Cells. 2018. 182. Pp. 188–195. DOI: 10.1016/j.solmat.2018.02.034.
24. Huang, J.-H., Hsu, M.-H., Hsiao, Y.-S., Chen, P., Yu, P., Chu, C.-W. Performance of chromophore-type electrochromic devices employing indium tin oxide nanorod optical amplification. Solar Energy Materials and Solar Cells. 2012. 98. Pp. 191–197. DOI: 10.1016/j.solmat.2011.10.027.
25. Shvetsov, O., Kondrat'ev, S. Performance of Protective Coatings for Aluminum Alloys in the Operating Conditions of Oil Production Equipment. E3S Web of Conferences. 2021. 225. Pp. 05003. DOI: 10.1051/e3sconf/202122505003.
26. Casa Software Ltd. Casa XPS software, version 2.3.18, 2020. URL: <http://www.casaxps.com> (date of application: 09.02.2021).
27. Vigdorovich, V.I., Matveeva, M. V. Hydrogen diffusion through a steel membrane from solutions of the C₂H₅OH-H₂O-HCl system: Effect of cathodic and anodic polarizations. Russian Journal of Electrochemistry. 2006. 42(12). Pp. 1332–1339. DOI: 10.1134/S102319350612010X.
28. Breki, A.D., Vasilyeva, E.S., Tolochko, O. V., Didenko, A.L., Nosonovsky, M. Frictional Properties of a Nanocomposite Material With a Linear Polyimide Matrix and Tungsten Diselenide Nanoparticle Reinforcement. Journal of Tribology. 2019. 141(8). Pp. 082002. DOI: 10.1115/1.4043853.
29. Wang, B., Wang, X., Li, M., Hou, J., Zhang, R. Study on the optical properties and electrochromic applications of LTO/TaOx ion storage-transport composite structure films. Ionics. 2018. 24(12). Pp. 3995–4003. DOI: 10.1007/s11581-018-2557-8.
30. Li, J., Takeuchi, A., Ozawa, M., Li, X., Saigo, K., Kitazawa, K. C₆₀ fullerol formation catalysed by quaternary ammonium hydroxides. Journal of the Chemical Society, Chemical Communications. 1993. (23). Pp. 1784. DOI: 10.1039/c39930001784.
31. Letenko, D.G., Nikitin, V.A., Semenov, K.N., Charykov, N.A., Ivanov, A.S. Conductivity of aqueous solutions of fullerol synthesized by direct oxidation. Russian Journal of Physical Chemistry A. 2012. 86(12). Pp. 1808–1815. DOI: 10.1134/S003602441212014X.
32. Semenov, K.N., Letenko, D.G., Charykov, N.A., Nikitin, V.A., Matuzenko, M.Y., Keskinov, V.A., Postnov, V.N., Kopyrin, A.A. Synthesis and identification of fullerol prepared by the direct oxidation route. Russian Journal of Applied Chemistry. 2010. 83(12). Pp. 2076–2080. DOI: 10.1134/S1070427210120025.

Information about authors:

Darya Strekalovskaya

ORCID: <https://orcid.org/0000-0001-9965-7966>

E-mail: darya.strek@gmail.com

Ludmila Baturova

PhD of Chemical Sciences

ORCID: <https://orcid.org/0000-0002-4740-8228>

E-mail: lpbat@yandex.ru

Aleksandr Semench

PhD of Chemical Sciences

ORCID: <https://orcid.org/0000-0003-2719-8726>

E-mail: asemencha@spbstu.ru

Elena Aleksandrova

ORCID: <https://orcid.org/0000-0002-1143-7836>

E-mail: aleksandrova_ek@spbstu.ru

Received 08.10.2021. Approved after reviewing 17.01.2022. Accepted 26.01.2022.



Research article

UDC 626/627

DOI: 10.34910/MCE.114.11



Assessment of crack resistance of ultra-high earth core rockfill dam by pore pressure

M.P. Sainov 

Moscow State University of Civil Engineering (National Research University), Moscow, Russia

✉ mp_sainov@mail.ru

Keywords: embankment dams, pore pressure, hydraulic fracturing, cracks, numerical analysis, finite element method, deformation, earth core rockfill dam (ECRD)

Abstract. An important problem at construction of high earth core rockfill dams (ECRD) is danger of hydraulic fracturing of their seepage control element. It is usually considered that the cause of hydraulic fracturing is presence of micro cracks in the core, which open due to deficit of compressive stresses at penetration of reservoir water into it. However, this theory ignores the presence of the force in the soil core which fractures it from the inside, i.e. the pore pressure force. The author proposes the criterion of core crack resistance based on consideration of pore pressure. With the aid of numerical modeling of stress-strain state, the impact of pore pressure on potential development of cracks in the core of a 330 m high ECRD was studied. The considered dam has an inclined sandy loam core. By the results of analysis, it was established that the value and development of pore pressure are greatly influenced by the degree of water saturation S_0 of clayey soil at its placement into the dam body. At $S_0 = 0.9$ pore pressure in the core exceeds 4 MPa, and the zone of high pore pressure covers the most part of the core. At that, stresses in the soil skeleton (effective stresses) are still compressive stresses, which formally evidences about the core integrity. However, at $S_0 = 0.9$ the zone of shear strength loss is formed in the core. It may be expected that failure of the core integrity during shear will result in hydraulic fracturing. Thus, pore pressure induces hydraulic fracturing. To prevent the core hydraulic fracturing, it is necessary to reduce pore pressure. Therefore, the clayey soil should be placed with moisture content by 15 % less than the optimal value.

Citation: Sainov, M.P. Assessment of crack resistance of ultra-high earth core rockfill dam by pore pressure. Magazine of Civil Engineering. 2022. 114(6). Article No. 11411. DOI: 10.34910/MCE.114.11

1. Introduction

Earth core rockfill dam (ECRD) may be of considerable height. The highest dam of this type is 300 m high Nurek dam in Tajikistan, which was built in the USSR in 1980. This dam is second highest in the world. Eleven more ECRDs are more than 200 m high. Four of them were built in the XXIth century: Tehri (H = 260.5 m, 2006), Nuozhadu (H = 261.5 m, China, 2012) [1-3], Changheba (H = 240 m, China, 2017) [1], San Roque (H = 210 m, Philippines, 2003). Besides, in the XXIth century a number of high dams was built: Karkheh (H = 127 m, Iran, 2001) [4-6], Masjed-e-Soleyman (H = 177 m, Iran, 2002) [7], Qiaoqi (H = 125,5 m, China, 2006) [8], Pubugou (H = 186 m, China, 2010) [9], Maoergai (H = 147 m, China, 2011) [8], Upper Gotvand Dam (H = 180 m, Iran, 2012).

Construction of high ECRDs has also further perspectives. In Tajikistan the dam of Rogun HPP with overall height 335 m is constructed and it should be the highest in the world. In China there considered construction alternatives of two ultra-high ECRD: Lianghekou (H = 295 m) [10], Shuangjiangkou (H = 314 m) [10,11].

These facts evidence about actuality in developing the theory of ECRD designing.

One of the important issues in ECRD designing is assessment of crack resistance of the seepage control core. In [12] there is information about failures of earthfill dams where loss of integrity occurred. There known the cases of core integrity loss at dams Balderhead (1967, United Kingdom, H = 48 m) [13], Hyttejuvet (1966, Norway, H = 93 m) [14]. There is information about formation of cracks in the core of El Infiernillo / Adolfo López Mateos dam (H = 149 m, Mexico) in 1969. Loss of core integrity is also proved by holes revealed in 1996 on the crest of Bennett ECRD (Canada, H = 183 m).

The problem of providing crack resistance of clayey cores is also urgent for Russian dams. In 1992 the core of Kureika dam project lost its integrity at the section where the dam height is 25 m [15, 16]. The data of geophysical investigations evidences that the core of the highest in Russia Kolyma dam (H = 134.5 m, 1988) is in a diluted state. Settlements of its crest exceeded 2.5 m.

Most sharp the issue of core crack resistance of rock-earthfill dams became after failure of 90 m high Teton dam (USA) in June 1976 [17]. From this moment the studies commenced on the processes of crack formation and development in ECRD cores. Large contribution in development of crack formation theory in ECRD was made by J.L. Sherard, B. Kjoernsli, G.W. Jaworski, H.B. Seed, S. Ngambi and others.

At present, theoretical studies of conditions leading to crack formation in ECRD cores are carried out as well as experimental tests of clayey soils resistance to rupture [8, 18]. Review of development of methods for assessing crack resistance of clayey cores is given in publications of S. Poudel et al. [19], M. Salari et al. [12], D.Q. Tran et al. [20]. The fullest and thorough review is given in [20].

At present the failures of dams Balderhead, Hyttejuvet and others are explained purely by hydraulic fracturing phenomenon. This notion was introduced by B. Kjoernsli. Hydraulic fracturing is connected with arch effect, when deficit of compressive stresses occurs in the core due to redistribution of stresses between the core and shells as well as with development in the core of tensile stresses due to non-uniform deformations of the dam. It is considered that in soil there are always micro cracks which open due to deficit of compressive stresses at penetration of upstream water into them. High hydrostatic pressure ruptures soil from inside, therefore, through cracks are developed in the core and this process is called hydraulic fracturing.

In [12] there given the proposed criteria of assessing potential hydraulic fracturing and their comparison. Classification of prediction methods of hydraulic fracturing is proposed by J. Wang [21]. They are divided into three groups. The first group of methods are analytical methods based on analysis of material stress state at presence of cracks in it. The second group of methods are empirical methods based on the results of experiments with soil samples. The third group of methods is based on experimental models and the theory of material fracture mechanics.

The condition for occurrence of hydraulic fracturing is assumed to be as follows:

$$p_f < \gamma_w h_w,$$

p_f is critical pressure at which hydraulic fracturing occurs; γ_w is unit weight of water; h_w is depth (head) of water.

Value p_f is determined by soil stress state as well as its tensile strength. It was established that hydraulic fracturing appears not only as a result of tensile stresses, but also due to shear stresses, as well as due to joint action of tensile and shear stresses.

Different authors proposed several alternatives of pressure criterial values (p_f). In Russia it is often assumed that direction of cracks is sub-horizontal (due to methodology of layered soil placement), accordingly, p_f is equal to the sum of vertical normal stress σ_y and tensile strength (cohesion) of soil σ_t . However, such an approach leads to overestimation of core crack resistance, because in other, not horizontal directions, soil is subject to considerably less compressive stresses.

As clear from the book [21; 7], most of the authors (A. Mori, M. Tamura [22]; A.K. Panah, E. Yanagisawa [23]; A. Ghanbari, S.S. Rad [24]) connect critical pressure p_f with total minor (minimum) principle stress (σ_3) in soil. Some authors express p_f through horizontal stress σ_x , which is close to σ_3 . The authors of publication [7] on the example of Bidvaz dam (H = 60 m, Iran) showed with the aid of numerical modeling that the core minimal margin of crack resistance is observed at calculation by Ghanbari

and Rad criterion, where critical pressure is expressed through σ_3 , and tensile strength (σ_t) of soil is not taken into account.

However, the conventional theory of hydraulic fracturing has not been sufficiently substantiated theoretically. The following disadvantages may be marked:

1. For hydraulic fracturing by hydrostatic pressure it is necessary that the upstream water should penetrate into the pores or micro cracks of soil. However, as a rule, the core water permeability is sufficiently small for establishment of seepage regime. In [25] with the aid of numeric modeling it was obtained that for hydraulic fracturing along the horizontal crack the initial weakness zone is required. Therefore, failures of ECRD occurred during the initial reservoir impoundment could be explained only due to defects of the core structure.

2. At assessment of crack resistance, it is assumed that along the whole core thickness the pressure in pores will correspond to hydrostatic pressure ($\gamma_w h_w$), though during seepage the head drop along the core thickness occurs.

3. The theory of hydraulic fracturing ignores the real force which may cause fracturing. This is pore pressure force.

Pore water pressure (PWP) is surplus (as compared to atmospheric) pressure in water and air filling soil pores. It is caused not only by hydrostatic pressure of water filtering in pores but it also appears at soil compaction (at decrease of pore size) under action of external loads. In 1999 in paper [14] A.K.L. Ng and J.C. Small with the aid of numeric modeling showed that pore pressure reduced effective stresses in the core of Hyttejuvet dam actually to 0, which could be the cause of hydraulic fracturing of this dam core.

Starting from the middle of the XXth century the pore pressure phenomenon in ECRD cores was studied by conducting field measurements.

In [26, 27] there given the data of field measurements of pore pressure at a number of ECRDs, built in the middle of the XXth century. These dams are: Nurek (Tajikistan, 1980), Pachkamar (H = 71 m, Uzbekistan, 1967), Charvak (H = 168 m, Uzbekistan, 1970), Aswan (H = 111 m, Egypt, 1970), Talbingo (H = 162 m, Austria, 1970). Their analysis shows that the processes of formation and dissipation of PWP in dams progress in different ways. At some dams (Aswan, Pachkamar) pore pressure in ECRD core did not exceed hydrostatic pressure, but the processes of soil consolidation developed quickly. At other dams (Talbingo, Charvak) pore pressure reached considerable values and dissipated slowly.

In ECRDs, constructed in the XXth century, measurements of pore pressure were also carried out. In the publications we can find the information about field measurements of pore pressure at the dams constructed in the XXIst century in Iran and China.

After construction of Karkhe dam (Iran) measurements of PWP were carried out [4-6]. It reached 1.0 MPa, i.e. comprising approximately half of total vertical stresses in the core. Consolidation of the core soil (dispersion of pore pressure) lasted about 5 years. In the inclined core of Bidvaz dam (H = 60 m, Iran) PWP exceeded 0.5 MPa [12]. In the core of 177 m high Masjed-e-Soleyman dam (Iran) PWP reached nearly 2.3 MPa [7].

In China measurements of pore pressure were conducted in the core of Nuozhadu dam (China, H = 261 m) [2,3]. This dam core is made of compact soil: gravel-clay soil, therefore, PWP is comparable with hydrostatic pressure [3].

Thus, in certain circumstances, pore pressure in ECRD cores may reach considerable values and become the cause of failure and loss of integrity of their cores. Therefore, the author proposes to assess core crack resistance by the value of pore water pressure. The following criterion of crack formation may be proposed:

$$\sigma_3 - p_w \geq \sigma_t,$$

where σ_3 is total minor (minimum) principle stress (positive stresses correspond to compression); p_w is pore water pressure; σ_t is tensile strength.

Difference ($\sigma_3 - p_w$) is minimum effective stress in soil $\sigma_{3,ef}$, i.e. minor (minimum) principal stress is soil solid phase.

For assessment of core crack resistance marginal value, the factor of core crack resistance is calculated based on the proposed criterion:

$$k = \frac{\sigma_3 + \sigma_t}{P_w} = 1 + \frac{\sigma_{3,ef} + \sigma_t}{P_w}.$$

With consideration of micro cracks in soil there may be considered that hydraulic fracturing may occur even at $k < 1.1 \div 1.2$.

Pore pressure should be determined by calculation for using the proposed approach of assessment of core crack resistance.

Methods of analyses of pore pressure in soils are based on works of K. Terzaghi (USA), H.M. Gersevanov (Russia), others. V.A. Florin (Russia) and M.E. Biot (Netherlands) created theories of soil consolidation. In them soil is considered as a three-phase medium, which consists of solid particles, pore water and air; soil deformation is considered as a dynamic process of these phases' interaction.

In Russia A.A. Nichiporovich and T.I. Tsybulnik developed an analytical method of calculating the value of pore pressure and its time dependent measurement for ECRD cores. This method of analysis is based on seepage consolidation theory developed by Florin and is an individual case of Biot theory.

For determination of pore pressure appearing at soil compaction under action of external forces (mostly of soil dead weight) on the core axis ($x = 0$), the following formula is used:

$$P_g(x=0, y) = \frac{4}{\pi\mu} v_\sigma \cdot f(t).$$

In this formula $P_g(x=0, y)$ is pore pressure from overlying soil weight at height y along the core axis (i.e. with $x = 0$); v_σ is rate of load rise in the process of construction; μ is coefficient related to coefficient of consolidation; $f(t)$ is dispersion function (time dependent decrease) of pore pressure at height y .

Averaged by time rate of load rise v_σ is expressed through pressure σ at height y , duration of construction t_{EOC} and time t_y of core construction to height y :

$$v_\sigma = \frac{\sigma}{t_{EOC} - t_y},$$

σ is average total stress in soil medium in the moment of construction completion from the weight of overlying soil at height y .

Coefficient μ is expressed through characteristics of physical and mechanical properties of soil: seepage coefficient k_f , coefficient of porosity ε and coefficient of compression m , as well as width B of the core at height y :

$$\mu = \frac{\pi^2(1+\varepsilon)k_f}{4B^2\gamma_w m}.$$

Values of k_f , ε and m are assumed to be constant at calculation. For consideration of their variation in the process of external loads' perception, these values are assumed to be averaged for the interval of stress variation from 0 to σ . Compression coefficient m [MPa⁻¹] expresses the material deformation:

$$m = \frac{\Delta\varepsilon}{\Delta\sigma}.$$

The function of time dependent pore pressure variation is calculated from formula:

$$f(t) = \sum_{i=1,3,5}^{\infty} \frac{1}{i^3} \left[e^{-i^2\mu\alpha(t-t_{EOC})} - e^{-i^2\mu\alpha(t-t_y)} \right],$$

where i is odd even figures; α is pore pressure coefficient expressing maximum pore pressure in fractions from total (full) average stress in soil medium; t is current moment of time (from the moment of construction commencement); t_y is time passed from the start of construction to construction of the core to height y , t_{EOC} is duration of construction.

The formula is valid only for the operation period, i.e. at $t \geq t_{EOC}$.

This analytical method permits not only predicting the value of pore pressure and time dependent progress of soil consolidation processes. Namely in paper [28] this method was used for prediction of pore pressure in the core of constructed Rogun dam.

However, due to the adopted assumptions the Nichiporovich and Tsybulnik method is an approximation method. For predicting PWP it is required to determine the values of average stresses σ in the core. As σ is formed not only under the action of soil dead weight, but also hydrostatic pressure on the core, its value may be analytically approximate. This decreases accuracy of PWP analyses. More precise load on the core may be accomplished with the aid of numerical modeling of the dam stress-strain state (SSS).

Development of SSS numerical modeling methods permitted obtaining more strict solutions on determination of pore pressure. With the aid of numerical modeling the analyses of pore pressure were conducted already in 1970-s at designing Mika dam ($H = 243$ m, USA, 1973) [29].

At present with the aid of numerical modeling, SSS analyses are conducted with consideration of PWP. Such analyses on the base of seepage consolidation theory were conducted with the aid of numerical modeling for Nuozhadu dam in China [3].

SSS analyses by the consolidation theory proposed by Biot, permits application of software package FLAC 3D. With its aid, SSS was numerically modeled with consideration of PWP for several dams in Iran: Bidvaz dam [12], Masjed-e-Soleyman dam [7], Siah Sang dam [12].

However, in these investigations the assessment of crack resistance with consideration of pore pressure was not fulfilled. Therefore, the aim of our study is assessment of high ECRD core crack resistance with consideration of pore pressure.

2. Materials and methods

The studies were conducted on the example of an ultra-high ECRD 330 m high. The constructed Rogun dam in Tajikistan is of such a height.

The considered design of the dam is a schematized structure of the dam of Rogun HPP. The dam has a flattened profile, the upstream slope is $1:2 \div 1:2.4$, the downstream slope is $1:2$ (Fig. 1). The dam lateral zones are made of gravel-pebble soil, but are weighted with rockfill. The dam core is constructed with inclination towards the upstream side, the angle of inclination with respect to vertical is 17° . The core is made of sandy loam. The core width at the bottom comprises 139.5 m, i.e. 42.3 % of the dam height.

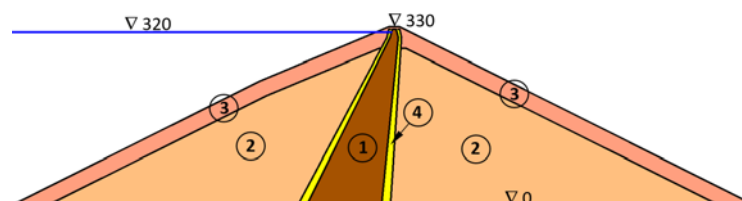


Figure 1. Structural diagram of ultra-high earth core rockfill dam
1 – sandy loam of core; 2 – gravel zone; 3 – rockfill zone; 4 – filter zone.

Analyses of the dam SSS were conducted in 2D formulation. The process of the dam SSS formation was modeled with consideration of sequence of its construction and reservoir impoundment. Firstly, the process of soil placement by layers was modeled, then gradual impoundment of the reservoir.

Deformation properties of the core sandy loam was assumed based on the results of experimental data on tests conducted in a stabilometer. In [27] there given a compression curve of sandy loam in the range of compressive stresses up to 3.2 MPa. Relationship between stresses and deformations are close to a linear one, therefore, modulus of linear deformation may be assumed to be constant. It is equal to 47 MPa. It was assumed that this compression curve corresponds to drained soil.

During analyses there was applied the model of soil deformation non-linearity which takes into account the following non-linear effects:

- presence in soils of two branches of loading (active loading and de-stressing),
- possible loss of shear strength or tensile strength,
- decrease of deformation at increase of lateral compression.

For consideration of soil deformation decrease at increase of lateral compression there was used dependence between soil solid skeleton modulus of linear deformation and compression stresses:

$$E = E_1 \left(\sigma_{3,ef} \right)^k,$$

where E_1 is modulus of linear deformation at compression stress 0.01 MPa; k is power index; $\sigma_{3,ef}$ is total minor (minimum) principal stress, characterizing the minimum level of lateral compression.

Poisson's ratio of soils in a strong state is considered to be constant. The parameters of the model are given in Table 1.

Mohr-Coulomb strength condition was used for determination of soil shear strength. At determining shear strength of coarse soils consideration was taken of decrease of internal friction angle value φ with increase of compressive stresses σ . Relationship between φ and σ was assumed to be linear at the section from φ_0 (at $\sigma = 0$) to φ_k (at $\sigma = 1.5 \div 2.0$ MPa).

Table 1. Parameters of physical-mechanical model of materials

Material	Density [g/cm ³]		Deformation parameters			Strength indices		
	ρ	ρ_{sat}	E_1 [MPa]	k	ν	φ_0	φ_k	c [kPa]
sandy loam of core	2.25–2.28	2.30	42.3	0.0	0.35	29°	29°	10
gravel	2.20	2.38	43.2	0.35	0.2	49°	38°	0
rockfill	2.00	2.25	43.2	0.35	0.2	50°	34°	0

Designations:

ρ , ρ_{sat} is soil density respectively at placement (with consideration of moisture content) and in a saturated state; ν is Poisson's ratio; φ_0 , φ_k is initial and final angle of internal friction respectively; c is specific cohesion.

Pore pressure is considered by introduction of an additional parameter, i.e. modulus of volumetric deformation $E_{0,w}$ of pore liquid. $E_{0,w}$ expresses relationship between pore pressure and volumetric deformations of soil. Expression for determination of $E_{0,w}$ was obtained from R. Boyle – E. Mariotte law:

$$E_{0,w} = \frac{p_a (1 + \varepsilon_0)}{\varepsilon_{0,air} + \beta \varepsilon_w - \Delta \varepsilon}.$$

In this formula p_a is atmospheric pressure; $\varepsilon_{0,air}$ is coefficient of soil porosity corresponding to pores filled with air, before start of compaction process; ε_w is coefficient of soil porosity corresponding to pores filled with water; β is coefficient of air solubility in water which may be assumed to be equal to 0.0245; $\Delta \varepsilon$ is variation of soil porosity coefficient at compaction.

When all air is squeezed from pores, the denominator of the formula will be equal to 0 and all the load will be transferred to water. In this case $E_{0,w}$ is equal to modulus of volumetric deformation of water (2000 MPa).

Dispersion of pore pressure was not taken into account in calculations.

Calculations were conducted for three alternatives of the value of initial degree of water saturation S_0 of core soil. S_0 is ratio between soil moisture content at placement and moisture content in a saturated

state. In alternative 1 $S_0 = 0,80$; alternative 2 $S_0 = 0,85$; alternative 3 $S_0 = 0.90$. Consequently, the core soil density varied from 2.25 to 2.28 g/cm³.

3. Results and Discussion

Analysis of the dam SSS was carried out for the moment of construction period completion when the reservoir had been impounded to $\nabla 320$ m (Fig. 2–5).

Fig. 2 shows distribution of pore water pressure (PWP) in the core. Maximum by value PWP is typical for the core lower part, because this zone is subject to maximum loads. Analyses revealed that PWP is greatly dependent on initial degree of soil water saturation S_0 . This is explained by the fact that at high degree of water saturation the volume of air in pores is small and at loading the soil is transferred more quickly from a three-phase state (solid particles, water, air) to a two-phase state (solid particles and water). In a two-phase state of soil all load is transferred only to pore water, which will lead to intensive growth of PWP. The more is S_0 , the more by value is the zone of high PWP and the higher is the maximum value of PWP. In alternative 1 the maximum value of PWP reaches 2.6 MPa (Fig. 2a), in alternative 2–3.4 MPa (Fig. 2b), and in alternative 3–4.3 MPa (Fig. 2c).

Obtained in alternatives 2 and 3 maximum values of PWP exceed the value of upstream hydrostatic pressure. In alternative 3 PWP exceeds hydrostatic pressure by 30 %.

For checking the obtained results there was calculated the maximum value of pore pressure with the aid of analytical method of Nichiporovich and Tsybulnik. It is reached at the core foot and axis at the moment of construction completion ($t = t_{EOC}$). In this calculation the coefficient of the core soil compression m was assumed equal $m = 0.029 \text{ MPa}^{-1}$, and seepage coefficient $k_f = 1 \cdot 10^{-8} \text{ m/s}$. Pressure from external loads was assumed equal $\sigma = 4.6 \text{ MPa}$ and coefficient of pore pressure $\alpha = 0.75$. Construction duration was proposed to last 5 years. Similar calculation of PWP was fulfilled in [28].

By the results of analysis by the method of Nichiporovich and Tsybulnik the maximum value of PWP comprised 3.5 MPa. This value is in the interval of PWP values obtained with the aid of numerical modeling, which evidences about agreement of both methods.

However, it should be noted that there is a difference in PWP distribution width-wise and height-wise the core. In the method of Nichiporovich and Tsybulnik pore pressure considerably decreases in the core lateral zones and nearly uniformly decreases height-wise. On the contrary, by the results of numerical modeling, PWP in the core upper part is considerably less than in the lower part and actually does not change width-wise the core.

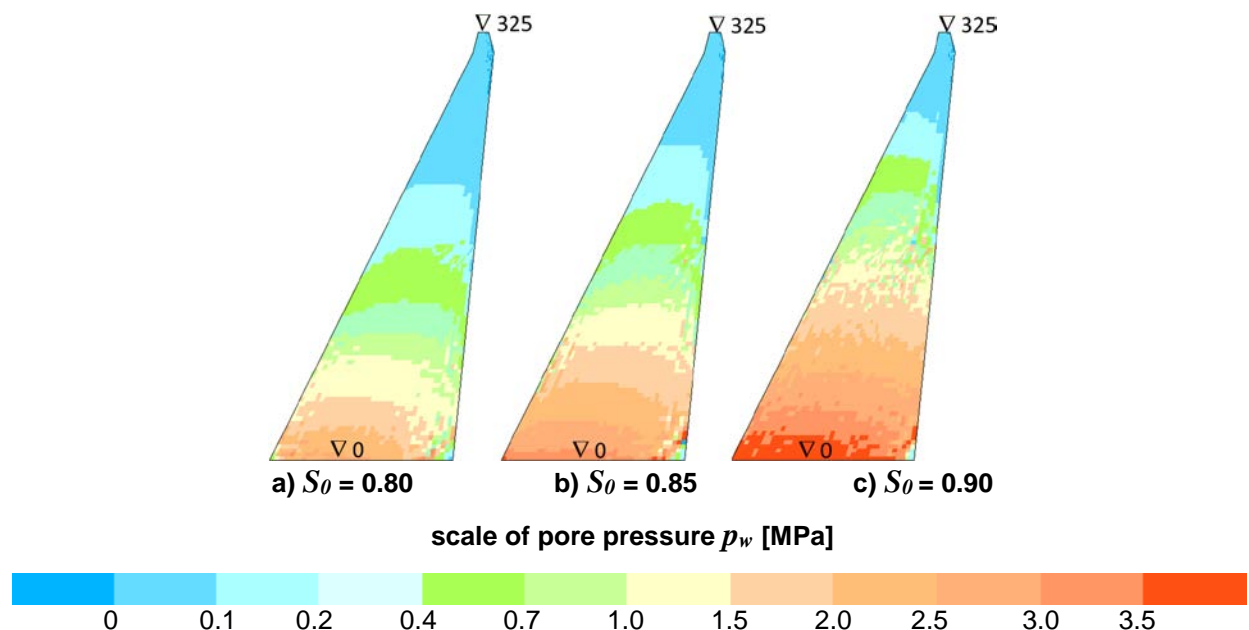


Figure 2. Value of pore water pressure in the core for different alternatives of initial water saturation degree S_0 .

High values of water pore pressure, obtained as a result of analysis, evidence about the fact that it threatens the core strength and crack resistance. For assessment of PWP effect on the core strength there were calculated the values of the core crack resistance coefficient k by the criterion suggested by the author. By the results of analysis, the core lower part where pore pressure is maximum has the lowest crack resistance safety factor (Fig. 2). Analysis shows that the core crack resistance is greatly dependent on coefficient of initial water saturation S_0 . In alternative 1 (Fig. 3a) the core crack resistance is provided by safety factor $k > 1,5$, and in alternative 3 (Fig. 3c) in the core lower part the crack resistance coefficient is lower than 1.2.

Minimum value of k exceeds 1, which from the formal point of view, testifies about provision of the core crack resistance, however, comprehensive analysis of SSS showed that it is not true. The thing is that at high pore pressure there is a decrease of effective stresses (stresses in solid phase) in soil and in its shear strength. By the results of calculations in alternative 3 in the core lower half the effective stresses σ_y comprise approximately 2.2÷2.3 MPa (Fig. 4b), which is less than PWP: the main portion of load is perceived by pore water.

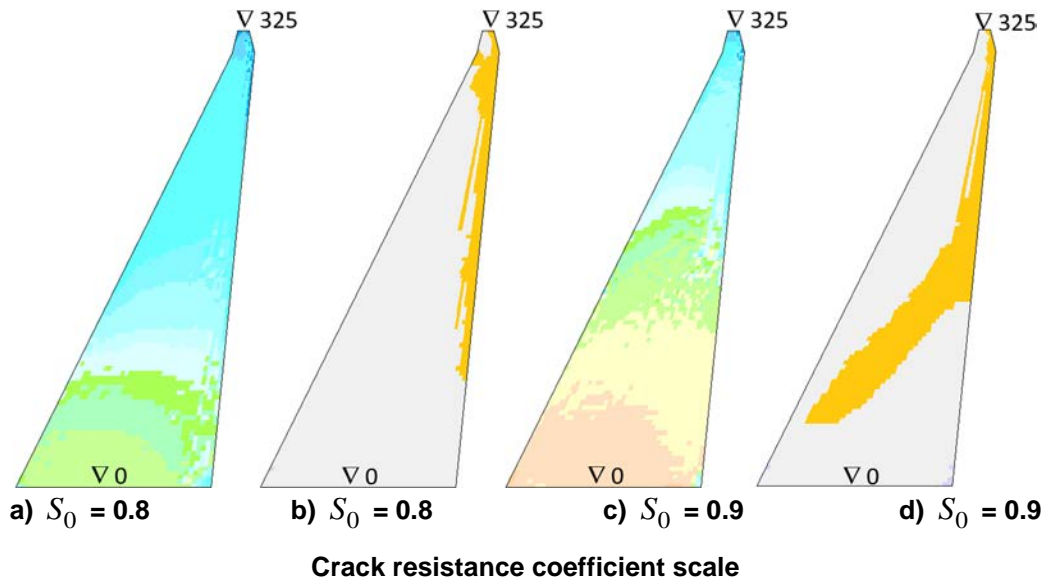


Figure 3. Coefficient of core crack resistance and location of zones with failure of shear strength.

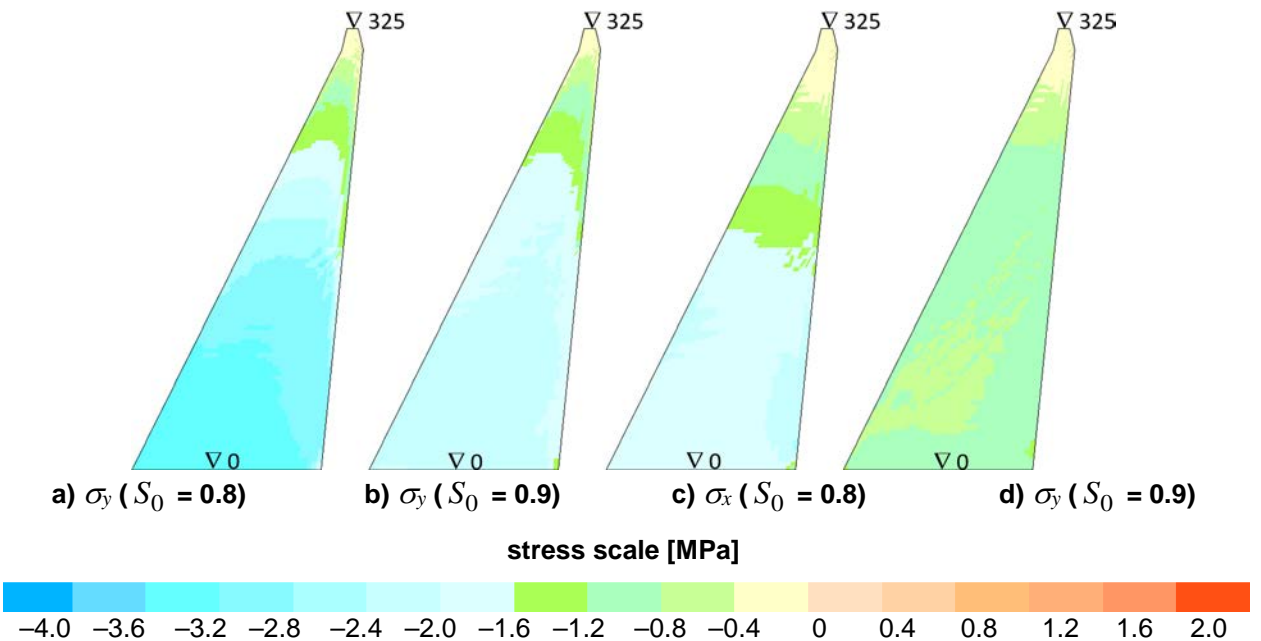


Figure 4. Effective stresses σ_y and σ_x in the core.

Effective stresses σ_x in alternative 3 are even less: 0.7÷0.8 MPa (Fig. 4d). This creates the danger of soil shear strength loss. By the results of analyses in alternative 3 in the core lower part a zone of shear strength loss is formed (Fig. 3d). It is located at an angle of 47° to horizontal. SSS calculation for the case where $S_0 = 0.92$ showed that the zone of shear failure increases. The effect of forming inclined shear zones in the core at high pore pressure was also obtained by numerical modeling in [7].

As shear failures are accompanied by development of cracks in soil, there arises the danger of the core hydraulic fracturing. Thus, pore water pressure is a potential cause of ECRD failures. Based on the obtained result there may be recommended the corrected criterion of the core crack resistance: $K > 1.3$.

Comparison of the results of analysis showed that development of pore pressure in the core greatly affects SSS of not only core, but of the whole dam as well. Coefficient of initial water saturation S_0 conditions shears U_x and U_y of the dam settlement.

In alternative 3 due to high PWP the core has great vertical stiffness. Due to this, decrease of the core settlements and the upstream shell occurs. While in alternative 1 maximum construction settlements of the dam reach 490 cm (Fig. 5a), in alternative 3 they comprised only 303 cm (Fig. 5b).

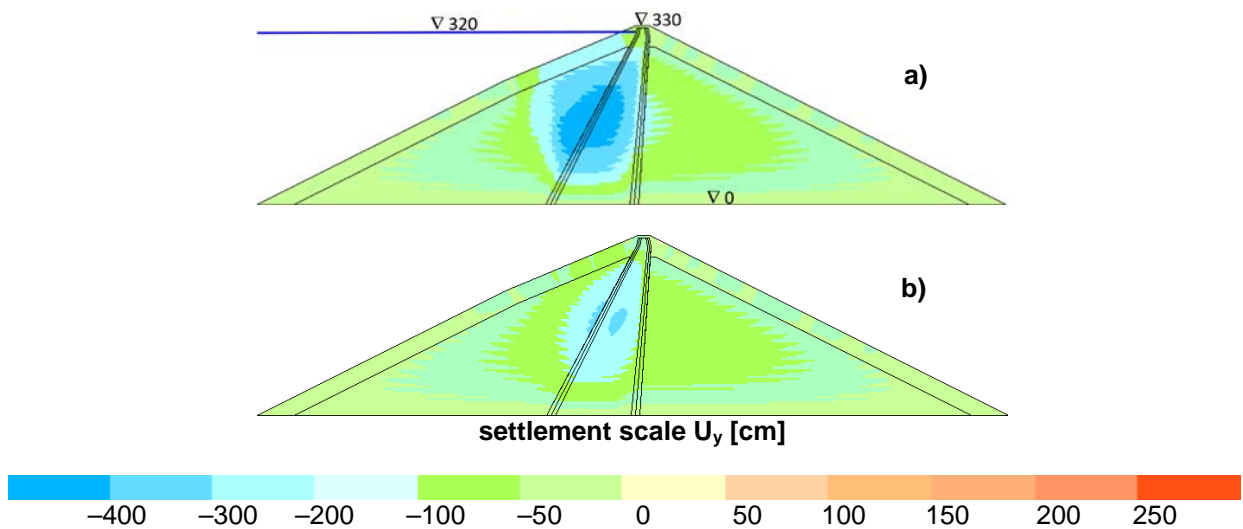


Figure 5. Dam settlement.

However, high PWP in the core of alternative 3 contributes to growth of horizontal displacements U_x in the upper part of the dam. In alternative 1 maximum horizontal displacement is observed in the core lower part and comprises 131 cm (Fig. 6a), and the crest displacement amounts to 43 cm. In alternative 3 maximum horizontal displacement (126 cm) is observed in the upper part of the dam, at that, the crest displacement reaches 74 cm (Fig. 6b).

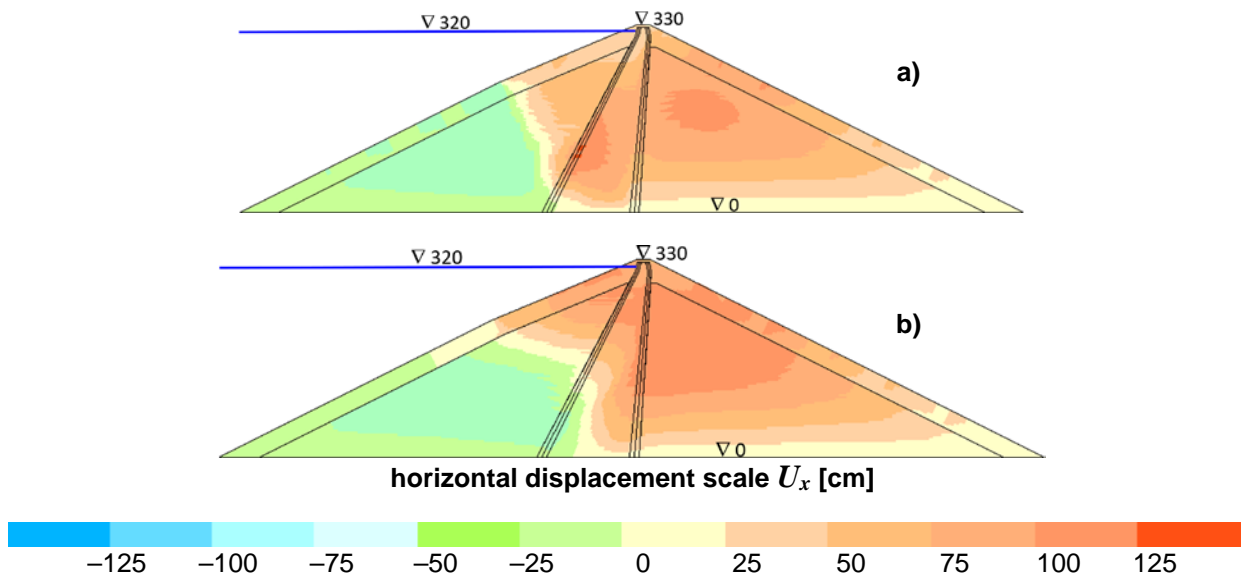


Figure 6. Dam horizontal displacements.**4. Conclusion**

1. Pore water pressure in the dam core plays an important role in formation of stress-strain state of not only core but of the whole dam. At numerical modeling of stress strain state of high ECRD it is necessary to take into account pore water pressure in the core. The core soil should be considered as a system consisting of several phases (solid, liquid and gas).

2. Pore water pressure is one of the main causes of earth core hydraulic fracturing. First of all, pore water pressure creates a force, wedging pores of soil, and secondly, it contributes to shear deformations. Micro cracks formed by pore water pressure initiate the core hydraulic fracturing.

3. Assessment of crack resistance of dam cores should be carried out with consideration of pore water pressure. The author proposed a criterion of assessment of the dam core hydraulic fracturing by pore water pressure.

4. The important role in formation of pore water pressure in the core of an ultra-high dam is played by soil moisture content at its placement into the dam body, to be more precise, the degree of its initial water saturation. Change of S_0 by 10 % leads to cardinal quantitative and qualitative changes of stress strain state of the dam and its core crack resistance. For preventing development of high pore water pressure in the core and crack formation, the coefficient of initial water saturation S_0 for sandy loam should not exceed $0.8 \div 0.85$, for loam and clay approximately 0.9.

References

1. Ma, H., Chi, F. Major Technologies for Safe Construction of High Earth-Rockfill Dams. *Engineering*. 2016. 2 (4). Pp. 498–509. DOI: 10.1016/J.ENG.2016.04.001
2. Lv, X., Chi, S. Strain Analysis of the Nuozhadu High Rockfill Dam during Initial Impoundment. *Mathematical Problems in Engineering*. 2018. 7291473. DOI: 10.1155/2018/7291473
3. Wu, Y., Zhang, B., Yu, Y., Zhang, Z. Consolidation analysis of Nuozhadu high earth-rockfill dam based on the coupling of seepage and stress-deformation physical state. *International Journal of Geomechanics*. 2016. 16(3). 04015085.
4. Hosseini, S.M.M.M., Fard, R.A. Pore pressure development in the core of earth dams during simultaneous construction and impounding. *Electronic Journal of Geotechnical Engineering*. 2003.
5. Razavi, B., Parehkar, M., Gholami, A. Investigation on Pore Water Pressure in Core of Karkheh Dam. *International Journal of Civil and Environmental Engineering*. 2011. 5 (11). Pp. 539–542.
6. Balanji, S.G., Davoudi, S., Merufinia, E. Investigation the Effects of Pore Water Pressure and Arching on Karkheh Earth Dam Considering the Instrumentation Results. *Advances in Environmental Biology*. 2014. 8(12). Pp. 1345–1353.
7. Akhtarpour, A., Salari, M. The deformation mechanism of a high rockfill dam during the construction and first impounding. *Scientia Iranica A*. 2020. 27 (2). Pp. 566–587. DOI: 10.24200/sci.2018.20778
8. Feng, R., He, Y.-L., Cao, X.-X. Different deformation patterns in high core wall rockfill dams: A case study of the Maoergai and Qiaoqi dams. *Advances in Civil Engineering*. 2019. 7069375. DOI: 10.1155/2019/7069375
9. Guo, Q., Pei, L., Zhou, Z., Chen, J., Yao, F. Response surface and genetic method of deformation back analysis for high core rockfill dams. *Computers and Geotechnics*. 2016. 74. Pp. 132–140. DOI: 10.1016/j.compgeo.2016.01.001
10. Yang, Z., Liu, C., Wu, M. Leading-edge Technologies in Hydropower Development in China. *Global Energy Interconnection*. 2019. 2(3). Pp. 244–253. DOI: 10.1016/j.gloi.2019.07.017
11. Li, S., Duan, B. The Highest Dam in the World under Construction: The Shuangjiangkou Core-Wall Rockfill Dam. *Engineering*. 2016. 2(3). Pp. 274–275. DOI: 10.1016/J.ENG.2016.03.018
12. Salari, M., Akhtarpour, A., Ekramifard, A. Hydraulic fracturing: a main cause of initiating internal erosion in a high earth-rock fill dam. *International Journal of Geotechnical Engineering*. 2018. DOI: 10.1080/19386362.2018.1500122
13. Nichiporovich, A.A., Teitel'baum, A.I. Evaluation of cracking in rock-fill dam cores. *Hydrotechnical Construction*. 1973. 7 (4). Pp. 319–325.
14. Ng, A.K.L., Small, J.C. A case study of hydraulic fracturing using finite element methods. *Canadian Geotechnical Journal*. 1999. 36 (5). Pp. 861–875.
15. Malyshev, L.I., Rasskazov, L.N., Soldatov, P.V. Condition of the Kureika hydroelectric station dam and engineering approaches to its repair. *Hydrotechnical Construction*. 1999. 33(1). Pp. 33–39.
16. Sainov, M.P., Anisimov, O.V. Stress-strain state of seepage-control wall constructed for repairs of earth rock-fill dam. *Magazine of Civil Engineering*. 2016. 68(8). Pp. 3–17. DOI: 10.5862/MCE.68.1
17. Bolton Seed, H., Duncan, J.M. The failure of Teton Dam. *Engineering Geology*. 1987. 24(1-4). Pp. 173–205.
18. Ji, E., Chen, S., Fu, Z. Research on Criteria of Hydraulic Fracturing in Earth Core Rockfill Dams. *IOP Conference Series: Earth and Environmental Science*. 2019. 304(2). 022032. DOI: 10.1088/1755-1315/304/2/022032
19. Poudel, S., Abbey, S.J., Ngambi, S. Mechanism of hydraulic fracturing in cohesive zone of embankment dam cores – A review. *International Journal of Civil Engineering and Technology*. 2017. 8(7). Pp. 1202–1213.
20. Tran, D.Q., Nishimura, S., Senge, M., Nishiyama, T. Risk of embankment dam failure from viewpoint of hydraulic fracturing: Statistics, mechanism, and measures. *Reviews in Agricultural Science*. 2020. 8. Pp. 216–229. DOI: 10.7831/ras.8.0_216
21. Wang, J.J., Zhu, J.G. Review on computing theories of hydraulic fracturing in soil. *Proceedings of the 2nd National Symposium on Geotechnical Engineering of China*. 2006. 2. Pp. 231–237. Wuhan: Science Press. (in Chinese)

22. Mori, A., and Tamura, M. Hydrofracturing pressure of cohesive soils. 1987. *Soils and Foundations*, 27(1). 14-22
23. Yanagisawa, E., and Panah, A. K. Two dimensional study of hydraulic fracturing criteria in cohesive soils. *Soils and Foundations*. 1994. 34(1). 1-9
24. Ghanbari, A., and S. S. Rad. Development of an Empirical Criterion for Predicting the Hydraulic Fracturing in the Core of Earth Dams. *Acta Geotechnica*. 2015. 10(2). 243–254. doi:10.1007/s11440-013-0263-2
25. Ji, E., Fu, Z., Chen, S., Zhu, J., Geng, Z. Numerical Simulation of Hydraulic Fracturing in Earth and Rockfill Dam Using Extended Finite Element Method. *Advances in Civil Engineering*. 2018. 1782686. DOI: 10.1155/2018/1782686
26. Aniskin, N.A., Rasskazov, L.N., Yadgorov, E.K. Seepage and Pore Pressure in the Core of a Earth-and-Rockfill Dam. *Power Technology and Engineering*. 2016. 50(4). Pp. 378–384.
27. Rasskazov, L.N., Yadgorov, E.K., Nikolaev, V.B. Field Observations of Soil Settlements, Displacements, and Pore Pressure in Dams. *Power Technology and Engineering*. 2018. 51(6). Pp. 611–620.
28. Aniskin, N.A., Rasskazov, L.N., Yadgorov, E.K. Filtration, pore pressure, and settling from consolidation of an ultra-high dam. *Power Technology and Engineering*. 2017. 50(6). Pp. 600–605.
29. Eisenstein, Zdenek, Law, Steven T.C. Analysis of consolidation behavior of Mica dam. *ASCE Journal of Geotechnical Engineering Division*. 1977. 103(8). Pp. 879–895.
30. Rashidi, M., Heidari, M., Azizyan, Gh. Numerical analysis and monitoring of an embankment dam during construction and First impounding Case study: Siah Sang Dam. *Scientia Iranica A*. 2018. 25(2). Pp. 505–516. DOI: 10.24200/sci.2017.4181

Information about author:

Mikhail Sainov,

Doctor of Technical Science

ORCID: <https://orcid.org/0000-0003-1139-3164>

E-mail: mp_sainov@mail.ru

Received 18.04.2021. Approved after reviewing 22.12.2021. Accepted 12.01.2022.



Research article

UDC 699.86

DOI: 10.34910/MCE.114.12



The influence of the sky radiative temperature on the building energy performance

S.V. Korniyenko 

Volgograd State Technical University, Volgograd, Russia

✉ svkorn2009@yandex.ru

Keywords: building, building energy performance, sky radiative temperature, sky emissivity, clear sky model, cloudy sky model, ambient air, solar radiation, environment.

Abstract. Most of the current sky models correlate with local climatic conditions and specific sites, while not covering different humidity-climatic conditions. In this work, sky emissivity and sky temperature models were reviewed, taking into account the common classification that includes simplified and detailed correlations. The clear-sky and cloudy-sky temperature models were also investigated in detail, employing them for different humidity-climatic conditions (wet, normal and dry) and evaluating their influence on building energy needs. Under clear-sky conditions in winter, the maximum difference between the ambient air temperature and sky temperature is 19 K regardless of humidity-climatic conditions. Under cloudy-sky conditions, it is possible to notice dissimilarities, ranging from 5 K (wet and normal conditions) to 10 K (dry conditions). In summer, under clear-sky conditions, the maximum values are ranging from 12 K (normal conditions) to 13 K (wet and dry conditions). Under cloudy-sky conditions, the maximum values are ranging from 5 K (normal conditions) to 10 K (dry conditions). Thus, the obtained results can be applied for the investigation of the radiative heat flux between a building surface and the sky, as a simplified model. Moreover, these results can be used when the sky temperature is not available from climatic data. The obtained results specified the simplified models according to ISO 13790. Finally, taking into account the influence of different correlations in building energy simulations, it was found that heating and cooling energy demands (using the example of a translucent roof) can be affected by significant percentage differences (the rounded values), ranging from +3 % to +11 % (no heat gain) for wet climatic conditions, from -61 % to +22 % for normal climatic conditions, and, finally, from -45 % to +8 % for dry climatic conditions. The comparison among the models can be useful to address the choice of users in building energy simulations and engineering applications. Future developments will regard the longwave sky radiation measurement under field conditions in the representative cities of the world in order to propose correlations for different climatic area.

Citation: Korniyenko, S.V. The influence of the sky radiative temperature on the building energy performance. Magazine of Civil Engineering. 2022. 114(6). Article No. 11412. DOI: 10.34910/MCE.114.12

1. Introduction

Heat transfer between the exterior surface of a building and the environment is based on convective and radiative phenomena [1]. This process included shortwave radiation, including direct, reflected and diffuse sunlight, longwave radiation to the environment, convective exchange with outside air [2, 3]. Thermal exchange associated to the sky longwave radiation can be related to an effective sky temperature [4]. Nowadays, building energy simulations use models able to estimate the temperature of the sky [3]. The sky can be thought as a heat sink for the exterior surfaces and the sky longwave radiation exchange is a function of the effective sky temperature [5–7]. The radiative cooling is highest during the night when the sky is clear, and humidity is low [8, 9]. In winter, the radiative cooling is negative factor as the temperature decrease on the exterior surface of a building increases heat loss [10]. In summer radiative passive cooling

is positive factor which employs thermal radiation properties for cooling an object or part of a building facing a colder surface, such as the sky [11–13]. The building sector covers about 40 % of total energy consumption [14–16]. Every second resident of the Earth lives in the city [17]. Buildings energy demand is increasing in connection with the growth of cities [18–23].

In order to evaluate radiative heat exchanges between a building and environment, sky emissivity and sky temperature needs to be assessed.

The first study related to the sky emissivity prediction was performed by Angström [24]. His model was developed starting from a long series of observations conducted in Algeria. The Angström's model is a function of the actual atmospheric vapor pressure. Many researchers developed their models starting from the Angstrom's correlation, modifying it with adapted coefficients.

Brunt [25] proposed a sky emissivity formula based on the correlation between sky temperature and the partial pressure of water vapor. This formula gives the sky emittance as a linear function of the square root of water vapor partial pressure. The equation needs the calculation of empirical coefficients, variable in function of the analyzed geographical region.

Clark and Allen [26] proposed formula for different meteorological conditions. This formula gives the clear sky emittance as a linear function of the natural logarithm of dew point.

Idso [27] proposed his correlation based on measurements conducted in Arizona (USA). His correlation can be employed for the whole range of wavelength, accounting water vapor pressure and ambient temperature.

Berdahl and Martin [27, 28] collected a set of almost 5 years sky longwave radiation data in 6 different cities. The model can be used for dew point temperatures which range between $-13\text{ }^{\circ}\text{C}$ and $+24\text{ }^{\circ}\text{C}$.

Many others studies have been conducted on sky emissivity and sky temperature models and different correlations have been proposed by researchers [26, 27, 29, 30, 31, 32] (authors E.L. Andreas, S.F. Ackley, C.V. Melchor, J.L. Hatfield, R.J. Reginato, B. Chen, D. Clark, J. Maloney, W. Mei, J. Kasher and W. Swinbank, et al). The paper [27] (authors L. Evangelisti, C. Guattari, F. Asdrubali) gives a critical review about the existing correlations for the calculation of sky emissivity and sky temperature, referring to different climatic conditions.

Sky models are related to local meteorological conditions and specific sites [33]. Most of these models are approximated due to the lack of detailed measured data. The aim of this paper is providing a comparative analysis of different model of the sky as the clear sky and cloudy sky, also the calculation of the sky emissivity and sky temperature, relating them to the different humidity conditions in Russia. The correlations were used to quantify similarities and differences among them. The effect of different correlations on heating and cooling energy demands was examined.

2. Methods

2.1. Sky emissivity and sky temperature models

The radiation related to the atmosphere can be expressed assuming that the sky has the same behavior of a black body (characterized by an emissivity equal to 1) or assuming that the sky is a grey body, distinguished by an apparent emissivity [32, 34]. According to this, two relations can be identified:

$$q_{sky} = \sigma T_{sky}^4, \quad (1)$$

$$q_{sky} = \varepsilon_{sky} \sigma T_{amb}^4, \quad (2)$$

where q_{sky} is the atmospheric radiation, σ is the Stefan-Boltzmann constant ($\sigma = 5.67 \cdot 10^{-8} \text{ W} \cdot \text{m}^{-2} \cdot \text{K}^{-4}$), T_{sky} is the sky radiative temperature (sky temperature), ε_{sky} is the emissivity of the sky and T_{amb} is the ambient temperature (temperatures T_{sky} and T_{amb} are in degrees Kelvin). Making equal Eqs. (1) and (2), it is possible to obtain:

$$T_{sky} = \sqrt[4]{\varepsilon_{sky} T_{amb}^4}. \quad (3)$$

The net radiative heat flux (q_{rad}) between a building surface and the sky can be quantified as follows [27, 34]:

$$q_{rad} = \varepsilon \sigma F (T_s^4 - T_{sky}^4), \quad (4)$$

where ε is the hemispherical emissivity of the surface, F is the sky view factor and T_s is the surface temperature.

T_{sky} can be defined as an equivalent temperature of the sky vault. It is worthy to notice that the sky temperature is an average over the sky dome. The coldest part of the sky is the dome overhead. At the horizon, the temperature of the sky is equal to the ambient temperature. Subsequently, the usual approximation of considering a sky view factor equal to 0.5 for vertical surfaces (implicitly assuming a uniform sky temperature) can be considered an approximation adopted in simulation codes to simplify calculations but it cannot be considered fully representative [10].

The mentioned equations make easier the estimation of the inward infrared radiation from the atmosphere. Nevertheless, this is not generally measured by weather stations. Therefore, correlations have been developed in order to relate the climatic parameters to the infrared atmospheric radiation.

It is worthy to notice that sky temperature and ambient temperature are different. Starting from ground and going upward, temperatures tend to decrease, with a resulting sky temperature lower than the air temperature [25]. Furthermore, the difference between sky and air temperatures is higher during the summer, especially when clear sky conditions occur. Moreover, the effective sky temperature depends on other many factors, such as dew point, clouds amount and the site conditions. Therefore, these factors need to be considered during the study and development of sky temperature models.

Several correlations are nowadays available to calculate the clear-sky emissivity and temperature of the sky [27], coming from different methods for the infrared radiation estimation. Table 1 lists the four main correlations for the sky emissivity under clear-sky conditions, are widely applicable in the sky radiation modeling.

Table 1. Empirical clear sky models based on emissivity correlations

Author	Correlation
Clark and Allen	$\varepsilon_{sky,clear} = 0.787 + 0.764 \cdot \ln(T_{dp} / 273)$
Martin and Berdahl	$\varepsilon_{sky,clear} = 0.758 + 0.521(T_{dp} / 100) + 0.625(T_{dp} / 273)^2$
Brunt	$\varepsilon_{sky,clear} = 0.618 + 0.056(P_{wv})^{0.5}$
Idso	$\varepsilon_{sky,clear} = 0.685 + 3.2 \times 10^{-5} (P_{wv}) \exp(1699 / T_{db})$

In Table 1: $\varepsilon_{sky,clear}$ is the clear sky emissivity, is the dew point temperature, in K for Clark and Allen, in $^{\circ}C$ for Martin and Berdahl, P_{wv} is the partial pressure of water vapor, in hPa, T_{db} is the drybulb temperature, in K ($T_{db} \approx T_{amb}$).

It is well-known that clear sky conditions are not continuous along time and cloudy conditions increase the infrared radiation. For this reason, the clear sky correlations have to be adapted to cloudy conditions. The impact of cloudiness on sky temperature is difficult to evaluate, and only a few researchers have attempted to predict it. Berdahl and Martin developed a cloudy emissivity model based on a cloudiness factor (CF). This factor ranges between 0 and 1, depending on clear sky conditions or totally cloudy sky. Thus, the sky temperature modeling is based on the following equation [27]:

$$T_{sky} = T_{amb} \left[\varepsilon_{sky,clear} + 0.8(1 - \varepsilon_{sky}) CF \right]^{0.25}. \quad (5)$$

It is worthy to notice that, in the above formula, a factor equal to 0.8 appears. The reason of this value (instead of 1) is related to a cloud base temperature significantly lower than the air temperature at screen height.

If weather data do not contain the sky cloudiness factor, it can be determined according to the Kasten and Czeplak formula [6]:

$$CF = \left(1.4286 \frac{G_{dif}}{G_{Glob,H}} - 0.3 \right)^{0.5}, \quad (6)$$

where G_{dif} is the diffuse radiation on the horizontal and $G_{Glob,H}$ is the total radiation on the horizontal. CF can be used to calculate the effective sky temperature by means of Eq. (3).

Nowadays, simplified methods for calculating the sky temperature are well-known.

Taking into account the heat transfers between buildings and the environment, if data for the sky temperature calculation are not available, ISO 13790 allows to calculate the temperature of the sky, considering the equations listed in Table 2. The standard provides a simplified calculation method for determining the annual energy requirement for heating in residential and non-residential buildings. Starting from the building location, it is possible to define the climatic area and consequently identify the suitable correlation. It is possible to distinguish different climatic areas, according to the common world climate classification proposed by Köppen [35]. It is worthy to notice that ISO 13790 takes into account a climate classification based only on latitudes, distinguishing sub-polar, temperate and tropical areas. The classification of humidity areas in Russia is proposed by Ilyinsky for simplified calculations according to SP 50.13330.2012 (National Standard). According to this classification, wet, normal and dry zones are distinguished.

Table 2. Simplified models according to ISO 13790.

Site	Correlation
Temperate areas	$T_{sky} = T_{amb} - 11$
Sub-polar areas	$T_{sky} = T_{amb} - 9$
Tropical areas	$T_{sky} = T_{amb} - 13$

Calculations using simplified models according to ISO 13790 are not always representative for temperate areas with humidity variations.

According to SP 50.13330.2012 (National Standard) the sky emissivity is equal to 1, and the sky temperature is equal to the ambient temperature. Obviously, this simplified model cannot ensure the representativeness and accuracy of the calculation results.

2.2. Outside surface heat balance

The different sky temperature models can be used to model a building energy performance. The heat balance on the outside face of building element is:

$$q_{asol} + q_{LWR} + q_{conv} - q_{cond} = 0, \quad (7)$$

where q_{asol} is the absorbed direct and diffuse solar (short wavelength) radiation heat flux, q_{LWR} is net long wavelength (thermal) radiation flux exchange with the air and surroundings, q_{conv} is convective flux exchange with outside air and q_{cond} is conduction heat flux into the building element (heat fluxes q_{asol} , q_{LWR} , q_{conv} , and q_{cond} are in W/m^2). Simplified procedures generally combine the first three terms by using the concept of a sol-air temperature [36].

Generally, the exterior surface heat flux (q_{se}) is given by equation:

$$q_{se} = -pG_{Glob} + h_{ce}(T_{se} - T_{out}) + h_{re}(T_{se} - T_{sky}), \quad (8)$$

where p is the solar absorptance coefficient, G_{Glob} is the total radiation on the surface, h_{ce} is the surface exterior convective heat transfer coefficient, T_{out} is the outdoor air temperature, h_{re} is the surface exterior radiative heat transfer coefficient and T_{sky} is the clear or cloudy sky temperature. A venerable equation for wind-driven convection was developed by W.H. McAdams (1954) which Palyvos (2008) casts in SI units as:

$$h_{ce} = 5.7 + 3.8V_z, \quad (9)$$

where V_z is the wind velocity that has been adjusted for height above ground using the z axis coordinate of the surface's centroid. This model can be applied to all surfaces and the relatively large constant is assumed to represent the natural convection portion of a total convection coefficient. The model is not sensitive to wind direction or surface roughness.

The surface radiative heat transfer coefficient can be approximately calculated according to formula ISO 6946:2017:

$$h_{re} = 4\sigma F \varepsilon T_{mn}^3, \quad (10)$$

where T_{mn} is the main thermodynamic temperature of the surface and its surroundings. Taking into account external surfaces, the long-wave radiation transfer at the external surface is accounted employing a sky temperature (T_{sky}) and a sky view factor (F_{sky}). For vertical walls and isolated buildings, a realistic value for F_{sky} is 0.5. If there are constructions or trees in front of the wall, the value of F_{sky} should be lower than 0.5. For horizontal surfaces F_{sky} is equal to 1.

The heat flux through the building element (q_{cond}) is given by well-known equation, so is not discussed in this paper.

3. Results and Discussion

3.1. Models comparison

Starting from the available empirical correlations, some of them were employed to calculate and compare sky emissivity and sky temperatures, employing the Typical Meteorological Years (TMY) [4] available for different cities, in particular considering locations characterized by different humidity-climatic conditions. The averaging period of climatic data of 10 years was considered according to ISO 13788:2012. Wet, normal and dry conditions were considered according to SP 131.13330.2018 (National Standard). According to this, three representative cities were selected (see Table 3).

Table 3. Cities, humidity-climatic zones and correlations tested under clear sky and cloudy sky conditions.

Correlation	City	Humidity-climatic conditions
Clark and Allen	St. Petersburg	Wet
Martin and Berdahl	Moscow	Normal
Brunt	Volgograd	Dry
Idso		

The average climatic data for each city (air temperature, humidity, cloudiness, wind speed) are calculated for the period of 10 years (from 2011 to 2020), using hourly or three-hour values. Different correlations were applied, considering clear and cloudy sky conditions. The comparison among the correlations was achieved taking into account two representative days of January and July.

The climate data calculated using averaging period of 10 years is given in Table 4. Analyzing obtained values, it is possible to identify that the mean values of climate data in whole are representative.

Table 4. Weather-data calculated using averaging period of 10 years.

	St. Petersburg		Moscow		Volgograd	
	January	July	January	July	January	July
Air temperature, °C	-5.0	17.1	-4.1	20.1	-5.4	24.3
Humidity, %	89	70	86	73	89	51
Cloudiness	0.89	0.52	0.92	0.69	0.55	0.30
Wind speed, m/s	4.1	3.6	1.2	1.7	5.9	4.0

Wet conditions. Analyzing wet conditions, the city of St. Petersburg was selected. Summer is short and wet; winter is long, cold and raw. The rainfall average value is equal to 662 mm per year. The average

annual temperature is equal to 5.8 °C. The lowest average temperatures during the year occur in January (minus 5.5 °C). July is the warmest month, characterized by an average temperature of 18.8 °C.

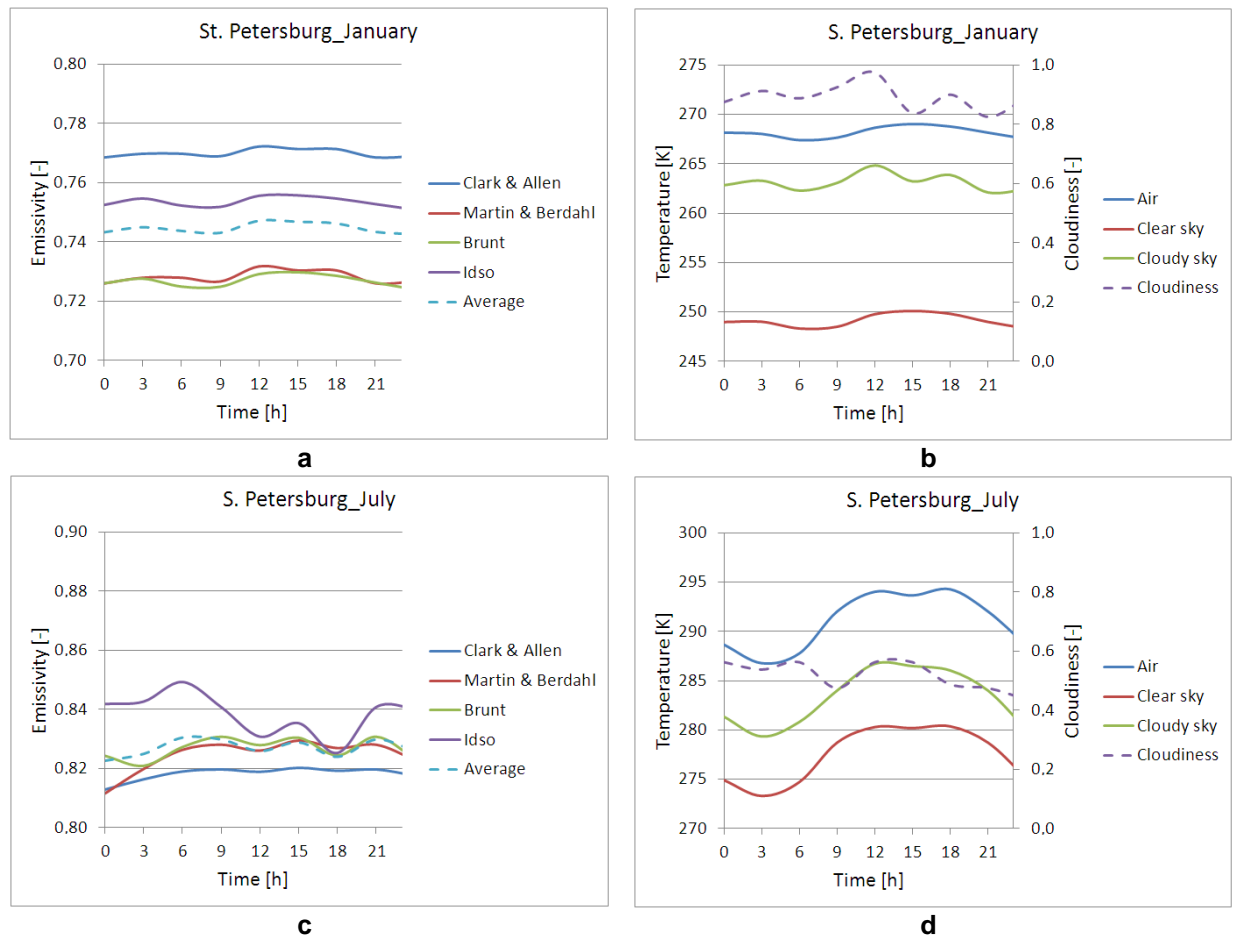


Figure 1. Comparison among the emissivity and sky temperatures calculated using different models in St. Petersburg, during January (a, b) and July (c, d).

Fig. 1 shows the emissivity and the sky temperatures obtained in January and July. In addition, Fig. 1b and d show cloudiness. Both in terms of emissivity and sky temperatures, it is possible to observe a wide variety of values. In winter, Clark and Allen formula provides the highest emissivity value (with a mean value equal to 0.77), followed by the almost constant trends provided by Idso (mean value equal to 0.73), Martin and Berdahl (mean value equal to 0.73) and Brunt (mean value equal to 0.73). Moreover, it is possible to observe that the Brunt's model allows to calculate emissivity values close to those achieved by means of Martin and Berdahl formula. The emissivity values calculated through the formulae are the lowest. In summer, it is possible to notice the same distribution among the sky emissivity correlations, with the highest values obtained from Idso's formula and the lowest obtained from Clark and Allen equation. In this case, Brunt's formula provides emissivity values very close to those obtained by means of Martin and Berdahl equation. The emissivity and cloudiness have an influence on sky temperature values, both in winter and in summer. The sky temperature only approximate to ambient air temperature in the case of very cloudy conditions. Analyzing Fig. 1, it is possible to identify that the mean values of emissivity and the sky temperature are fully representative.

Normal conditions. Moscow was selected to analyze the normal climatic condition. The climate of Moscow is moderately continental, with clear seasonality. The average annual temperature is equal to 5.8 °C. January is the coldest month, characterized by an average temperature of minus 6.5 °C. July is the warmest month (with average temperature of 19.2 °C).

Fig. 2 shows the emissivity and the sky temperatures obtained for a representative day of January and July. In January (Fig. 2a), it is possible to observe low emissivity values related to low ambient temperatures. The highest average value can be obtained applying the Clark and Allen correlation ($\varepsilon_{avg} = 0.77$). On the contrary, the lowest one is obtained with the Martin and Berdahl as well as equation Brunt equations ($\varepsilon_{avg} = 0.73$). During the day the emissivity are quite constant and, subsequently also the sky temperatures are constant (see Fig. 2b). The lowest sky temperatures can be obtained applying the

clear sky model. The highest sky temperatures can be obtained applying the fully cloudiness sky model. All the other correlations provide sky temperature values between these two limit values. On the other hand, in July emissivity and sky temperatures (see Fig. 2c, d) are more variables than in January. In this case, the highest emissivity values are obtained using Idso's correlation. On the contrary, the lowest emissivity values can be obtained applying the Clark and Allen equation.

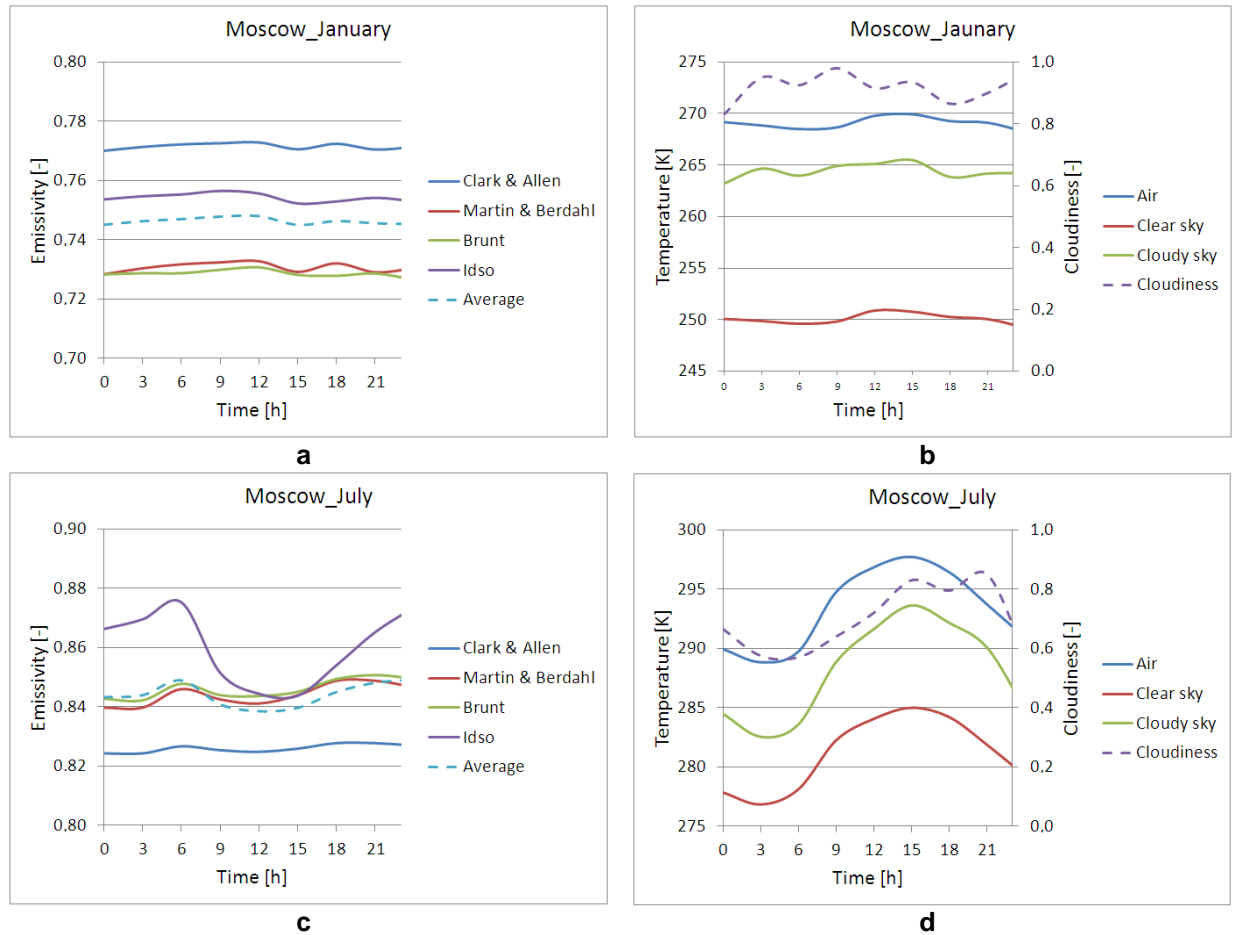
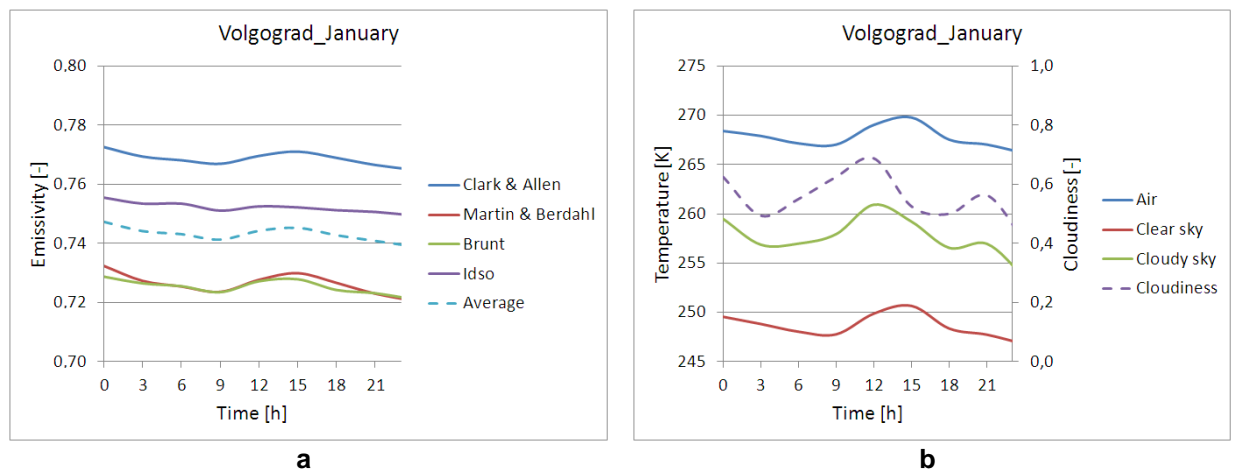


Figure 2. Comparison among the emissivity and sky temperatures calculated using different models in Moscow, during January (a, b) and July (c, d).

Dry conditions. Considering dry conditions, Volgograd (until 1961 – Stalingrad) was selected. The climate is continental. The average rainfall is 267 mm per year. Winter is mild, with frequent thaws, summer is hot and long, at all times of the year sharp temperature variations are possible. The average annual temperature is 8.8 °C. January is the coldest month of the year, with an average temperature of minus 5.7 °C. July is the hottest month of the year, with an average temperature of 24.2 °C. Temperatures during the whole year are characterized by variations approximately equal to 15 °C, on average. The highest total (direct and diffuse) radiation on the horizontal surface in July is 866 W/m².



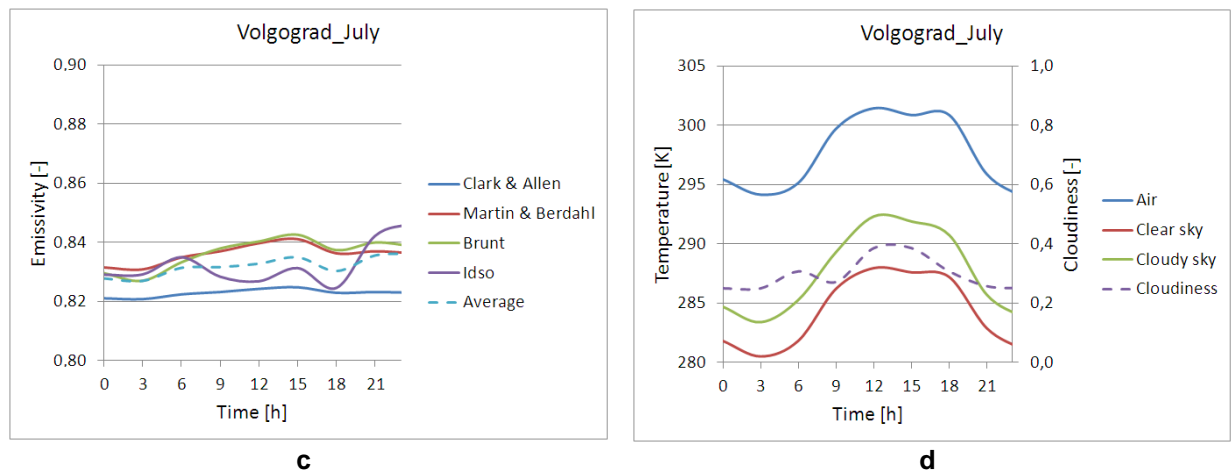


Figure 3. Comparison among the emissivity and sky temperatures calculated using different models in Volgograd, during January (a), (b) and July (c), (d).

Fig. 3a and c show the emissivity values obtained by applying the correlations mentioned before. Fig. 3b and d provide sky temperatures, compared to ambient temperatures in January and July. In January, the correlations suggested by Martin and Berdahl and Brunt provide very similar emissivity. On the other hand, Martin and Berdahl correlation is quite higher. Clark and Allen equation provides the highest emissivity values. Analyzing the sky emissivity in July, similar values can be obtained applying all the correlations. Fig. 3 shows that the sky temperatures are totally characteristic.

In order to make a comparison, all the average sky emissivity and the average sky temperatures calculated for the aforementioned climatic conditions are summarized in Table 5, 6.

Table 5. Average sky emissivity for clear sky conditions.

Month	Correlation	St. Petersburg (Wet)	Moscow (Normal)	Volgograd (Dry)
January	Clark and Allen	0.77	0.77	0.77
	Martin and Berdahl	0.73	0.73	0.73
	Brunt	0.73	0.73	0.73
	Idso	0.75	0.75	0.75
July	Clark and Allen	0.82	0.83	0.82
	Martin and Berdahl	0.82	0.84	0.84
	Brunt	0.83	0.85	0.84
	Idso	0.84	0.86	0.83

Table 6. Average sky emissivity, cloudiness and sky temperatures for clear and cloudy sky conditions.

Site	Clear sky				Cloudy sky			
	January		July		January		July	
	ϵ_{avg}	$T_{sky,avg}, K$	ϵ_{avg}	$T_{sky,avg}, K$	CF_{avg}	$T_{sky, avg}, K$	CF_{avg}	$T_{sky, avg}, K$
St. Petersburg (Wet)	0.74	249	0.83	277	0.89	263	0.52	283
Moscow (Normal)	0.75	250	0.84	281	0.92	264	0.69	288
Volgograd (Dry)	0.74	249	0.83	284	0.55	258	0.30	287

Analyzing the average sky emissivity in January and July, the correlations suggested by Clark and Allen, Martin and Berdahl, Brunt and Idso provide very similar emissivity. The sky emissivity values in July are more than in January. This conclusion is well correspond to results of Evangelisti, Guattari, Asdrubali and other researchers [27]. Moreover, it is possible to observe that emissivity values are almost the same for different humidity areas; therefore, any correlation can be used, distinguishing winter and summer conditions.

Distinguishing winter and summer conditions, it is possible to observe the sky temperature range obtained by applying the different correlations (see Table 7). Under wet conditions, the sky temperature ranges between 249 K and 263 K in winter (for clear and cloudy sky). During summer, it ranges between 277 K and 283 K. Under winter normal conditions, the sky temperature ranges from 250 K to 264 K, and

during summer, it ranges between 281 K and 288 K. Finally, under dry conditions, the range goes from 249 K to 258 K, and during summer, it goes from 284 K to 287 K.

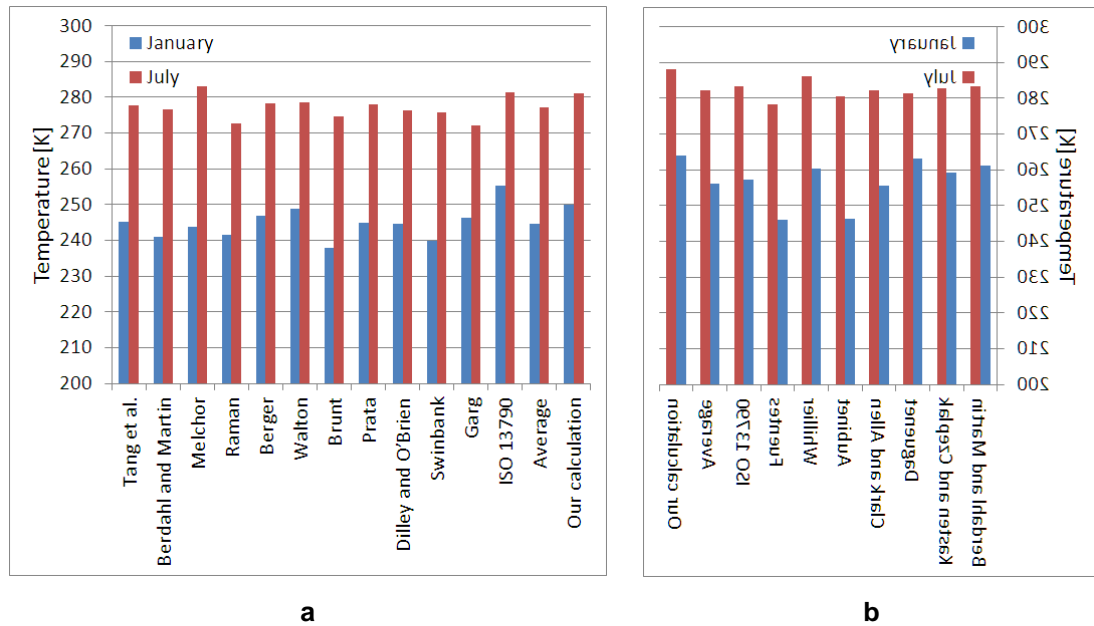


Figure 4. Comparison among the sky temperatures calculated using different models in January (a) and July (b).

Analyzing the obtained data (see Fig. 4) it is worthy to notice that the average sky temperature in whole correlation with results of different study [27]. Percentage differences obtained by using different correlation under clear sky conditions are 2.16 % (in January) and 1.42 % (in June); for cloudy sky conditions – 3.04 % and 2.03 %, respectively.

The obtained results can be applied for specification of the simplified sky temperature models (ISO 13790 and SP 50.13330.2012) taking account the sky model, humidity-climatic conditions and season (see Table 7).

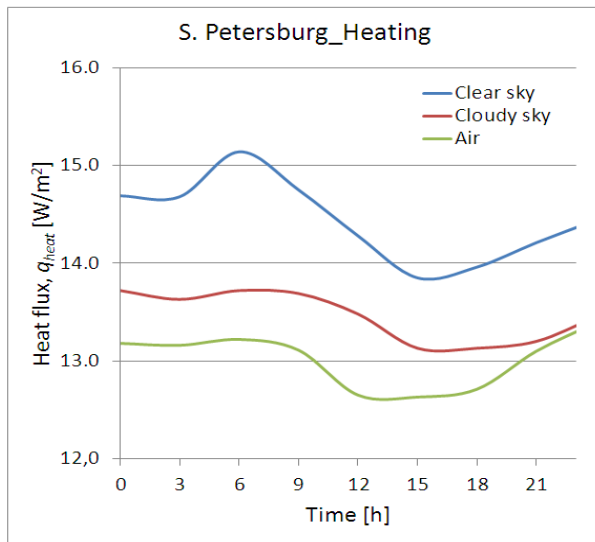
Table 7. Simplified sky temperature model (our suggestions).

Humidity-climatic conditions	Correlation			
	Clear sky		Cloudy sky	
	Winter	Summer	Winter	Summer
Wet	$T_{sky} = T_{amb} - 19$	$T_{sky} = T_{amb} - 13$	$T_{sky} = T_{amb} - 5$	$T_{sky} = T_{amb} - 8$
Normal	$T_{sky} = T_{amb} - 19$	$T_{sky} = T_{amb} - 12$	$T_{sky} = T_{amb} - 5$	$T_{sky} = T_{amb} - 5$
Dry	$T_{sky} = T_{amb} - 19$	$T_{sky} = T_{amb} - 13$	$T_{sky} = T_{amb} - 10$	$T_{sky} = T_{amb} - 10$

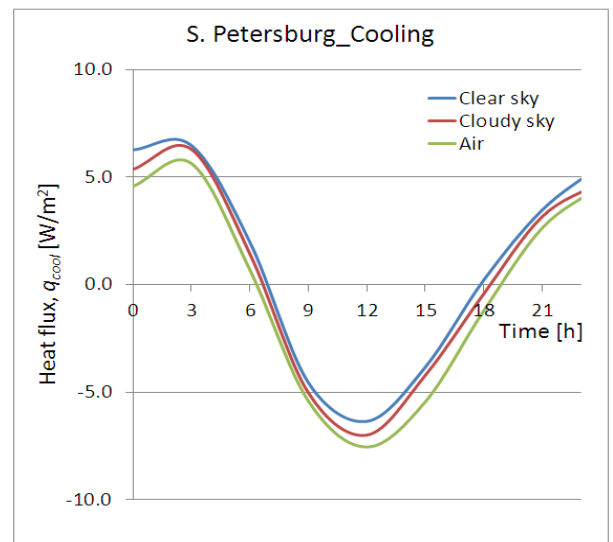
Thus, the obtained results can be applied for investigation the radiative heat flux between a building surface and the sky, as simplified model. Also these results can be used when the sky temperature is not available from climatic data.

3.2. Influence of the sky temperature in building energy simulations

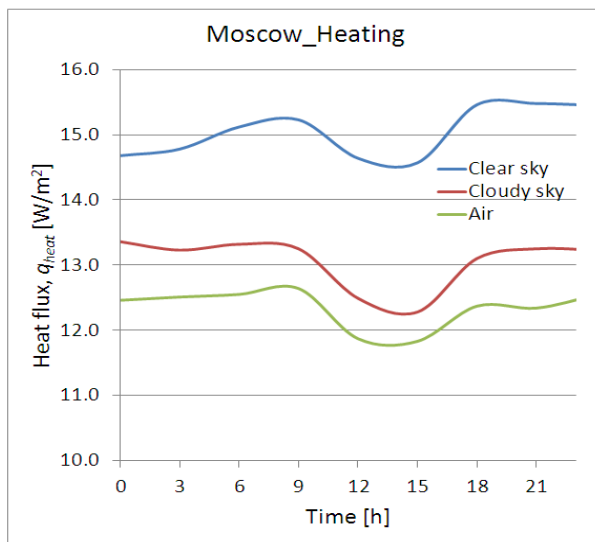
The simple isolated building component was modeled considering the typical construction technique of the most recent buildings. The modeling object is a light-transmitting roof. The structure consist some material layers as a “no mass” materials. This assumption essentially says that these layers add nothing to the thermal mass of the overall construction and only add to the overall resistance (R-value) of the construction as a whole. For this reason under passive steady state the heat balance equation for the building element are provided. The thermal resistance of the roof is equal to 1.73 m²·K/W. The envelope has a solar absorptance coefficient equal to 0.7. Heat losses and heat gains through other building elements is expected to be negligible. The indoor setpoint temperature was set equal to 20 °C for heating and 24 °C for cooling.



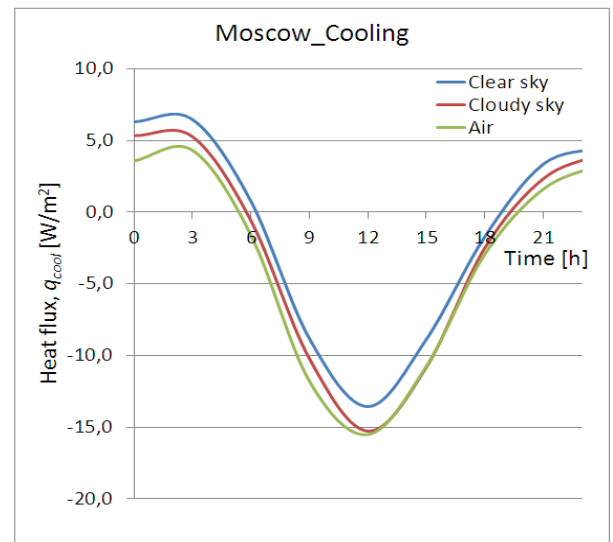
a



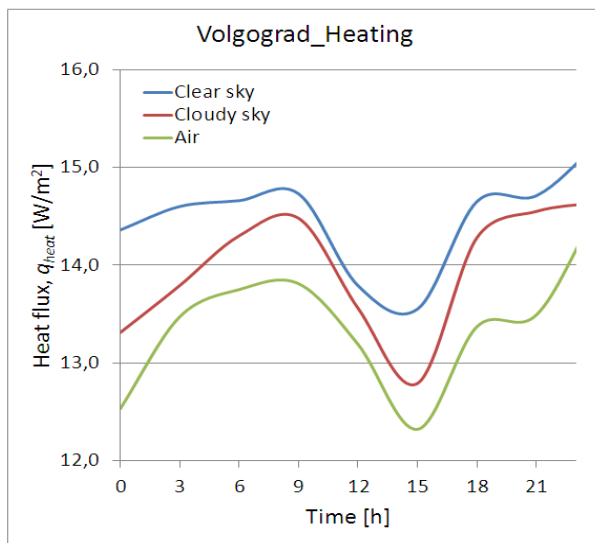
b



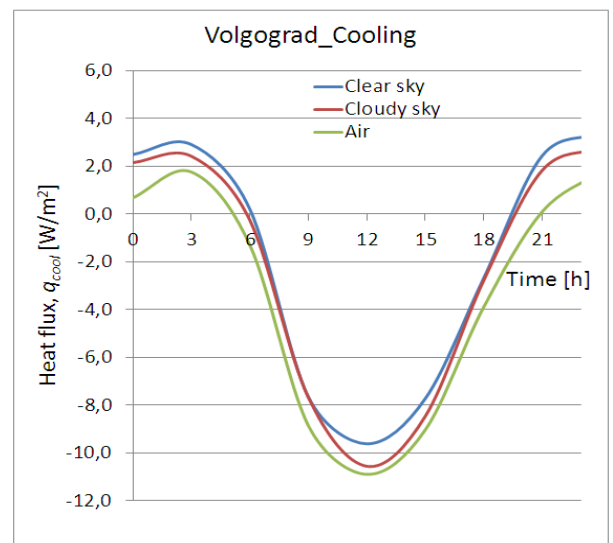
c



d



e



f

Figure 5. Heat flux variations for heating (q_{heat}) and cooling (q_{cool}), using different sky temperature models. St. Petersburg (a, b); Moscow (c, d); Volgograd (e, f).

Starting from this, heating and cooling energy needs were simulated (for coldest and hottest days), and the obtained results are shown in Fig. 5. In this stage, three models were tested (clear sky, cloudy sky and ambient air).

Analyzing the data it is worthy to notice that the heat flux fluctuations through the building component are different in winter and summer. Positive values of the heat flow correspond to heat losses, negative values are the heat gains. In January, the heat flux fluctuations are non-harmonic, which can be explained by the variable effect of the heat and cold waves on the structure. The maximum heat flux values occur during the morning and evening, minimum values – in daytime. In July, the heat flux fluctuations are harmonic, with maximum values at 0–3 a.m. and minimum values at 12 p.m. The heat flux is vary depending on the sky temperature. The highest heat flux value can be obtained applying the clear sky model, the lowest value in the case of ambient temperature.

Table 8 lists the percentage differences obtained comparing heating and cooling daily energy needs. The comparison takes into account the three mentioned humidity-climatic conditions and allows to observe what is reported below.

Table 8. Percentage differences (%) obtained by using different sky temperature models.

Sky temperature models	St. Petersburg		Moscow		Volgograd	
	Heating	Cooling	Heating	Cooling	Heating	Cooling
Clear sky	+10.97	no heat gain	+21.87	–61.01	+8.13	–45.16
Cloudy sky	+3.41	no heat gain	+5.76	–24.75	+4.34	–30.66
Ambient air	0.00	0.00	0.00	0.00	0.00	0.00

Wet conditions: in this case, only heating energy need has to be considered. The highest differences can be obtained by using clear sky model (+11 %). The cloudy sky model allows to obtain the differences energy need is +3.4 %.

Normal conditions: the climatic conditions in Moscow produce high heating energy needs. Use the different sky models allow to obtain percentage differences between +21.9 % and +5.8 %. Analyzing cooling energy demands, the percentage difference values are much higher than the other humidity-climatic conditions (–61 % to –24.8 %) but they refer to almost negligible demands for cooling.

Dry conditions: in this case both heating and cooling energy needs have to be simulated. Considering heating energy demands, the highest differences can be obtained by using clear sky model (+8.1 %). The lowest percentage differences can be achieved using the cloud sky model (+4.3 %). The employment of the cloud sky model represents inter-mediate situation, with percentage differences +4.3 %. Analyzing cooling energy demands, the highest differences can be obtained clear sky model (–45.2 %). If the cloud sky model is applied, the percentage difference equal to –30.7 %.

Thus, the temperature of the sky changes the building energy performance: in winter heat losses increase, in summer heat gains decrease. Taking into account the temperature of the sky in the heat transfer process through the building components makes it possible to more accurately calculate the heating and cooling needs of the buildings.

4. Conclusions

Previously, several sky temperature models and different their correlations have been defined by the researchers. Most of the current sky models are correlated to local climatic conditions and specific sites and they do not cover different humidity-climatic conditions. In this work, sky emissivity and sky temperature models were reviewed, taking into account the common classification that includes simplified and detailed correlations. The clear-sky and cloudy-sky temperature models were also investigated in detail, employing them for different humidity-climatic conditions (wet, normal and dry) and evaluating their influence on building energy needs. In winter, under clear-sky conditions the maximum difference between the ambient air temperature and sky temperature is 19 K regardless of humidity-climatic conditions. Under cloudy-sky conditions it is possible to notice dissimilarities, ranging from 5 K (wet and normal conditions) to 10 K (dry conditions). In summer, under clear-sky conditions, the maximum values are ranging from 12 K (normal conditions) to 13 K (wet and dry conditions). Under cloudy-sky conditions, the maximum values are ranging from 5 K (normal conditions) to 10 K (dry conditions). Thus, the obtained results can be applied for investigation the radiative heat flux between a building surface and the sky, as simplified model. Also these results can be used when the sky temperature is not available from climatic data. The obtained results specified the simplified models according to ISO 13790. Finally, taking into account the influence of different correlations in building energy simulations, it was found that heating and cooling energy demands (using the example of a translucent roof) can be affected by significant percentage differences (the rounded

values), ranging from +3 % to +11 % (no heat gain) for wet climatic conditions, from –61 % to +22 % for normal climatic conditions, and, finally, from –45 % to +8 % for dry climatic conditions. The comparison among the models can be useful to address the choice of users in building energy simulations and engineering applications [20, 22]. Future developments will regard the longwave sky radiation measurement under field conditions in the representative cities of the world in order to propose correlations for different climatic area.

References

1. Sparrow, E.M., Cess, R.D. Radiation heat transfer. 1978. 366. ISBN: 0-89116-923-7
2. Kreith, F., Black, W.Z. Basic heat transfer. 1980. 45 (6). DOI: 10.1201/9780203755570-15
3. Musta, L.G., Zhurov, G.N., Belyaev, V.V. Modeling of a solar radiation flow on an inclined arbitrarily oriented surface. *Journal of Physics: Conference Series*. 2019. 1333 (3). DOI: 10.1088/1742-6596/1333/3/032054
4. Zhang, Q, Joe, H., Lang, S. Development of typical year weather data for Chinese location. *ASHRAE Transactions*. 2002. 108 (2). LBNL-51436.
5. Walkenhorst, O., Luther, J., Reinhart, C., Timmer, J. Dynamic annual daylight simulations based on one-hour and one-minute means of irradiance data. *Solar Energy*. 2002. 72 (5). Pp. 385–395. DOI: 10.1016/S0038-092X(02)00019-1
6. Rommel, M. On the estimation of atmospheric radiation from surface meteorological data. 1996. 56 (4). Pp. 349–359.
7. Skartveit, A., Olseth, J.A., Czeplak G. On the estimation of atmospheric radiation from surface meteorological data. *Solar Energy*. 1996. 56 (4). Pp. 349–359.
8. Vall, S., Castell, A. Radiative cooling as low-grade energy source: A literature review. *Renewable and Sustainable Energy Reviews*. 2017. 77 (August 2016). Pp. 803–820. DOI: 10.1016/j.rser.2017.04.010
9. Parker, J. The Leeds urban heat island and its implications for energy use and thermal comfort. *Energy and Buildings*. 2021. 235(September 2013). DOI: 10.1016/j.enbuild.2020.110636
10. Evangelisti, L., Guattari, C., Gori, P., Bianchi, F. Heat transfer study of external convective and radiative coefficients for building applications. *Energy and Buildings*. 2017. 151. Pp. 429–438. DOI: 10.1016/j.enbuild.2017.07.004
11. Liao, W., Hong, T., Heo, Y. The effect of spatial heterogeneity in urban morphology on surface urban heat islands. *Energy and Buildings*. 2021. 244. DOI: 10.1016/j.enbuild.2021.111027
12. Korniyenko, S.V., Astafurova, T.N., Kozlova, O.P. Energy Efficient Major Overhaul in Residential Buildings of the First Mass Series. *IOP Conference Series: Materials Science and Engineering*. 2020. 753 (4). DOI: 10.1088/1757-899X/753/4/042039
13. Millers, R., Korjajins, A., Lešinskis, A., Borodinecs, A. Cooling panel with integrated PCM layer: A verified simulation study. *Energies*. 2020. 13 (21). DOI: 10.3390/en13215715
14. Kalamees, T., Lupišek, A., Sojková, K., Mørck, O.C., Borodinecs, A., Almeida, M., Rovers, R., Op'Tveld, P., Kuusk, K., Silva, S. What kind of heat loss requirements NZEB and deep renovation sets for building envelope? CESB 2016 – Central Europe Towards Sustainable Building 2016: Innovations for Sustainable Future. 2016. (October 2019). Pp. 137–144.
15. Baranova, D., Sovetnikov, D., Borodinecs, A. The extensive analysis of building energy performance across the Baltic Sea region. *Science and Technology for the Built Environment*. 2018. 24 (9). Pp. 982–993. DOI: 10.1080/23744731.2018.1465753.
16. Gaujena, B., Borodinecs, A., Zemitis, J., Prozuments, A. Influence of building envelope thermal mass on heating design temperature. *IOP Conference Series: Materials Science and Engineering*. 2015. 96 (1). DOI: 10.1088/1757-899X/96/1/012031
17. Borodinecs, A., Prozuments, A., Zajacs, A., Zemitis, J. Retrofitting of fire stations in cold climate regions. *Magazine of Civil Engineering*. 2019. 90 (6). Pp. 85–92. DOI: 10.18720/MCE.90.8
18. Borodinecs, A., Geikins, A., Prozuments, A. Energy consumption and retrofitting potential of Latvian unclassified building. 2020. DOI: 10.1007/978-981-32-9868-2_27.
19. Dimdina, I., Krumins, E., Lesinskis, A. Indoor Air Quality in Multi-Apartment Buildings before and after Renovation. *Construction Science*. 2015. 16 (1). Pp. 3–10. DOI: 10.1515/cons-2014-0006
20. Korniyenko, S. Complex analysis of energy efficiency in operated high-rise residential building: Case study. *E3S Web of Conferences*. 2018. 33. DOI: 10.1051/e3sconf/20183302005
21. Vatin, N., Korniyenko, S.V., Gorshkov, A.S., Pestryakov, I.I., Olshevskiy, V. Actual thermophysical characteristics of autoclaved aerated concrete. *Magazine of Civil Engineering*. 2020. 96 (4). Pp. 129–137. DOI: 10.18720/MCE.96.11
22. Korniyenko, S.V., Vatin, N.I., Gorshkov, A.S. Thermophysical field testing of residential buildings made of autoclaved aerated concrete blocks. *Magazine of Civil Engineering*. 2016. 64 (4). Pp. 10–25. DOI: 10.5862/MCE.64.2
23. Liepiņš, S., Lešinskis, A., Iljins, U. Low-emission heat insulation for roof constructions. *Research for Rural Development*. 2012. 2. Pp. 105–108.
24. Observations, U., Nocturnal, T.H.E. Smithsonian Miscellaneous Collections. *Nature*. 1924. 114 (2855). Pp. 85–85. DOI: 10.1038/114085a0
25. Li, M., Jiang, Y., Coimbra, C.F.M. On the determination of atmospheric longwave irradiance under all-sky conditions. *Solar Energy*. 2017. 144. Pp. 40–48. DOI: 10.1016/j.solener.2017.01.006
26. Chen, B., Maloney, J., Clark, D., Mei, W.N. Measurement of night sky emissivity in determining radiant cooling from cool storage roofs and roof ponds. *Proceedings of the National Passive Solar Conference*. 1995. 20 (1). Pp. 1–6.
27. Evangelisti, L., Guattari, C., Asdrubali, F. On the sky temperature models and their influence on buildings energy performance: A critical review. *Energy and Buildings*. 2019. 183. Pp. 607–625. DOI: 10.1016/j.enbuild.2018.11.037
28. Levinson, R., Akbari, H., Berdahl, P. Measuring solar reflectance-Part I: Defining a metric that accurately predicts solar heat gain. *Solar Energy*. 2010. 84 (9). Pp. 1717–1744. DOI: 10.1016/j.solener.2010.04.018
29. Andreas, E.L., Ackley, S.F. On the differences in ablation seasons of Arctic and Antarctic sea ice. 1982. 0469 (December). DOI: 10.1175/1520-0469(1982)039<0440
30. Flerchinger, G.N., Xaio, W., Marks, D., Sauer, T.J., Yu, Q. Comparison of algorithms for incoming atmospheric long-wave radiation. *Water Resources Research*. 2009. 45 (3). DOI: 10.1029/2008WR007394

31. Chen, J., Lu, L. Development of radiative cooling and its integration with buildings: A comprehensive review. *Solar Energy*. 2020. 212 (October). Pp. 125–151. DOI: 10.1016/j.solener.2020.10.013
32. Maghrabi, A., Clay, R. Nocturnal infrared clear sky temperatures correlated with screen temperatures and GPS-derived PWV in southern Australia. *Energy Conversion and Management*. 2011. 52 (8–9). Pp. 2925–2936. DOI: 10.1016/j.enconman.2011.02.027
33. Environments, U. *Healthy, Intelligent and Resilient Buildings and Urban Environments*. 7th International Buildings Physics Conference, IBPC2018. 2018. (September 2018). Pp. 6.
34. Incropera, F.P., DeWitt, D.P. *Fundamentals of Heat and Mass Transfer*. 1996. (December 2018). Pp. 890. DOI: 10.1016/j.ap-thermaleng.2011.03.022
35. Chen, D., Chen, H.W. Using the Köppen classification to quantify climate variation and change: An example for 1901-2010. *Environmental Development*. 2013. 6 (1). Pp. 69–79. DOI: 10.1016/j.envdev.2013.03.007
36. Porcaro, M., Ruiz de Adana, M., Comino, F., Peña, A., Martín-Consuegra, E., Vanwalleghem, T. Long term experimental analysis of thermal performance of extensive green roofs with different substrates in Mediterranean climate. *Energy and Buildings*. 2019. 197. Pp. 18–33. DOI: 10.1016/j.enbuild.2019.05.041

Information about author:

Sergey Korniyenko,

Doctor in Technical Science

ORCID: <https://orcid.org/0000-0002-5156-7352>

E-mail: svkorn2009@yandex.ru

Received 02.06.2021. Approved after reviewing 17.11.2021. Accepted 29.11.2021.



Research article

UDC 691.3

DOI: 10.34910/MCE.114.13



High-performance fine-grained nanostructured concrete based on low strength aggregates

A.S. Rassokhin¹ , A.N. Ponomarev² , A.I. Karlina³ 

¹ Peter the Great St. Petersburg Polytechnic University, St. Petersburg, Russia

² Peoples' Friendship University of Russia, Moscow, Russia

³ Moscow State University of Civil Engineering, Moscow, Russia

✉ rassokhinaleksandr@gmail.com

Keywords: high-performance concrete, compressive strength, fine-grained concrete, basalt fiber, silica fume

Abstract. This paper continues the authors' previous research on developing high-performance concretes based on low-strength aggregates. Unlike the previous work, where a low-strength crushed stone was used, the current research investigates a low-strength fine aggregate-based concrete. With modern construction chemistry in combination with pozzolan and high dispersed ground additives and nanomodification, it is possible to obtain high strength and operational characteristics concretes. The work carried out studies of three cement manufacturers for suitability in high-strength hydrotechnical concrete and phase analysis of the aggregates used in this study. Strength (7, 28, 180 days), density, waterproofness, freeze-thaw resistance of fine-grained concrete based on low-strength and high-strength aggregates were compared in the research. The final result is a concrete recipe with freeze-thaw resistance class F400, Waterproofing class W20 and compressive strength of 60.5 MPa at the age of 28 days (71.9 MPa at 180 days).

Citation: Rassokhin, A.S., Ponomarev, A.N., Karlina, A.I. High-performance fine-grained nanostructured concrete based on low strength aggregates. Magazine of Civil Engineering. 2022.

1. Introduction

This paper is a path forward from the author's previous work on this topic [1], devoted to developing heavy hydrotechnical structural concrete based on low-strength aggregate. In this work, a matrix was developed to obtain high-strength hydrotechnical concrete based on low-strength aggregate. Concretes with a strength of about 100 MPa has been developed using a crushed stone fraction of 10–20 mm and about 80 MPa when using a crushed stone fraction of 3–10 mm. The freeze-thaw resistance of these concretes was F400 and the waterproofing class was W20. Using the proposed matrix, it became possible to achieve high strength and operational characteristics of concrete based on low-strength aggregate from gneissic granite.

The developed matrix is of huge interest for use in concrete and other low-strength aggregates, which can be crushed construction waste [2], as well as industrial waste, such as slag [3–5]. Therefore, it was decided to develop formulations of high-performance concrete based on this matrix but using fine aggregate.

The study on the suitability of using a matrix with small aggregate opens up even greater possibilities for reuse, for example, construction waste when recycling old buildings [6, 7]. Moreover, fine-grained concrete has advantages over coarse-grained concrete, [8, 9], especially in conditions of lower

temperatures, since it has higher freeze-thaw resistance [10]. However, fine-grained concrete has extensive air entrainment [11] and, accordingly, a lower density, leading to a decrease in strength. For this reason, more cement is used to obtain a similar mechanical strength and performance in fine-grained concrete than coarse aggregate-based concrete. However, to get high strength fine-grained concrete, it is impossible to infinitely increase the cement content.

Moreover, the maximum amount of cement in concrete is regulated by regulatory documents and recommendations. In addition, 21st-century construction science allows using less cement to produce high-strength concretes. Modern high-efficiency plasticisers significantly reduce the water-cement ratio while maintaining the same flowability of the concrete mixture, which leads to a significant increase in strength and performance. Also, strength and performance characteristics can be improved by using industrial waste such as silica fume [12, 13] and shale ash. They have pozzolan activity and can be used as additional binders for civil concretes and even unique, heat-resistant concretes and alternative binders for composite binders [14, 15]. Silica fume and shale ash combined with water reduction minimize the permeability of concrete, leading to an increase in frost resistance and chemical resistance of concrete. They are also waste from industries, so their using in concrete helps to remove the environmental load from the region since these materials can be disposed of in concrete. In addition, the use of complex additives consisting of pozzolan and finely ground additives, concrete chemistry in combination with fibers allows you to obtain high-performance concretes with increased operational characteristics. This issue has been investigated in these publications [16–19].

Based on the above, the following research tasks can be distinguished:

- study of the characteristics of gneissic granite crushed stone extracted from the Kem river bed, as well as an alternative crushed stone;
- investigation of the properties of cement available in the northern regions of Russia in large volumes that are suitable for hydrotechnical construction;
- development of concrete recipes of high-performance fine-grained hydrotechnical nanostructured concrete based on scientific literary data, as well as author's research;
- production of high-performance fine-grained concrete using cement amount not exceeding 550 kg/m³;
- preparation of the concrete samples for determination of principal characteristics, including mechanical parameters, water absorption, waterproofing, freeze-thaw resistance;
- testing of principal characteristics of concrete, defining quality of high-performance fine-grained nanostructured concrete: mechanical characteristics, water absorption, waterproofing, freeze-thaw resistance.

2. Methods

2.1. Concrete aggregates

Fine inert aggregate from the boulders of gneissic granite has been used for the development of empirical research. Boulders have been mined in the Kem river bed (Karelia, northern Russia) and have been crushed down in several steps on a laboratory jar mill 80JM-1a.

At the first stage, the boulders were crushed into small fragments, into fractions of 150–200 mm, and further on, into fractions of crushed stone of 3–10, of 10–20 mm. Fractions were obtained by sieving on laboratory sieves. Gneissic granite sand of a fraction of 0–2.5 mm was pulverized from the fraction of 0–3 mm.

For comparison, gabbro-diabase sand of Goloday-gora Ltd. mine was also investigated. Also, concrete was made on the basis of this sand for comparison with gneissic granite sand-based concrete. Crushability was determined by the fraction of sand of 5–10 mm, which was taken during crushing large stones into sand. This is since regulatory documents do not provide for the determination of crushability by smaller fractions.

2.2. Determination of gneissic granite sand characteristics

The crushability (ΔC) of gneissic granite sand was determined by the grain destructiveness during compression (crushing) in the cylinder. A steel cylinder with a diameter and height of 75 mm according to Russian State Standard GOST 8269.0-97 was used for the purpose. Sand samples are filled into the cylinder, and 50 kN load was made using the hydraulic laboratory testing machine WK-18 ZARZAD SPRZETU (Poland). The loading speed was 1 kN/s. Laboratory scales VTB-12 were used to determine the mass.

$$\Delta C = \frac{m - m_1}{m} 100, \quad (1)$$

where m is the mass of crushed stone test sample, g; m_1 is the mass of residue on the control sieve after sieving of crushed stone sample crushed in the cylinder, g.

Radiographic studies were conducted for the determination of the mineral composition of the crushed stone. Radiographic studies were conducted by using the automatic powder diffractometer D2Phaser (Bruker) (radiation of an x-ray tube is CoK α 1+2, wavelengths CoK α 1 = 1.78900 Å и CoK α 2 = 1.79283 Å, tube operating mode 30 kW/10 mA, position-sensitive detector, geometry on reflection, scheme of focusing Bregg-Brentano, speed of rotation of a sample of 20 revolutions per minute, the interval of angles of diffraction 2theta = 5–80°, scanning step 0.02°, exposition in a point is 1.0 seconds, T = 25 °C, the atmosphere is air).

The sample was made by dry pressing of the studied substance in low-background to a ditch of single-crystal silicon (depth is 0.5 mm, the diameter of the studied area is 20 mm). The identification of the phases was contacted by using the base of powder diffraction data of the Powder Diffraction File. The results of the quantitative X-ray phase analysis are given in Table 3.

Grain size distribution, the content of dust and clay particles, specific gravity, packed density were determined according to the method described in Russian State Standard GOST 8735-88.

2.3. Preparation of concrete samples and determination of their characteristics

Laboratory mixing of concrete according to Russian State Standard GOST 10180-2012 was carried out according to the following recipes:

Table 1. Concrete recipe №2

Components	recipe №1	recipe №2
	kg per m ³	
Portland Cement CEM I 42.5 N manufactured by JSC Mordovcement	550	550
Gneissic granite sand (fraction of 0 – 2.5)	1442	–
Gabbro-diabase sand (fraction of 0 – 2.5)	–	1442
Dry mix of:		101
1. Silica fume manufactured by pilot production of the INRTU		
2. Shale ash Zolest-bet manufactured by PCV LLC		
3. Modified basalt microfiber manufactured by NTC of Applied Nanotechnologies	101	
4. Plasticizing agent REOMAX PC 3901P manufactured by KUBAN-POLYMER LLC		
5. Carbon nanoparticles Astralene manufactured by NTC of Applied Nanotechnologies		
6. Defoaming agent Geos P150 manufactured by KUBAN-POLYMER LLC		
Water of mixing according to Russian national standard GOST 23732-2011	210	210

The concrete was mixed as follows. Initially, water and cement were first mixed in the concrete gravity batch mixer Eco CM-71 for one minute. After that, the dry mix of admixes was introduced and mixing lasted another minute. The final mixing also lasted for one minute. Finally, sand was introduced last into the concrete mixture.

Nanomodifiers (Astralene) were introduced into concrete by serial dilution method [20]. Astralene were deposited on the basalt microfiber (TC 5761-014-13800624-2004), and microfiber was introduced into the concrete as a component of dry mix. This resulted in a more uniform distribution of nanomaterials throughout the concrete volume.

The volume of concrete mixing was 40 litres.

Concrete density was determined according to Russian national standard GOST 10181-2014.

Concrete cubes with dimensions of 100x100x100 mm in the quantity of 30 pieces were made according to Russian national standard GOST 10180-2012.

The concrete samples were prepared in moulds and removed from the moulds after 1-day curing at room temperature. All the samples (and the control samples) have been hardened in thermo-humidity conditions for 28 days according to Russian national standard GOST 10180-2012.

The compressive strength test of concrete cubes with dimensions of 100x100x100 mm was carried out on the hydraulic laboratory testing machine MP-1000 «Nutcracker» according to Russian national standard GOST 10180-2012.

The freeze-thaw resistance was determined on the climatic chamber SM 55/50-120 SB according to Russian national standard GOST 10060-2012. The freeze-thaw resistance was determined in a water-saturated state (F_1). The dispersion of the density values of individual samples in the series before their saturation did not exceed 30 kg/m³.

Waterproofing of concrete control samples by air permeability was determined by the device AGAMA-2 according to Russian national standard GOST 12730.5-2018.

3. Results and discussion

3.1. Cement analysis

The paper carried out a comparative analysis of two regional suppliers of Portland cement (Pikalevsky Cement JSC and Petersburg Cement LLC). These are some of the northernmost cement producers with large production volumes MordovCement PJSC. The results of this comparison give all reasons for the choice in favour of non-additive Portland cement 42.5, produced according to GOST 10178-85, GOST 30515 - 2013 MordovCement PJSC, as the best object for modelling concrete mixtures for the development of high-performance concrete formulations.

Table 2. Comparative table of characteristics of three types of cement of different manufacturers in the Russian Federation

Composition	Safe amount, %	Pikalevsky Cement JSC	Petersburg Cement LLC	Mordov Cement PJSC
Cl ⁻ content	0.1	0,009	0,016	0,008
SO ₃	3.5	2.9	3.41	3
C ₃ S	–	64.4	61,07	63,3
C ₃ A	–	5,3	8,03	6,6
C ₂ S	–	15,6	12,58	13,6
C ₄ AF	–	10,8	10,6	13,5
MgO	5	1.24	2,52	1,23
Free alkalis as per Na ₂ O	0,8	1,16	1,12	0,78

The cement of MordovCement PJSC has the best values for the minimum concentration of chlorine ions (0.008 %), which is essential for the operating conditions of reinforced structures [21, 22]. But most importantly, at present only MordovCement PJSC produces Portland cement with a level of free alkalis in 0.78 %, which meets the requirements of the existing regulatory and technical documentation (Russian national standard GOST R 55224-2012), while in the regulatory document "Bridges and Pipes" 46.13330-2010-2010 this level was adopted even tougher – no more than 0.6 %. The amount of free alkalis in terms of Na₂O determines the degree of alkaline corrosion of concrete, especially if the aggregate contains compounds capable of reacting with free alkalis of cement to form products that change their volume and density [23–25]. As a result, cracks are formed and start to develop in concrete, up to the destruction of structures (especially with temperature differences towards lower temperatures) [22]. Thus, it can be argued that free alkalis in the cement composition and the presence/absence of reactive acidic components in the filler significantly determine the frost resistance and durability of concrete and concrete structures.

Unfortunately, in the northern regions of Russia, there is a problem with access to cement, which in quality would be suitable for use in special hydrotechnical concrete without complaints. The delivery of cement from other regions leads to an increase in the cost of construction and the need for more detailed incoming control of each batch of cement, since with long transportation, the probability of violation of cement storage conditions during operation increases.

3.2. Concrete fine aggregates

The Table 3 shows the quantitative phase analysis of the components that make up the gneissic granite crushed stone. The purpose of this analysis was to search for harmful components that make up the crushed stone.

Table 3. Quantitative phase analysis of gneissic granite sample (weight. %) according to the full-height analysis by Rietveld method

Minerals	Chemical formula	% of masses	
		10 – 20 mm	0 – 5 mm
Quartz	SiO ₂	41.2	29.4
Microcline	K(AlSi ₃ O ₈)	17.6	17.9
Albite	Na(AlSi ₃ O ₈)	24.3	25.1
Biotite	K(Mg,Fe) ₃ [AlSi ₃ O ₁₀](OH,F)	5.3	5.2
Amphibole	(Na,Ca) ₂ (Mg,Fe ³⁺ ,Fe ²⁺ ,Al,Ti) ₅ Si ₈ O ₂₂ (OH,F) ₂	4.1	4.5
Magnetite	Fe ²⁺ Fe ³⁺ ₂ O ₄	2.0	2.3
Chlorite	(Mg,Fe) ₆ Si ₄ O ₁₀ (OH) ₈	3.9	4.2
Talc	Mg ₃ Si ₄ O ₁₀ (OH) ₂	1.2	1.4
Calcite	CaCO ₃	trace levels	trace levels
Zirconium silicate	ZrSiO ₄	trace levels	trace levels

One of the first concerns was the fear that all the least stable waste in the production of other fractions fell into the 0–2.5 mm fraction. Because of this, a completely different chemical composition would arise compared to other fractions, which would lead to a significant deterioration in the properties of the 0–5 mm fraction and the impossibility of its use in concrete. However, after the phase analysis (Table 3), it was found that the fears were not justified. The mineral composition of the sand of a fraction of 0–2.5 mm had only slight differences from the composition of the starting material.

From these experiments it was concluded that the majority of the minerals, which are a part of crushed stone, received from sedimentary rocks of a bed of the Kem river (88.8 % of masses) is not specified on the "blacklist" of harmful components and impurity under the table A of the Russian national state standard GOST 8267-93 „Crushed stone and gravel of solid rocks for construction works. Specifications”. Chlorite (4.2 % of masses), magnetite (2.3 % of masses) and biotite (rock-forming mica, 5.2 %) make the exception.

However, according to Table A of the Russian national standard GOST 8267-93 is allowed when the total amount of layered silicates (micas, hydromicas, chlorites) will not exceed 15 % of the mass. In this case this condition is met.

Based on Table 3, it can be concluded that there are no mineralogical and physicochemical restrictions for the use of gneissic granite crushed stone in concrete. This allows to study the mechanical characteristics of gneissic granite crushed stone, as well as the characteristics of concrete based on gneissic granite crushed stone and their compliance with actual Russian national construction standards GOST 8267-93 and GOST 26633-2015.

Table 4. Determined properties of gneissic granite sand

Parameter	Freeze-thaw resistance	Crushability	Specific gravity	Packed density	Water absorption
Value	300 cycles	28–35 %	2606 g/sm ³	1.45 g.sm ³	2.2 %

The value of crushability corresponds to the grade of 200 according to Russian national standard GOST 8267-93, the lowest rate declared in Russian national standard GOST.

Table 5. Main properties of gabbro-dabase sand declared by the manufacturer

Parameter	Freeze-thaw resistance	Crushability	Specific gravity	Packed density	Water absorption
Value	300 cycles	3.6 %	2986 g/sm ³	1.62 g/sm ³	0.1 %

The value of crushability corresponds to the grade of 1400 according to Russian national standard GOST 8267-93, the lowest rate declared in Russian national standard GOST.

Table 6. Main properties of concretes

Properties	Recipe №1	Recipe №2
Compressive strength (7 days), MPa	48.4	52.1
Compressive strength (28 days), MPa	60.5	68.3
Compressive strength (180 days), MPa	71.9	80.8
Fresh concrete density, kg/m ³	2303	2327
Concrete density (28 days), kg/m ³	2255	2261
Concrete density (180 days), kg/m ³	2239	2248
Freeze-thaw resistance, cycles	400	400
Water absorption, %	3.9	3.6
Waterproofing, Class	W20	W20
Flowability, Class	F4	F4

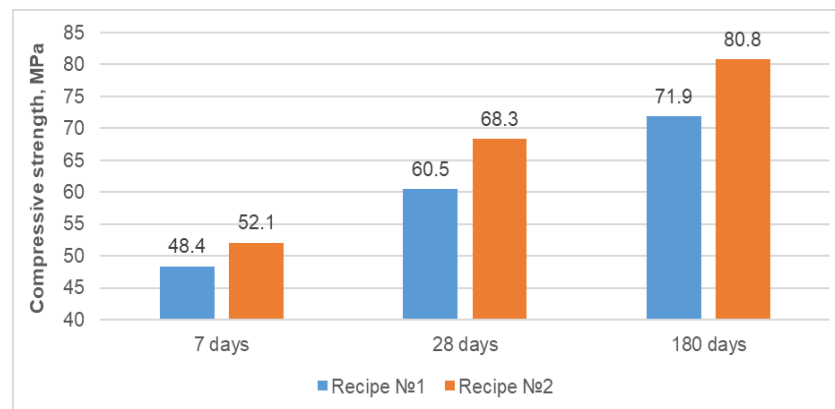
**Figure 1. Compressive strength of concrete, MPa.**

Table 6 and Fig. 1 show that the compressive strength of concrete with gneissic granite sand of fraction of 0–2.5 mm differs from the compressive strength with gabbro-diabase sand of fraction of 0–2.5 mm only by 12.9 % at the age of 28 days and 12.4 % at the age of 180 days. This is a rather nonsignificant difference considering the strength (crushability) of the sand. The grade of gneissic granite in strength (crushability) was only 200 according to Russian national standard GOST 8269.0-97. On the other hand, the grade of gabbro-diabase was 1400, which is the maximum strength (crushability) grade of crushed stone according to GOST 8269.0-97. By comparing absolute values, compressive strength of concrete with gneissic granite sand of fraction of 0–2.5 mm differs from the strength of concrete with gabbro-diabase sand of fraction 0–2.5 mm by 7.8 MPa at the age of 28 days, and 8.9 MPa at the age of 180 days.

Compressive strength values at the age of 7 days were determined as additional to characterize the concrete hardening process. At the age of 7 days, concrete with gneissic granite sand of fraction of 0–2.5 mm had 80 % of compressive strength compared to concrete compressive strength at the age of 28 days, on the concrete of gabbro-diabase sand of fraction of 0–2.5 mm had 76 % of compressive strength compared to concrete compressive strength at the age of 28 days.

However, following the regulatory documents for hydrotechnical concrete, it is possible to determine the grade strength at 180 days. Due to the operation of hydrotechnical concrete in a water-saturated state, the strength gain does not stop at the age of 28 days but continues to gain strength further.

The difference in compressive strength in 28 and 180 days corresponds to regulatory documents, which provide for increasing factors for analysing the strength gain of concrete after 28 days of maturing. This is also supported by numerous experimental data from other researchers [26–28].

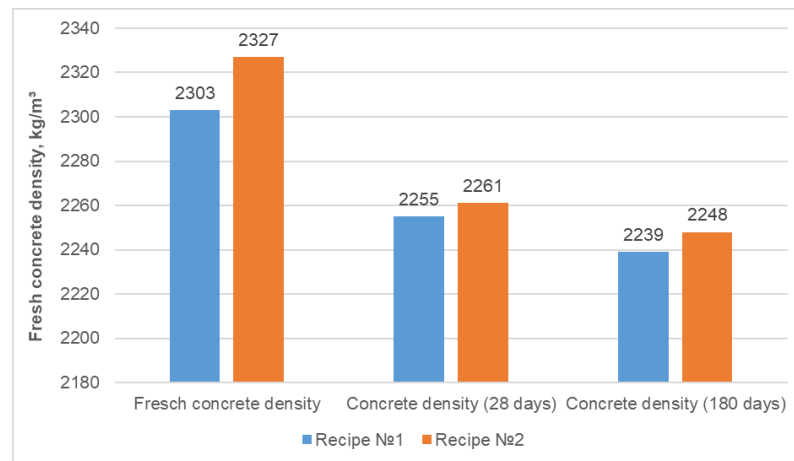


Figure 2. Fresh concrete density, kg/m³.

Table 6 and Fig. 2 show that the concrete density of all recipes is practically equal at the same age. The concrete density value is quite typical for sand concrete with coarse aggregate. This demonstrates that the structure of concrete is not disturbed when replacing one sand with another.

The high water absorption values of gneissic granite compared to gabbro diabase raised the author's concerns. This could affect the concrete mixture's flowability, rheology, and adhesion between the aggregate and the binder. However, as with coarse aggregate gneissic granite concrete [1], this does not significantly affect the flowability and rheology of the concrete. Furthermore, the introduction of toroidal nanoparticles (Astralene) led to a better penetration of suspension from water and binding materials deep into the crushed stone and directed the crystallization of cement stone. This mechanism lies in the fact that due to the shape of the torus, the Astralenes have. This allows the formation of volumetric structures several micrometers long in concrete, which is actually self-reinforcement of concrete. The mechanism is described in more details in the previous paper of the authors [29].

This moment also has a substantial positive effect. Gneissic granite crushed stone has relatively large pores, which leads to saturation with a suspension of water and binder materials. It also strengthens the crushed stone itself and stronger adhesion between the crushed stone and the binder.

The obtained freeze-thaw resistance value F400 according to Russian national standard GOST 10060-2012 is a very high class of freeze-thaw resistance even for concrete with high-quality aggregates. On the other hand, the freeze-thaw resistance class of concrete the most frequently used in civil engineering is class F50-150.

Concrete with freeze-thaw resistance class F400 belongs to the group of high freeze-thaw resistance. Concretes with this class of frost resistance belong to the group of special concretes. They are intended for use in exceptional cases. For example, such concretes are used when there is a variable level of water contacting the concrete structure in addition to low temperatures.

The high waterproofing class (maximum according to GOST 12730.5-2018) indicates that this concrete does not need additional water isolation. And even more, the concrete itself becomes a water isolation material. This is a significant factor, as it simplifies water isolation tasks during construction when temporary and financial resources are spent on additional water isolation.

A high class of freeze-thaw resistance, in sum with a high level of waterproofing, makes this one also more durable. When concrete is used in the north of Russia, the durability of concrete directly depends on its freeze-thaw resistance and waterproofing.

The pozzolan and finely ground additives used in this study have proven to be highly effective in improving the mechanical and operational characteristics of concrete. Their use as additional binders undoubtedly has a positive effect on the structure of concrete, as well as on its permeability and frost resistance. The effect of silica fume on concrete permeability has been considered in these papers [5, 30, 31]. Moreover, the used basalt microfiber has a complex positive effect on concrete properties, particularly on concrete's freeze-thaw and permeability.

These materials are also actively used by other researchers to obtain concretes with unique characteristics [32–34], as well as to reduce the amount of cement in the composition of concrete [35].

It should be noted that this study has initially been aimed at demonstrating the real possibility for developing high-strength concretes using low-quality aggregate. However, the matrix used provides extensive further concrete development opportunities for practical applications using solid industrial and construction waste, which meets the global challenges facing building in the 21st century [36]. Moreover,

for the production of civil and even special-purpose concretes of low classes, it is possible to significantly decrease the amount of cement (up to 150–200 kg/m³) using analogues of the developed matrix.

It also stands to mention that this paper was not aimed at studying the effect of nanomodifiers on the properties of concrete. The influence of nanomodifiers has already been studied in previous works by the authors of this paper and other researchers. Nanomodifiers were used as additives to concrete, such as silica fume, shale ash etc., the effectiveness of which has already been proven in concrete.

4. Conclusions

1. The properties of three types of cement available in large quantities in the northern regions of Russia were investigated. The most suitable for use in special concretes, in particular hydrotechnical, is the cement produced by MordrovCement PJSC since it has the least amount of free alkalis in terms of Na₂O (0.78 %). And he also has the best indicators for the minimum concentration of chlorine ions (0.008 %), which is important for the operating conditions of reinforced structures [23, 37, 38].
2. The suitability of the proposed combination of pozzolan and fine-ground additives with modern construction chemistry for producing high-performance fine-grained concrete based on low-strength aggregates was tested.
3. High-strength fine-grained hydrotechnical concretes with a strength of 60.5 MPa at the age of 28 days on the basis of gneissic granite crushed sand were developed. Concrete strength increased up to 71.9 MPa after 180 days of maturation.
4. Obtained values of compressive strength of concrete based on low-quality gneissic granite crushed sand differed not too significantly from compressive strength of concrete made according to the same recipe using high-strength gabbro-dabase crushed sand of the same fraction. Compressive strength value was 68.3 MPa (28 days) and 80.8 MPa (180 days) for gneissic granite and gabbro-dabase crushed stone, respectively.
5. This nonsignificant difference in compressive strength of concrete compared to the huge difference in strength (crushability) of the crushed stone is due to the fact that in the case of using a low-strength aggregate, the main load was taken by the concrete matrix, not the aggregate. Due to the high value of water absorption of the crushed stone, crushed stone was saturated with a suspension of water and binder materials, which led to the strengthening of the crushed stone, as well as stronger adhesion to the concrete matrix, which made it possible to distribute the load more evenly.
6. The developed matrix makes it possible to produce high-strength concrete in hard-to-reach and remote regions with difficult access to high-strength concrete aggregates. It also makes it possible to obtain high-strength concretes when using aggregates from industrial and construction waste, which meets the global challenges facing construction in the 21st century [36].
7. The grade F400 of freeze-thaw resistance concrete is a severe achievement since a low-strength aggregate of gneissic granite was used. Moreover, the frost resistance of crushed stone was only 200 cycles. Frost resistance is a crucial characteristic of concrete for the construction of buildings and structures in the northern regions, as this determines the durability and reliability of the design.
8. The combination of high compressive strength, low water absorption value, high water waterproofing class and high freeze-thaw resistance makes the developed concrete unique since a low-strength aggregate was used.

References

1. Rassokhin, A.S., Ponomarev, A.N., Karlina, A. Nanostructured high-performance concretes based on low-strength aggregates. Magazine of Civil Engineering. 2022. (02).
2. Kirchmann, H., Börjesson, G., Kätterer, T., Cohen, Y. From agricultural use of sewage sludge to nutrient extraction: A soil science outlook. *Ambio*. 2017. 46 (2). Pp. 143–154. DOI: 10.1007/s13280-016-0816-3
3. Thomas, M.D.A., Bamforth, P.B. Modelling chloride diffusion in concrete effect of fly ash and slag. *Cement and Concrete Research*. 1999. 29 (4). Pp. 487–495. DOI: 10.1016/S0008-8846(98)00192-6
4. Miithun, B.M., Narasimhan, M.C. Performance of alkali activated slag concrete mixes incorporating copper slag as fine aggregate. *Journal of Cleaner Production*. 2016. 112. Pp. 837–844. DOI: 10.1016/j.jclepro.2015.06.026. URL: <http://dx.doi.org/10.1016/j.jclepro.2015.06.026>
5. Fang, G., Ho, W.K., Tu, W., Zhang, M. Workability and mechanical properties of alkali-activated fly ash-slag concrete cured at ambient temperature. *Construction and Building Materials*. 2018. 172. Pp. 476–487. DOI: 10.1016/j.conbuildmat.2018.04.008. URL: <https://doi.org/10.1016/j.conbuildmat.2018.04.008>
6. Batayneh, M., Marie, I., Asi, I. Use of selected waste materials in concrete mixes. *Waste Management*. 2007. 27 (12). Pp. 1870–1876. DOI: 10.1016/j.wasman.2006.07.026

7. Power, A. Does demolition or refurbishment of old and inefficient homes help to increase our environmental, social and economic viability? *Energy Policy*. 2008. 36 (12). Pp. 4487–4501. DOI: 10.1016/j.enpol.2008.09.022
8. Sokolov, B.S., Radaikin, O.V. Features of the fine-grained concrete physical and mechanical properties and obtaining a “ τ - γ ” Deformation curve for it based on the author’s theory. *IOP Conference Series: Materials Science and Engineering*. 2020. 913 (3). DOI: 10.1088/1757-899X/913/3/032040
9. Begich, Y.E., Klyuev, S.V., Jos, V.A., Cherkashin, A.V. Fine-grained concrete with various types of fibers. *Magazine of Civil Engineering*. 2020. 97 (5). DOI: 10.18720/MCE.97.2
10. Bogas, J.A., De Brito, J., Ramos, D. Freeze-thaw resistance of concrete produced with fine recycled concrete aggregates. *Journal of Cleaner Production*. 2016. 115. Pp. 294–306. DOI: 10.1016/j.jclepro.2015.12.065. URL: <http://dx.doi.org/10.1016/j.jclepro.2015.12.065>
11. Bazhenov, Y., Bulgakov, B., Alexandrova, O. Modified fine-grained concrete for facing and repair of the hydraulic structures. *MATEC Web of Conferences*. 2016. 86. DOI: 10.1051/mateconf/20168603009
12. Rassokhin, A.S., Ponomarev, A.N., Figovsky, O.L. Silica fumes of different types for high-performance fine-grained concrete. *Magazine of Civil Engineering*. 2018. 78 (2). Pp. 151–160. DOI: 10.18720/MCE.78.12
13. Galishnikova, V.V., Abdo, S., Fawzy, A.M. Influence of silica fume on the pervious concrete with different levels of recycled aggregates. *Magazine of Civil Engineering*. 2020. 93 (1). Pp. 71–82. DOI: 10.18720/MCE.93.7
14. Ponomarev, A., Steshenko, D., Rassokhin, A. Development of technology for production of fire-resistant nanocomposite constructional rebar and structural elements based on it. *MATEC Web of Conferences*. 2018. 245. Pp. 1–6. DOI: 10.1051/mateconf/201824504001
15. Slavcheva, G.S., Artamonova, O.V., Shvedova, M.A., Khan, M.A. Clinkerless slag-silica binder: hydration process and hardening kinetics (part 2). *Magazine of Civil Engineering*. 2020. 97 (5). DOI: 10.18720/MCE.97.12
16. Nizina, T.A., Balykov, A.S., Volodin, V.V., Korovkin, D.I. Fiber fine-grained concretes with polyfunctional modifying additives. *Magazine of Civil Engineering*. 2017. 72 (4). Pp. 73–83. DOI: 10.18720/MCE.72.9
17. Nizina, T.A., Ponomarev, A.N., Balykov, A.S., Pankin, N.A. Fine-grained fibre concretes modified by complexed nanoadditives. *International Journal of Nanotechnology*. 2017. 14 (7–8). Pp. 665–679. DOI: 10.1504/IJNT.2017.083441
18. Murali, G., Fediuk, R. A Taguchi approach for study on impact response of ultra-high-performance polypropylene fibrous cementitious composite. *Journal of Building Engineering*. 2020. 30 (January). Pp. 101301. DOI: 10.1016/j.job.2020.101301. URL: <https://doi.org/10.1016/j.job.2020.101301>
19. Chernysheva, N., Lesovik, V., Fediuk, R., Vatin, N. Improvement of performances of the gypsum-cement fiber reinforced composite (GCFRC). *Materials*. 2020. 13 (17). DOI: 10.3390/ma13173847
20. Ben-David, A., Davidson, C.E. Estimation method for serial dilution experiments. *Journal of Microbiological Methods*. 2014. DOI: 10.1016/j.mimet.2014.08.023
21. Šavija, B., Pacheco, J., Schlangen, E. Lattice modeling of chloride diffusion in sound and cracked concrete. *Cement and Concrete Composites*. 2013. 42. Pp. 30–40. DOI: 10.1016/j.cemconcomp.2013.05.003
22. Valcarce, M.B., Vázquez, M. Carbon steel passivity examined in solutions with a low degree of carbonation: The effect of chloride and nitrite ions. *Materials Chemistry and Physics*. 2009. 115 (1). Pp. 313–321. DOI: 10.1016/j.matchemphys.2008.12.007
23. Glass, G.K., Buenfeld, N.R. The presentation of the chloride threshold level for corrosion of steel in concrete. *Corrosion Science*. 1997. 39 (5). Pp. 1001–1013. DOI: 10.1016/S0010-938X(97)00009-7
24. Cai, Y., Zhang, W., Yu, L., Chen, M., Yang, C., François, R., Yang, K. Characteristics of the steel-concrete interface and their effect on the corrosion of steel bars in concrete. *Construction and Building Materials*. 2020. 253. Pp. 2021. DOI: 10.1016/j.conbuildmat.2020.119162
25. Liang, C., Ma, H., Pan, Y., Ma, Z., Duan, Z., He, Z. Chloride permeability and the caused steel corrosion in the concrete with carbonated recycled aggregate. *Construction and Building Materials*. 2019. 218. Pp. 506–518. DOI: 10.1016/j.conbuildmat.2019.05.136
26. Menéndez, G., Bonavetti, V., Irassar, E.F. Strength development of ternary blended cement with limestone filler and blast-furnace slag. *Cement and Concrete Composites*. 2003. DOI: 10.1016/S0958-9465(01)00056-7
27. Uthaman, S., Vishwakarma, V., George, R.P., Ramachandran, D., Kumari, K., Preetha, R., Premila, M., Rajaraman, R., Mudali, U.K. Enhancement of strength and durability of fly ash concrete in seawater environments: Synergistic effect of nanoparticles. *Construction and Building Materials*. 2018. DOI: 10.1016/j.conbuildmat.2018.07.214
28. Singh, M., Srivastava, A., Bhunia, D. Long term strength and durability parameters of hardened concrete on partially replacing cement by dried waste marble powder slurry. *Construction and Building Materials*. 2019. DOI: 10.1016/j.conbuildmat.2018.12.005
29. Ponomarev, A., Knezević, M., Vatin, N., Kiski, S., Ageev, I. Nanosize scale additives mix influence on the properties of the high performance concretes. *Journal of Applied Engineering Science*. 2014. DOI: 10.5937/jaes12-6161
30. Sabet, F.A., Libre, N.A., Shekarchi, M. Mechanical and durability properties of self consolidating high performance concrete incorporating natural zeolite, silica fume and fly ash. *Construction and Building Materials*. 2013. 44. Pp. 175–184. DOI: 10.1016/j.conbuildmat.2013.02.069
31. Ramezani-pour, A.A., Malhotra, V.M. Effect of curing on the compressive strength, resistance to chloride-ion penetration and porosity of concretes incorporating slag, fly ash or silica fume. *Cement and Concrete Composites*. 1995. 17 (2). Pp. 125–133. DOI: 10.1016/0958-9465(95)00005-W
32. Shi, C., Wu, Z., Xiao, J., Wang, D., Huang, Z., Fang, Z. A review on ultra high performance concrete: Part I. Raw materials and mixture design. *Construction and Building Materials*. 2015. 101. Pp. 741–751. DOI: 10.1016/j.conbuildmat.2015.10.088
33. Poon, C.S., Kou, S.C., Lam, L. Compressive strength, chloride diffusivity and pore structure of high performance metakaolin and silica fume concrete. *Construction and Building Materials*. 2006. 20 (10). Pp. 858–865. DOI: 10.1016/j.conbuildmat.2005.07.001
34. Qing, Y., Zenan, Z., Deyu, K., Rongshen, C. Influence of nano-SiO₂ addition on properties of hardened cement paste as compared with silica fume. *Construction and Building Materials*. 2007. 21 (3). Pp. 539–545. DOI: 10.1016/j.conbuildmat.2005.09.001

35. Imbabi, M.S., Carrigan, C., McKenna, S. Trends and developments in green cement and concrete technology. *International Journal of Sustainable Built Environment*. 2012. 1 (2). Pp. 194–216. DOI: 10.1016/j.ijsbe.2013.05.001
36. Raut, S.P., Ralegaonkar, R.V., Mandavgane, S.A. Development of sustainable construction material using industrial and agricultural solid waste: A review of waste-create bricks. *Construction and Building Materials*. 2011. DOI: 10.1016/j.conbuildmat.2011.04.038
37. Win, P.P., Watanabe, M., Machida, A. Penetration profile of chloride ion in cracked reinforced concrete. *Cement and Concrete Research*. 2004. 34 (7). Pp. 1073–1079. DOI: 10.1016/j.cemconres.2003.11.020
38. Martín-Pérez, B., Zibara, H., Hooton, R.D., Thomas, M.D.A. Study of the effect of chloride binding on service life predictions. *Cement and Concrete Research*. 2000. 30 (8). Pp. 1215–1223. DOI: 10.1016/S0008-8846(00)00339-2

Information about authors:

Aleksandr Rassokhin,

ORCID: <https://orcid.org/0000-0001-7416-927X>

E-mail: rassokhinaleksandr@gmail.com

Andrey Ponomarev,

ORCID: <https://orcid.org/0000-0003-2803-8281>

E-mail: 9293522@gmail.com

Antonina Karlina,

ORCID: <https://orcid.org/0000-0003-3287-3298>

E-mail: karlinat@mail.ru

Received 06.07.2021. Approved after reviewing 13.12.2021. Accepted 16.12.2021.



Research article

UDC 691.3

DOI: 10.34910/MCE.114.14



Comprehensive assessment for optimal wind energy use in cottage construction

A.A. Fedorovskaya , S.G. Sheina 

Don State Technical University, Rostov-on-Don, Russia

✉ bina-87@mail.ru

Keywords: energy efficiency, renewable energy sources, optimization, energy conservation, sustainable development

Abstract. The article considers the significance of an integrated assessment of the territory to ensure its sustainable development and use of its results when choosing a particular type of alternative energy source for a particular built-up area. RES (renewable energy sources) are types of energy that are continuously renewed in the Earth's biosphere (solar, wind, water, tidal energy, waves of water objects, including water bodies, rivers, seas, oceans, biogas, gas produced by waste products and consumption in landfills of such waste, gas generated from coal mining). The research presents a database of a geoinformation system for the selection and use of RES for housing construction, while multi-criteria evaluation is used in this case to determine the level of sustainable development of the territory of municipalities. The main factors in the selection and introduction of renewable energy sources in housing construction are the natural parameters, i.e. the wind region. Climate-forming factors of territory estimation are presented, as well as their dependence on climatic conditions. This system of territory assessment has been tested on the example of the Rostov Region in area of wind energy. Based on the maps built in ArcGIS ESRI, the territory of the Rostov Region is visually represented and its suitability is estimated for the introduction and development of wind energy source. The developed system is compared with the well-known works in the field of renewable energy sources; the use of GIS technologies reveals the advantages of the authors' system. Detailed conclusions were made based on the results of the study: an integrated system for choosing the location of the RES are adapted for the conditions of the Rostov region.

Citation: Fedorovskaya, A.A., Sheina, S.G. Comprehensive assessment for optimal wind energy use in cottage construction. Magazine of Civil Engineering. 2022. 114(6). Article No. 11414.
DOI: 10.34910/MCE.114.14

1. Introduction

The goal of the energy policy at present is to provide conditions for energy supply to people while preserving the environment. This can be achieved by reducing power requirement and introducing renewable energy resources (hereinafter referred to as RES) into the economy. It is definitely worth highlighting and considering wind power engineering, which steadily holds the world leadership among new technologies of renewable energy resources. The most advantageous regions of Russia from the viewpoint of wind power generation are the territories located far from the main power generating capacities of the country. By analogy, at the level of a constituent entity of the Russian Federation these are the territories of rural settlements remote from urban districts, but having natural and resource potential for the development of this area and for the use of RES [1–3].

The object of the research is the Rostov region territory, because since 2020 the following three wind-power stations were developed and commissioned in Rostov region: Kamensk wind-power station (hereinafter referred to as WPS), Sulin WPS, and Gukovo WPS. On March 1, 2020, Sulin WPS began supplying electricity and power to the Wholesale Electricity and Power Market (WEPM). Active work at sites

under the three projects of the Wind Energy Development Fund is currently being carried out in Rostov region. WPSs provide very low average annual specific electrical output (capacity), which is hundredfold or thousandfold lower than that of conventional power plants, however, the use of these capacities in cottage construction is quite reasonable from the point of view of sustainable development, preservation of natural and resource potential of the territory. In addition, one of the goals of the Strategy of Rostov region for the period until 2030 is to stimulate and develop housing construction, including low-rise housing construction, which confirms the relevance of the study undertaken.

The definition of the theoretical and methodological foundations for the development of renewable energy, the placement of RES installations in the context of the use of GIS are in the focus of attention of modern researchers. Foreign energy specialists already have successful experience in applying GIS technologies in the energy industry [4].

In the studies of Russian scientists, the features of the use of GIS in making managerial decisions on the energy development of territories are actively studied. V.L. Badenko analyzes the issues of effective search for RES sites, comparison of sites in the GIS environment in order to make the most effective management decision and meet the requirements of the investor [5].

It should be noted that in some regions of the Russian Federation there are favorable prerequisites for organizing the process of using and developing RES, including the natural and technical resources of the territory [4, 5].

RES in consumers isolated from the centralized electricity grid is a worthy alternative to traditional energy sources. At the same time, the topic of suburban low-rise housing using RES is relevant both in terms of environmental friendliness and sustainable development, as well as in terms of development of the architecture of energy-efficient houses and territorial planning.

According to the Renewable Energy Policy Network for the 21st Century (REN21) [6] tens of millions of people use renewable energy installations today. In rural areas of developing countries, 25 million people use biogas and solar plants for cooking and lighting their homes. It is interesting to note that developing countries account for only about 40% of the total capacity of all power plants based on renewable energy sources, 60% of installations are used in developed countries, which indicates their fairly high competitiveness in relation to other modern energy technologies.

The purpose of the study is to develop an integrated system for selecting a renewable energy source for cottage construction using the example of the Rostov region.

As part of the implementation of this goal, the following tasks have been identified:

- to determine the factors for the use of RES;
- to demonstrate the proposed system for selecting a territory for the use of RES for housing construction using the example of the Rostov region;
- to consider the concept of an eco-house, the pros and cons of this type;
- to demonstrate the practical application of the developed system within the framework of the construction of a low-rise cottage village on the territory of the Rostov region with the use of renewable energy sources [7].

A theoretical toolkit for combining the choice of a place for WPS construction with the choice of a place for cottage estate construction in the territory of Rostov region is presented in the study. The possibility of reducing energy consumption in the sphere of housing construction through the introduction of energy-saving technologies with the definition of their energy efficiency and economic feasibility is considered separately.

2. Methods

The preliminary stage of choosing a place for WPS necessary for low-rise housing construction is creation of a database in the geoinformation system. The scheme of creating a database is presented in Figure 1. It includes collection and analysis of legislative and normative acts, as well as different provisions of strategic documents and territorial planning, climatology and urban development zoning documents.

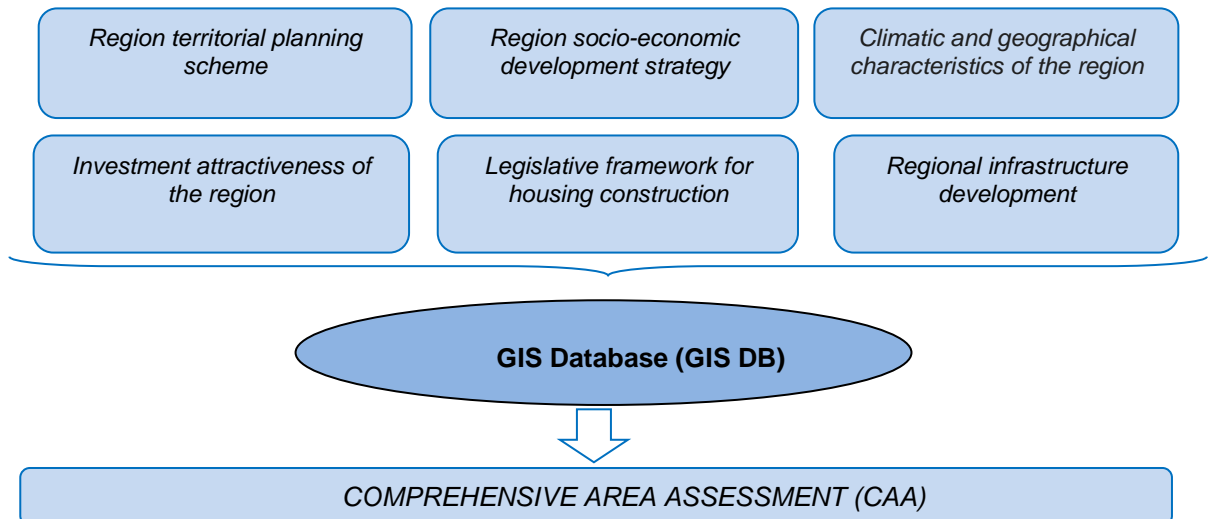


Figure 1. Scheme of creation of the database of the geoinformation system for selection and use of WPS for housing construction.

Collection and analysis of actual information on the region of construction allows creating the database of the geoinformation system of selection and use of WPS for housing construction. Complex assessment of the territory is a set of factor-based cartographic, statistical and tabular materials concerning the state of the territory of the Russian Federation constituent entity, integrated into a single shell, systematized and presented in the form of electronic maps [3,8]. According to the presented scheme, the initial data are systematized and used for creating the information system (GIS DB). The analysis of the legislative base in the sphere of housing construction and use of WPSs (in our case, for Rostov region) is carried out.

All the information collected and analyzed is the basis for making decisions and conducting a comprehensive assessment of the region. In order to select the territory for WPS construction and to construct necessary facilities for its use for energy saving, it is necessary to take into account various factors, both natural and infrastructural and spatial-economic [7]. Therefore, the system of factors is interpreted for the purposes of WPS selection and housing construction and is presented in Table 1. Cartographic, statistical and tabular materials concerning the state of the territory of the Russian Federation constituent entity are interpolated and given in the single score-based system of assessment within the limits from 0 to 1. The assessment sites are the borders of the municipal units of the Russian Federation constituent entity.

Table 1. System of factors of comprehensive assessment of the territory using renewable wind energy sources in housing construction.

Factor group	Factor	Score rating
Natural (climate-forming) factors [9]	Wind velocity	0–1
	Differences in elevation of the earth surface	0–1
Infrastructural factors	Water supply and sewerage	0–1
	Gas supply	0–1
	Transport	0–1
	Communication networks	0–1
Spatial and economic factors	Investment attractiveness of the region	0–1
	Distance to major regional centers	0–1

Electronic maps, which allow visualizing the results of complex evaluation by factors, are created in ArcGIS ESRI environment by filling in attributive tables. As an example, maps concerning climatic and infrastructural factors of the Rostov region territory as fundamental factors in the resource-based constituent of WPS association with the objects of the planned housing construction are presented. The distribution of points in determining the average monthly wind velocity is presented in Table 2.

Table 2. Territory assessment based on the average monthly wind velocity in different areas of Rostov region.

No.	Wind velocity, m/s	Score
1.	0–2.5	0
2.	2.5–3	0.50
3.	3–4.5	0.75
4.	>5	1.00

Nevertheless, it should be noted that the territory of Rostov region is assessed by all factors of complex assessment, and color classification allows visualizing the results obtained (Figure 2).

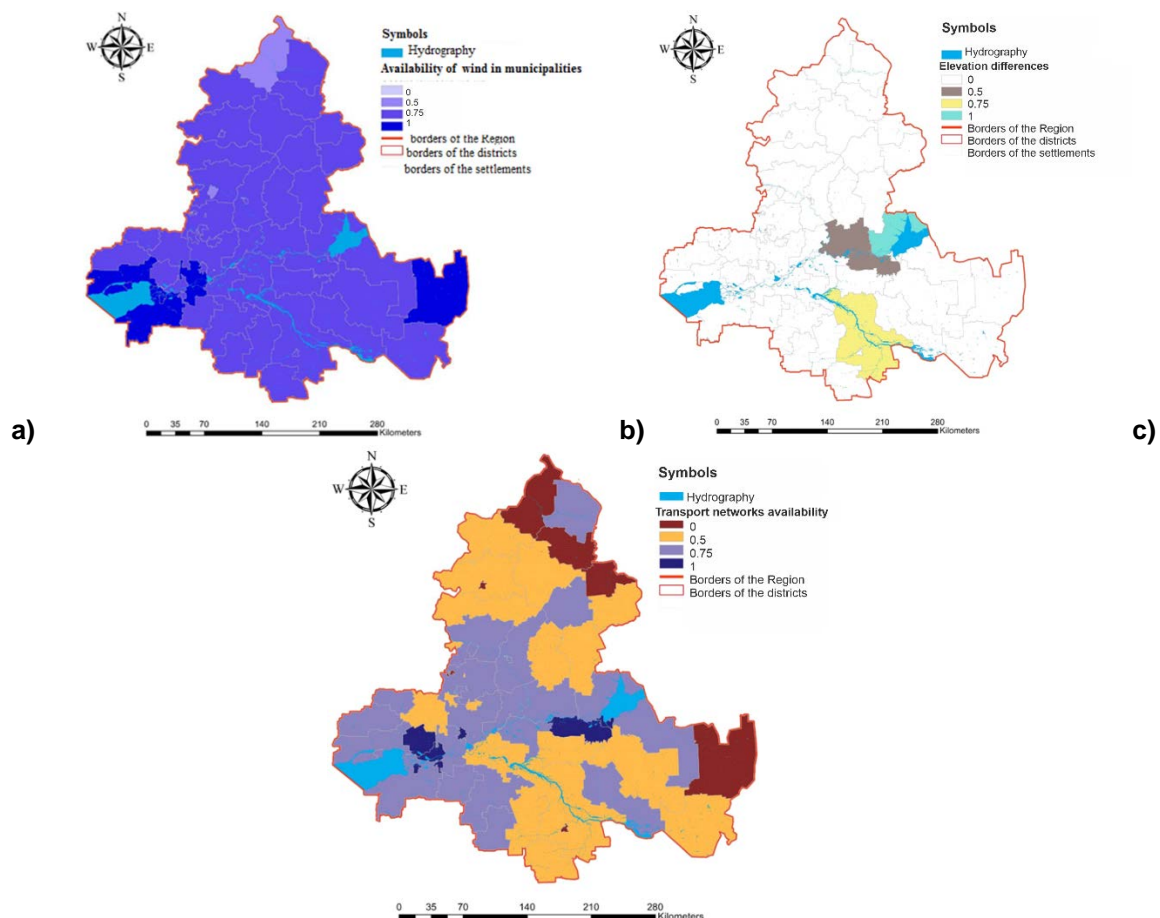


Figure 2. Comprehensive assessment of the Rostov region territory by climate formative factors: a) monthly average wind velocity, b) elevation differences, c) transport networks availability.

It is expedient to use wind-driven generators and wind turbines in districts, municipalities or urban districts, the assessment of the territory of which based on the average monthly wind velocity corresponds to 1 [5, 10]. However, after this assessment, it is required to additionally analyze the territory of the region in terms of the parameter - the average monthly wind speed, because the wind speed >5 m/s is a rather diffuse value.

According to the Territory Comprehensive Assessment Maps (Figure 2), areas having such a high natural resource-based (score – 1) and infrastructure-based (score: 0.75–1) potential are Azov, Aksay and Oktyabrsky areas. The majority of the municipal areas have medium potential for WPS placement. As an example of WPS placement, as well as for the purpose of the construction of low-rise cottage estate on the basis of the comprehensive assessment of the territory of Rostov region, Azov area was chosen.

Within the framework of the study, a system of refined territory assessment has been developed. It allows analyzing the territory of a municipal entity from the point of view of low-rise construction

development and application of energy-efficient technologies [6]. In order to carry out a more accurate comprehensive assessment of a municipal entity, it is necessary to determine the assessment factors (TCOT factors). The system of factors has been created for the purpose of WPS selection and low-rise cottage construction. Cartographic, statistical and tabular materials concerning the state of rural settlements of Azov area are interpolated and given in the form of the unified system of assessment within the limits from 0 to 1. The assessed sites are the boundaries of the rural settlements of the Azov area (Table 3).

Table 3. Factors of more accurate comprehensive area assessment.

Factor group	Factor	Score rating
Natural (climate-forming) factors	Wind velocity	0–1
	5–6	0.25
	7–8	0.50
	9–10	0.75
	>10	1
Free areas	Periphery existence	0–1
Low-rise (cottage) construction	Environmental burden	0–1
	The remoteness of the construction area from industrial zones	0–1
	Existence of recreational zones in rural settlements	0–1

An example of the results of the refined comprehensive assessment of the territory of Azov area is shown in Figure 3. The color classification of the factor is the existence of periphery in rural settlements of Azov area of Rostov region and in the urban district of the town of Azov. It should be noted that electronic maps of the refined comprehensive assessment are created for all four factors [11].

To obtain data on the average monthly wind speed in the Azov area, the natural resource potential of the Azov area was analyzed, which is characterized by an average monthly wind speed of 5.5 m/s, but data on wind speed in the region vary significantly. It became known that the average monthly wind speed on the coast of the Azov sea is 7 m/s, and in winter this figure rises to 9.4 m/s (0.75 score in updated estimate). Therefore, according to the main climatic factor, it is worth choosing the coastal settlements of the Azov region [10, 29].

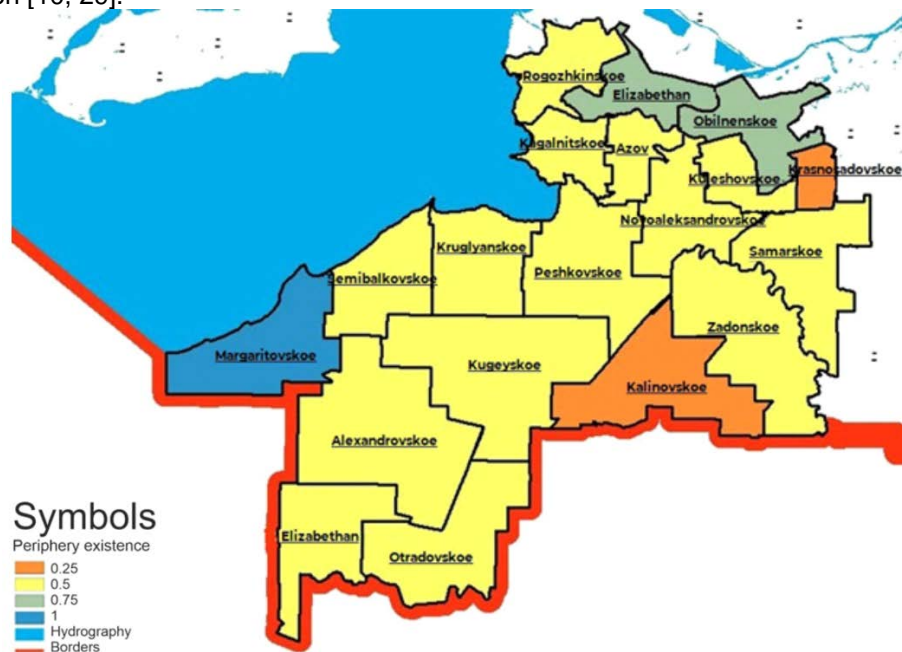


Figure 3. Periphery existence in rural settlements of Azov area of Rostov region and in the urban district of the town of Azov.

Based on the constructed maps, we can conclude that Margaritovskoe rural settlement, located on the coast of the Azov sea, is suitable for the construction of a low-rise cottage village using renewable energy. This conclusion allows choosing a place for the construction of a wind farm. For this purpose, we have analyzed the master plot plan of Margaritovskoye rural settlement, the balance of the territory, and the ecological situation. A plan of measures to improve the ecological situation in Azov area of Rostov region, as well as directly in Margaritovskoye rural settlement has also been developed. The results of

implementation of a set of environmental and infrastructure measures in Margaritovskoye rural settlement are shown in Table 4.

Table 4. Results of implementing a set of environmental and infrastructure measures [12].

No.	Factor	Measures	Efficiency (result of improvement)
1	Atmospheric air condition	Creation of sanitary protection zones, purification plants, introduction of technologies with lower emissions, purification of emissions of impurities [14]	Decrease in the complex air pollution index
2	Contamination of soils with heavy metals	Development of systems for processing of production wastes converting such wastes to secondary material resources; replacement of toxic wastes with non-toxic ones; replacement of non-recyclable wastes with recyclable ones	Decrease in soil pollution, decrease in the amount of waste entering the soil
3	Drinking water quality	Development of various types of drainless technological systems and water recycling on the basis of waste water treatment methods	Reduction in the amount of waste water emissions and the concentration of pollutants in them
4	Ecological potential of territories	Withdrawal of industrial enterprises from large cities and construction of new ones in sparsely populated areas with lands hardly suitable or unsuitable for agricultural use; optimal location of industrial enterprises taking into account the topography of the area and the rose of winds [16]	Improvement of the composite environmental quality indicator in the region [15]

Then a project for the construction of a wind farm has been developed. The project is a 90 MW wind-power station (WPS) located in the southwest of Rostov region, on the border with Krasnodar territory (Figure 4).

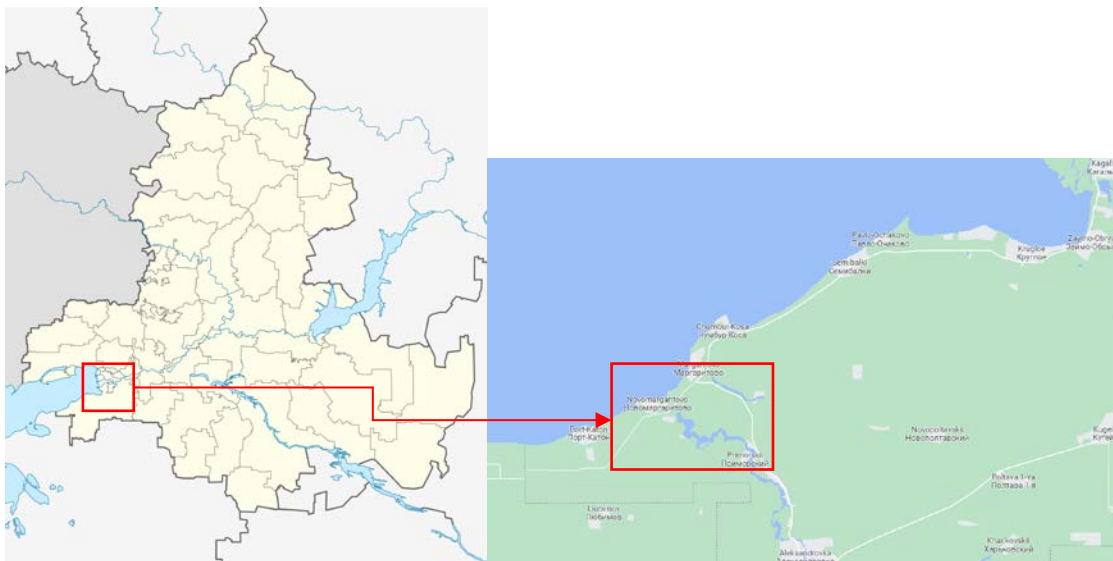


Figure 4. WPS project location.

The land plot selected for the construction of the WPS is located 2 km west of the village of Port-Katon in the territory of Margaritovskoye rural settlement of Azov area of Rostov region. The total area considered for construction of the WPS is 1093 hectares. It is the territory of the former Azov-City gambling zone.

It is assumed that 30 wind turbine generator sets (hereinafter referred to as WTGS) with capacity of 3 MW each, crane bases adjacent to each turbine, temporary construction sites for internal roads, internal power supply network, power substation including a control room and connection to the power grid will be placed. Other types of WTGS can be used to improve the efficiency of WPSs. In this case, the number of turbines can be reduced, while the unit capacity of the turbine will vary between 2.0 and 3.3 MW. In accordance with the feasibility evaluation, connection of the WPS project to the grid is envisaged by connecting it to the existing 35 kV overhead power line, which was constructed for Azov-City gambling zone and is not currently in operation. The overhead power line is led from the eastern side of the WPS project. To connect the wind farm to the electric power network, work on the modernization of the existing power line will be carried out, and new overhead power lines will be constructed.

A project of a low-rise cottage estate in the territory of Margaritovskoye rural settlement of Azov area of Rostov region has been developed. The planning design of the settlement provides for the placement of 320 cottage-type individual houses on the territory of 52 hectares. (Figure 5).

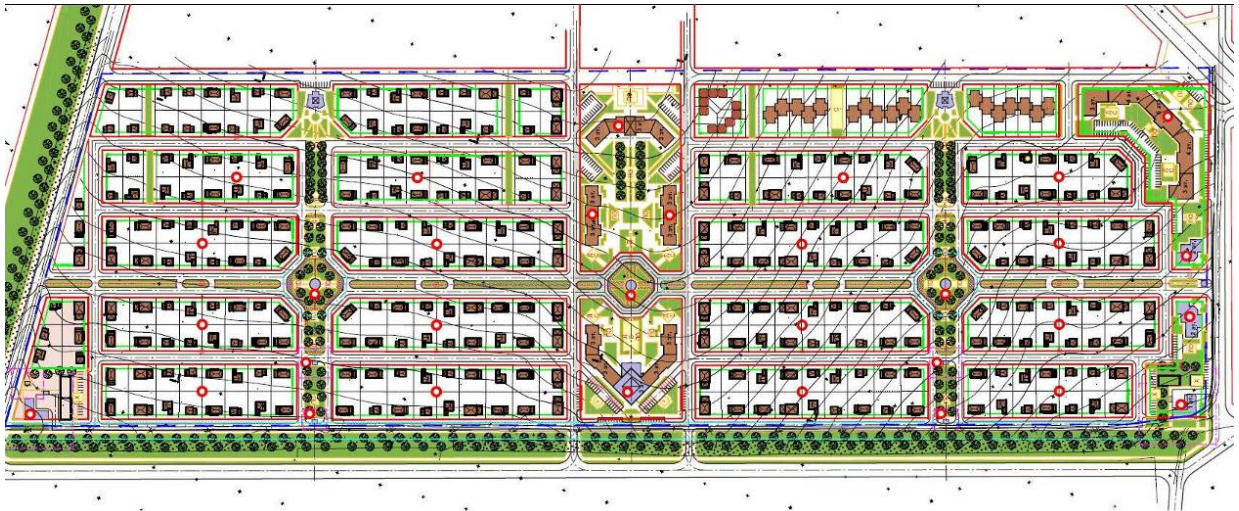


Figure 5. Settlement planning design.

The architectural and landscape design of the settlement has a single style. The cottage estate living conditions will be as comfortable as in the city: gas, water, electricity, central sewerage, individual hot water and heating boilers are provided in each house.

The project envisages the use of 15 types of cottages and 2 types of townhouses.

Each project also has from 2 to 4 variants of facade and interior layout. There are several options for the external design of the house, developed in a single style, which will give the effect of a variety of options for the houses of the settlement, maintaining a single basic set of structures of the house, which facilitates equipment recording and construction. In spite of all variety and plurality of projects, the given approach guarantees that any chosen variant will harmoniously fit in the general architectural concept of the complex. However, there is no single concept for the introduction of energy-saving technologies in the projects of the cottages [17, 18]. Thus, there is another problem at the local level: the choice of energy efficient technologies in cottage construction.

The significant cost of energy efficiency measures allows choosing only those solutions that have a relatively low cost and give maximum benefit from their use. On this basis, the expected efficiency of energy-saving technologies will be calculated by comparing the costs of their installation and purchase with the energy saving from their use, taking into account relevant information on the payback period [19, 20].

Passive energy-saving technologies have been largely successful to date in the energy-efficient low-rise construction in Russia. The main passive energy saving methods used are as follows:

- installation of energy-efficient equipment,
- use of high-tech systems (Smart Home system) [21, 22],
- application of Canadian structural insulating panel construction technology (SIP),
- improvement of the thermal efficiency of building envelopes (heat insulators ISOVER, ROCKWOOL) [23].

Let us consider the main indicators of these energy-saving solutions given in Table 5 and make a comparative analysis in terms of their economic and energy efficiency.

Table 5. Comparative analysis of energy-saving solutions applied in low-rise (cottage) construction.

Energy-efficient measure	Value (cost)	Energy output, kW·h/year	Saving of energy per year, Russian rubles (RUB)	Payback period, years
Energy-efficient equipment	1 541 658 RUB	34000	122 433.1	8–16
Smart Home system	5–7 thousand RUB/m ²	3212	12 000	15–40
Canadian SIP house	20–30 thousand RUB/m ²	15000	54 000	10–20
Multi-comfort ISOVER house	Rise in price 15–18%	11 710	42 156	15–40
Energy-efficient house Green Balance	Rise in price 14.5%	9 125	32 850	15–40

According to the data obtained, the most cost-effective application of energy-efficient measures in low-rise construction is the use of energy efficient equipment. The expediency of using such equipment is determined by the largest amount of energy produced in comparison with other options and energy-efficient measures considered in this paper, as well as by the corresponding economic component achieved by saving energy costs, which is reproduced by alternative sources [24–25].

3. Results and Discussion

The construction of WPSs in the territory of Rostov region has attracted considerable investments, which will increase the workload of logistics centers, as well as provide design, construction, electrical and other organizations and companies with additional work [26]. The technical and economic indicators of the WPS construction project are presented in Table 6.

Table 6. Technical and economic indicators of the WPS construction project.

No.	Name of indicator	Unit of measure	Design value
	Azov wind-power station (WPS)		
	power (capacity)	MW	90
	electric power output	thousand kW·h	442 072
	electric power supply	thousand kW·h	418 556
	Substation 110/35/10kW WPS	MVA	2x63
	Total length of power lines (along the route) / number of lines, including	km	
	High-voltage power lines 110 kV	km/line	121/2
	Cable lines 35 kV WPS	km	1
	Occupied area		133
	Design lands of WPSs	ha	225
	High-voltage power lines	ha	5
	Total cost of construction, according to the limit values of capital costs included in the competitive indicators for the selection of investment projects for the construction of generating projects operating on renewable energy sources for the years 2014–2024	thousand RUB	9 870 300
	Construction duration	month	20
	Number of workplaces at the stage of operation	person	20–30
	Investment payback period	year	15

Nevertheless, it should be noted that the development and implementation of the WPS project in Rostov region will allow diversification of generating capacities without harming the environment.

Comparing the results of the work, one can refer to Badenko's research; the developed GIS RES can be valuable when an investor/user chooses a solution for implementing a project in the field of renewable energy:

- based on the results of the study, an analysis of social, economic and environmental factors in choosing the location of a RES facility was carried out, as well as practical steps or a package (composition) of work within the framework of the implementation of GIS RES;

- development of a decision support system for the placement of renewable energy facilities in the form of an information and analytical geoinformation system "Renewable energy sources of St. Petersburg and the Leningrad region" will determine the limiting factors for the choice of renewable sources, create interactive maps of St. Petersburg and the Leningrad region [27, 28].

However, Badenko does not use climatic factors in the process of optimizing management decisions, which are the main ones in the placement of RES. This validates uniqueness and relevance of the system developed in our study.

4. Conclusions

1. Renewable energy sources (RES) are not developed in the territory of Russia, as the housing stock must meet specific technical requirements to implement RES programs. However, at present the housing stock of the Russian Federation is in unsatisfactory condition. As a rule, the introduction of RES is technically possible in the majority of cases, when it comes to new housing. The factors for the use of RES are determined. We can say with even greater certainty that low-rise cottage construction objects have the best conditions for RES introduction.

2. The demonstrated theoretical toolkit allows for a comprehensive assessment of the territory for the use and construction of wind-power stations (WPS) both at the level of a constituent entity of the Russian Federation and at the level of a municipality combining engineering infrastructure, environmental, planning, natural-resources and spatial and economic aspects. The proposed system for selecting a territory for the use of RES for housing construction using the example of the Rostov region are demonstrated.

3. The development of WPS projects is a promising area of the energy industry worldwide. The production of wind-powered generators is a high-tech industry, the development of which is characterized by attracting large investments. In addition, on the basis of the considered data it is possible to draw a conclusion that the most effective energy saving measure in low-rise construction is the use of unconventional kinds of energy, which replace the use of external energy sources, allowing a building to exist independently. Practically, the concept of an eco-house with the pros and cons of this type are shown in this research in detail.

4. The paper demonstrated the practical application of the developed system within the framework of the construction of a low-rise cottage village on the territory of the Rostov region with the use of renewable energy sources. The method has shown the maximum economic feasibility and has the most useful effect in comparison with other technologies considered in the study.

References

1. Borodikhina, E.V., Chikurova, O.S., Obukhova, A.A. Renewable energy. Book of reports. International research-to-practice conference 'Ural Mining School – for regions'. [Online]. System requirements: URL: http://science.ursmu.ru/upload/doc/2017/06/27/sbornik_dokladov_ugpd-2017.pdf (date of application: 01.02.2017).
2. Motulevich, A.V. Prospects of using renewable energy in Russia and abroad. Energy reliability and safety. [Online]. System requirements: URL: <https://elibrary.ru/item.asp?id=27149293> (date of application: 01.02.2017).
3. Mottaeva, A. Innovative Aspects of Ecological and Economic Management of Investment and Construction Activities for the Sustainable Development of the Region. MATEC Web Conf. 2016. 73. 07020. DOI: 10.1051/mateconf/20167307020
4. Badenko V.L., Epova E.I. The concept of creating a geoinformation system "Renewable energy sources of St. Petersburg and the Leningrad region". Collection of materials of the II international scientific-practical conference "Geodesy, cartography, geoinformatics and cadastres. From idea to implementation". Polytechnic. St. Petersburg, 2017. Pp. 500-504.
5. Siksnyte, I., Zavadskas, E.K., Streimikiene, D., Sharma, D. An overview of multi-criteria decision-making methods in dealing with sustainable energy development issues. Energies. MDPI AG. 2018. DOI: 10.3390/en11102754
6. Renewable Energy Policy Network for the 21st Century [REN21] [Online]. URL: <https://www.ren21.net/> (reference date: 01.02.2017).
7. Sheina, S.G., Fedorovskaya, A.A., Sheveleva, A.A. Comprehensive area assessment as a mechanism for selecting the location and type of alternative energy source. CEB: Construction Equipment Bulletin. 2017. [Online]. URL: <https://elibrary.ru/item.asp?id=30030804> (date of application: 20.05.2020).
8. Phillis, A., Grigoroudis, E., Kouikoglou, V.S. Assessing national energy sustainability using multiple criteria decision analysis. International Journal of Sustainable Development and World Ecology. 2020. 1–18. DOI: 10.1080/13504509.2020.1780646.

9. Kuzhin, M., Chepik, E., Baranova, A. Influence of natural and climatic factors on the organization of construction. E3S Web of Conferences. EDP Sciences. 2020. 164. DOI: 10.1051/e3sconf/202016408006.
10. Global Wind Energy Council, Global wind report [GWEC] [Online]. URL: <https://gwec.net/global-wind-report-2018/> (reference date: 05.07.2018).
11. Shcherbina, E.V., Gorbenkova, E.V. Modelling the rural settlement development. Materials Science Forum. Trans Tech Publications Ltd. 2018. 931. Pp. 877–882. DOI: 10.4028/www.scientific.net/MSF.931.877.
12. Kasyanov, V.F., Gribov, D.V. Energy saving measures in urban planning [Bulletin of Moscow State Construction University]. MSCU. 2011. 8. Pp. 44–49.
13. Oke, T.R., Mills, G., Christen, A., Voogt, J.A. Urban climates. Urban Climates. Cambridge University Press. 2017. DOI: 10.1017/9781139016476.
14. Jayasooriya, V.M., Ng, A. W. M., Muthukumar, S., Perera, B. J. C. Green infrastructure practices for improvement of urban air quality. Urban Forestry and Urban Greening. 2017. 21. Pp. 34–47. DOI: 10.1016/j.ufug.2016.11.007.
15. Bespalov, V., Kotlyarova, E. Improving the environmental assessment of objects in the system of construction engineering. E3S Web of Conferences. EDP Sciences. 2020. 164. DOI: 10.1051/e3sconf/202016401009.
16. Graboviy, P. Environmental aspects of substantiation of the production decision efficiency. MATEC Web of Conferences. EDP Sciences. 2018. 193. DOI: 10.1051/mateconf/201819305017.
17. Sheina, S.G., Khamavova, A. A. Spatial analysis of energy efficiency in municipal housing stock by the example of Rostov-on-Don [Bulletin of Moscow State Construction University]. MSCU. 2011. 3-1. Pp. 310–313.
18. Kasyanov, V., Danilchenko, V., Amelin, V., Tolmacheva, V. Environmental risk management. Forecasting and modeling of emergency risk management situations. MATEC Web of Conferences. EDP Sciences. 2018. 251. DOI: 10.1051/mateconf/201825106030.
19. Kasyanov, V., Prelovskaya, Y. Allocation private building in urban city and along the transport arteries for creating a modern energy-efficient living environment. IOP Conference Series: Earth and Environmental Science. Institute of Physics Publishing. 2017. 90. DOI: 10.1088/1755-1315/90/1/012008.
20. Bai, Y., Zadeh, P.A., Staub-French, S., Pottinger, R. Integrating GIS and BIM for community-scale energy modeling. International Conference on Sustainable Infrastructure 2017: Methodology - Proceedings of the International Conference on Sustainable Infrastructure. American Society of Civil Engineers (ASCE). 2017. Pp. 185–196. DOI: 10.1061/9780784481196.017.
21. Zilberova, I.Yu., Petrova, N.N. Modernization of buildings for the purpose of improving energy efficiency, comfort and safety of living, as well as extending the service life of residential buildings. Don Engineering Bulletin. 2012. [Online]. URL: ivdon.ru/magazine/archive/n4p1y2012/1120 (reference date: 01.02.2017).
22. Zilberova, I.Yu., Petrova, N.N., Petrov, K.S. Energy efficient reconstruction of the brownfield construction of residential areas and neighborhoods. Don Engineering Bulletin. 2012. [Online]. URL: ivdon.ru/magazine/archive/n4p2y2012/1295 (reference date: 01.02.2017).
23. Sibikin, Yu. D., Sibikin, M. Yu. Unconventional and renewable energy sources. Moscow: Knorus, 2012. 232 p.
24. Chourabi, H., Nam, T., Walker, S., Gil-Garcia, J. R., Mellouli, S., Nahon, K., Scholl, H. J. Understanding smart cities: An integrative framework. Proceedings of the Annual Hawaii International Conference on System Sciences. IEEE Computer Society. 2012. Pp. 2289–2297. DOI: 10.1109/HICSS.2012.615.
25. Shcherbina, E., Gorbenkova, E., Slepnev, M. Urban-planning sustainability problems in a city natural framework. MATEC Web of Conferences. EDP Sciences. 2017. 106. DOI: 10.1051/mateconf/201710601032.
26. Ivanova, Z., Yudenkova, O., Naimaviciene, J. Biosphere Compatibility as a Principle of Sustainable Urban Development. MATEC Web of Conferences. EDP Sciences. 2016. 73. DOI: 10.1051/mateconf/20167307008.
27. Epova, E.I. Theoretical and methodological aspects of creating a decision support system for the development of non-traditional energy in the form of an information and analytical geoinformation system "Renewable energy sources of St. Petersburg and the Leningrad region". XXIV International Scientific and Practical Conference of Students, Postgraduates and Young Scientists "Lomonosov". Moscow, 2017. Pp. 37–39.
28. Epova, E.I. Theoretical and methodological aspects of creating a geoinformation system "Renewable energy sources of St. Petersburg and the Leningrad region". International scientific-practical conference for students, graduate students and young scientists "Theory and practice of modern geographical research", dedicated to the 220th anniversary of the outstanding Russian navigator, geographer, vice-chairman of the Russian Geographical Society F.P. Litke as part of the XIII Great Geographical Festival. Own Publishing House. St. Petersburg, 2017. Pp. 551–553.
29. Aleksenko, V.N., Martynova, M.I. Geography of the Rostov region. Rostov-on-Don: Terra, 2005. 153 p.

Information about authors:

Albina Fedorovskaya,
PhD of Technical Science
 ORCID: <https://orcid.org/0000-0002-6096-5889>
 E-mail: bina-87@mail.ru

Svetlana Sheina
Doctor of Technical Science
 ORCID: <https://orcid.org/0000-0001-5214-0767>
 E-mail: rqsu-gsh@mail.ru

Received 26.07.2020. Approved after reviewing 18.02.2022. Accepted 22.02.2022.

